2012

Recurrent novae and Type Ia supernova progenitors

Ashley Sara Pagnotta
Louisiana State University and Agricultural and Mechanical College

RECURRENT NOVAE AND TYPE IA SUPERNOVA PROGENITORS

A Dissertation

Submitted to the Graduate Faculty of the
Louisiana State University and
Agricultural and Mechanical College
in partial fulfillment of the
requirements for the degree of
Doctor of Philosophy

in

The Department of Physics and Astronomy

by
Ashley Sara Pagnotta
B.A., Physics, Texas A&M University, 2007
B.A., Mathematics, Texas A&M University, 2007
M.S., Physics, Louisiana State University, 2010
May 2012

Dedication

For everyone who has ever gazed upon the night sky with wonder.

"We are all in the gutter, but some of us are looking at the stars."
Oscar Wilde, *Lady Windermere's Fan*

"I have loved the stars too fondly to be fearful of the night."
Sarah Williams, *The Old Astronomer to His Pupil*

Acknowledgments

First and foremost, I would like to thank my parents, Tony and Margaret Pagnotta, and my brother, Alex Pagnotta, for their never-ending support and encouragement as I have pursued my dreams.

I would also like to thank my advisor, Bradley Schaefer, for consistently expecting more of me than I thought myself capable of. His guidance and instruction have been invaluable.

Many members of the LSU Department of Physics and Astronomy have taught me in and out of the classroom over the past five years. In particular my committee members Robert Hynes, Juhan Frank, and Gabriela Gonzalez, as well as Geoffrey Clayton and Arlo Landolt, have been instrumental in my success. Thanks also to my collaborators Eric Schlegel and Michael Shara for many helpful discussions and even more letters of recommendation. I have been blessed to have a number of wonderful math and science teachers over the years, who deserve many thanks: Stephanie Ingle, Loweta Jorgensen, and Onnie Sherrer at Kingwood High School, and Roland Allen, Harold Boas, N. Sivakumar, and Michael Stecher at Texas A&M University.

To the grad students and postdocs who shared their advice and experiences, I am forever indebted: Jen Andrews, Jeff Kissel, and Shannon Fritz, for more than I could ever express, but most especially for their friendship; Sarah Caudill, my writing partner; Andrew Collazzi and Limin Xiao, fellow group members extraordinaire; Brent Budden, Zach Byerly, Tiffany Driscoll Barboza, Nicole Gugliucci, Azadeh Keivani, Valerie Mikles, Sherry Myers, Geoff and Gena Nichols, Bill Plick, James Rodi, Erin Ryan, and Emma Walker, for exceptional amounts of help and encouragement.

Thank you to my non-physics friends, most especially Amanda Borowski, Amy Palmer, Erin Greenberg, Liz Cooke, Kim Guillot, Sara DeRosa, and Kristin Budden, who never failed to listen when I rambled incessantly about exploding stars. Along the same lines, thank you to my knitting groups, both analog and digital, who kept me laughing.

Many thanks go to the staff at the Harvard and Sonneberg Plate Archives, especially Alison Doane, Jaime Pepper, Josh Grindlay, and Ed Los at Harvard, and Peter Kroll and Klaus Löchel at Sonneberg, for their help and hospitality.

The following observers contributed to the 2010 eruption of U Sco; we could not have had a successful observing campaign without them: Arlo Landolt, James Clem, Kim Page, Julian Osborne, Gerald Handler, Fred Walter, Douglas Hoffman, Sebastien Lepine, Michael Bode, Matthew Darnley, Hannah Worters, Bill Allen, Tom Krajci, Berto Monard, Robert Rea, Thomas Richards, George Roberts, William Stein, Chris Stockdale, Jennie McCormick, Sean Dvorak, Tomas Gomez, Barbara Harris, Arne Henden, George Sjoberg, Thiam Guan Tan, Matthew Templeton, Arto Oksanen, Seiichiro Kiyota, and Hiroyuki Maehara.

This work has been supported in part by National Science Foundation grants AST-0708079 and AST-1109420, the LSU Board of Regents, the LSU Graduate School, the Louisiana Space Consortium, the National Optical Astronomy Observatory, and the American Astronomical Society.

Table of Contents

List of Tables

List of Figures

Abstract

We investigated two types of stellar explosions, recurrent novae (RNe) and Type Ia supernovae (SNe Ia). SNe Ia are the most useful distance markers in astrophysics, but we do not know the identity of their progenitor systems. RNe are good progenitor candidates that consist of a white dwarf (WD) that accretes material from a companion star. The material builds on the surface of the WD until a runaway thermonuclear eruption is triggered, which ejects the accreted material and causes the system to brighten dramatically. We studied the demographics of the nova population and concluded that approximately 25% of classical novae are actually RNe for which only one eruption has been discovered. Importantly, this means that there are enough RNe in our galaxy to provide a significant fraction of the SNe Ia. We present a list of good RN candidates; for one such system, V2487 Ophiuchi, we sought and found a previous eruption in the astronomical plate archives.

We examined two known RNe in detail. T Pyxidis has a unique shell; we used observations of the shell and central star to produce a new model for the long-term evolution of the system, which will never become a supernova. U Scorpii erupted in 2010 as predicted. We led a worldwide collaboration of astronomers that discovered the eruption and comprehensively observed it from start to finish. We discovered three new phenomena and were able to make the best-yet measurement of the amount of mass ejected during the eruption.

We searched the centers of nearby SN Ia remnants looking for ex-companion stars left behind after the WD exploded centuries ago. For one remnant, SNR 0509-67.5, we can definitively state that there are no ex-companion stars in the center of the remnant and therefore the system must have consisted of two WDs that collided to form the SN Ia. The other nearby remnants have possible ex-companion stars; more observations are needed to determine which, if any, are the true ex-companions. Some large fraction of the SNe Ia must come from double-WD systems, but there is a possibility that RNe provide a significant fraction as well.

1. Introduction

1.1 Classical and Recurrent Novae

The stellar eruptions known as novae have been recorded as far back as 134 BC by Hipparchus of Nicaea (Fontanille 2007) and yet are still not well understood, despite centuries of observations, including recent comprehensive observing campaigns. Novae come in two main types, classical and recurrent. Both involve the same system components–a white dwarf (WD, the dense core of an old star) in a close binary orbit with another, non-degenerate star–and eruption mechanism: the high gravitational pull of the WD combined with the proximity of the companion star creates a steady transfer of mass, known as accretion, onto the surface of the WD. This gas, mostly hydrogen, builds up on the surface of the WD until the conditions at the base of the accreted layer reach a point at which nuclear burning is ignited, and a thermonuclear runaway eruption is triggered. The eruption propels the accreted material away from the WD in an expanding shell, with velocities that range from a few hundred to a few thousand kilometers per second, and is seen as a sudden brightening of the system, which lasts for a period of hours to days, followed by a slow decline in brightness over the next few weeks to months. The name "nova" comes from "stella nova", Latin for "new star", which describes the appearance of a new star in the sky where none was seen before. After the eruption, the WD remains intact, and the accretion process resumes.

In recurrent novae (RNe), as the name implies, the eruptions recur on observable timescales, usually defined as more than one eruption in a given century. Two system characteristics contribute to this short inter-eruption timescale: a high-mass WD and a high accretion rate (Sekiguchi 1995; Townsley 2008). The high-mass WD has a correspondingly high surface gravity, so a smaller amount of accreted mass is needed before the eruption is triggered (Yaron et al. 2005). The high accretion rate means that matter is piled onto the surface of the WD more quickly, so it takes less time to accumulate the needed trigger mass.

Table 1.1. The Known Galactic Recurrent Novae[a]

Nova	P_{orb} (days)	$V_{quiescence}$ (mags)	V_{peak} (mags)	Eruption years
T Pyx	0.076	15.5	6.4	1890, 1902, 1920, 1944, 1967, 2011
IM Nor	0.102	18.3	8.5	1920, 2002
CI Aql	0.62	16.7	9.0	1917, 1941, 2000
V2487 Oph	∼1	17.3	9.5	1900, 1998
U Sco	1.23	17.6	7.5	1863, 1906, 1917, 1936, 1945, 1969, 1979, 1987, 1999, 2010
V394 CrA	1.52	18.4	7.2	1949, 1987
T CrB	228	9.8	2.5	1866, 1946
RS Oph	457	11.0	4.8	1898, 1907, 1933, 1945, 1958, 1967, 1985, 2006
V745 Sco	510	18.6	9.4	1937, 1989
V3890 Sgr	519.7	15.5	8.1	1962, 1990

[a] Adapted from Schaefer (2010). Updated to include the 2010 eruption of U Sco and the 2011 eruption of T Pyx.

In classical novae (CNe), these eruptions are observed to occur only once on any observable timescale (although it is possible that they do recur on timescales of $\sim 10^5$ years). The WD has a smaller mass (on average $\sim 0.6-0.8 M_{\odot}$) and the accretion rate is much lower ($\sim 10^{-9} M_{\odot} \mathrm{yr}^{-1}$). More mass is needed to trigger the eruption, and it is piled on more slowly than in RNe, so a much longer time is needed. During this long accretion period, mixing occurs between the accreted gas and the surface of the WD (Yaron et al. 2005). In RNe, where the accretion time is much shorter, theory indicates that mixing does not occur (Yaron et al. 2005), however recent observations have raised some questions about this (Mason 2011, and Section 4.10).

There are approximately 250 galactic CNe and 10 known galactic RNe. I discovered the tenth galactic RN, V2487 Ophiuchi (V2487 Oph), during the course of my dissertation work; this discovery is described in detail in Section 2.6.2. Table 1.1 summarizes the main properties of the galactic RNe, giving their orbital period (in days), magnitude in quiescence and at the peak of the eruption (in V-band mags), and the years in which eruptions have been recorded.

The first identified RN was T Pyxidis (T Pyx), which was discovered in 1913 by H. Leavitt in the Harvard plate archive (Leavitt & Pickering 1913). (Before the advent of modern digital imaging, astronomical observations were recorded on glass plates. The plates were coated with a photoemulsion, attached to the telescope, and then exposed and developed in a method similar to that used with film. See Section 2.6.1 for more detailed information

about plate archives.) Leavitt discovered the 1902 eruption first, and then searched the rest of the plates to find the 1890 eruption. T Pyx has since been observed in outburst four more times, in 1920, 1944, 1967, and 2011. Although T Pyx was the first RN discovered, it is actually quite an atypical system, with an accretion rate that is higher than it should be for such a short orbital period (Knigge et al. 2000) as well as a variable recurrence time, $t_{\rm rec}$, the amount of time between eruptions. Chapter 3 describes our detailed analysis of the T Pyx system using a combination of Hubble Space Telescope (*HST*) and archival observations. We found that the current RN phase of the system was triggered by a large CN eruption in 1866 ± 5. This RN phase is not expected to last for much longer, as the accretion rate in the system is steadily declining. Eventually, T Pyx will enter a state of hibernation, with essentially no active accretion occurring for approximately 2.6 million years. During this hibernation state, gravitational radiation will slowly return the system to a phase of active accretion, which will start the CN to RN to hibernation cycle again from the beginning.

Another notable RN is U Scorpii (U Sco), a depiction of which can be seen in Figure 1.1. U Sco has had ten eruptions observed to date (1863, 1906, 1917, 1936, 1945, 1969, 1979, 1987, 1999, 2010), and is very regular, going into outburst every 10 ± 2 years. Because of its regularity, U Sco has been well observed over its lifetime, particularly the most recent few eruptions. The 2010 eruption was predicted with good accuracy by Schaefer (2005), and I helped coordinate a worldwide observing campaign to discover the outburst early on and comprehensively follow it back to quiescence (Schaefer et al. 2010c). Early discovery was critical to a successful observing campaign, as U Sco has the fastest known eruption among all novae, both classical and recurrent. The campaign was wildly successful, with a combination of professional and amateur astronomers obtaining more than 35,000 observations of U Sco during the two month eruption. Chapter 4 discusses these observations and their implications in detail.

The other RNe are each unique in their own ways, but they all share certain characteristics as a group. In Chapter 2, I will explore this set of characteristics, and how we can use them

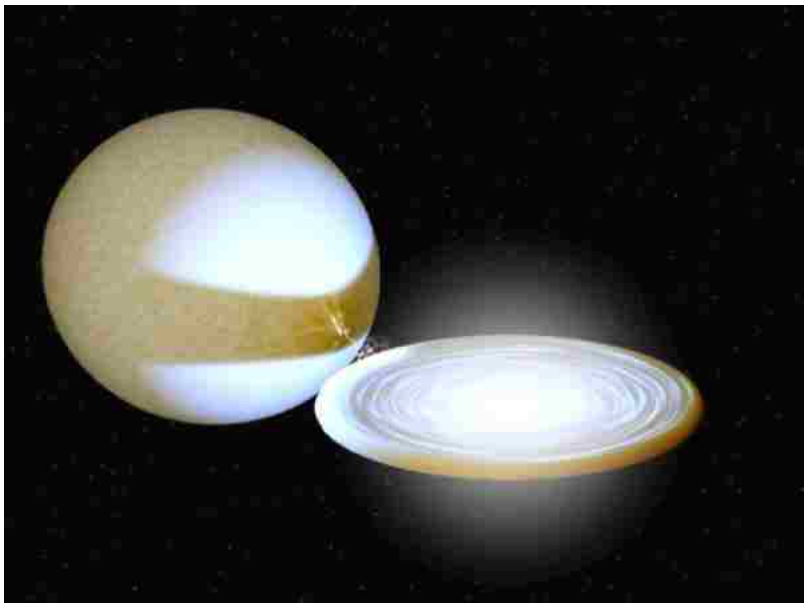

Figure 1.1 The Recurrent Nova U Scorpii. This image shows a computer depiction of the recurrent nova U Sco during the quiescent phase between eruptions, with its high-mass white dwarf accreting material from a subgiant companion. Eruptions of U Sco have been observed in 1863, 1906, 1917, 1936, 1945, 1969, 1979, 1987, 1999, and 2010. It is the most regular of the recurrent novae, and it also has the shortest eruption duration. We coordinated a comprehensive, worldwide observing campaign to discover and follow the predicted 2010 eruption. A collaboration of professionals and amateurs observed the eruption from all over the world and many space telescopes, in all wavelengths from radio to X-ray. The results of this campaign are detailed in Chapter 4. Image created with BinSim (http://www.phys.lsu.edu/ rih/binsim/)

to find new RNe from among the set of CNe. Complete knowledge of the RN population is an important step in determining the connection between RNe and Type Ia supernovae.

1.2 Type Ia Supernovae

Supernova explosions are much more powerful than those of novae (Baade & Zwicky 1934). They involve the total destruction of the star that is exploding, and come in two basic varieties: thermonuclear (Type Ia) and core collapse. I will focus on Type Ia supernovae (SNe Ia), which were first identified as a useful subclass in the mid-1980s (Panagia 1985; Uomoto & Kirshner 1985; Wheeler & Levreault 1985); Figure 1.2 shows an image of an SN Ia, known as SN 1994D, taken with *HST*. SNe Ia are uniquely identified by their spectrum during explosion. SN Ia spectra are hydrogen-deficient and show strong Silicon II lines. The lack of hydrogen implies that the star must be evolved, having burned all of its available hydrogen into heavier elements before exploding. The current consensus is that this star is a WD consisting mainly of carbon and oxygen (CO WD). WDs are no longer able to power continual nuclear fusion at their centers, and are held up instead by electron degeneracy pressure resisting the force of gravity as it tries to compress the star further and further. Because of this, they are known as degenerate stars, and their structure is determined by the laws of quantum physics. One of the unusual consequences of this is that WDs *decrease* in size as they *increase* in mass and therefore have a maximum mass limit, at which point they can get no smaller (Chandrasekhar 1931, 1934). This is key to the transition from WD to SN Ia: as the WD nears this mass limit ($\sim 1.4 M_{\odot}$, known as the Chandrasekhar mass, $M_{\rm Ch}$), the central pressure increases until it reaches a point at which the carbon and oxygen in the WD ignite and spark a thermonuclear runaway explosion, ripping the WD apart in one of the most powerful events observed in our universe.

Because of the supposedly-identical nature of SNe Ia, they have been used as standard candles for measuring cosmological distances. Since we know the absolute magnitude (inherent luminosity) of the explosions, when we observe them in distant galaxies we can measure

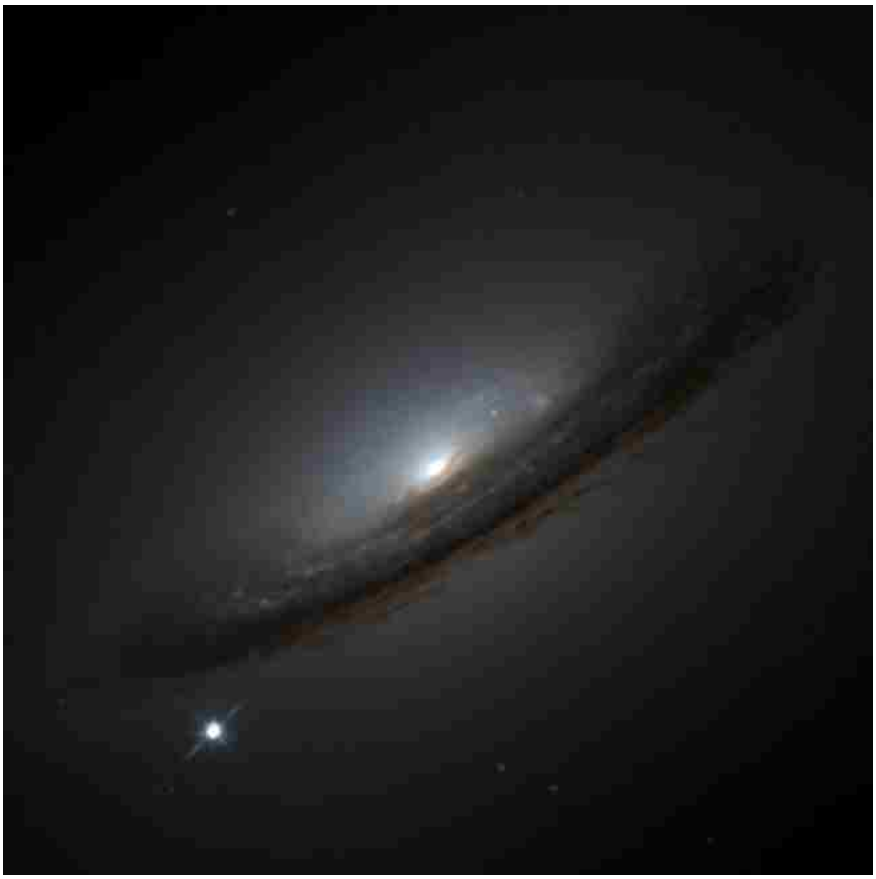

Figure 1.2 Supernova 1994D. This *HST* image shows SN 1994D, a Type Ia supernova that exploded in the outskirts of the galaxy known as NGC 4526. Type Ia supernovae can be calibrated and used as "cosmic yardsticks" to measure extragalactic distances. They were used by two teams in the late 1990s to measure the acceleration of the expansion of the universe, an effect which is still poorly understood and has been attributed to a mysterious Dark Energy. A primary goal of my dissertation is to identify the progenitor systems of SNe Ia, which will allow for more accurate distance measurements and a better understanding of Dark Energy. Image credit: High-Z Supernova Search Team, HST, NASA

the apparent magnitude (the brightness seen here on Earth) and use the difference between the magnitudes to calculate the distance: $m - M = 5 \times log_{10}(d) - 5$, where m is the apparent magnitude, M is the absolute magnitude, and d is the distance from Earth to the supernova, measured in parsecs (pc, 1 pc = 3.09×10^{13} km). A spectrum of the SN is taken to identify the subtype (there are many different types of SNe, but here we are interested only in Type Ia events) and can also be used to measure the radial velocity of the star (along the line of sight) based on the Doppler shift in the spectral lines. A shift toward the redder end of the spectrum, known as a redshift, indicates the object is moving away from Earth, whereas a shift to the blue, called a blueshift, indicates the object is moving towards Earth. Plotting the distance versus the velocity gives the famous Hubble Diagram, which shows the expansion history of the universe.

In the late 1990s, SNe Ia came into prominence when two independent teams used observations of SNe Ia to construct Hubble Diagrams, an example of which can be seen in Figure 1.3, which showed that the expansion of the universe was not steady or decelerating, as had been previously assumed, but was in fact accelerating, flying apart faster and faster as time has gone on (Riess et al. 1998; Perlmutter et al. 1999). The nature of this acceleration is still unknown and has been attributed to a mysterious Dark Energy which pervades the known universe. The SN result has since been extended to higher redshifts (greater distances) and much larger sample sizes (Amanullah et al. 2010; Conley et al. 2011; Rodney et al. 2012), as well as confirmed by measurements from the Wilkinson Microwave Anisotropy Probe (WMAP, Spergel et al. 2007) and Baryon Acoustic Oscillations (BAO, Eisenstein et al. 2005).

At this point in the supernova cosmology game, the sample sizes are getting large enough that the statistical (measurement) errors have been reduced to $\sim$6%, but the unknown systematic errors are still around 10% (R. Kirshner 2012, Heineman Prize Lecture). Although it is important to continue to observe SNe Ia, especially as we are able to push to higher redshifts (further distances), this can only improve the statistical errors; it is crucial to

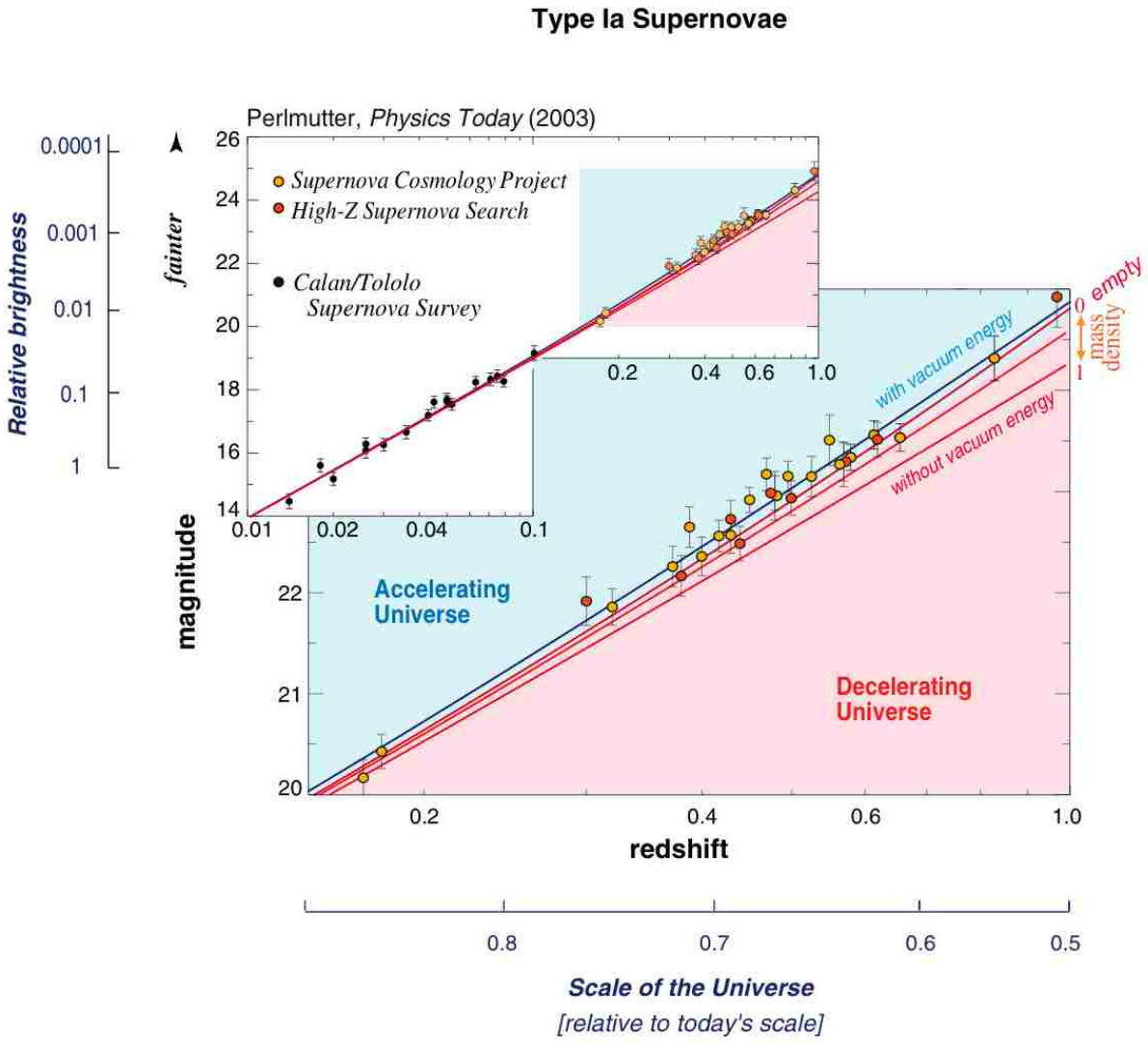

Figure 1.3 Supernova Hubble Diagram. A Hubble Diagram such as this one plots the observed magnitude of an SN Ia on the y-axis vs. the redshift (distance) on the x-axis. One can then match up the observed points with the predicted models of the expansion history of our universe and it can be seen that the points fall in the "accelerating universe" part of the plot, along the line labeled "with vacuum energy". This unexpected result from supernova observations in the late 1990s was the first indication that the expansion of our universe was in fact accelerating, not decelerating as had previously been assumed. Figure credit: Perlmutter (2003)

the upcoming so-called "Era of Precision Cosmology" that we reduce the systematic errors as well. One key way to accomplish this is to identify the progenitor systems of SNe Ia. Questions have been raised about how the composition and evolution of the progenitor star can affect the energetics of SN Ia explosions, which in turn affects the luminosities (brightnesses) and therefore the distance measurements (Domínguez et al. 2001). A definitive progenitor identification will allow theorists to more accurately calculate its effects on the luminosity of the explosion, improving the SN Ia standard candle and therefore obtaining better measurements of the effects of Dark Energy.

1.3 Type Ia Supernova Progenitors

A number of systems have historically been proposed as possible SN Ia progenitors. They can be divided into two main classes, the single-degenerate (SD; Iben & Tutukov 1984; Whelan & Iben 1973) and the double-degenerate (DD; Tutukov & Yungelson 1981; van Kerkwijk et al. 2010) systems. SD systems consist of one CO WD and one non-degenerate star, whereas the DD systems consist of two CO WDs. In all progenitors, the total combined mass of the system components must be $\geq M_{\rm Ch}$ and there must be some type of mass transfer that pushes the primary WD over the Chandrasekhar limit. In SD systems, that mass transfer is generally ascribed to the accretion process described in Section 1.1. In DD systems, it has historically been described as a binary inspiral, in which the two WDs spiral around each other at ever-decreasing distances until they collide, but recent theory suggests that the primary (heavier) WD disrupts the secondary (lighter) WD and then accretes that material directly (Piersanti et al. 2003).

Because they feature high-mass WDs that are rapidly accreting material from a companion star, RNe have long been considered good SN Ia progenitor candidates (Hachisu & Kato 2001). There are three open questions, however, that must be answered to determine whether RNe truly are viable progenitors: (1) Are there enough RNe to provide the observed SN Ia rate? (2) Do RNe gain mass over their lifetimes, i.e. do they accrete more mass than

they blow off during eruptions, so that there is a net mass increase? (3) Do the RNe have CO WDs, as required for SNe Ia, or are they one of the other two types, He or ONe? I will address the first two questions directly, in Chapters 2, 3, and 4, and discuss results pertaining to the third question in Section 4.10.

Consideration of the full array of WD binaries (Branch et al. 1995; Parthasarathy et al. 2007) provides a list of all reasonable SD models. The currently-published models are: RNe (Hachisu & Kato 2001), symbiotic systems (Hachisu et al. 1999a), supersoft X-ray sources (Hachisu et al. 1999b), helium stars (Wang et al. 2009), and spin-up/spin-down systems (Justham 2011; Di Stefano et al. 2011). After the SN explosion, the non-degenerate star is left behind and this now ex-companion star can be used to identify the SN progenitor. The lack of an ex-companion star is also useful, as it can exclude SD progenitors. Chapter 5 describes the results of a search for these ex-companion stars in four Type Ia supernova remnants (SNRs) in the Large Magellanic Cloud, a satellite galaxy of our Milky Way. We find that we can definitively identify the progenitor of one system (SNR 0509-67.5) as a double-degenerate (Section 5.4) and place strict limits on the progenitor of a second system (SNR 0519-69.0; Section 5.5). For the other two systems, we have many possible ex-companion stars; further observations should help identify the true ex-companion.

1.4 This Work

In the following chapters, I will describe the work I have done over the past five years as a graduate student at Louisiana State University investigating the RN population in general (Chapter 2), several specific RN systems (Section 2.6.2, and Chapters 3 and 4), the possible connection between RNe and SNe Ia (Sections 2.7, 3.9, and 4.11), and the nearby SN Ia progenitors (Chapter 5).

2. Recurrent Nova Demographics: A Masquerade[1]

Knowledge of the basic properties of the recurrent nova population, particularly the number of recurrent novae in our galaxy, is important to our understanding of the systems and crucial to the question of whether or not recurrent novae can provide a significant fraction of the observed Type Ia supernova explosions. This chapter explores the demographics of the recurrent nova population.

2.1 Recurrent Nova Demographics

Both classical and recurrent novae consist of a white dwarf accreting material from a companion star. The accreted material accumulates until reaching a critical temperature/pressure at the base of the accreted layer, at which point thermonuclear runaway is triggered and the nova eruption occurs. Although the outburst mechanism is essentially identical for both CNe and RNe, the recurrence timescale varies by multiple orders of magnitude, with RNe seen to erupt at least once per century. The systems classified as CNe have only one *discovered* eruption, but more undiscovered eruptions could have occurred within the last century. The truly non-recurrent systems do not have any more eruptions on timescales of less than a century. There are two characteristics of RNe that combine to cause their short recurrence time: a high-mass white dwarf (where $M_{\rm WD}$ is near the Chandrasekhar mass limit) and a high accretion rate ($\dot{M}$). There is a given trigger mass of accreted material that must be reached for the nova eruption to occur; this trigger mass is smaller for high-mass WDs (Yaron et al. 2005) and is more quickly reached when matter is being accumulated at a high rate

[1]Section 2.6.2 reproduced by permission of IOP Publishing Limited (Pagnotta et al. 2009). Portions of Sections 2.1, 2.2, 2.3, 2.4, 2.5, and 2.6 reproduced by permission of IOP Publishing Limited (Pagnotta & Schaefer 2012, Submitted to ApJ). The permission statements are available in Appendix B. Portions of the sections have been updated and adapted to the dissertation format. I was primarily responsible for the analysis presented in Sections 2.1-2.4 and 2.6-2.7; Section 2.5 includes a large amount of work done my advisor in addition to my contributions.

(high $\dot{M}$), thus the combination of these two factors yields–and is in fact required for–the short recurrence times seen in the RNe (Sekiguchi 1995; Townsley 2008).

These two factors are also exactly what are needed to cause a WD to explode as a Type Ia supernova, which is why RNe are among the best possibilities for a solution to the long-standing SN Ia progenitor problem. The reliability of these SNe as standard candles (Hamuy et al. 1996) has been key for the measure of the acceleration of the expansion of the universe (Riess et al. 1998; Perlmutter et al. 1999). Questions have been raised, however, about potential evolution in the SN Ia population that could cause peak absolute magnitude variations of up to 0.2 mag and impact the precision cosmology measurements that are made using SNe Ia (Domínguez et al. 2001). An understanding of the dominant progenitor channel, or channels (Brandt et al. 2010), will help answer these questions and reduce the systematic errors which currently dominate the uncertainties in supernova cosmology. The RN channel is a potential good solution to this key problem, but a critical question is whether there are enough RNe in our Milky Way galaxy to account for the observed SN Ia rate (della Valle & Livio 1996; Branch et al. 1995). A substantial problem with prior work (by roughly a factor of a hundred) is the lack of consideration for the efficiency of nova discoveries; as we will show, many so-called CNe are actually RNe. We provide the first consideration of the numbers and fractions of RNe that are masquerading as CNe, addressing both the RN demographics question and the SN Ia progenitor problem.

The discovery efficiencies of nova eruptions and RNe are well understood (Pagnotta et al. 2009; Schaefer 2010). Eruptions over the last century can easily be missed if they happen when the star is too close to the Sun, or during the full moon, or during any of many intervals when no one was watching, or if the search did not go deep enough even if someone was searching in the right area at the right time. For CNe, the discovery efficiency is 22% for novae peaking at $V = 6$ mag and 9% for novae peaking at $V = 10$ mag, even in ideal conditions; this rate remains fairly constant from 1890 to 2012. For the ten known RNe, the undirected discovery efficiency for a single eruption varies from 0.6% to 19%, with a median

of 4%. Allowing for multiple eruptions since 1890, an approximately correct situation is a discovery rate of ∼10%, so two eruptions are discovered 1% of the time (and the system is recognized as an RN), and just one eruption is discovered 18% of the time (so the system is classified as a CN), leaving zero eruptions discovered 81% of the time. For every known RN, there must be an order of magnitude more RNe currently masquerading as CNe. The best place to find new RNe is therefore in the catalog of known CNe.

This chapter presents a comprehensive analysis of the RNe hiding in the nova catalogs. Section 2.2 systematizes seven criteria for identifying RNe in the nova catalogs on a probabilistic basis. Two of these criteria are newly presented here. Section 2.3 analyzes the many prior claims of RN candidates; most of the claims are no longer believable. Section 2.4 presents an exhaustive compilation of the measured properties (those relevant for our seven RN criteria) of 237 CNe with useful amounts of information (out of 394 currently known novae) as well as the 10 known galactic RNe. From this information, we identify ten strong RN candidates and 29 systems that are likely RNe. Section 2.5 presents three independent analyses that measure the fraction of currently cataloged CNe that are actually RNe which have had multiple eruptions within the last century. Section 2.6 presents results from our exhaustive searches for prior eruptions within archival material from the Harvard and Sonneberg astronomical plate collections. Part of the original motivation for this work was to develop a list of confident RN candidates for future exhaustive searches for previous eruptions. Section 2.7 discusses the broad implications of this work, which are dominated by the realization that the total number of RNe in our Milky Way galaxy is ∼160× more than in prior estimates.

2.2 Recurrent Nova Candidate Criteria

RNe and CNe have substantial overlap in the observed distributions of their properties. Indeed, this is expected, since many CNe are really RNe. Nevertheless, a variety of properties are greatly different between the CNe and the RNe. For example, most RNe have orbital

Table 2.1. Efficiency of RN Identification Characteristics

Indicator	% of RNe	% of CNe
$A - [14.5 - 4.5\log(t_3)] < 0$	80	2.3
$P_{orb} > 0.6$ days	80	13
$J - H > 0.7$ mag & $H - K > 0.1$ mag	40	17
FWHM of H$\alpha > 2000$ km s^{-1}	100	52
High-Excitation Lines (He II or Fe X)	100	22
P class (plateau in light curve)	60-90	17
$M_{WD} > 1.2$ M$_\odot$	100	26

periods longer than 0.6 days, while most CNe have orbital periods shorter than 0.3 days. Such properties can be used as indicators for recognizing RNe among the CNe. Due to the overlapping distribution of properties, no one property (other than multiple observed nova eruptions) can be used to definitively distinguish the CN or RN nature of any system. We never *prove* an RN by any means other than finding multiple eruptions. The presence of multiple positive indicators, however, with none contrary, can make a strong case for the RN nature of a system.

We collect here all known RN indicators plus two strong new ones. Importantly, we sketch out the physical bases for almost all the indicators, so that they are much stronger than simple empirical correlations. Table 2.1 lists each indicator and its efficiency, and each indicator is developed in detail in the following subsections.

2.2.1 Amplitude/t_3

All RNe have a high $\dot{M}$ and about half of them have a red giant companion. Both of these conditions contribute to RNe being more luminous than CNe during quiescence. Empiricially, RNe peak at approximately the same absolute magnitude as CNe (Schaefer 2010). Taken together, these two facts mean that RNe have smaller-amplitude outbursts. Additionally, RNe tend to have shorter-duration outbursts, as measured by t_3, which is the amount of time (in days) it takes for the system brightness to decline three magnitudes from peak. The faster declines are due to the RNe, with their high-mass WDs, having a smaller trigger mass (Yaron et al. 2005) and therefore a smaller eruption envelope mass, within which the

photosphere will recede faster, causing a faster decline. Various researchers have previously noted that RNe empirically have small amplitudes and fast declines, but many CNe were either fast or had small amplitude, so the individual criteria were not good indicators for recurrence. Duerbeck (1987) combined these two indicators to create a single criterion that selected out almost all RNe and only a few CNe. This criterion can be expressed in a plot of the nova outburst amplitude (A) versus decline speed (t_3), where the RNe are both fast *and* small-amplitude. With this 'Duerbeck plot', the few CNe within the RN region become prime RN candidates.

We can refine the Duerbeck plot as illustrated in Figure 2.1 by adding the RNe which have been identified since 1987, and by using improved measures of the amplitude and t_3 (Schaefer 2010; Strope et al. 2010). This allows us to better define the region Duerbeck described as "void of classical novae". We define the amplitude of the edge of this region with the relation $A_0 = 14.5 - 4.5 \times \log(t_3)$. We can quantify the position of any nova on the Duerbeck plot by its distance from this threshold line, $A - A_0$. Eighty percent of the known RNe have negative $A - A_0$, whereas only 2.3% of the CNe are inside the $A - A_0 < 0$ region of the Duerbeck plot. We note that T Pyx and IM Nor are outliers among RNe (with $A - A_0$ values of 2.7 and 3.9 mag, respectively), which is not unexpected due to the unusual nature of the systems (Schaefer 2010). With this, we recognize that novae with $A - A_0 < 0$ are very likely RNe, while novae with something like $A - A_0 > 5$ mag are very likely CNe. Presumably, a substantial fraction of the systems just above the threshold line could also be RNe, so we also note the systems with $A - A_0 < 1$ as interesting.

A substantial problem is that other classes of 'novae' can occupy the RN region of the Duerbeck plot. Most commonly, large-amplitude dwarf novae can be confused with RNe. Fortunately, most dwarf novae have amplitudes smaller than RNe, and dwarf novae can be recognized uniquely from their spectral lines during outburst as well as their recurrence timescales of less than a few years. X-ray novae (e.g., V404 Cyg and V616 Mon [Nova Mon 1917 and 1975]) are another class with good potential for confusion. X-ray novae are caused

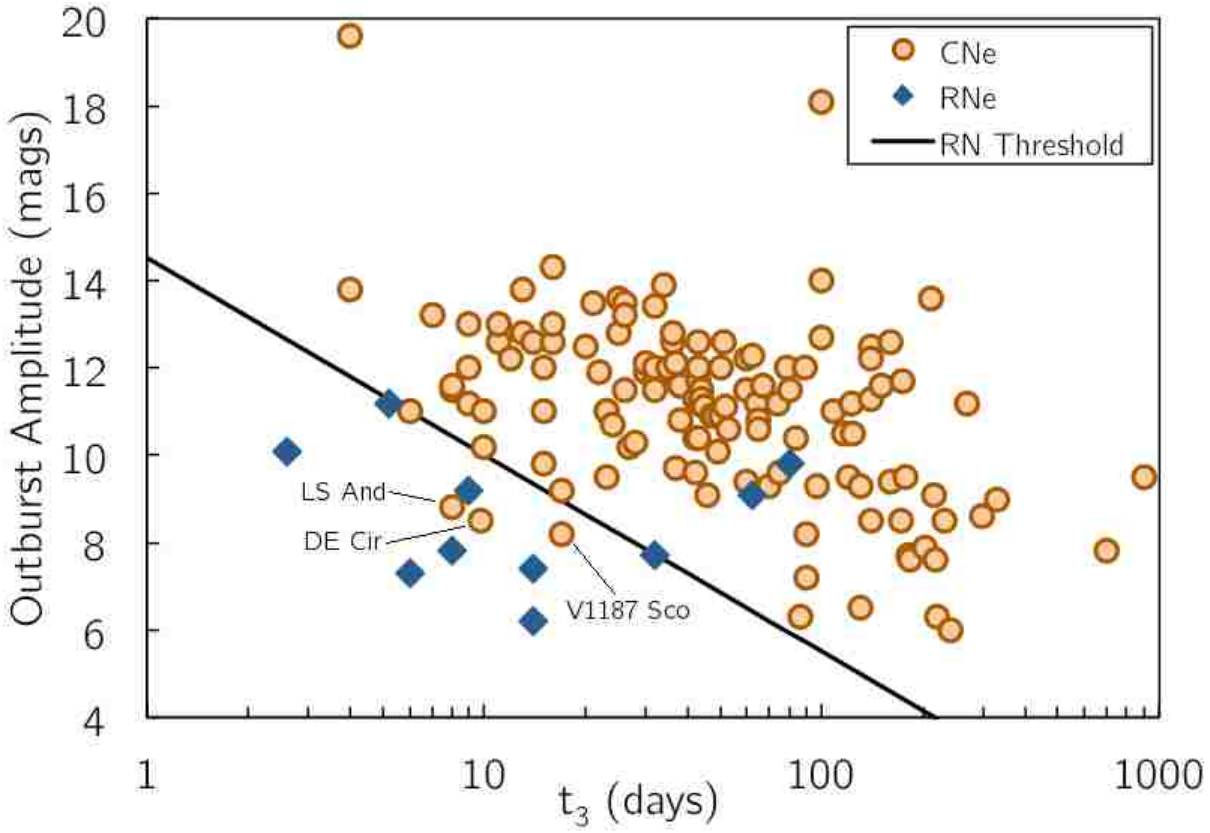

Figure 2.1 Amplitude/t_3 Relation. This relation, first published in Duerbeck (1987), plots the amplitude of the nova eruption against the time to decline by 3 mags from peak, t_3. All novae peak at approximately the same absolute magnitude, but RNe have higher average accretion rates and therefore brighter average quiescent magnitudes. This leads to small eruption amplitudes. Additionally, because of the smaller trigger masses required for RNe, the eruptions are shorter and faster than in CNe, so the t_3 values are smaller. The RNe are therefore clustered in the bottom left corner of this plot, with low amplitudes and low t_3 values. T Pyx and IM Nor are the notable exceptions, which is not surprising since they are unusual systems. To quantify the region that Duerbeck (1987) described as "void of classical novae", we define a threshold line of $A_0 = 14.5 - 4.5 \times \log t_3$, which is drawn on the plot. 80% of the RNe have $A - A_0$ values < 0, while only three CN systems (2.3% of our sample) do. Those three systems (LS And, DE Cir, and V1187 Sco) are marked on the figure above. Another six systems (V868 Cen, CP Cru, V4361 Sgr, V697 Sco, V723 Sco, and V477 Sct) have $A - A_0 < 1$, marking them as interesting.

by accretion disk instabilities in binaries with black holes. The amplitude is typically 5−8 mags while the decline time is typically 40−120 days (Chen et al. 1997), so many of these systems will appear to satisfy our $A - A_0 < 0$ criterion. These systems can be distinguished by their bright *hard* X-ray luminosity during outburst as well as by their distinct light curve morphologies (Chen et al. 1997). Symbiotic novae also have small amplitude outbursts, typically with amplitudes from 2−6 magnitudes (Kenyon 1986). Symbiotic novae (e.g., RR Tel and PU Vul) are greatly different from novae on symbiotic stars (e.g., RS Oph and T CrB), so there is nothing to be learned from one class that is applicable to the other class, despite the unfortunate similarity in names. Symbiotic novae can be distinguished by the presence of a red giant star with heavy stellar winds, resultant long orbital periods (from years to decades), and incredibly long decline times (from years to over a century). Any well-observed nova event can be easily distinguished from dwarf novae, X-ray novae, and symbiotic novae, but a sparsely observed event can easily be confused between the classes.

Figure 2.1 also shows 131 CNe, with the input data coming from Table 2.3, as described in Section 2.4. Three CNe—LS And, DE Cir, and V1187 Sco—are definitely located in the RN region. Therefore the $A - A_0 < 0$ criterion is satisfied by only 2.3% of the CNe. Six more systems are within 1 mag of the threshold ($0 < A - A_0 < 1$) and therefore also noted as interesting: V868 Cen, CP Cru, V4361 Sgr, V697 Sco, V723 Sco, and V477 Sct.

2.2.2 Evolved Companion Stars

Empirically, we know that most (eight out of ten) RNe have evolved companion stars, either sub-giants (e.g. U Sco) or red giants (e.g. RS Oph). Physically, this makes sense because the evolutionary expansion of these companions easily provides (via Roche Lobe overflow) the high $\dot{M}$ needed to drive the fast accumulation of accreted material on the surface of the WD (Schaefer 2010). There are two ways we can identify an evolved companion star in nova systems: long orbital period, $P_{\rm orb}$, and infrared color excess.

Roche Lobe geometry tells us that $P_{\rm orb} \propto R_{\rm donor}^{1.5}$, where $R_{\rm donor}$ is the radius of the mass donating star, so a large evolved companion requires a long $P_{\rm orb}$. 80% of galactic RNe have

orbital periods longer than 0.6 days. This is starkly different from CNe, for which only 21% are longer than 0.3 days, and only 13% are longer than 0.6 days. The difference between 80% and 13% implies that, all else being equal, a $P_{\rm orb} > 0.6$ day system is likely an RN, although without high confidence. The threshold of 0.6 days is somewhat loose, as a shorter-period system could easily contain an evolved star driving a high $\dot{M}$. But the age of our galaxy and the main-sequence lifetime of stars combine to put a lower limit of roughly 0.3 days, below which there can be no evolved donor star. So we can set a formal criterion of $P_{\rm orb} > 0.6$ days, while acknowledging that systems with orbital periods from 0.3−0.6 days also have a chance of having an evolved companion star.

The presence of an evolved companion can also be inferred by looking at the infrared colors of the system in quiescence. An evolved companion, particularly a red giant, locates the system in a distinct area on a $J - H$ vs. $H - K$ color-color diagram; Figure 2.2 shows such a diagram for all of the novae in Tables 2.2 and 2.3 for which both colors are known. The region with evolved companion stars has imperfectly defined edges, but we will take it to be for $J - H > 0.7$ mag and $H - K > 0.1$ mag; this region is marked in Figure 2.2. Four of the known RNe have red giant companions and occupy this region of the infrared color-color plot. Only 17% of the CNe have colors which indicate the presence of a red giant. The contrast between 40% and 17% is not high, so we consider the infrared colors to be only a weak indicator.

The presence of an evolved companion star is the dominant means by which RNe achieve high $\dot{M}$, but CNe can have evolved companions as well. RNe must also have a WD mass near the Chandrasekhar limit, while a system with a lower mass WD will necessarily have a long recurrence timescale (Yaron et al. 2005). The presence of an evolved companion will substantially increase the expectation that the system might be an RN, but this property alone cannot provide any high confidence.

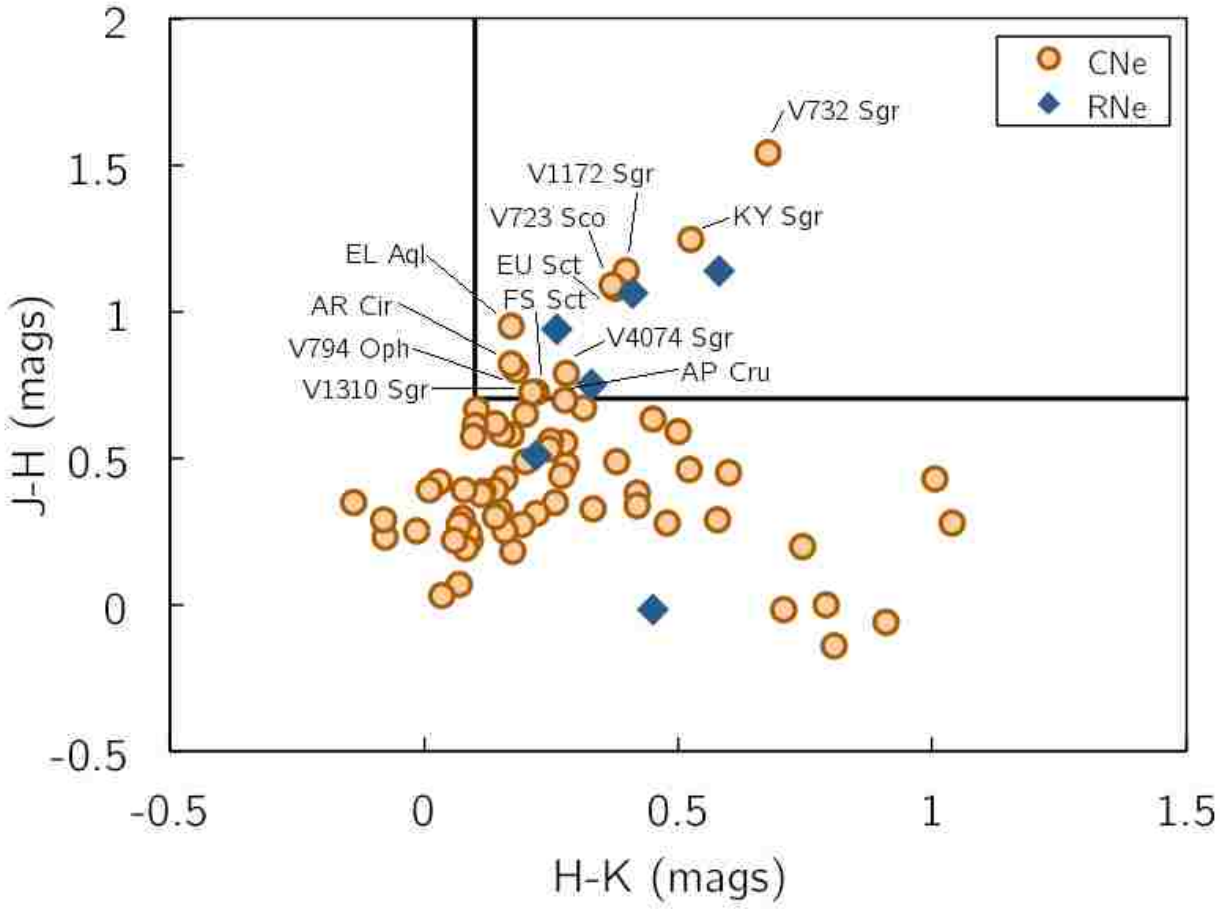

Figure 2.2 Infrared Color-Color Diagram. This color-color diagram plots two near-IR colors and allows us to identify stars with an infrared excess indicative of a red giant companion. Our threshold is $J - H > 0.7$ and $H - K > 0.1$. This identifies 12 CNe as having likely red giant companions: EL Aql, AR Cir, AP Cru, V794 Oph, KY Sgr, V732 Sgr, V1172 Sgr, V1310 Sgr, V4074 Sgr, V723 Sco, EU Sct, and FS Sct. Systems with red giants are likely RNe since the evolutionary expansion of the red giant companion can easily drive the high accretion rate needed for a short recurrence time, however it is not a given that these systems are recurrent, as RNe also require a high mass WD. Nevertheless, these are interesting systems.

2.2.3 High Expansion Velocity

The expansion velocity of the ejected material in nova eruptions is measured using widths of emission lines. The spectra and line widths in the literature cover a wide variety of spectral ranges and elements, which vary in complex manners, but the one nearly universally covered wavelength is that of the Hα line. The width of the Hα line is measured and reported as the FWHM or the FWZI, but the latter quantity is difficult to measure consistently with accuracy. Therefore, we chose to use the full-width at half-maximum (FWHM) of the Hα line as a standard measure because this line is ubiquitous in nova spectra and the FWHM of the line is commonly reported.

RNe should systematically have high Hα FWHMs. RNe are distinguished from CNe by having a WD near the Chandrasekhar mass, and such WDs must have high mass and a small radius (when compared to the WDs in CNe). This necessary condition will lead to the WD having a high escape velocity, $v_{esc} = \sqrt{2GM_{\rm WD}r_{\rm WD}^{-1}}$, much higher than for any CN. For detailed numbers, the WD escape velocity is 4300, 6800, 9000, and 12700 km s^{-1} for WDs with masses 0.6, 1.0, 1.2, and 1.35 $M_{\odot}$, resepctively. Roughly, the RNe should have a WD escape velocity that is double or triple that of CNe. In general, for explosive ejections, the typical ejection velocity is comparable to the escape velocity. Hence, RNe should have double or triple the ejection velocities as CNe, and the RNe Hα FWHMs should be double or triple those of CNe. Kato & Hachisu (2003a) have made detailed models of the velocity outflows in RNe, which can achieve the high observed velocities. They point out that the ejection velocity depends sensitively on the WD mass.

Every known RN has a FWHM of Hα greater than 2000 km s^{-1}, and the median velocity is 4300 km s^{-1}. The highest velocity is 10,000 km s^{-1}, for V2487 Oph. This is in contrast to the CNe, where only 52% meet or exceed 2000 km s^{-1}. With this, we take a nova that has FWHM $<$ 2000 km s^{-1} to be a likely CN. We take 3500 km s^{-1} (with 70% of the RNe and 13% of the CNe) to be a threshold above which the systems have a high probability of being recurrent. On this basis, from our unbiased sample of 237 novae, DE Cir, V693 CrA,

V838 Her, V4160 Sgr, V4643 Sgr, V4739 Sgr, and V1142 Sco are good RN candidates. From later novae that are not part of this sample, V1721 Aql, V2491 Cyg, and V2672 Oph are also strong RN candidates.

2.2.4 High Excitation Lines

RNe also display unusually high excitation lines in their early outburst spectra. Again this is due to the high-mass WD, which sits inside a deep potential energy well. Large amounts of energy are needed to propel the ejected material out of this well, and this is reflected in the spectra.

We have two primary indications of high-excitation: the He II and Fe X emission lines. Sometimes the highest excitation conditions produce Fe XI and Fe XIV lines, as well as N V lines. These emission lines are sought in the spectra from near-peak and soon thereafter. Spectra taken too long after the peak will often pick up the He II emission line that is normal for the nebular phase, which we must avoid.

For the ten known RNe, 5 out of 8 show high-excitation iron lines, and all ten show He II lines. The presence of Fe X or He II lines is thus a strong criterion for candidate RNe. We can say with reasonable confidence that any nova that does not show He II or Fe X, when both would have been seen, is likely a CN. For CNe, Williams (1993) classifies the majority as Fe II class, the quintessential case for low excitation. Out of 36 CN systems for which both Fe and He II lines were sought, only 22% of them show high excitation lines. Of the full sample, only one system, CP Pup, shows both He II and Fe X. Fe X alone is seen in DN Gem, V446 Her, and CT Ser, while twelve systems show just He II.

2.2.5 Light Curve Plateaus

Hachisu et al. (2008c) have pointed to eruption light curve plateaus as RN markers. The fast emergence of the supersoft X-ray source irradiates the re-formed accretion disk and companion star, providing reprocessed optical light that—for a time—dominates over the

fast fading shell light. The supersoft X-ray luminosity does not vary greatly, until some fairly fast turn off, resulting in a plateau in the optical light curve.

The Strope et al. (2010) analysis defines seven light curve classes based on the shapes of the light curves. The most common light curve classes are S (smoothly declining), D (dust dips), and J (large random jitters from before the peak until the transition phase); other classes include O (periodic oscillations around the transition phase), F (flat-topped), and C (a slow-rising fast-fall cusp around the transition phase). Of importance here, the P class light curves are characterized by a plateau around the transition phase, with this plateau being an interruption of the otherwise-smooth decline from peak, at which point the light curve goes nearly flat for a measurable amount of time, then abruptly returns to its steep decline, often at a faster rate than before the plateau phase. Strope et al. (2010) calculate that only 17% of CNe have plateaus.

The massive collection and analysis of virtually all extant photometry of RNe (Schaefer 2010) provides a quantitative and definitive measure of the fraction of RNe that have plateaus in their light curve. Schaefer (2010) and Strope et al. (2010) found that all RN light curves are certainly either S or P class, with 60% to 90% of them being P class. The uncertainty in the plateau fraction for RNe is due to poor late-time light curves for three of the systems. Only one RN (T CrB) was certainly an S class event.

Thus 60-90% of RNe are P class, while 17% of CNe are P class. This provides good empirical support for the model predictions of Hachisu et al. (2008c). Hence, a plateau provides a reasonable indicator of an RN, while the lack of a plateau is a reasonable indicator of a CN. While this is a clear indicator, the fractions indicate that this is not a strong case by itself. A substantially stronger case can be made that all D and J class novae are low energy events (Strope et al. 2010) and hence not RNe.

2.2.6 White Dwarf Mass

One requirement for RNe is that their WD must be near the Chandrasekhar mass. There is no firm lower limit, but grids of nova models (Yaron et al. 2005) suggest a limit of roughly $1.20-$

$1.25M_{\odot}$. WD masses have been measured in some nova systems, but mass measurements are notoriously difficult and have large uncertainties. Nevertheless, a high-mass WD is necessary to produce an RN and a low-mass WD appears to preclude an RN, so we can say that a system is a likely RN if $M_{\rm WD} > 1.2M_{\odot}$, while a system is likely to be a CN if $M_{\rm WD} < 1.1M_{\odot}$. Presumably, all RNe pass this criterion. I. Hachisu and M. Kato have a series of papers (Hachisu & Kato 2004, 2005, 2006, 2007; Hachisu et al. 2008a,c; Hachisu & Kato 2009, 2010; Kato & Hachisu 2003b, 2007; Kato et al. 2009; Kato & Hachisu 2011) wherein they model 34 CN light curves and derive $M_{\rm WD}$. Of the systems listed in Table 2.3, 7 of 27 have $M_{\rm WD} > 1.2M_{\odot}$, for 26%, and two newer systems do as well. These 9 systems are: V693 CrA, V2491 Cyg, V838 Her, V445 Pup, V598 Pup, V5115 Sgr, V1188 Sco, V477 Sct, and V382 Vel. These nine need not be RNe, as their accretion rate might not be high enough to allow for a short recurrence time scale, but they are certainly still interesting.

2.2.7 Triple-Peaked Emission Lines

Another uncommon characteristic that likely indicates an RN is a triple-peaked, or castellated, structure in the outburst emission lines, most often observed in the Balmer series. This unusual line profile has been identified in three known RNe (U Sco, YY Dor, and Nova LMC 2009) and a number of suspected RNe, including DE Cir, KT Eri, and V2672 Oph (F. Walter 2010, private communication), V1721 Aql (Helton et al. 2008a), and V838 Her (Iijima & Cassatella 2010). When such triple-peaked features are seen in supernovae, they are attributed to expanding toruses of gas. However, Walter & Battisti (2011) make a good case that the triple peaks cannot be from an expanding torus, but rather come from an accretion disk, which has somehow re-formed very soon after the peak of the eruption. Currently, there is no complete theoretical explanation for these triple-peaked emission lines. On the empirical side, only one of the ten known galactic RN (U Sco) has the triple peaked features, for a rate of 10%, even though most have adequate spectral coverage, so perhaps the low fraction is due to low inclinations. For CNe, triple-peaked features have not been reported for many systems, although old spectra of V603 Aql in outburst are described as

being triple-peaked. With these numbers and limited coverage, we cannot make this into a standalone RN indicator, but such triple peaks apparently increase the likelihood of an RN if they are observed.

2.3 Previously-Proposed Recurrent Nova Candidates

Many CNe have been identified as likely RNe in the past, for a variety of reasons. Most are identified because of one particular characteristic, such as infrared colors in quiescence (Harrison 1992; Weight et al. 1994; Hoard et al. 2002), eruption light curves indicating high-mass WDs (Hachisu et al. 2002), the existence of pre-existing dust possibly left over from previous nova eruptions (Kawabata et al. 2000), or the speed of decline of the outburst light curve (Shears & Poyner 2007). This is a reasonable method of constructing an initial list of possible RNe, but fails to create a rigorous set of candidates because there are many CNe which display one indicator of a short recurrence time. Considering only one characteristic produces many false positives. Duerbeck (1987) attempted to address this issue by combining two characteristics, outburst amplitude and duration (Section 2.2.1), to identify good RN candidates. We expand this by considering a total of seven characteristics, each of which indicate a short recurrence time. This allows us to focus on systems with multiple strong indicators and therefore maximize our chances of discovering new RNe.

We are also able to take a broader look at the previously-published candidates to better determine their current status. Various of these suggestions are weak and should now be discarded, while others are strong, and we should recognize the original proposers. We discuss each of these systems in the following subsections.

2.3.1 LS And, V794 Oph, V909 Sgr, MU Ser

Duerbeck (1988) points to four CNe as likely RNe because of their positions in the amplitude/t_3 diagram. Unfortunately, nothing is known about LS And other than its position on the Duerbeck plot. While this points strongly to LS And being an RN, the lack of any other

information means that the confidence in this conclusion is not high. For example, with no additional information, Rosenbush (1999) identified LS And as an X-ray nova. V794 Oph lies outside our RN regions in both Figures 2.1 and 2.2, and with its 220 day t_3, it is almost certainly not recurrent. V909 Sgr has little known other than its position on the Duerbeck plot, but with $A - A_0 = 2.5$ mag, the case for it being an RN is weak. For MU Ser, the Duerbeck (1988) amplitude is very uncertain, as the system counterpart is not definitively identified, so it is likely even farther from the threshold than the $A - A_0 = 0.7$ mag calculated using Duerbeck's values. In all, LS And is weakly likely to be an RN, while the other three are most likely CNe.

2.3.2 V368 Aql, V604 Aql, V841 Aql, AR Cir, BT Mon, GK Per, V794 Oph, V1172 Sgr, V3645 Sgr, V723 Sco, EU Sct, FS Sct

Various groups have used infrared colors as a proxy for a post-main-sequence companion, and hence a likely RN. On this basis, the following candidate RNe have been identified: V723 Sco by Harrison (1996); EU Sct and V3645 Sgr by Weight et al. (1994); GK Per, AR Cir, EU Sct, V604 Aql, and V841 Aql by Szkody (1994); V1172 Sgr by Hoard et al. (2002); V3645 Sgr, FS Sct, V794 Oph, BT Mon, and V368 Aql by Surina et al. (2011). For many of these stars, the presence of an evolved companion might well indicate the recurrent nature of the systems. Nevertheless, there are a variety of problems with some of these candidates. BT Mon and GK Per will be discussed individually in detail below (Sections 2.3.8, 2.3.11) and are certainly not RNe. AR Cir is in fact a symbiotic nova, distinct from a standard classical nova in a symbiotic system (Harrison 1996). V3645 Sgr may also be a symbiotic nova, based on its small eruption amplitude ($\Delta m = 5.4$ mags; Downes et al. 2001). EU Sct, V604 Aql, V794 Oph, and V368 Aql fail the amplitude/t_3 criterion (Section 2.2.1). Additionally, EU Sct and FS Sct have no high excitation lines (Section 2.2.4), so we judge these to be weak cases. Two proposed candidates with post-main-sequence secondary stars, however, present hopeful cases: V1172 Sgr has an Hα FWHM of 2000-3000 km s^{-1} (Strömgren & Shapley

1951) as well as IR colors that indicate a giant companion, and V723 Sco has a fast decline ($t_3 = 17$ days) (Shafter 1997) combined with IR colors that indicate an evolved companion, possibly a giant.

2.3.3 V1721 Aql

V1721 Aql (Nova Aql 2008) is a poorly observed nova that was never seen brighter than $V = 14$ mag, due to high extinction (11.6 ± 0.2 mag) in the V band. Hounsell et al. (2011) describe the various features that indicate an RN. The light curve fades very quickly ($t_3 = 10$ days). The FWHM of Hα is 6450 km s^{-1}, and the outburst spectrum shows broad, triple-peaked emission lines. The infrared colors show that the companion star is not a red giant, but may be a late main-sequence star or a subgiant. With the information available, V1721 Aql appears to be a good RN candidate.

2.3.4 V1330 Cyg

V1330 Cyg has been proposed as a candidate RN based on its light curve and amplitude (Rosenbush 1999). However, it has an S class light curve (Strope et al. 2010), the IR colors show no post-main-sequence star companion, and the value of $A - A_0 = 3.6$, all of which point to a likely CN.

2.3.5 V2491 Cyg

V2491 Cyg (Nova Cyg 2008b) displays a remarkable cusp in its eruption light curve; it is the first known example of a C class nova, a class for which even now only three members are known (Strope et al. 2010). Tomov et al. (2008) proposed V2491 Cyg as an RN based on vague similarities in its spectrum to those of two known RNe. Such arguments without any theoretical support are weak, especially since they could have alternatively pointed to CN examples. Indeed, Naik et al. (2009) point out various substantial differences between the spectra of V2491 Cyg and those of the RNe. Among the indicators discussed in this chapter, we have an inconclusive situation. The FWHM of the Hα line is very large (4800

km s^{-1}; Naik et al. 2009) and the decline is fast (t_3 = 16 days; Strope et al. 2010), both of which suggest an RN. The other characteristics of V2491 Cyg, however, indicate that it is not an RN, as it has an orbital period of ∼0.1 days (Darnley et al. 2011), a 10 mag amplitude (Ribeiro et al. 2011), and a confusing situation among the emission lines, with a high iron line of Fe II (Lynch et al. 2008) but possible (blended) He II (Helton et al. 2008b). A model for this nova has produced an estimated WD mass of $1.3 \pm 0.02 M_{\odot}$ (Hachisu & Kato 2009). The cusp light curve is unlike all known RN light curves and the implication is that substantially different physics is occurring (Hachisu & Kato 2009), so it is unclear whether an RN is even possible. V2491 Cyg presents a conflicted case.

2.3.6 KT Eri

KT Eri (Nova Eri 2009) has an outburst amplitude close to 8 mag and a fast decline (t_3 = 10 days; Hounsell et al. 2010). The FWHM of Hα is 3400 km s^{-1} (Yamaoka et al. 2009) and Hα shows a triple-peaked line structure (F. Walter 2010, private communication). The system has a red giant companion star, based on its IR colors and claimed 737 day photometric orbital period (Jurdana-Šepić et al. 2012). KT Eri is a good RN candidate.

2.3.7 HR Lyr

Shears & Poyner (2007) point to HR Lyr (Nova Lyr 1919) as a possible RN based on its modest amplitude (9.5 mag), 'fast' t_3 of 93 days, a hypothetical orbital period of 0.1 days, and an absolute magnitude in quiescence of +2.6 mag. Unfortunately, the decline is slow by RN standards, and the star lies 3.7 mag above the dividing line on the amplitude/t_3 plot. Additionally, even if there were a reasonable case for a 0.1 day orbital period, it would indicate a CN. Finally, the absolute magnitude in quiescence is inside the range for CNe, and it is based on a dubious distance derived from the decline rate relations that are known to often be very wrong for RNe (Schaefer 2010). So we do not agree with the arguments of Shears & Poyner (2007). Nevertheless, J. Thorstensen (2009, private communication)

reports a tentative photometric periodicity of 0.91 days, although he tells us that there is a substantial amount of uncertainty. With this, there is a weak case for HR Lyr being an RN.

2.3.8 BT Mon

Surina et al. (2011) selected a number of old novae based on their amplitude and t_3 and then obtained optical and IR colors for each system. They point to the old nova BT Mon as a possible RN of the U Sco type. BT Mon's relatively long (for a CN) orbital period (0.334 days, Downes et al. 2001) is also suspicious. With our two new RN criteria (broad Hα and high excitation lines), the 2010 km s^{-1} FWHM of Hα and presence of He II (Sanford 1940) are also indicative of a short recurrence time. Despite these suspicions, however, BT Mon has two properties that strongly indicate it is not recurrent: its 182 day t_3 and its F class (flat top at maximum) light curve (Strope et al. 2010). There are two additional measured physical quantities that strongly show that BT Mon is not recurrent: the mass of the WD is $1.04 \pm 0.06 M_{\odot}$ (Smith et al. 1998), which is too low for a short recurrence time, and the mass ejected by the 1939 eruption was $0.00003 M_{\odot}$ (Schaefer & Patterson 1983), which is too high to occur in a system with a short recurrence time. Additionally, a combination of archival data as well as magnitudes from the literature (Collazzi et al. 2009; Strope et al. 2010) demonstrate that BT Mon had no undiscovered eruptions in the 122 years from 1890 to 2012. In all, we have strong reasons to reject BT Mon as an RN. This demonstrates that suspicions based on even three positive indicators can be incorrect.

2.3.9 V2487 Oph

V2487 Oph (Nova Oph 1998) was proposed as an RN candidate by Hachisu et al. (2002) due to its very rapid decline and light curve plateau. In a detailed eruption model they derived an ejecta mass of $\sim 6 \times 10^{-6} M_{\odot}$ and a WD mass of $1.35 \pm 0.01 M_{\odot}$, both of which are strong indicators of an RN. In addition, we noted in 2009 that V2487 Oph was in the RN region of the amplitude/t_3 diagram (Section 2.2.1), that it had a record high FWHM of 10,000 km s^{-1}, and prominent He II emission lines. As such, V2487 Oph was an excellent

RN candidate. On this basis, we made V2487 Oph the first target in our exhaustive search for previous eruptions in the Harvard and Sonneberg archival plate collections. We found a 1900 eruption in the Harvard collection, making V2487 Oph the tenth confirmed galactic RN (Pagnotta et al. 2009). This ideal case represents one of the main goals of this work, wherein we identify good candidates and then prove their RN nature by finding additional eruptions. Section 2.6.2 contains full details of this discovery.

2.3.10 V2672 Oph

V2672 Oph (Nova Oph 2009) is another nova with heavy extinction and relatively little observational data. Munari et al. (2011) note many RN properties and claim that V2672 Oph is a clone of U Sco. The nova is nearly the fastest known, with $t_3 = 4.2$ days, and has a near-record FHWM of 8000 km s^{-1} for Hα; the Hα line also shows the triple-peaked line structure (F. Walter 2010, private communication). The light curve apparently plateaus at roughly 6 mags below peak. The lack of any 2MASS counterpart indicates that the secondary star is not a red giant. In all, four positive indicators (two of which are extreme) point to V2672 Oph being a strong RN candidate.

2.3.11 GK Per

GK Per (Nova Per 1901) is notable as the first known and best example of a number of classic CN phenomena: periodic oscillations in the outburst light curve (O class), an expanding nova shell, a light echo, and subsequent dwarf nova eruptions. Nevertheless, there has long been a persistent suspicion (e.g. Szkody 1994) that GK Per might be an RN because it has an evolved companion star (based on IR colors and $P_{\rm orb}$=1.9968 days; Szkody 1994, Downes et al. 2001). This suspicion is increased by the *HST* observation of its clumpy nova shell (M. Shara 2012, private communication), a property that is unique among novae except for the RN T Pyx (Schaefer et al. 2010b). Nevertheless, GK Per is certainly not recurrent. In the 122 years from 1890 to the present it has been very well observed, and there has been only one nova eruption. Additionally, the mass of the WD has been measured to be $0.9 M_{\odot}$

(Crampton et al. 1986), $\geq 0.87 \pm 0.24 M_{\odot}$ (Morales-Rueda et al. 2002), and $1.15 \pm 0.1 M_{\odot}$ (Hachisu & Kato 2007); such low masses indicate that the recurrence timescale must be very long. This demonstrates that the presence of a post-main-sequence companion does not guarantee an RN.

2.3.12 V445 Pup

The unique Helium nova V445 Pup was observed to have strong IR dust emission roughly one month after its maximum, which suggested that the dust was pre-existing, from a previous eruption not too far in the past, indicating that V445 Pup is an RN (Lynch et al. 2001b). However, the subsequent development of the light curve (with a deep and long-lasting minimum) demonstrated that the dust was formed in the current eruption, so the only evidence of the recurrent nature of V445 Pup is no longer valid.

2.3.13 V1017 Sgr

V1017 Sgr has had four eruptions observed, in 1901, 1919, 1973, and 1991. The 1919 eruption was longer and brighter than the other three events, with a light curve typical of a standard CN eruption. The other three small eruptions are typical dwarf nova eruptions, and the two most recent have been spectroscopically confirmed as such (Vidal & Rodgers 1974; Webbink et al. 1987). This system is similar to GK Per, wherein a single CN event is surrounded by dwarf nova eruptions.

2.3.14 V4444 Sgr

V4444 Sgr has also been suggested to have a pre-existing circumstellar dust cloud, based on spectropolarimetry (Kawabata et al. 2000). The lack of a detectable dip in the light curve argues against the dust being created in the current eruption (Venturini et al. 2002) and points to it being an RN (Kato et al. 2004). This is a plausible argument, although the lack of a model for the pre-existing dust cloud makes for less confidence in its RN status. In addition, there is possibly a plateau in the light curve, based on only two isolated magnitudes

(Kato et al. 2004), with this pointing to its RN status. However, Strope et al. (2010) have greatly extended the light curve and all evidence for any plateau disappears. The light curve is very fast ($t_3 = 9$ days; Strope et al. 2010), a characteristic of most RNe. Nevertheless, V4444 Sgr displays no high excitation lines in the outburst spectrum and the FWHM of the Hα line is only 800 km s^{-1}; such low energy properties are exhibited by none of the known RNe. In all, we have a situation with conflicting indicators.

2.3.15 NSV 1436

NSV 1436 (Ross 4) is generally fainter than $B = 15$, but occasionally brightens to $B = 13$ and brighter, leading Brown et al. (2010) to suggest that it is possibly an RN. Recent monitoring by the American Association of Variable Star Observers (AAVSO), however, has revealed two eruptions from $V = 16.5$ to $V = 13$ within the past year, so NSV 1436 is certainly an ordinary dwarf nova.

2.4 Recurrent Nova Candidate Search

We compiled the criteria described in Section 2.2 for both the RNe and the CNe; the compilations can be seen in Tables 2.2 and 2.3, respectively. Tables 2.2 and 2.3 are identical in structure. After the name of the system, the outburst characteristics are given: amplitude (in mags), t_3 (in days), $A - A_0$ (in mags), the FWHM of Hα (in km s^{-1}), whether there is He II, the highest reported Fe line, and the light curve class. Following these, the quiescence characteristics are listed: the orbital period (in days), the $J - H$ and $H - K$ colors, and whether it is in the red giant region on the $J - H$ vs. $H - K$ color-color diagram (cf. Figure 2.2). The final column lists other indicators such as WD mass (cf. Section 2.2.6), including those published by other groups.

We can identify the CNe which have multiple characteristics indicative of a short recurrence time; these are our RN candidates. The more RN-like characteristics a CN system shows, the more likely it is actually an unrecognized RN. Our good candidates are presented

in Table 2.4. This list includes seven systems from Table 2.3 as well as three novae which erupted after the 2006 cut-off for Table 2.3. Our best candidate systems are V1721 Aql, DE Cir, CP Cru, KT Eri, V838 Her, V2672 Oph, V4160 Sgr, V4643 Sgr, V4739 Sgr, and V477 Sct.

2.5 Recurrent Nova Fraction in Classical Nova Lists

Knowledge of the number of currently-listed CNe which are actually RNe, called the RN fraction $F_{\rm RN}$, is crucial for ascertaining the number of RNe in the Milky Way, for answering the question of whether the RN death rate equals the SN Ia rate, and thus for deciding whether RNe are acceptable SN Ia progenitor candidates. The following subsections describe the three different methods we used to estimate the RN fraction.

2.5.1 RN Fraction From CN Properties

The first way to estimate the RN fraction is to closely examine the known CNe and identify the percentage that are likely RNe. For this analysis, it is vital to have an unbiased set of novae that were selected without any regard to their possible recurrent nature. We use the time-limited sample presented in Table 2.3, which consists solely of the CNe identified in Downes et al. (2001), which was frozen on 2006 February 1. Some novae which erupted after that date are included in Table 2.4 and therefore should not be used for statistical analysis as they have been selected because they are good candidates.

Table 2.2. Properties of the Known Recurrent Novae

Nova	Amplitude (mag)	t_3 (days)	$A - A_0$	FWHM Hα	He II	Highest Iron	Light Curve	P_{orb} (days)	$J - H$	$H - K$	Red Giant?	Other
CI Aql	7.7 [1]	32 [1]	-0.03	2250 [3]	Yes [3]	Fe VII [4]	P [5]	0.618 [6]	0.51 [7]	0.22 [7]	N [2]	...
V394 CrA	11.2 [1]	5.2 [1]	-0.08	4600 [8]	Yes [8,9]	...	...	1.516 [10]	...	...	N [2]	...
T CrB	7.3 [1]	6 [1]	-3.70	4980 [11]	Yes [11]	Fe X, XIV [11]	S [5]	227.569 [6]	0.94 [12]	0.26 [12]	Y [2]	...
IM Nor	9.8 [1]	80 [1]	3.86	2380 [13]	Yes [13]	Fe X [13]	P [5]	0.103 [6]	...	...	N [2]	...
RS Oph	6.2 [1]	14 [1]	-3.14	3930 [14]	Yes [15]	Fe X, XI, XIV [16]	P [5]	455.720 [6]	0.75 [12]	0.33 [12]	Y [2,16]	...
V2487 Oph	8.2 [1]	8 [1]	-2.64	10000 [18,19]	Yes [18]	...	P [5]	...	...	...	N [2]	$M_{\rm WD} = 1.35 \pm 0.01 {\rm M}_{\odot}$ [20]
T Pyx	9.1 [1]	62 [1]	2.67	5350 [21]	Yes [21]	Fe II [21]	P [5]	0.076 [6]	-0.02 [12]	0.45 [12]	N [2]	...
V3890 Sgr	7.4 [1]	14 [1]	-1.94	2140 [27]	Yes [9]	Fe X [9]	S [5]	519.7 [10]	1.06 [12]	0.41 [12]	Y [2]	...
U Sco	10.1 [1]	2.6 [1]	-2.53	5700 [22]	Yes [22]	Fe III [23]	P [5]	1.231 [6]	0.401 [24]	...	N [2]	Triple-Peaked Hα [28]
V745 Sco	9.2 [1]	9 [1]	-1.01	3600 [9]	Yes [15]	Fe X, XI [24]	...	510 [10]	1.14 [12]	0.58 [12]	Y [2]	...

[a]Reference Key: 1 = Schaefer (2010); 2 = This Paper; 3 = Kiss et al. (2001); 4 = Schmeja et al. (2000); 5 = Strope et al. (2010); 6 = Downes et al. (2001); 7 = Harrison (1992); 8 = Sekiguchi et al. (1989b); 9 = Williams et al. (1991); 10 = Schaefer (2009); 11 = Bloch et al. (1946); 12 = Harrison et al. (1993); 13 = Orio et al. (2005); 14 = Bode et al. (2007); 15 = Joy (1961); 16 = Dufay et al. (1964a); 17 = Szkody (1994); 18 = Lynch et al. (2000); 19 = Filippenko et al. (1998); 20 = Hachisu et al. (2002); 21 = Catchpole (1969); 22 = Sekiguchi et al. (1988); 23 = Anupama & Dewangan (2000); 24 = Hoard et al. (2002); 25 = Sekiguchi et al. (1990); 26 = Duerbeck & Augusteijn (1989); 27 = Wagner et al. (1990); 28 = F. Walter, private communication

Table 2.3. Properties of the Classical Novae

Nova	Amplitude (mag)	t_3 (days)	$A - A_0$	FWHM Hα	He II	Highest Iron	Light Curve	P_{orb} (days)	$J - H$	$H - K$	Red Giant?	Other
LS And	8.8 [1]	8 [2]	-1.64	...	...	...	...	...	...	...	...	Amp/t_3 [3]
OS And	11 [4]	23 [4]	2.63	1740 [5]	...	...	D [4]	...	...	...	...	$M_{WD} = 1.0M_\odot$ [6]
DO Aql	9.5 [4]	900 [7]	8.29	...	...	Fe III [8]	F [4]	0.168 [1]	0.554 [9]	0.277 [9]	No [10]	...
EL Aql	13.6 [1]	25 [7]	5.39	...	...	...	...	...	0.95 [11]	0.17 [11]	Yes [10]	...
EY Aql	9.5 [1]	...	...	...	...	...	...	...	...	...	...	...
V356 Aql	11.3 [4]	140 [4]	6.46	...	No [8]	Fe II [8]	J [4]	...	0.85 [11]	-0.77 [11]	No [10]	...
V368 Aql	10.4 [1]	42 [7]	3.20	...	Yes [8]	Fe II [8]	...	0.691 [12]	0.383 [9]	0.114 [9]	No [10]	...
V500 Aql	11.2 [1]	43 [13]	4.06	...	...	...	...	0.145 [1]	...	...	...	...
V528 Aql	11.6 [4]	38 [4]	4.21	...	No [8]	Fe II [8]	S [4]	...	...	...	...	...
V603 Aql	12.2 [4]	12 [4]	2.56	...	Yes [14]	Fe II [8]	O [4]	0.138 [15]	0.25 [11]	0.16 [11]	No [10]	Triple-Peaked Hα [8]
V604 Aql	12.8 [1]	25 [7]	4.59	...	...	...	...	...	...	...	...	...
V606 Aql	10.6 [1]	65 [7]	4.26	...	Yes [8]	...	...	...	...	...	...	...
V841 Aql	...	...	...	...	No [8]	...	...	...	...	...	...	...
V1229 Aql	11.5 [4]	32 [4]	3.77	...	...	...	P [4]	...	0.59 [9]	0.5 [9,16]	No [10]	...
V1301 Aql	10.7 [1]	...	...	...	...	...	...	...	...	...	...	...
V1370 Aql	10.3 [4]	28 [4]	2.31	...	...	...	D [4]	...	0.45 [11]	0.6 [11]	No [19]	...
V1378 Aql	11 [1]	15 [7]	1.79	...	...	...	...	...	...	...	...	...
V1419 Aql	13.4 [4]	32 [7]	5.67	...	...	...	D [4]	...	...	...	...	...
V1425 Aql	12 [4]	79 [4]	6.04	1340 [17]	...	Fe II [17]	S [4]	0.256 [1]	...	...	...	...
V1493 Aql	10.9 [4]	50 [4]	4.05	3280, 3400 [18]	...	...	C [4]	0.156 [1]	...	...	...	...
V1494 Aql	13 [4]	16 [4]	3.92	2470 [19]	...	Fe II [19]	O [4]	0.135 [1]	0.479 [9]	0.279 [9]	No [10]	$M_{WD} \sim 1.06 \pm 0.07M_\odot$ [20]
V1548 Aql	>7.2 [4]	...	...	1100 [21]	No [21]	Fe II [21]	...	...	...	...	...	...
OY Ara	11.5 [1]	80 [7]	5.56	...	...	...	...	0.155 [1]	...	...	...	...
T Aur	10.4 [4]	84 [4]	4.56	...	No [8]	Fe II [8]	D [4]	0.204 [1]	0.3 [22]	0.141 [23]	No [10]	...
QZ Aur	11.5 [1]	26 [24]	3.37	...	...	...	...	0.357 [1]	0.556 [23]	0.249 [23]	No [10]	...
RS Car	11 [1]	...	...	...	...	...	...	...	...	...	...	...
V365 Car	8.4 [1]	...	...	...	...	...	...	...	...	...	...	...
BC Cas	6.7 [1]	...	...	...	...	...	...	...	0.488 [9]	0.379 [9]	No [10]	...
V705 Cas	11.6 [1]	67 [4]	5.32	...	...	...	D [4]	0.228 [24]	0.349 [9]	0.259 [9]	No [10]	...
V723 Cas	8.6 [4]	299 [4]	5.24	...	No [25]	Fe III [25]	J [4]	0.693 [1]	0.196 [9]	0.744 [9]	No [10]	$M_{WD} = 0.59M_\odot$ [26]
V812 Cen	9.4 [1]	...	...	...	...	...	...	...	...	...	...	...
V842 Cen	10.9 [4]	48 [27]	3.97	760 [28]	...	...	D [4]	...	0.294 [9]	0.076 [9]	No [10]	...
V868 Cen	11.2 [4]	9 [7]	0.99	700 [29]	...	...	J [4]	...	...	...	...	...
V888 Cen	7.2 [4]	90 [4]	1.49	...	...	...	O [4]	...	...	...	...	...
V1039 Cen	11.7 [4]	174 [4]	7.28	...	...	...	J [4]	0.247 [1]	...	...	...	...
V1047 Cen	...	...	...	840 [30]	...	...	...	...	...	...	...	$M_{WD} = 0.7M_\odot$ [31]
IV Cep	9.7 [1]	37 [7]	2.26	...	No [32]	Fe II [32]	...	...	0.326 [9]	0.333 [9]	No [10]	...
RR Cha	12.2 [1]	60 [7]	5.70	...	...	...	...	0.140 [1]	...	...	...	...
X Cir	...	170 [7]	...	...	...	...	...	...	...	...	...	...
AR Cir	8.99 [33]	330 [33]	5.82	...	...	...	...	...	0.82 [11]	0.17 [11]	Yes [10,11]	...
BY Cir	10.5 [4]	124 [4]	5.42	1500 [34]	...	Fe II [34]	P [4]	0.282 [1]	...	...	...	...
DD Cir	12.6 [4]	16 [4]	3.52	...	...	...	P [4]	0.097 [1]	0.291 [9]	0.578 [9]	No [10]	...
DE Cir	8.5 [1]	10 [35]	-1.54	5100 [36]	Yes [37]	...	...	...	0.529 [9]	0.245 [9]	No [10]	Triple-Peaked Hα [37]
V655 CrA	9.6 [1]	...	...	...	...	...	...	...	...	...	...	...
V693 CrA	>14 [4]	18 [4]	...	4500 [38]	...	...	S [4]	...	...	...	...	$M_{WD} = 1.3M_\odot$ [6]
AP Cru	11 [1]	...	...	...	...	...	...	0.213 [1]	0.696 [9]	0.276 [9]	Yes [10]	...
CP Cru	10.2 [1]	10 [39]	0.20	2000 [40]	Yes [40]	...	...	0.944 [1]	...	...	...	...
V450 Cyg	8.5 [1]	171 [13]	4.05	...	No [8]	Fe II [8]	...	...	...	...	...	...
V465 Cyg	12.2 [1]	140 [7]	7.36	...	No [8]	Fe II [8]	...	...	...	...	...	...
V476 Cyg	14.3 [4]	16 [4]	5.22	...	No [8]	Fe II [8]	D [4]	...	0.42 [9]	0.029 [9]	No [10]	...
V1330 Cyg	7.6 [4]	217 [4]	3.61	...	...	...	S [4]	...	0.574 [9]	0.097 [9]	No [10]	Light Curve [41]
V1500 Cyg	19.6 [4]	4 [4]	7.81	...	...	...	S [4]	0.140 [1]	...	...	...	$M_{WD} = 1.15M_\odot$ [42,43]
V1668 Cyg	13.5 [4]	26 [4]	5.37	2400 [44]	...	Fe II [44]	S [4]	0.138 [1]	...	...	...	$M_{WD} \sim 0.95M_\odot$ [43]
V1819 Cyg	7.7 [4]	181 [4]	3.36	2742 [45]	...	...	J [4]	...	...	...	...	...
V1974 Cyg	12.6 [4]	43 [4]	5.45	...	...	...	P [4]	0.081 [1]	0.389 [9]	0.078 [9]	No [10]	$M_{WD} \sim 1.0M_\odot$ [43]
V2274 Cyg	>8.5 [4]	33 [4]	...	950 [46]	...	Fe II [46]	D [4]	...	...	...	...	...
V2275 Cyg	11.5 [4]	8 [4]	1.06	2100 [47]	...	...	S [4]	0.315 [1]	...	...	...	...

Table 2.3—Continued

Nova	Amplitude (mag)	t_3 (days)	$A - A_0$	FWHM Hα	He II	Highest Iron	Light Curve	P_{orb} (days)	$J - H$	$H - K$	Red Giant?	Other
V2361 Cyg	...	...	...	3200 [48]	...	...	...	...	...	...	...	$M_{WD} = 1.05 M_\odot$ [43]
Q Cyg	12.6 [1]	11 [7]	2.79	...	Yes [8]	Fe II [8]	...	0.420 [15]	0.319 [23]	0.149 [23]	No [10]	...
HR Del	8.5 [4]	231 [4]	4.64	...	...	...	J [4]	0.214 [1]	0.07 [11]	0.07 [11]	No [10]	$M_{WD} = 0.595 M_\odot$, $0.9 M_\odot$ [49,50]
DM Gem	11.9 [1]	22 [7]	3.44	...	No [8]	...	...	...	...	...	...	...
DN Gem	12 [4]	35 [4]	4.45	...	No [8]	Fe X [8]	P [4]	0.128 [15]	0.231 [23]	-0.077 [23]	Yes [23]	...
DQ Her	12.7 [4]	100 [4]	7.20	...	No [8]	Fe II [8]	D [4]	0.194 [1]	0.274 [23]	0.194 [23]	No [10]	...
V446 Her	11.3 [4]	42 [4]	4.10	...	...	Fe X, XI [51]	S [4]	0.207 [52]	0.38 [11]	0.42 [11]	No [10]	...
V533 Her	12 [4]	43 [4]	4.85	...	...	...	S [4]	0.210 [24]	0.032 [23]	0.035 [23]	No [10]	...
V827 Her	10.6 [1]	53 [4]	3.86	...	...	...	S [4]	...	...	...	...	...
V838 Her	13.8 [4]	4 [4]	2.01	5000 [53]	Yes [54]	Fe II [55]	P [4]	0.298 [1]	0.666 [9]	0.104 [9]	No [10]	$M_{WD} = 1.35 M_\odot$, Triple-Peaked Hα [56,57]
CP Lac	13 [4]	9 [4]	2.79	...	No [8]	Fe II [8]	S [4]	0.145 [15]	0.291 [9]	-0.08 [9]	No [10]	...
DI Lac	10.4 [1]	43 [7]	3.25	...	No [8]	Fe II [8]	...	0.544 [1]	0.18 [23]	0.175 [23]	No [10]	...
DK Lac	7.9 [4]	202 [4]	3.77	...	No [8]	Fe II [58]	J [4]	...	0.443 [23]	-1.6 [16,23]	No [10]	...
HY Lup	10.9 [1]	...	...	2700 [59]	...	...	...	...	...	...	...	...
HR Lyr	9.3 [1]	97 [60]	3.74	...	...	Fe II [8]	...	0.91: [61]	0.249 [9]	-0.014 [9]	No [10]	Amp/t_3 [60]
BT Mon	7.6 [1]	182 [4]	3.27	2100 [62]	Yes [62]	...	F [4]	0.334 [1]	0.43 [11]	0.16 [11]	No [10]	$M_{WD} = 1.04 M_\odot$ [63]
GI Mon	11 [1]	23 [7]	2.63	...	No [8]	...	...	0.180 [1]	0.311 [23]	0.22 [23]	No [10]	...
KT Mon	...	40 [7]	...	...	Yes [64]	...	...	...	...	...	...	...
GQ Mus	11.1 [1]	45 [7]	4.04	...	...	...	...	0.059 [1]	...	...	...	$M_{WD} = 0.70 \pm 0.05 M_\odot$ [65]
LZ Mus	>9.5 [4]	12 [4]	...	...	...	...	P [4]	...	...	...	...	...
IL Nor	11 [1]	108 [7]	5.65	...	...	...	...	...	0.485 [9]	0.199 [9]	No [10]	...
V382 Nor	...	...	...	...	...	...	...	...	...	...	...	$M_{WD} = 1.15 \pm 0.10 M_\odot$ [31]
V553 Oph	9.5 [1]	...	...	...	...	...	...	...	...	...	...	...
V794 Oph	6.3 [1]	220 [27]	2.34	...	...	...	...	...	0.797 [23]	0.182 [23]	Yes [10]	...
V840 Oph	12.8 [1]	36 [7]	5.30	...	...	...	...	...	...	...	...	...
V841 Oph	9.3 [1]	130 [7]	4.31	...	...	...	...	0.601 [15]	0.39 [11]	0.14 [11]	No [10]	...
V849 Oph	11.2 [4]	270 [4]	7.64	...	No [8]	Fe II [8]	F [4]	0.173 [1]	...	...	...	...
V906 Oph	...	25 [7]	...	...	...	...	...	...	...	...	...	...
V908 Oph	...	...	...	...	...	...	...	...	...	...	...	...
V972 Oph	9.5 [1]	176 [7]	5.10	...	...	...	...	...	0.672 [23]	0.315 [23]	No [10]	...
V1012 Oph	8.2 [1]	...	...	...	...	...	...	...	...	...	...	...
V2024 Oph	...	...	...	...	...	...	...	...	...	...	...	...
V2104 Oph	11.7 [1]	...	...	...	...	...	...	...	...	...	...	...
V2109 Oph	7.2 [1]	...	...	...	...	...	...	...	...	...	...	...
V2214 Oph	12 [1]	89 [4]	6.27	1025 [66]	No [66]	Fe II [66]	S [4]	0.118 [1]	...	...	...	...
V2264 Oph	>11 [4]	30 [4]	...	2300 [67]	No [67]	Fe II [67]	S [4]	...	...	...	...	...
V2290 Oph	...	50 [7]	...	...	...	...	...	...	...	...	...	...
V2295 Oph	>11.7 [4]	16 [4]	...	...	...	...	F [4]	...	...	...	...	...
V2313 Oph	>12.5 [4]	17 [4]	...	2500 [68]	No [68]	Fe II [68]	S [4]	...	...	...	...	...
V2540 Oph	>12.9 [4]	115 [4]	...	...	No [69]	...	J [4]	0.285 [1]	...	...	...	...
V2573 Oph	...	99 [70]	...	...	...	...	...	...	...	...	...	...
V2574 Oph	...	...	...	1500 [71]	No [71]	Fe II [71]	...	...	...	...	...	...
V Per	9.3 [1]	...	...	...	...	...	...	0.107 [1]	...	...	...	...
GK Per	12.8 [4]	13 [4]	3.31	...	No [8]	Fe II [8]	O [4]	1.997 [1]	...	...	...	$M_{WD} \sim 0.9 M_\odot$ [31,72,73]
V400 Per	11.7 [1]	43 [7]	4.55	...	...	...	...	...	...	...	...	...
RR Pic	11.2 [4]	122 [4]	6.09	...	No [8]	Fe II [8]	J [4]	0.145 [1]	0.22 [11]	0.06 [11]	No [10]	...
CP Pup	>17.3 [4]	8 [4]	...	...	Yes [8]	Fe X [8]	P [4]	0.061 [1]	0.39 [11]	0.01 [11]	No [10]	...
DY Pup	12.6 [1]	160 [7]	8.02	...	...	...	...	0.139 [1]	...	...	...	...
HS Pup	10.8 [1]	65 [7]	4.46	...	...	...	...	...	0.462 [23]	0.52 [23]	No [10]	...
HZ Pup	9.3 [1]	70 [7]	3.10	...	...	...	...	0.213 [1]	0.243 [23]	0.087 [23]	No [10]	...
V351 Pup	13.2 [1]	26 [7]	5.07	...	...	...	P [4]	0.118 [1]	...	...	...	$M_{WD} = 1.0 M_\odot$ [6]
V445 Pup	6 [4]	240 [4]	2.21	...	...	Fe II [74]	D [4]	...	0.337 [23]	0.418 [23]	No [10]	$M_{WD} \sim 1.35 M_\odot$ [75]
V574 Pup	10.2 [4]	27 [4]	2.14	2830 [76]	...	Fe II [77]	S [4]	...	...	...	...	$M_{WD} \sim 1.05 \pm 0.05 M_\odot$ [20]
WY Sge	15.3 [1]	...	...	...	...	...	...	0.154 [24]	...	...	...	...
HS Sge	13.5 [4]	21 [4]	4.95	...	...	...	P [4]	...	...	...	...	...
AT Sgr	8 [1]	...	...	...	...	...	...	...	...	...	...	...
BS Sgr	7.8 [1]	700 [7]	6.10	...	...	...	...	...	0.61 [11]	0.1 [11]	No [10]	...

Table 2.3—Continued

Nova	Amplitude (mag)	t_3 (days)	$A - A_0$	FWHM Hα	He II	Highest Iron	Light Curve	P_{orb} (days)	$J - H$	$H - K$	Red Giant?	Other
FL Sgr	11.7 [1]	32 [7]	3.97	...	...	...	...	...	...	...	...	...
FM Sgr	11.9 [1]	30 [7]	4.05	...	...	...	...	...	...	...	...	...
GR Sgr	5.2 [1]	...	...	...	...	...	...	...	0.35 [23]	-0.14 [23]	Yes [23]	...
HS Sgr	5 [1]	...	...	...	...	...	...	...	...	...	...	...
KY Sgr	9.4 [1]	60 [7]	2.90	...	...	...	...	...	1.244 [9]	0.525 [9]	Yes [10]	...
V363 Sgr	11.2 [1]	64 [7]	4.83	...	...	...	...	...	...	...	...	...
V441 Sgr	...	53 [7]	...	...	...	...	...	...	...	...	...	...
V630 Sgr	13 [1]	11 [7]	3.19	...	No [8]	...	...	0.118 [1]	...	...	...	...
V726 Sgr	8.2 [1]	90 [78]	2.49	...	...	...	...	...	...	...	...	...
V732 Sgr	9.6 [4]	75 [4]	3.54	...	...	...	D [4]	...	1.542 [23]	0.676 [23]	Yes [10,23]	...
V787 Sgr	11.2 [1]	74 [7]	5.11	...	...	...	...	...	...	...	...	...
V909 Sgr	13.2 [1]	7 [7]	2.50	...	...	...	...	0.14: [24]	...	...	...	...
V927 Sgr	12 [1]	15 [7]	2.79	...	...	...	...	...	...	...	...	...
V928 Sgr	11.6 [1]	150 [7]	6.89	...	No [8]	Fe II [8]	...	...	...	...	...	...
V990 Sgr	...	24 [8]	...	...	...	...	...	...	...	...	...	...
V999 Sgr	9.4 [1]	160 [7]	4.82	...	...	...	...	...	...	...	...	...
V1012 Sgr	12 [1]	32 [7]	4.27	...	...	...	...	...	...	...	...	...
V1014 Sgr	9.1 [1]	...	...	...	...	...	...	...	...	...	...	...
V1015 Sgr	13.9 [1]	34 [7]	6.29	...	...	...	...	...	...	...	...	...
V1016 Sgr	8.5 [1]	140 [7]	3.66	...	...	...	...	...	0.647 [9]	0.198 [9]	No [10]	...
V1017 Sgr	6.5 [1]	130 [7]	1.51	...	...	...	...	5.780 [1]	0.58 [79]	0.17 [79]	No [10]	...
V1059 Sgr	13.2 [1]	...	...	...	...	...	...	0.286 [80]	0.27 [11]	0.07 [11]	No [10]	...
V1148 Sgr	...	...	...	...	...	...	...	...	0.22 [9]	0.09 [9]	No [10]	...
V1149 Sgr	13.6 [1]	210 [7]	9.55	...	...	...	...	...	...	...	...	...
V1150 Sgr	...	...	...	...	...	...	...	...	...	...	...	...
V1151 Sgr	8.9 [1]	...	...	...	...	...	...	...	...	...	...	...
V1172 Sgr	9 [1]	...	...	2000-3000 [81]	...	...	...	...	1.14 [23]	0.396 [23]	Yes [10,23]	...
V1174 Sgr	...	...	...	...	...	...	...	...	...	...	...	...
V1175 Sgr	...	...	...	...	...	...	...	...	...	...	...	...
V1275 Sgr	11 [1]	10 [7]	1.00	...	...	...	...	...	0.582 [23]	0.154 [23]	No [10]	...
V1310 Sgr	...	...	...	...	...	...	...	...	0.722 [9]	0.212 [9]	Yes [10]	...
V1572 Sgr	...	...	...	...	...	...	...	...	...	...	...	...
V1583 Sgr	12.1 [1]	37 [7]	4.66	...	...	...	...	...	...	...	...	...
V1944 Sgr	...	...	...	...	...	...	...	...	...	...	...	...
V2415 Sgr	...	...	...	...	...	...	...	...	...	...	...	...
V2572 Sgr	11.5 [1]	44 [7]	4.40	...	...	...	...	...	...	...	...	...
V3645 Sgr	5.4 [1]	...	...	...	...	...	...	...	0.558 [9]	...	Yes [82]	...
V3888 Sgr	12 [1]	...	...	...	...	...	...	...	...	...	...	...
V3889 Sgr	12.6 [1]	14 [7]	3.26	...	...	...	...	...	...	...	...	...
V3964 Sgr	...	32 [7]	...	...	...	...	...	...	0.343 [23]	...	...	...
V4021 Sgr	9.1 [4]	215 [4]	5.10	...	...	...	P [4]	...	...	...	...	...
V4027 Sgr	...	...	...	...	...	...	...	...	...	...	...	...
V4049 Sgr	9 [1]	...	...	...	...	...	...	...	...	...	...	...
V4074 Sgr	...	...	...	...	...	...	...	...	0.79 [79]	0.28 [79]	Yes [10]	...
V4077 Sgr	14 [1]	100 [7]	8.50	...	...	...	...	0.16: [24]	...	...	...	...
V4121 Sgr	11.5 [1]	60 [7]	5.00	...	...	...	...	...	...	...	...	...
V4135 Sgr	11.5 [1]	60 [7]	5.00	1000 [83]	...	...	...	...	...	...	...	...
V4157 Sgr	...	41 [70]	...	...	...	...	...	...	...	...	...	...
V4160 Sgr	>12 [4]	3 [4]	...	4500 [84]	Yes [84]	...	S [4]	...	...	...	...	...
V4169 Sgr	>9.1 [4]	36 [4]	...	...	...	...	S [4]	...	...	...	...	...
V4171 Sgr	12.5 [1]	20 [70]	3.85	1200 [85]	...	Fe II [85]	...	...	...	...	...	...
V4327 Sgr	...	30 [70]	...	2400 [86]	...	Fe II [86]	...	...	...	...	...	...
V4361 Sgr	6.3 [1]	86 [70]	0.51	...	...	Fe II [87]	...	...	...	...	...	...
V4362 Sgr	...	...	...	450 [88]	...	Fe II [88]	...	...	0.426 [23]	1.005 [23]	No [10]	...
V4444 Sgr	>13.4 [4]	9 [4]	...	800 [89]	...	Fe II [89]	S [4]	...	-0.143 [9]	0.807 [9]	No [10]	Dust [90]
V4579 Sgr	5.5 [1]	...	...	...	...	...	...	...	...	...	...	...
V4633 Sgr	11.3 [4]	44 [4]	4.20	1600 [91]	Yes [92]	Fe II [91]	P [4]	0.126 [1]	-0.017 [23]	0.706 [23]	No [10]	...

Table 2.3—Continued

Nova	Amplitude (mag)	t_3 (days)	$A - A_0$	FWHM Hα	He II	Highest Iron	Light Curve	P_{orb} (days)	$J - H$	$H - K$	Red Giant?	Other
V4642 Sgr	...	125 [70]	...	...	...	Fe II [93]	...	...	...	...	...	...
V4643 Sgr	>8.3 [4]	6 [4]	...	4700 [94]	...	...	S [4]	...	...	...	...	...
V4739 Sgr	>10.8 [4]	3 [4]	...	5510 [95]	...	...	S [4]	...	...	...	...	...
V4740 Sgr	>11.3 [4]	33 [4]	...	...	...	Fe II [96]	S [4]	...	...	...	...	...
V4741 Sgr	...	28 [70]	...	2800 [97,98]	No [97]	Fe II [97,98]	...	...	...	...	...	...
V4742 Sgr	...	23 [4]	...	2500 [99]	...	Fe II [99]	S [4]	...	...	...	...	...
V4743 Sgr	>10.1 [4]	12 [4]	...	2400 [100]	...	Fe II [100]	S [4]	0.281 [1]	...	...	...	$M_{WD} \sim 1.15 \pm 0.06 M_\odot$ [20]
V4744 Sgr	...	...	...	...	...	...	...	...	...	...	...	[0]
V4745 Sgr	>9.7 [4]	190 [4]	...	...	...	...	J [4]	...	...	...	...	...
V5113 Sgr	...	...	...	550 [101]	...	Fe II [102]	...	...	...	...	...	...
V5114 Sgr	>12.9 [4]	21 [4]	...	2000 [103]	No [103]	Fe II [103]	S [4]	...	...	...	...	...
V5115 Sgr	>10.1 [4]	13 [4]	...	1300 [104]	...	Fe II [105]	S [4]	...	...	...	...	$M_{WD} \sim 1.2 \pm 0.1 M_\odot$ [31]
V5116 Sgr	>8.4 [4]	26 [4]	...	970 [30]	No [106]	...	S [4]	...	...	...	...	$M_{WD} \sim 1.07 \pm 0.07 M_\odot$ [20]
KP Sco	11.6 [1]	38 [7]	4.21	...	...	...	...	...	...	...	...	...
V696 Sco	12 [1]	9 [7]	1.79	...	...	...	...	...	0.191 [23]	0.082 [23]	No [10]	...
V697 Sco	9.8 [1]	15 [7]	0.59	...	...	...	...	0.187 [1]	...	...	...	...
V707 Sco	10.1 [1]	49 [7]	3.21	...	...	...	...	...	...	...	...	...
V719 Sco	10.7 [1]	24 [7]	2.41	1800 [107]	No [108]	Fe II [108]	...	...	...	...	...	...
V720 Sco	13.5 [1]	...	...	...	No [8]	Fe II [8]	...	...	...	...	...	...
V721 Sco	...	...	...	...	...	...	...	...	0.374 [9]	0.111 [9]	No [10]	...
V722 Sco	...	18 [7]	...	...	...	...	...	...	...	...	...	...
V723 Sco	9.2 [1]	17 [7]	0.24	...	...	...	...	...	1.09 [11]	0.37 [11]	Yes [10,11]	...
V729 Sco	8 [1]	...	...	...	...	...	...	...	...	...	...	...
V733 Sco	7.5 [1]	...	...	...	...	...	...	...	...	...	...	...
V734 Sco	5.3 [1]	...	...	...	...	...	...	...	...	...	...	...
V825 Sco	7 [1]	...	...	...	...	...	...	...	...	...	...	...
V902 Sco	9 [1]	...	...	...	...	...	...	...	...	...	...	...
V960 Sco	9.5 [1]	...	...	...	...	...	...	...	...	...	...	...
V977 Sco	11.6 [1]	8 [7]	1.16	...	No [109]	Fe II [109]	...	...	0.617 [23]	0.14 [23]	No [10]	...
V992 Sco	9.5 [4]	120 [7]	4.36	800 [82]	...	Fe II [82]	D [4]	0.154 [1]	0.277 [9]	0.477 [9]	No [10]	...
V1141 Sco	9.1 [1]	46 [70]	2.08	3200 [110]	...	Fe II [111]	...	...	...	...	...	...
V1142 Sco	...	...	...	3800 [112]	...	...	...	...	...	...	...	...
V1178 Sco	...	...	...	1300 [113]	...	...	...	...	...	...	...	...
V1186 Sco	>8.3 [4]	62 [4]	...	500 [114]	...	...	J [4]	...	...	...	...	...
V1187 Sco	8.2 [4]	17 [4]	-0.76	3000 [115,116]	...	...	S [4]	...	...	...	...	...
V1188 Sco	>10.1 [4]	23 [4]	...	1730 [117]	...	...	S [4]	...	...	...	...	$M_{WD} \sim 1.25 M_\odot$ [31]
EU Sct	9.6 [1]	42 [7]	2.40	...	No [8]	Fe II [8]	...	...	1.078 [9]	0.375 [9]	Yes [10,11,118]	...
FS Sct	9.2 [1]	...	...	...	No [8]	Fe II [8]	...	...	0.724 [9]	0.221 [9]	Yes [10]	...
FV Sct	7.5 [1]	...	...	...	...	...	...	...	...	...	...	...
V366 Sct	...	...	...	...	...	...	...	...	...	...	...	...
V368 Sct	12.1 [1]	30 [7]	4.25	...	...	...	...	...	...	...	Yes [16]	...
V373 Sct	>12.2 [4]	79 [4]	...	...	...	...	J [4]	...	...	...	...	...
V443 Sct	>11.5 [4]	60 [4]	...	1400 [119]	No [119]	Fe II [119]	J [4]	...	...	...	...	...
V444 Sct	9.5 [1]	23 [70]	1.13	...	...	...	...	...	...	...	...	...
V463 Sct	...	...	...	990 [120]	...	Fe II [120]	...	...	...	...	...	$M_{WD} = 1.1 M_\odot$ [26]
V476 Sct	...	...	...	...	...	Fe II [121]	...	...	...	...	...	$M_{WD} \sim 0.95 M_\odot$ [31]
V477 Sct	11 [4]	6 [122]	0.00	2900 [123]	Yes [124]	...	...	...	...	...	...	$M_{WD} \sim 1.3 M_\odot$ [31]
X Ser	9.4 [1]	...	...	...	...	...	...	1.480 [1]	0.63 [11]	0.45 [11]	No [10]	...
CT Ser	8.7 [1]	>100 [24]	...	...	No [8]	Fe X [8]	...	0.195 [1]	-0.06 [11]	0.91 [11]	No [10]	...
DZ Ser	7 [1]	...	...	...	...	...	...	...	...	...	...	...
FH Ser	12.3 [4]	62 [4]	5.87	...	...	...	D [4]	...	0 [11]	0.79 [11]	No [10]	...
LW Ser	11.1 [4]	52 [4]	4.32	...	...	...	D [4]	...	...	...	...	...
MU Ser	> 12.1 [2]	5 [7]	...	...	...	...	...	...	...	...	...	...
V378 Ser	...	...	...	1100 [125]	...	Fe II [125]	...	...	...	...	...	$M_{WD} \sim 0.7 \pm 0.1 M_\odot$ [31]
XX Tau	12.6 [1]	51 [13]	5.79	...	...	...	...	...	...	...	...	...
RW UMi	12.5 [1]	140 [24]	7.66	...	...	...	...	0.081 [24]	...	...	...	...
CN Vel	7.6 [1]	...	...	...	...	...	...	...	...	...	...	...

Table 2.3—Continued

Nova	Amplitude (mag)	t_3 (days)	$A - A_0$	FWHM Hα	He II	Highest Iron	Light Curve	P_{orb} (days)	$J - H$	$H - K$	Red Giant?	Other
CQ Vel	12 [1]	50 [7]	5.15	...	...	...	...	...	...	...	...	...
V382 Vel	13.8 [4]	13 [4]	4.31	2390 [126]	...	Fe II [126]	S [4]	0.158 [1]	...	...	...	$M_{WD} = 1.23 \pm 0.05 M_\odot$ [20]
CK Vul	18.1 [1]	100 [7]	12.60	...	...	...	...	...	0.28 [127]	1.04 [127]	Yes [16,127]	...
LU Vul	...	21 [7]	...	...	...	...	...	...	...	...	...	...
LV Vul	10.8 [4]	38 [4]	3.41	...	...	...	S [4]	...	0.44 [11]	0.27 [11]	No [10]	...
NQ Vul	11 [4]	50 [4]	4.15	...	...	...	D [4]	...	0.1 [11]	2.03 [11]	No [10]	...
PW Vul	10.5 [4]	116 [4]	5.29	...	...	...	J [4]	0.214 [128]	...	...	...	...
QU Vul	12.6 [4]	36 [4]	5.10	...	...	...	P [4]	0.112 [1]	...	...	...	...
QV Vul	10.9 [4]	47 [4]	3.92	920 [129]	...	...	D [4]	...	...	...	...	...

[a]Reference Key: 1 = Downes et al. (2001); 2 = Duerbeck (1988); 3 = Duerbeck (1987); 4 = Strope et al. (2010); 5 = Sheffer & Krisciunas (1987); 6 = Kato & Hachisu (2007); 7 = Shafter (1997); 8 = Payne-Gaposchkin (1964); 9 = Simbad database; 10 = This Paper; 11 = Harrison (1992); 12 = Marin & Shafter (2009); 13 = Extrapolated from Shafter (1997)'s t_2 using the empirical relation $t_3 = 0.91 \times t_2 + 0.46$; 14 = Wyse (1940); 15 = Peters & Thorstensen (2006); 16 = Szkody (1994); 17 = Ohshima et al. (1995); 18 = Tomov et al. (1999); 19 = Kiss & Thomson (2000); 20 = Hachisu & Kato (2010); 21 = Shemmer (2001); 22 = Szkody & Feinswog (1988); 23 = Hoard et al. (2002); 24 = Diaz & Bruch (1997); 25 = Iijima (2006); 26 = Hachisu & Kato (2004); 27 = Woudt & Warner (2003); 28 = Sekiguchi et al. (1989a); 29 = Jablonski et al. (1991); 30 = Liller et al. (2005); 31 = Hachisu & Kato (2007); 32 = Aikman et al. (1973); 33 = Duerbeck & Grebel (1993); 34 = Liller et al. (1995); 35 = AAVSO database; 36 = Liller et al. (2003); 37 = The STONY BROOK / SMARTS Spectral Atlas of Southern Novae; 38 = Brosch & Leibowitz (1981); 39 = Lyke et al. (2003); 40 = della Valle & Benetti (1997); 41 = Rosenbush (1999); 42 = Horne & Schneider (1989); 43 = Hachisu & Kato (2006); 44 = Klare et al. (1980); 45 = Whitney & Clayton (1989); 46 = Iijima (2001); 47 = Kiss et al. (2002); 48 = Naito et al. (2005a); 49 = Kuerster & Barwig (1988); 50 = Bruch (1982); 51 = Dufay et al. (1964b); 52 = Thorstensen & Taylor (2000); 53 = Feast et al. (1991); 54 = Iijima et al. (1991); 55 = della Valle et al. (1991); 56 = Kato et al. (2009); 57 = Iijima & Cassatella (2010); 58 = Wellmann (1951); 59 = della Valle (1993); 60 = Shears & Poyner (2007); 61 = J. Thorstensen 2009, private communication; 62 = Sanford (1940); 63 = Smith et al. (1998); 64 = Kato & Yamaoka (2002); 65 = Hachisu et al. (2008a); 66 = Weller & Heathcote (1988); 67 = Wagner & Starrfield (1991); 68 = Wagner et al. (1994); 69 = Puetter et al. (2002); 70 = Burlak & Henden (2008); 71 = Puetter et al. (2004); 72 = Crampton et al. (1986); 73 = Morales-Rueda et al. (2002); 74 = Iijima & Nakanishi (2008); 75 = Kato & Hachisu (2003a); 76 = Siviero et al. (2005); 77 = Ayani (2004); 78 = Mayall (1938); 79 = Harrison et al. (1993); 80 = Thorstensen et al. (2010); 81 = Strömgren & Shapley (1951); 82 = della Valle & Smette (1992); 83 = McNaught et al. (1987); 84 = Kingsburgh & English (1991); 85 = Stringfellow & Gregg (1992); 86 = della Valle et al. (1993); 87 = Martini et al. (1996); 88 = Austin et al. (1994); 89 = Garnavich et al. (1999); 90 = Kato et al. (2004); 91 = della Valle et al. (1998); 92 = Lynch et al. (2001a); 93 = Wagner et al. (2000); 94 = Ayani & Kawabata (2001); 95 = Vanlandingham et al. (2001); 96 = Patat et al. (2001); 97 = Fujii et al. (2002); 98 = Gosset (2002); 99 = Duerbeck et al. (2002); 100 = Kato et al. (2002a); 101 = Brown et al. (2003); 102 = Ruch et al. (2003); 103 = Ederoclite et al. (2006); 104 = Ayani & Kawabata (2005); 105 = Rudy et al. (2005); 106 = Russell et al. (2005); 107 = Henize & McLaughlin (1951); 108 = McLaughlin (1951); 109 = Duerbeck & Augusteijn (1989); 110 = Fujii & Kawakita (1997); 111 = Mason et al. (1997); 112 = Fujii (1998); 113 = Fujii (2001); 114 = Pojmanski et al. (2004); 115 = Yamaoka et al. (2004); 116 = Lynch et al. (2004); 117 = Naito et al. (2005b); 118 = Weight et al. (1994); 119 = Barbon & Rosino (1989); 120 = Kato et al. (2002b); 121 = Perry et al. (2005); 122 = Munari et al. (2006); 123 = Fujii & Yamaoka (2005); 124 = Mazuk et al. (2005); 125 = Yamaoka & Fujii (2005); 126 = Steiner et al. (1999); 127 = Harrison (1996); 128 = Hacke (1987); 129 = Gallagher et al. (1987)

Table 2.4. Properties of the Good Recurrent Nova Candidates

Nova	Amplitude (mag)	t_3 (days)	Amp/t_3	FWHM Hα	He II	Highest Iron	Light Curve	P_{orb} (days)	$J-H$	$H-K$	Red Giant?	Other
V1721 Aql	>6 [1]	10: [2]	...	6450 [2]	...	...	...	...	...	...	...	Triple-Peaked Hα [3]
DE Cir	8.5 [4]	9.8 [1]	-1.54	5100 [5]	Yes [6]	...	...	...	0.529 [7]	0.245 [7]	No [8]	Triple-Peaked Hα [6]
CP Cru	10.2 [4]	10 [9]	0.2	2000 [10]	Yes [10]	...	...	0.944 [4]	...	...	...	...
KT Eri	7.7: [1]	10 [11]	-2.3	3200-3400 [12]	No [12]	No [13]	P [1]	737 [14]	0.46 [14]	0.7 [14]	Yes [8,14]	Triple-Peaked Hα [13]
V838 Her	13.8 [15]	4 [15]	2.01	5000 [16]	Yes [17]	Fe II [18]	P [15]	0.297635 [4]	0.666 [7]	0.104 [7]	No [8]	$M_{WD} = 1.35M_{\odot}$, Triple-Peaked Hα [19,20]
V2672 Oph	>10 [1]	6: [1]	...	8000 [21]	Yes [22]	...	...	...	...	...	...	Triple-Peaked Hα [22]
V4160 Sgr	>12 [15]	3 [15]	...	4500 [23]	Yes [23]	...	S [15]	...	...	...	...	...
V4643 Sgr	>8.3 [15]	6 [15]	...	4700 [24]	...	...	S [15]	...	...	...	...	...
V4739 Sgr	>10.8 [15]	3 [15]	...	5510 [25]	...	...	S [15]	...	...	...	...	...
V477 Sct	11 [15]	6 [26]	0.002	2900 [27]	Yes [28]	...	...	...	...	...	...	$M_{WD} \sim 1.3M_{\odot}$ [29]

[a]Reference Key: 1 = AAVSO database; 2 = Hounsell et al. (2011); 3 = Helton et al. (2008a); 4 = Downes et al. (2001); 5 = Liller et al. (2003); 6 = The STONY BROOK/SMARTS Spectral Atlas of Southern Novae; 7 = Simbad database; 8 = This Paper; 9 = Lyke et al. (2003); 10 = della Valle & Benetti (1997); 11 = Hounsell et al. (2010); 12 = Yamaoka et al. (2009); 13 = F. Walter 2010, private communication; 14 = Jurdana-Šepić et al. (2012); 15 = Strope et al. (2010); 16 = Feast et al. (1991); 17 = Iijima et al. (1991); 18 = della Valle et al. (1991); 19 = Kato et al. (2009); 20 = Iijima & Cassatella (2010); 21 = Ayani et al. (2009); 22 = Schwarz et al. (2009); 23 = Kingsburgh & English (1991); 24 = Ayani & Kawabata (2001); 25 = Vanlandingham et al. (2001); 26 = Munari et al. (2006); 27 = Fujii & Yamaoka (2005); 28 = Mazuk et al. (2005); 29 = Hachisu & Kato (2007)

With the collected data from Tables 2.2 and 2.3 and our criteria from Section 2.2, we can place each of our 247 novae into one of six categories, labeled A-F. Category A contains the known RNe, for which multiple eruptions have been confidently observed, listed in Table 2.2. Category B contains strong RN candidates, for which many of our indicators strongly point to the system being recurrent, with only one eruption observed thus far, listed in Table 2.4. Category C contains likely RN candidates, for which our evaluation of the characteristics in Table 2.3 indicates that the probability is $\geq$ 50% that the system is recurrent. This 50% probability is not quantitatively calculated, but instead is a judgment call based on our extensive experience with these systems. In order to reduce systematic errors due to personal bias, each system was categorized independently by both my advisor and myself. Upon comparing our lists we found only a few discrepancies between our category assignments, and we resolved those by more closely examining each system and all known indicators. Although this method is not perfect, it is robust, and good enough to use for obtaining statistics. Category D contains likely CNe, despite the system perhaps showing some small number of positive RN indicators. Category E contains systems which are certainly CNe based on the indicators in Table 2.3. In particular, systems showing any the following properties were automatically added to D or E: $A - A_0 > 5.0$ mag; FWHM of Hα < 1500 km s^{-1}; neither He II nor high-excitation iron lines when both would have been visible; D, J, or F light curve classes; and measured $M_{\rm WD} < 1.1$ M$_\odot$. Category F contains systems for which there is not enough information to determine the status of the system. Table 2.5 presents the number of systems in each of the six categories. The fraction of RNe in CN lists is then $F_{\rm RN} = (B+C)/(B+C+D+E)$. The uncertainty is $[F_{\rm RN} \times (1-F_{\rm RN})/(B+C+D+E)]^{0.5}$.

Category A systems are listed in Table 2.2, and Category B systems are listed in Table 2.4. The Category C systems are V368 Aql, V606 Aql, V1229 Aql, V1493 Aql, DD Cir, V693 CrA, V2275 Cyg, Q Cyg, DN Gem, HR Lyr, LZ Mus, CP Pup, V574 Pup, V1172 Sgr, V1275 Sgr, V4327 Sgr, V4361 Sgr, V4633 Sgr, V4742 Sgr, V4743 Sgr, V696 Sco, V697 Sco, V723 Sco, V1141 Sco, V1187 Sco, V1188 Sco, X Ser, CT Ser, and QU Vul.

Table 2.5. Recurrent Nova Fractions

	Complete Sample	Strope Sample
A = # known RNe	10	8
B = # strong candidate RNe	7	4
C = # likely RNe candidates	29	15
D = # likely CNe	91	45
E = # certain CNe	21	15
F = # not enough information	89	3
A+B+C+D+E+F = sample size	247	90
(B+C)/(B+C+D+E) = RN fraction	24.3%±3.5%	24.1%±4.8%

A concern is that our sample of 247 systems may have a bias because many of the novae have relatively little data—even beyond our exclusion into Category F—and a poorly-observed nova is less likely to be recognized as an RN. To address this, we examine the subset of well-observed novae in Strope et al. (2010). This sample has thorough light curve coverage, and generally good spectroscopic and quiescence observations as well. The statistics for the Strope sample are also presented in Table 2.5.

The two samples give RN fractions of 24.3%±3.5% and 24.1%±4.8%, so we take 24%±4% as the final result for this first method. Since there are approximately 400 known CNe to date, ∼96 of them should be RNe. The ratio of unidentified RNe to the known RNe is therefore ∼10 : 1.

2.5.2 RN Fraction from Number of Known RNe

There must be some proportionality between the number of known RNe and the number of RNe masquerading as CNe. The fact that there are ten known RNe can thus be used to estimate the number of hidden RNe and therefore the RN fraction. To do this, we must have a good understanding of the discovery efficiencies for individual nova events. If the probability of discovering an individual nova eruption is low, there must be a high RN fraction to produce the ten known RNe. If the discovery efficiency is high, the RN fraction should be relatively low. To recover the RN fraction, we need a detailed model that examines the discovery efficiencies for novae as a function of the individual system properties.

We have previously studied the discovery efficiencies of nova events extensively (Pagnotta et al. 2009 and Section 2.6.2; Schaefer 2010). This was done in part using our detailed listings of plate times and depths for many novae, for many years, for both the Harvard and Sonneberg plate archives. We also used our comprehensive listings of search epochs, cadences, and magnitude limits for both amateur and professional nova searches conducted by many people and groups throughout the world. The results are detailed and include our extensive knowledge of the sizes of the solar, lunar, and observational gaps, i.e., the fraction of time over which someone could and would have discovered a nova eruption. We have pieced this together to derive a relatively simple formula that quantifies the discovery efficiency for an undirected nova search picking up an eruption (Schaefer 2010). This discovery efficiency is

$$F_{\rm disc} = f_{\rm disc}(V_{\rm peak}) \times 0.67 \times (t_3/44). \tag{2.1}$$

The factor $f_{\rm disc}(V_{\rm peak})$ is the discovery efficiency for a $t_3 = 44$ day nova that is well placed in the sky, and its values are 1.0 for $V_{\rm peak} = 2$ mag or brighter, 0.35 for $V_{\rm peak} = 4$ mag, 0.22 for $V_{\rm peak} = 6$ mag, 0.14 for $V_{\rm peak} = 8$ mag, and 0.09 for $V_{\rm peak} = 10$ mag. We take a linear interpolation between these values and assume the efficiency falls linearly to zero at $V_{\rm peak} = 16$ mag. Importantly, this discovery efficiency is measured to be essentially constant from 1890 to the present, with the modern CCD all-sky surveys yielding no more discoveries than the old surveys by amateurs.

The discovery of the first eruption of a system is always from an undirected search. The discovery of the second eruption is generally also from an undirected search. Once a system is known to be an RN, then *directed* searches are made, both ongoing into the future as well as with archival data into the past. The directed discovery efficiency is higher than the undirected discovery efficiency, and can in fact be quite high. For example, U Sco had a high directed discovery efficiency in the several years leading up to its 2010 eruption because the prediction of its eruption led to intense surveillance by many professional and amateur astronomers, with the amateurs able to push the monitoring deep into the solar gap. Here,

it only matters that we have a fairly accurate measure of the undirected discovery efficiency for a known $V_{\rm peak}$ and t_3.

For each of the novae in Table 2.3, we have a known peak magnitude, and 72% have a known t_3. Those that do not have a t_3 are assigned the value of 44 days, which is the median value for CNe. In addition, we must handle the 147 novae that are not listed in Table 2.3, including 91 poorly observed eruptions that are in Downes et al. (2001) but not Table 2.3 as well as 56 systems which erupted after the stop date of the Downes et al. (2001) catalog. For these, we have cloned the parameters for the first 147 novae in Table 2.3. For the 10 known RNe, we use their parameters from Table 2.2. With this, we can calculate the probability that any one nova event will be discovered for each of the 394 novae currently known.

We can now simulate (with a Monte Carlo analysis) the discoveries of all the novae and determine which systems have one eruption discovered and which systems have more than one discovered. This simulation has only one free parameter: the fraction of the discovered systems that are actually RNe with multiple eruptions. There are large populations of recurrent and non-recurrent systems which have had at least one eruption since 1890. Out of the many thousands of eruptions, only a small fraction are discovered, and this leads to the 394 systems currently known. Of these 394 systems, some fraction (the RN fraction) are recurrent and have had multiple eruptions since 1890. Of these RNe, most have had only one eruption discovered, and a few have had two or more eruptions detected. Our simulation models all these numbers based on the RN fraction input. If the RN fraction is near zero, then we would recognize near zero RNe, while if the RN fraction is large then we would recognize many more than ten RNe. For a given RN fraction, we run the simulation many times and calculate the number of discovered RNe, then average these numbers and calculate their RMS scatter. We then vary the RN fraction until the number of discovered RNe is 10, exactly as is observed out of the 394 systems known to date. The 1σ uncertainty on this derived RN fraction is the range over which the observed number (10) is within one RMS of the average number for that assumed RN fraction.

In each Monte Carlo simulation, each star is assigned a random number that determines whether it is recurrent based on the RN fraction. The RNe are then assigned a randomly selected recurrence time scale (τ_{rec}) from a distribution. The adopted distribution is flat in $\log[\tau_{rec}]$ from 10 to 100 years, which is a reasonable match for the ten known RNe, after correction for selection effects. For the simulated τ_{rec} and a random phase in this recurrence cycle in the year 1890, the number of eruptions from 1890 to 2012 is calculated. For each of these eruptions, a random number is compared to the undirected search efficiency to decide whether that particular eruption is "discovered". The total number of discovered eruptions is then tallied up. If this is zero, then the simulation is repeated until a non-zero number of eruptions for that nova is found. We then get the total number of detected eruptions from all of the CNe (one each) and all of the simulated RNe (one or more each). From this list, we then count the number of discovered RNe (i.e., those recurrent systems that have two or more simulated eruptions discovered). Such simulations are repeated many times for the same set of inputs to beat down the usual statistical variations. These variations are important because they show the typical variations that we should expect for the nova population that is actually realized in the sky.

The result of this Monte Carlo analysis is the average number (and its RMS scatter) of detected RNe as a function of the RN fraction. With this, we find that the population of 394 known nova systems will produce 10 known RNe for an RN fraction of $12\% \pm 3\%$.

2.5.3 RN Fraction From RN Discovery Efficiency

The RN fraction can also be determined by the discovery efficiency of each of the ten known RNe. If it is highly probable that an individual RN will be recognized as recurrent, then most of them will have already been discovered and few will be lurking among the CN lists. If the identification of two or more eruptions occurs with low probability, then there must be many RNe for which only one eruption has been detected. Our third method takes the discovery efficiency for each of the known RNe and deduces how many similar systems must exist to allow for the one system recognized as an RN. We can also calculate how many of

Table 2.6. Recurrent Nova Discovery Rates

Recurrent Nova	$F_{\rm disc}$	$\tau_{\rm rec}$	f_0	f_1	$f_{\geq 2}$	$N_{\rm CN}$	$N_{\rm RN}$
CI Aql	0.05	24	73%	23%	4%	7	28
V394 CrA	0.013	30	93.4%	6.4%	0.2%	31	476
T CrB[a]	0.09	80	90%	9%	1%	9	100
IM Nor	0.15	82	78%	21%	1.0%	19	91
RS Oph	0.06	14.7	58%	33%	9%	4	11
V2487 Oph[b]	0.012	18	92.4%	3.2%	4.4%	1	23
T Pyx[b]	0.19	19	25%	6%	69%	0	2
V3890 Sgr	0.03	25	88.3%	11.2%	0.5%	23	208
U Sco[b]	0.006	10.3	96.2%	1.3%	2.5%	1	40
V745 Sco	0.014	21	92.7%	7.1%	0.2%	44	625

[a]For T CrB, the case is for undirected searches for both events with observations extended from 1850 to 1890 (with a 10% detection efficiency).

[b]The second-discovered eruption is taken to be a product of a directed nova search.

these similar systems will have only one discovered eruption, and hence how many RNe are masquerading as CNe.

Full discovery details, undirected discovery efficiencies ($F_{\rm disc}$), and recurrence time scales ($\tau_{\rm rec}$) are known for all ten RNe (Schaefer 2010). Values for $F_{\rm disc}$ and $\tau_{\rm rec}$ are taken from Tables 18 and 21 of Schaefer (2010) and summarized in our Table 2.6. Given that the first discovered eruption is always from an undirected search and that few CNe are monitored with any useful directed nova search even for short times, the relevant efficiency of the discovery of RNe is that of undirected searches in general.

The discovery statistics for systems like the known RNe can be calculated using another Monte Carlo simulation. For each simulation, for each RN, the number of eruptions from 1890 to 2012 is determined by the given $\tau_{\rm rec}$ and a randomly chosen phase within this recurrence cycle. For each eruption that occurs, a random number is selected for comparison with the undirected discovery efficiency to ascertain whether the eruption is identified. The number of discovered eruptions is tallied for each RN and simulation. We tabulate the fraction of the time that zero eruptions are discovered (f_0), one eruption is discovered (f_1), and two or more eruptions are discovered ($f_{\geq 2}$) for 10,000 simulations and report these in Table 2.6.

Since most RNe are never identified, there must be many in existence for any one of the

known RNe to be recognized. We can consider the example of RS Oph as an illustration. For 100 RS Oph-like systems, 58 would never be seen to erupt, 33 would have one discovered eruption and be classified as CNe, and 9 would be recognized as RNe since multiple eruptions would be discovered. To turn it in the other direction, since we observe one RS Oph system, there should be 11 such RNe currently active, with ∼6 of those never seen, ∼4 identified as CNe, and the 1 recognized RN. In general, for every known RN, there should be $N_{\rm CN} = f_1/f_{\geq 2}$ apparent CNe recorded. The required number of false CNe is tabulated for each RN in Table 2.6, rounded to the nearest integer. Additionally, for every known RN, there must be roughly $N_{\rm RN} = 1/f_{\geq 2}$ other RNe in existence.

We must be careful to which known RNe we apply this logic. The original calculation assumes that *both* of the first two eruptions were discovered with undirected nova searches during the years 1890-2012. This assumption is incorrect for several of the known RNe. V2487 Oph's first eruption (in 1998) was discovered by an amateur during an undirected search (Nakano et al. 1998), but its RN-like properties led us to perform a directed search to find the second-discovered 1900 eruption. Similarly, the second-discovered eruptions of T Pyx and U Sco were found during directed searches (Leavitt & Pickering 1913; Thomas 1940). For T CrB, L. Peltier followed up the 1866 eruption with a long-running directed search, but this does not affect the statistics because the 1946 eruption was discovered by many independent amateurs during undirected searches. For T CrB, the two discovered eruptions are not from 1890-2012, since the first one appeared in 1866. In all four of these cases, there need be substantially fewer similar hidden RNe to produce the ones that we know.

For the three known RNe for which the second discovery came during a directed search, the probability of detecting the second eruption increases significantly since directed searches are much more efficient. Schaefer (2010)'s Table 20 quantifies the directed search efficiencies for each known RN for each year after 1890. For T Pyx, the probability of the second discovery increases from 0.19 to near unity. For V2487 Oph, the probability goes from 0.012

to 0.33. For U Sco, the probability increases from 0.006 to 0.43. For each of these cases, the fractions can be calculated analytically. For T CrB, we take the probability of discovering an eruption to be 10% from 1850 to 1890, based on broad experience with historical variable star work, because detailed lists of observing epochs and depths are unavailable.

With this, the sum over $N_{\rm CN}$ for all ten RNe is 139; these 139 so-called CNe are actually RNe for which only one eruption has been discovered. The sum over $N_{\rm RN}$ is 1604; there are currently roughly 1600 active RNe in our galaxy. Due to the low discovery efficiencies, this large number is required to produce the ten known RNe. The uncertainties on these estimates are large and difficult to estimate because the error bars for $F_{\rm disc}$ and $\tau_{\rm rec}$ are poorly known.

Roughly 139 of the currently cataloged CNe are actually RNe, but this is not out of the 247 novae listed in Tables 2.2 and 2.3, because this list includes neither the many faint novae with sketchy data, nor the novae discovered since the beginning of 2006. Indeed, the second eruptions of half of the known RNe (IM Nor, CI Aql, V394 CrA, V745 Sco, and V3890 Sgr) came as a complete surprise from 1987 to 2002, since the first eruption of each system has fewer than a dozen magnitudes and no spectroscopy. The poorly observed CNe provide a large pool of systems which could be RNe. If we count all poorly-observed systems, as well as those featured in our Table 2.3, there are 338 novae in the Downes et al. (2001) catalog, as well as 56 novae which have been discovered since the end of 2005. Thus, the real pool of so-called CNe contains 394 systems, and the RN fraction from 139 out of 394 systems is 35%.

2.5.4 Final RN Fraction

We have calculated the RN fraction using three greatly different techniques. The scatter in these values gives an idea of the robustness of the measures. We find RN fractions of 24%±4%, 12%±3%, and 35%. There is no reliable uncertainty for the third method. For the first two methods with stated uncertainties, the possibility of low RN fractions is confidently rejected. The three measures differ by more than their stated errors, and this is a sign that

systematic effects enter in at the 50% level. These systematic errors are all multiplicative. In this case, it is not clear how to combine our three measures. We can conclude that the RN fraction is somewhere between one-eighth and one-third, with a middle estimate of one-quarter, and in all cases the RN fraction is significantly larger than zero.

2.6 Searches for Prior Eruptions

Presented in Table 2.4 is a list of good recurrent nova *candidates*; we stress that a system cannot be definitively classified as recurrent until two or more eruptions are observed, traditionally within 100 years or so. There are two ways to find these eruptions: looking forward and looking backward. Looking forward requires frequent monitoring of candidates. It is currently not feasible to do this comprehensively for a large number of systems, but in the future, all-sky surveys with real time results (such as ASAS, PanSTARRS, and LSST) may turn this into a reasonable option if one is willing to wait many decades. Looking backward takes advantage of the extensive astronomical plate archives at the Harvard College Observatory (HCO) in Cambridge, MA, and the Sonneberg Observatory in Sonneberg, Germany, which provide regular all-sky coverage dating back to 1890.

2.6.1 Astronomical Plate Archives

Before the advent of CCDs, astronomical imaging was performed using glass plates coated with a photoemulsion. The plates were inserted in holders attached to the telescope at either the primary or secondary focus and were exposed and then developed in much the same way as film. The vast majority of plates are blue-sensitive, so magnitudes obtained from them are taken to be in the Johnson B-band. (In fact, this is how the B-band was defined.) Red- and yellow-sensitive emulsions were developed as well, but they were not widely used. One major drawback of plates is that the response of the emulsion is non-linear, so converting from the densities (which are what is actually recorded by the emulsion) to intensities is nontrivial. The most commonly used reliable method of obtaining magnitudes of a given

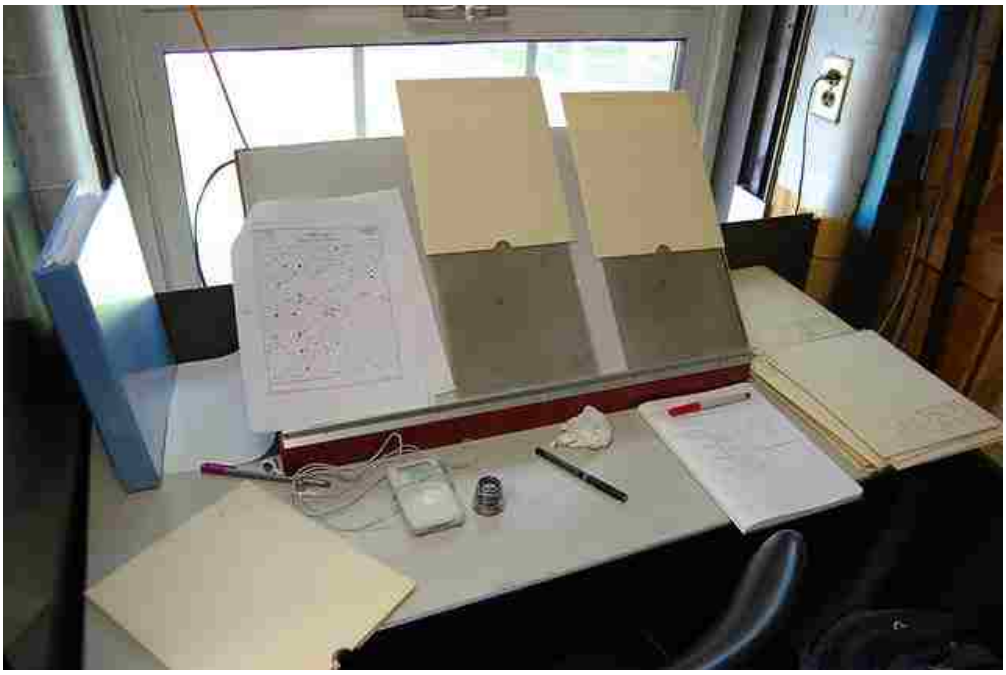

Figure 2.3 Photographic Plates. A typical set-up for examining archival photographic plates, at Harvard College Observatory. The plates are set against a light desk and target stars are looked for with a hand loupe. The date of observation, pointing location, length of exposure time, and other facts about the plate are recorded on the envelopes in which the plates are stored.

star is to compare it to a sequence of comparison stars in the same field which have been calibrated using modern CCD photometry. This produces magnitudes which are accurate to within ∼0.1 mag (Schaefer et al. 2008).

There are two main types of plates: patrol plates, which cover a large area of the sky ($20 - 60$ square degrees) to an average magnitude of $B \sim 14$, and deep plates, which cover a much smaller area ($\sim$ a few degrees square) to a much deeper limiting magnitude, $B \sim 18$ and sometimes even fainter. The majority of plate stack work I have done has been by hand, using a loupe and light desk, with a typical set-up shown in Figure 2.3.

The largest, best plate archive is located at the Harvard College Observatory in Cambridge, MA. HCO has ∼500,000 plates taken by their astronomers at observatories all over the world, from Massachusetts, to Peru, to South Africa, to New Zealand. The plates cover the time periods from 1890 to 1953 and from the 1960s to the 1980s. The DASCH (Digital

Access to a Sky Century at Harvard) project has undertaken the immense task of digitizing all of the plates, using a custom-built scanner and software pipeline that captures the plate image, identifies the location on the sky (by fitting the astrometry of the visible stars), and calculates a magnitude for each star on the plate.

The second largest plate archive is located at the Sternwarte Sonneberg (Sonneberg Observatory) in Sonneberg, Thüringen, Germany. Sonneberg has ∼300,000 plates, the earliest of which date to the 1920s, although the observations do not become regular until after the mid-1940s. The majority of the plates were taken at the Observatory, so the coverage is heavily concentrated in the North, but some Southern observing expeditions were made, primarily during the earlier years of the Observatory, so there is a significant amount of Southern coverage. A large-scale all-sky survey program is still being carried out at Sonneberg, although they have transitioned to using films instead of plates, as plates are no longer being manufactured.

Twenty RN eruptions have been observed on the plates at HCO and Sonneberg, including the discovery of the 1900 eruption of V2487 Oph, which is detailed in Section 2.6.2 and Pagnotta et al. (2009). One strong candidate (V838 Her) has been essentially fully checked at both archives, and another (V2672 Oph) has been fully checked at HCO, but no prior eruptions have been found. This is not unexpected, for the same reasons that contribute to the low overall discovery efficiencies for RNe in general, namely short eruption durations that can easily be missed during solar and lunar gaps, as well as times of less frequent sky monitoring. Four other good candidates are at various stages of being checked; although the procedure is simple, the process is time-consuming. A summary of our searches to date can be seen in Tables 2.7 and 2.8, which give a breakdown of which plate series have been checked, how many plates were present for each series, the center location of the plate series (for the patrol plates), and a rough idea (in the footnotes) of what time period each series covers, for twelve systems. Table 2.7 shows six good RN candidates for which targeted searches have been performed as well as V2487 Oph which was proven to be recurrent. Table 2.8 shows

weaker RN candidates which have been secondarily observed because they were on the same plates as other candidates. The digitization projects that are currently in progress at HCO and Sonneberg will make it much easier to check all candidates for previous eruptions. We note that many Baade's Window plates had been pulled for scanning at HCO during recent trips there. We made every attempt to examine all of the pulled plates for the series listed as checked, however it is possible that some small number were missed.

2.6.2 V2487 Ophiuchi

Using the set of criteria discussed in Section 2.2, V2487 Oph rapidly came to our attention as a strong RN candidate. The nova was discovered by K. Takamizawa at magnitude 9.5 on 1998 June 15 (Nakano et al. 1998). We have constructed a light curve from AAVSO observations, Liller & Jones (1999), Hanzl (1998), and our own CCD observations at quiescence in 2002 and 2003. From this light curve we derive $V_{\rm max} = 9.5$, $B_{\rm max} = 10.1$, $t_3 = 8$ days, and an amplitude of 8.2 mag. This fast, low-amplitude nova easily satisfies the Duerbeck criterion (Section 2.2.1). From its outburst spectrum (Lynch et al. 2000), we see an expansion velocity of 10,000 km s^{-1} and He II lines.

V2487 Oph had previously been suspected to be recurrent. Hachisu et al. (2002) describe the system as a "strong candidate recurrent nova" based on their analysis of the light curve from the 1998 outburst. They call particular attention to the rapid decline and the plateau phase of the outburst light curve, both of which are characteristic of fast RNe. Based on the mass transfer rate in quiescence, they estimate a recurrence time of 40 years. They also note that the system has a high-mass white dwarf accretor ($M_{\rm WD} \approx 1.35 \pm 0.01 M_{\odot}$), based on their model, which makes it a prime candidate for a Type Ia supernova progenitor in addition to being a probable RN. Rosenbush (2002) also names V2487 Oph as a potential RN, and places it in his CI Aql group, based on the shape of the outburst light curve. Additionally, Hernanz & Sala (2002) point to V2487 Oph as in interesting case, as it was apparently seen in X-rays before the 1998 outburst, as part of the ROSAT All-Sky Survey.

Table 2.7. Plate Search Status — Strong Recurrent Nova Candidates

Plate Series[a]	V838 Her		V2487 Oph		V2672 Oph		V1172 Sgr		V4160 Sgr		V4643 Sgr		V723 Sco	
A[b]	15[c]		20		70		...		...		...		...	
AM/AC/AX/AY	200	(18^h, +15°)	500	(17^h, -15°)	500	(17^h, -15°)	500	(17^h, -15°)	150	(17^h, -15°)	500	(17^h, -15°)	...	(17^h, -30°)
AM/AC/AX/AY	700	(18^h, 0°)	150	(17^h, -30°)	150	(17^h, -30°)	200	(18^h, -15°)	...	(17^h, -30°)	...	(17^h, -30°)	300	(17^h, -45°)
AM/AC/AX/AY	700	(19^h, +15°)	250	(18^h, -15°)	300	(17^h, -45°)	300	(18^h, -30°)	300	(17^h, -45°)	300	(17^h, -45°)	300	(18^h, -30°)
AM/AC/AX/AY	300	(18^h, 0°)	100	(18^h, -30°)	200	(18^h, -15°)	...		50	(18^h, -15°)	200	(18^h, -15°)	100	(18^h, -45°)
AM/AC/AX/AY	x[d]		x		300	(18^h, -30°)	x		300	(18^h, -30°)	300	(18^h, -30°)	x	
AM/AC/AX/AY	x		x		100	(18^h, -45°)	x		100	(18^h, -45°)	50	(18^h, -45°)	x	
AI/BI	200	(19^h, +15°)	...		200	(17^h, -15°)	...		200	(17^h, -15°)	200	(17^h, -15°)	200	(17^h, -15°)
AI/BI	...		...		125	(17^h, -30°)	...		100	(18^h, -15°)	100	(18^h, -15°)	100	(18^h, -15°)
AI/BI	...		...		100	(18^h, -15°)	...		...		...		...	
AI/BI	...		...		80	(18^h, -30°)	...		...		...		...	
B	500		90		100		...		...		...		...	
Damons	200	(18^h, 0°)	40	(17^h, -15°)	40	(17^h, -15°)	50	(17^h, -15°)	...		...		35	(17^h, -45°)
Damons	70	(19^h, +15°)	60	(18^h, -30°)	60	(18^h, -30°)	50	(18^h, -15°)	...		...		60	(18^h, -30°)
Damons	...		...		x		10	(17^h-19^h, -15°)	...		...		40	(19^h, -45°)
I	50		...		10		...		...		...		...	
IR	...		...		10		...		...		...		...	
MC/MF/MA	10		50	(MF only)	70		...		...		...		...	
RH/RB	150	(18^h, +15°)	250	(17^h, -15°)	230	(17^h, -15°)	200	(18^h, -15°)	...		...		200	(18^h, -30°)
RH/RB	200	(18^h, 0°)	150	(17^h, -30°)	150	(17^h, -30°)	100	(18^h, -30°)	...		...		...	
RH/RB	200	(19^h, +15°)	200	(18^h, -15°)	200	(18^h, -15°)	...		...		...		...	
RH/RB	200	(19^h,0°)	100	(18^h, -30°)	100	(18^h, -30°)	...		...		...		...	
X	...		...		10		...		...		...		...	
Sonneberg Patrols	680	(19^h, +0°)	1800	(17^h, -20°)	...		1700	(17^h, -20°)	...		...		...	
Sonneberg Deep	...		x		...		...		...		...		...	

[a] All plates are at Harvard College Observatory, except for the last two series, which are at Sonneberg Observatory.

[b] The average time coverage for each series is as follows: A (1893-1950), AM/AC/AX/AY (1898-1953), AI/BI (1900-1953), B (1890-1953), Damons (1962-1989), I (1890-1946), IR (1934-1953), MC/MF/MA (1905-1953, 1960-1984), RH/RB (1928-1953), X (1890-1951), Sonneberg Patrols and Deep (1920-1945 sparse, 1945-present well covered)

[c] The given numbers are good estimates, but not exact. On average they are correct within ∼20%.

[d] In this table, "..." indicates that the series has not yet been checked, while "x" indicates that the series does not have any coverage of the system.

Table 2.8. Plate Search Status — Weaker Recurrent Nova Candidates

Plate Series[a]	V2275 Cyg		BS Sgr		V1016 Sgr		V3645 Sgr		V4444 Sgr	
A[b]	...[c]		...		...		...		...	
AM/AC/AX/AY	...		200	(18^h, -15°)	300	(18^h, -30°)	300	(18^h, -30°)	300	(18^h, -30°)
AM/AC/AX/AY	...		...		200	(18^h, -15°)	200	(18^h, -15°)	200	(18^h, -15°)
AM/AC/AX/AY	...		...		...		...		...	
AM/AC/AX/AY	...		...		...		...		...	
AM/AC/AX/AY	...		...		...		...		...	
AM/AC/AX/AY	...		...		...		...		...	
AI/BI	...		...		...		...		...	
AI/BI	...		...		...		...		...	
AI/BI	...		...		...		...		...	
AI/BI	...		...		...		...		...	
B	...		...		...		...		...	
Damons	...		50	(18^h, -15°)	50	(18^h, -15°)	50	(18^h, -15°)	50	(17^h, -15°)
Damons	...		10	(17-19^h, -30°)	10	(17-19^h, -30°)	10	(17-19^h, -30°)	50	(18^h, -15°)
Damons	...		...		...		...		10	(17-19^h, -30°)
I	...		...		...		...		...	
IR	...		...		...		...		...	
MC/MF/MA	...		...		...		...		...	
RH/RB	...		200	(18^h, -15°)	200	(18^h, -15°)	200	(18^h, -15°)	100	(18^h, -30°)
RH/RB	...		100	(18^h, -30°)	100	(18^h, -30°)	100	(18^h, -30°)	...	
RH/RB	...		...		...		...		...	
RH/RB	...		...		...		...		...	
X	...		...		...		...		...	
Sonneberg Patrols	1775[d]	(20^h, +40°)	...		...		...		...	
Sonneberg Deep	860		...		...		...		...	

[a] All plates are at Harvard College Observatory, except for the last two series, which are at Sonneberg Observatory.

[b] The average time coverage for each series is as follows: A (1893-1950), AM/AC/AX/AY (1898-1953), AI/BI (1900-1953), B (1890-1953), Damons (1962-1989), I (1890-1946), IR (1934-1953), MC/MF/MA (1905-1953, 1960-1984), RH/RB (1928-1953), X (1890-1951), Sonneberg Patrols and Deep (1920-1945 sparse, 1945-present well covered)

[c] In this table, "..." indicates that the series has not yet been checked, while "x" indicates that the series does not have any coverage of the system.

[d] The given numbers are good estimates, but not exact. On average they are correct within ∼20%.

Eruption Discovery

In the summer of 2008 we completed an exhaustive search of all plates at Harvard showing V2487 Oph. I discovered the 1900 outburst of V2487 Oph at magnitude $B = 10.27 \pm 0.11$ on plate AM 505, which was taken on 1900 June 20 (JD 2415191.617). AM 505 is part of the AM patrol plate series taken at Arequipa, Peru, is centered at right ascension 17^h and declination -15°, has a blue-sensitive emulsion, and has a limiting magnitude of $B = 11.3$.

All other plates housed at Harvard that could possibly show the 1900 outburst were examined. There are no plates covering the position of V2487 Oph to a sufficient depth during the months surrounding the eruption to provide confirmation. On plate B 25522 it can be seen that V2487 Oph was not up on 1900 June 2. Plate I 25510 covers the area on 1900 June 30, but has a limiting magnitude of $B = 11.3$. By this time, approximately 10 days after peak, V2487 Oph had decreased in brightness to $B \sim 13.6$ and thus there is no chance of seeing it on the plate. During this time period, patrol images of a field were only taken approximately every two weeks, and deep plates were only taken for specific observing campaigns. When combined with the short duration of the V2487 Oph outburst, it is therefore not surprising that no other plates show evidence of the outburst. While there are no confirmation plates, there are none for which the lack of detection is inconsistent with an outburst on 1900 June 20.

With only one plate showing the outburst, we must provide reasons for our confidence in this discovery. A $1.8'$ trailing in right ascension gives all of the star images on the plate a distinct dumbbell shape. In Figure 2.4, it can be seen that the object at the location of V2487 Oph has the same dumbbell shape, and therefore the light forming the image came from a fixed location in the sky. This provides strong proof that the image is not any type of plate defect. Trailing such as this is not unusual on the Harvard plates, though most plates show a more typical (circular) point spread function (PSF). In this case, the imperfect tracking provides a unique PSF which, when combined with the fact that the image is in focus, indicates that the light originated beyond the Earth's atmosphere and then passed

through it on its way to the telescope, a further argument against a plate defect or local light source. The fact that the trail over the 61-minute exposure has the same length and orientation as the trails of nearby stars demonstrates that the point source cannot be an asteroid or other Near-Earth Object. The Minor Planet Center confirms that there were no minor planets in this location at that time (B. Marsden 2008, private communication).

Quantitative astrometry on the scanned plate places the star image in the correct location in relation to other stars in the area to within 2″ in declination and 15″ in right ascension. For this plate series, 15″ corresponds to 0.025 mm on the plate. The limiting magnitude of the plate precludes the possibility of the image being a background star, except in the case that the background star was undergoing a flare greater than 10 magnitudes, which is extremely improbable. In all, despite having only one image, we have strong proof that the light forming the image was from a point source above the telescope, outside the Earth's atmosphere and our Solar System, and from the location of a specific nova suspected to have had prior eruptions. Thus we conclude that we found a previously-undiscovered nova eruption of V2487 Oph. Combined with the nova outburst observed in 1998 (Nakano et al. 1998), we can be confident that V2487 Oph is a recurrent nova.

In addition to the Harvard plates, we also checked all of the available plates in the archive at the Sonneberg Observatory. Sonneberg has approximately 300,000 plates, the majority of which were taken in Germany, so the southern coverage is not as complete as at Harvard. Despite this, there are still approximately 1,800 plates that cover V2487 Oph during the time span from 1926 to 1994. While there was no possibility of finding a confirmation plate for the 1900 outburst, we continued the search in an attempt to find more undiscovered outbursts of V2487 Oph. It is reasonable to expect that there should be other outbursts because of purely statistical reasons (cf. the following section on Discovery Statistics), and because of the 40 year recurrence time estimated by Hachisu et al. (2002). We did not find any additional eruptions.

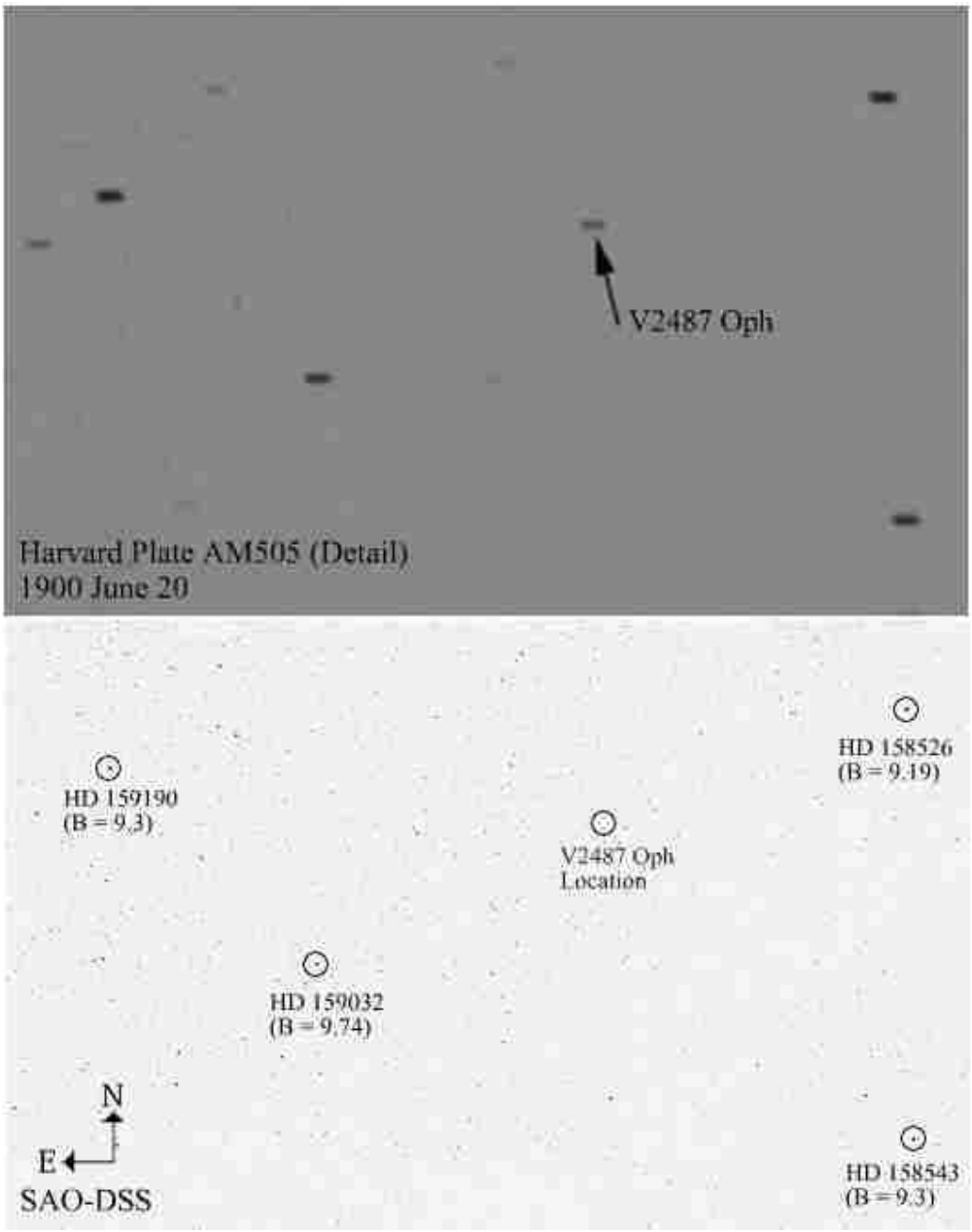

Figure 2.4 V2487 Ophiuchi. *Top:* Scanned image of Harvard plate AM505. V2487 Oph is marked with the arrow. The field is approximately 60′ wide by 30′ tall; north is up, and east is to the left. The 1.8′ image trail of V2487 Oph is identical to that of the neighboring stars, providing evidence that the image is not a plate defect, a near-telescope light source, or a solar system object. The image is within 15″ (0.025 mm on the plate) of the sky position of V2487 Oph, which is a small fraction of the length of the trail. *Bottom:* SAO-DSS image of the same field. The four most prominent stars from the plate are marked and labeled, as is the position of V2487 Oph.

Discovery Statistics

Nova eruptions are missed for many reasons, such as the solar gap when the nova is too close to the sun to be observed, the lunar gap when nova searchers generally pause due to the brightness of the Moon, and the scarcity of nova searchers who observe to faint magnitudes over the whole sky. (Shafter (2002) shows that half of the novae peak fainter than 7th mag.) Our detailed study of observing times and limits from the many nova hunters and archival plate collections around the world shows a discovery efficiency ranging from 0.6% to 19% over the last century, for undirected searches, depending on the peak magnitude and t_3 of the system (Schaefer 2010). We distinguish between directed and undirected searches because there is a much higher chance of catching a system in outburst during a directed search, i.e., when we monitor a known recurrent system or search through the archives because there is reason to believe the system has had multiple nova eruptions.

Most novae, however, are discovered during undirected searches; they just happen to be observed, often during completely unrelated observations, or during general variable star searches. Shafter (2002) has presented a comparison of model and observed magnitude distributions which demonstrates that only $\sim$10% of faint nova eruptions (with an apparent $m_{\rm peak} > 8$ mag) are discovered. Our calculations based on the known properties of the CNe and RNe indicate that approximately one-quarter of the known CNe are actually RNe (Section 2.5).

The likelihood of discovering an eruption can be calculated by considering the properties of the system and all possible discovery sources. An operational definition of the discovery efficiency is the fraction of the days in a year on which the nova can peak and the eruption would be detected. This will depend on the dates and limiting magnitudes of the observations, as well as the eruption light curve of the nova. Let us here work out an equation for calculating the discovery efficiency (ϵ) based on the properties of a given nova system. The coverage can usually be reasonably idealized as having some nearly constant limiting magnitude, and the nova light curve will be brighter than that limit for some length of time,

t_{vis}. For example, the light curve of V2487 Oph is brighter than $B = 11$ mag for 3 days, and brighter than $B = 14$ mag for 13 days (Schaefer 2010). If we had a plate series that covered the position of V2487 Oph to $B = 14$ on every night of the year, then the discovery efficiency would be unity because all eruptions that year would be discovered.

The reality, however, is that most sets of observations have a significant gap of duration G_s due to the passage of the Sun close to the position of the nova. An eruption during most of this time period will go undiscovered. The length of the solar gap depends on the series of observations, the latitude of the observers, and the declination of the nova. To give typical examples for other RNe, the Harvard plates have average solar gaps of 100 days for T Pyx, 150 days for U Sco, and 235 days for RS Oph. To take a specific example, suppose we had a plate series that went to $B = 14$ for 183 consecutive days in a year, with the solar gap covering the other half of the year. In such a case, a V2487 Oph eruption could be discovered if the nova peaked anytime during the 183 consecutive days *plus* anytime in the last 13 days of the solar gap, as the declining tail of the eruption would be seen on the first post-gap plate. The eruption would be discovered if the peak occurred on any of 196 days in the year, for an efficiency of 196/365=0.54. In general for this simple case, the efficiency would be $\epsilon = [365 - (G_s - t_{vis})]/365$. In this equation, the subtracted quantity $(G_s - t_{vis})$ must never be allowed to become negative. The numerator should be the number of days in the year on which the nova could peak and the eruption could be discovered. To give an important example, the recurrent nova T Pyx has a solar gap of near zero for AAVSO observations ($G_s \approx 0$) and yet the nova is brighter than the typical AAVSO limiting magnitude of $V = 14.0$ mag for a duration of 270 days ($t_{vis} = 270$ days), so we take the $G_s - t_{vis}$ value to be zero. With this, $\epsilon = 1.0$, and we realize that any eruption of T Pyx after 1967 would certainly be discovered.

The observations which might discover an eruption are almost never conducted nightly outside the solar gap, and indeed most data series have substantial gaps even when the nova is well placed in the sky. Moon interference is a common cause of these gaps: if the moon is

bright and close to the system, the limiting magnitude of the observations is too bright to be useful. Because of this, many observers do not work on nights with a bright moon, causing gaps in the observational record. Short gaps in the record can arise for other reasons. The most common cause is simply a lack of observations, for example, during the early years at both HCO and Sonneberg when fewer plates were taken, so the ones that do exist are spaced further apart. For purposes of calculating ϵ, the cause of the gap does not matter; they are all taken together and called lunar gaps. In practice, these gaps vary from month to month and year to year, but typical gaps are $15-20$ days for lunar gaps and $20-40$ days when gaps are caused by sparse records.

Ideally, every gap would be meticulously recorded, but in reality the recording of every plate time would provide no useful improvement in accuracy. Instead, we have recorded all plate times for many sample years and use average observed gap durations (G_l). The number of days on which the peak would be missed due to a lunar gap is $G_l - t_{vis}$, again with this number never being allowed to fall below zero. For example, a fast nova with $t_{vis} = 10$ days, when covered by a source with a 20 day lunar gap, could be observed, on average, if it erupted on 20 days in a given month – the 10 days at the end of the lunar gap and the 10 days outside the lunar gap. If the nova is slow enough so that the eruption would be visible on the plates for longer than the lunar gap, then the existence of the lunar gap does not impact the discovery efficiency. Multiple lunar gaps occur during the time outside the solar gap; on average there are N_l lunar gaps per year. With this, the number of possible nova peak days that would result in a missed eruption is $N_l(G_l - t_{vis})$. The final general equation for the discovery efficiency is then

$$\epsilon = \frac{365 - (G_s - t_{vis}) - N_l(G_l - t_{vis})}{365} \tag{2.2}$$

where the terms in parentheses cannot go negative. Patrol plates are taken regularly, at evenly-spaced intervals, providing regular gap structures and good coverage during the observable times, at a cadence that is usually fast enough to catch most nova events. Deep plates are not taken with as much regularity as the patrols; the coverage depends strongly on

the field and the time period, and therefore deep plates do not always contribute significantly to the overall discovery efficiency of a particular system. The total number of plates enters into this calculation only to the extent that the average gap durations can be reduced when there are a lot of plates, but in practice, an increase in the number of observations does little to decrease the gap durations because the sun and bright moon still dominate. We now have a general way of calculating the discovery efficiency, and this only depends on the length of time that the nova would be visible and on the gap structure of the data series.

Let us give a typical worked example for V2487 Oph. For the year 1990, the dominant detection source is the plate archive at Sonneberg. The average solar gap for these plates is $G_s = 210$ days, and there are four lunar gaps averaging $G_l = 15$ days each. The limiting magnitude of the plates is typically $B = 12$ mag. Based on the 1998 eruption light curve, a V2487 Oph eruption would be visible for $t_{vis} = 6$ days total. The discovery efficiency in this case is therefore

$$\epsilon = \frac{365 - (G_s - t_{vis}) - N_l(G_l - t_{vis})}{365} = \frac{365 - (210 - 6) - 4 \times (15 - 6)}{365} = 0.34$$

for V2487 Oph in 1990. That is, had the eruption peaked on any of 34% of the nights in 1990, the eruption would have been recorded on the Sonneberg plates and discovered by us.

The low amplitude and short t_3 of V2487 Oph are two of the reasons it was a strong candidate RN, but they also lead to a short amount of time during which the eruption is brighter than plate limits, and therefore a low discovery efficiency. Because of these characteristics, it is possible for an outburst to happen completely during a solar or lunar gap, leaving no observable evidence on the plates.

The nova searches we considered are undirected photographic and visual searches by amateurs and professionals, the Harvard plate collection, the Sonneberg plate collection, the All Sky Automated Survey (ASAS-3) (Pojmanski 2002), and the observations of the American Association of Variable Star Observers. For V2487 Oph, we have calculated the average detection rate on a year-by-year basis. These results can be seen in Figure 2.5. From 1890 to 2008, the discovery efficiency of V2487 Oph ranges from 1% to 73%, and averages

30%. The years before the beginning of plate archive coverage are not considered, because V2487 Oph has such a low apparent magnitude that the probability of detection is negligible.

We can estimate the number of missed eruptions and the recurrence time scale in two ways. First, we have used a Monte Carlo simulation to calculate the probability that a given recurrence time scale would produce exactly two discovered eruptions given the yearly probability of discovery from Figure 2.5. Supposing that the recurrence timescale is 98 years, then the average probability that a randomly-phased series of eruptions separated by 98 years will have exactly two discovered eruptions is 1.2%. Supposing that the recurrence time scale is $98/2 = 49$ years, then the mean probability that a randomly-phased series of eruptions separated by 49 years will have exactly two discovered eruptions is just 9.1%. Supposing that the recurrence time scale is 98/N years, then the average probability that a randomly phased series of eruptions will produce exactly two discovered eruptions will continue rising as N rises from 1 to 5 and then start falling. For example, with $N = 10$, we would have expected many more than two eruptions to have been discovered since 1890. The probability of getting exactly two eruptions is $> 30\%$ for $4 \leq N \leq 7$, while the probability is $< 10\%$ for N values of 1, 2, and > 12. The most probable hypothesis is that $N \sim 5$. The $N = 5$ case corresponds to a recurrence time scale of 20 years and a total of six eruptions in the last 118 years, four of which were missed.

Using the second method, we can directly estimate the most likely number of eruptions since 1890 by using the number of discovered eruptions and the 30% average discovery efficiency. Thus, the total number of eruptions should be 2/0.30, or 6.7 total eruptions in the past 118 years (four or five of which were missed). The average recurrence time scale is then $118/6.7 = 18$ years. Because of the large uncertainties in these methods, this is not inconsistent with the 40 year recurrence time predicted by Hachisu et al. (2002).

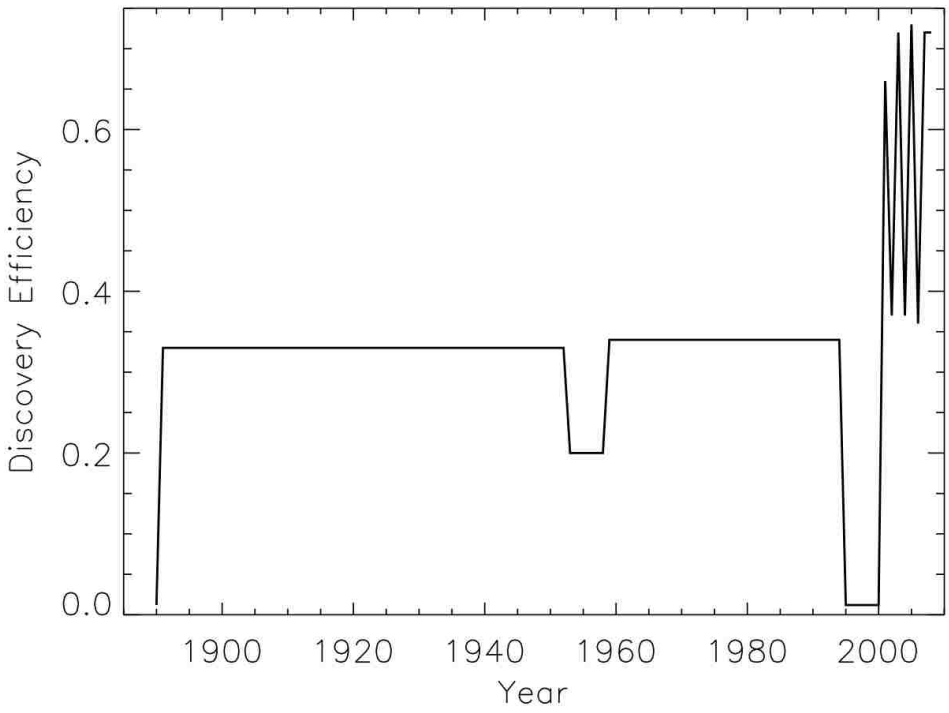

Figure 2.5 V2487 Oph Discovery Efficiency. This plot shows the yearly discovery efficiency for V2487 Oph, the percentage of days each year on which the nova can erupt and be detected. The detection sources we consider are undirected photographic and visual searches, the Harvard plate collection, the Sonneberg plate collection, the All Sky Automated Survey (ASAS-3), and the observations of the American Association of Variable Star Observers. The average discovery efficiency over the past 118 years is 30%. With two eruptions discovered, we estimate the total number of eruptions to be $2/0.30 = 6.7$, which implies that four or five eruptions have likely been missed. This indicates an average eruption timescale of 18 years, and the possibility of the next eruption occurring as soon as 2016.

2.7 Implications

We conclude that the RN fraction is roughly 25%, and is somewhere between 12% and 35%. With this, we expect that roughly 100 (or between 50 and 140) of the 394 systems labeled as CNe are in fact currently active RNe for which only one eruption has thus far been discovered. We can expect many more second eruptions to be discovered in the upcoming decades, with most of these coming from old, largely-ignored novae with scanty data.

One implication is the imperative to seek second eruptions in archival data for the Category B systems listed in Table 2.4. When seeking new RNe, the fastest, most time-effective method is to search through old astronomical photographs now residing in the archives, most of which are at Harvard and Sonneberg. A directed archival search led to the discovery of a previous eruption of V2487 Oph, confirming our suspicions that it was in fact recurrent and improving our knowledge of the demographics of the RN population. At this point, it is worthwhile to obtain more information on V2487 Oph because of the relatively small number of RNe. In particular, its orbital period, spectrum and spectral energy distribution at quiescence, and long- and short-term photometric variability should be investigated. As a recurrent nova with a recurrence time on the order of 18 years, V2487 Oph could have another outburst as soon as 2016. The monitoring of V2487 Oph should be increased, both by amateurs and professionals.

Another implication is for nova researchers to realize that roughly a quarter of the systems they are studying are in fact RNe. Hopefully, with our criteria, the likely recurrent systems can be picked out and recognized. With this realization, models will be constructed differently, and anomalies might get explanations. Additionally, some key questions might receive deserved attention, for example whether the RN candidates have WDs that are carbon-oxygen or oxygen-neon-magnesium types.

The most important conclusion is that there must be $\sim$1600 completely undiscovered RNe in the galaxy, which has vital implications for RN demographics. The previous study (della Valle & Livio 1996) did not account for discovery efficiencies, and hence their RN

death rate must be revised upward by a factor of 1600/10. This completely changes the conclusion of della Valle & Livio (1996), with RNe then being common enough to account for approximately half of the observed Type Ia supernova events.

3. T Pyxidis: Astronomical Archaeology[1]

3.1 The Unusual T Pyx

T Pyx is unique, even among the already-unusual RNe. At $P_{\rm orb} = 0.076$ days, it has by far the shortest orbital period of the RNe, and is the only RN below the CV period gap (Patterson et al. 1998; Schaefer et al. 1992; Uthas et al. 2010). Its quiescent luminosity is $L_{\rm bol} \gtrsim 10^{36}$ erg s^{-1}, which is much higher than the predicted luminosity for such a short period CV. CV luminosity is powered almost exclusively by the accretion in the system, so we know there must be a correspondingly higher-than-expected accretion rate, which is confirmed by the frequency of the RN eruptions, and has been measured to be $> 10^{-8}$M$_\odot$ yr^{-1} (Patterson et al. 1998; Selvelli et al. 2008). Knigge et al. (2000) postulate that the unusually high accretion rate is driven by sustained nuclear burning on the surface of the WD, which irradiates and puffs up the companion. As the companion expands, more material is pushed past the L1 point and onto the WD. Canonically, sustained nuclear burning in CVs is expected be observed as supersoft X-ray emission, which has not been seen for T Pyx (Selvelli et al. 2008), but recent theory indicates that many nuclear burning WDs do not in fact radiate brightly in supersoft X-rays (Di Stefano 2010a,b), so the lack of quiescent X-ray brightness in T Pyx does not invalidate the Knigge et al. (2000) theory.

Another unusual feature of T Pyx is its long-term (secular) decline in brightness. T Pyx's quiescent B-band magnitude fell from 13.8 before the 1890 eruption to 15.5 in 2004 (Schaefer 2005) to 15.7 in 2009 (Schaefer et al. 2010b). T Pyx is the only RN to show a decline like this. This drop of 1.9 mags corresponds to a factor of 5.7 decrease in the B-band flux, since $\Delta m = 2.5 \log F_2/F_1$. In general, for RNe with accretion disks, $\dot{M} \propto F^{2.0}$, where

[1]This chapter is adapted from Schaefer, Pagnotta, & Shara (2010). The permission statement is available in Appendix B. It has been updated and adapted to the dissertation format. I was primarily responsible for the analysis presented in Sections 3.1-3.5; Sections 3.6-3.9 include a large amount of work done by my advisor in addition to my contributions.

F is the B-band flux. This implies that the accretion rate has dropped by a factor of 33 since 1890. The recent behavior of T Pyx, however—namely, the 2011 eruption—indicates that for T Pyx, $\dot{M} \propto F^{1.0}$, which corresponds to a drop in the accretion rate that is slightly less drastic, although still quite unusual. (See Section 3.8 for more discussion of the 2011 eruption and its implications.)

3.2 The Nova Shell Around T Pyx

T Pyx is the only RN known to have a nova shell surrounding it. The shell, which has a radius of $\sim 5''$, was discovered by Duerbeck & Seitter (1979), using the 3.6m ESO telescope at La Silla, Chile. Williams (1982) imaged the shell in Hα and [N II] using the Cerro Tololo Inter-American Observatory (CTIO) 4m Blanco Telescope and found that the shell was spectrally similar to known planetary nebulae, with near solar abundances. Shara et al. (1989) discovered a faint outer halo around the shell, extending out to a radius of $\sim 10''$. A model was introduced by Contini & Prialnik (1997) which proposed that the spectral line fluxes in the shell are caused by shock heating when the ejecta from a newer nova eruption run into slower ejecta from a previous eruption. The first *HST* images of the T Pyx shell were taken in 1994 and 1995 by Shara et al. (1997) using the WFPC2[2], and they showed that the shell was composed of more than 2000 individual knots. Over the short time baseline between the two observations (1.7 years), no expansion in the knots was detected. Figure 3.1 shows a comparison between a good ground-based image (taken in 1995 using the European Southern Observatory's 5.58m New Technology Telescope in La Silla, Chile) and the 1994/1995 *HST* image.

3.3 New Hubble Space Telescope Observations

In 2007 we obtained new HST observations of T Pyx and its shell. Time was originally granted on the ACS[3], which has greater sensitivity and resolution than the WFPC2 camera

[2]See Appendix A.3.2 for more information on WFPC2.
[3]See Appendix A.3.1 for more information on ACS.

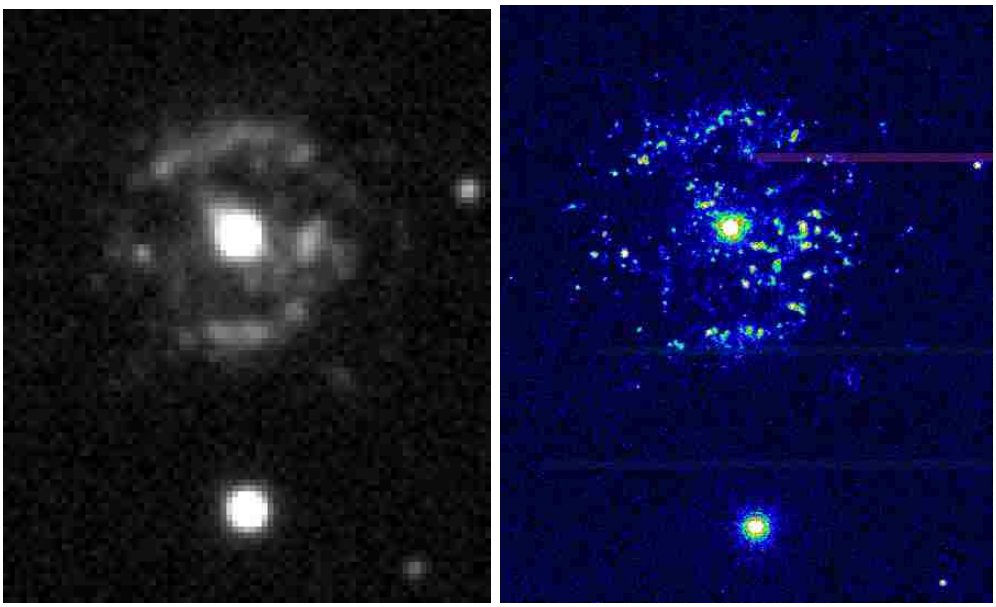

Figure 3.1 The Shell of T Pyxidis. T Pyx and its shell, as seen from the ground (left, from the ESO 5.58m NTT) and from space (right, from *HST* WFPC2). The shell is very visible in both images, but the excellent angular resolution of *HST* is necessary to see that the shell in fact consists of thousands of small knots. The knots allow us to accurately measure the expansion of the shell as well as obtain reasonable estimates of the shell mass. We combine this with other observed properties of the system to construct a new model for the evolution of T Pyx. Image Credit: M. M. Shara, R. E. Williams, and D. R. Zurek (STScI); R. Gilmozzi (ESO); D. Prialnik (Tel Aviv University); NASA

that was used by Shara et al. (1997) in 1994 and 1995, however a malfunction in the ACS detector led to our observations being rescheduled for the WFPC2. The primary science loss was in sensitivity, so our 2007 images do not go very deep. The primary benefit was that the 2007 observations were taken on the exact same instrument, with the exact same filters, as the 1994 and 1995 observations, which makes comparisons easier and more reliable.

Our 2007 observations were taken with the F658N filter, which has a central wavelength of 659.1 nm and a bandwidth of 2.9 nm[4]. This filter covers the Hα emission line as well as the bright [N II] line, which is ideal for T Pyx since the shell and knots are bright in both of those lines (Williams 1982). The observations were made for 1900 seconds each, on two separate orbits on 2007 June 29, for a total of 3800 seconds of observation. The 800 pixel $\times$800 pixel field ($35'' \times 35''$) covers T Pyx, the full shell, and a comparison star slightly to the south of T Pyx, labeled "Check" in Schaefer et al. (2010b), which provides a photometric standard ($B = 16.56$, $V = 15.81$, $R = 15.33$, $I = 14.95$, $J = 14.31$, $H = 13.94$, and $K = 13.89$) for the field.

The observation strategy included dithering[5] to allow for removal of cosmic rays and other defects, so the images were combined using the PyRAF MultiDrizzle package provided by STScI, achieving good results with the values recommended by the WFPC2 Drizzling Cookbook[6]. The full 2007 image and a zoomed version showing just the shell can be seen in Figure 3.2. The 1994 and 1995 observations were downloaded and processed identically to ensure the comparison would be robust. The knots in the 2007 image were identified using IRAF's *daofind* routine with a high detection threshold, to ensure that only the most well-detected knots were used. We analyzed a flux-selected sample of 30 knots; a summary of the knots and their properties, as well as the results of the analysis (which will be described in the following subsections) can be seen in Table 3.1, where the knots are organized and named in order of increasing distance from T Pyx. (There are fainter knots visible in the 2007

[4]http://www.stsci.edu/hst/wfpc2/documents/wfpc2_filters_archive.html

[5]c.f. the HST Phase II at http://www.stsci.edu/observing/phase2-public/10834.pdf for the full observing strategy, updated for the change to WFPC2.

[6]http://www.stsci.edu/hst/wfpc2/analysis/WFPC2_drizzle_4ditherWF.html

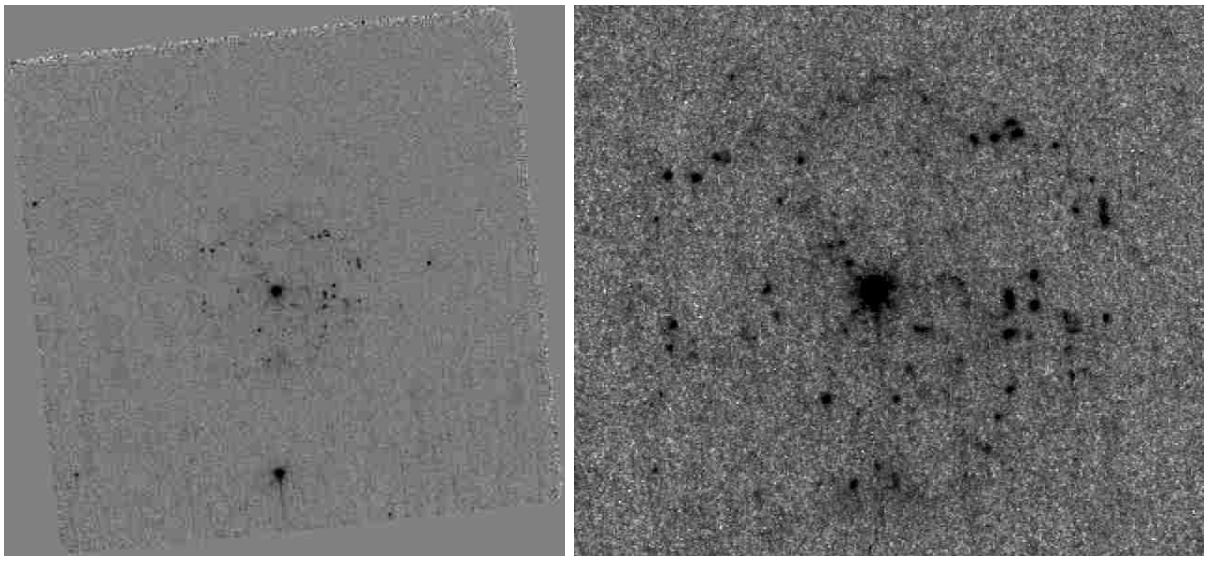

Figure 3.2 New Observations of T Pyx. The full *HST* WFPC2 image (left), as well as a zoomed version that shows just the shell (right) from our 2007 observations, both of which are oriented with north up and east to the left. The images are a combination of two 1900 second exposures, taken on two separate orbits, for a total of 3800 seconds of observation, and were taken using the F658N filter. This filter was chosen because it covers the Hα and [N II] emission lines, and the T Pyx knots are bright in both of those lines. Our 2007 images show fewer knots than the deeper 1994/1995 images (Figure 3.1) because of a shorter exposure time, but enough knots are visible for us to obtain an accurate measurement of the shell expansion. We identify 30 knots with strong significance; these are listed in Table 3.1 along with their positions, magnitudes, and changes from the 1994 and 1995 images.

image, but they are detected with less confidence, so we chose not to use them.) The IRAF *phot* routine was used to obtain centroids and aperture photometry of each knot (using a 2.0 pixel radius circular aperture) as well as T Pyx and Check. The knot locations ($X - X_T$ and $Y - Y_T$, in pixels, relative to T Pyx in X and Y, with a 1σ error of 0.2 pix), position angles (θ_{2007}, measured west of north, in degrees), radial distances from T Pyx (R_{2007}, in pixels), and magnitudes (Δm_{07}, relative to the magnitude of Check) are reported in Columns 2-6 of Table 3.1.

Table 3.1. Knot Summary

Knot	$X - X_T$	$Y - Y_T$	θ_{2007}	R_{2007}	Δm_{07}	θ_{1995}	R_{1995}	Δm_{95}	θ_{1994}	R_{1994}	Δm_{94}	R_{95}/R_{07}	R_{94}/R_{07}	Δm_{07-95}	Δm_{95-94}
K1	-13.3	14.0	-44	19.3	5.61	-41	18.4	6.41	-30	15.3	5.97	0.953	0.793	-0.80	0.44
K2	-17.0	24.9	-34	30.1	6.03	-34	28.0	5.64	-34	27.4	5.77	0.930	0.910	0.39	-0.13
K3	24.1	-21.0	131	32.0	5.76	131	28.4	4.94	131	28.0	4.97	0.888	0.875	0.82	-0.03
K4	-23.5	23.4	-45	33.1	6.03	-45	30.6	5.15	-45	30.6	5.31	0.924	0.924	0.88	-0.16
K5	-57.0	0.3	-90	57.0	5.56	-89	51.7	6.64	-88	51.0	6.78	0.907	0.895	-1.08	-0.14
K6	12.1	-58.1	168	59.3	5.73	168	53.5	4.64	168	52.9	5.41	0.902	0.892	1.09	-0.77
K7	-25.4	-58.2	-156	63.5	4.84	...	...	...	...	...	...	...	...	...	...
K8	71.8	-2.4	92	71.8	4.77	93	66.4	4.44	93	65.8	4.39	0.925	0.916	0.33	0.05
K9	72.5	-8.1	96	73.0	4.77	...	...	...	...	...	...	...	...	...	...
K10	71.7	-23.4	108	75.5	5.06	107	69.9	4.67	107	69.5	4.67	0.926	0.921	0.39	0.00
K11	-39.2	69.7	-29	80.0	5.72	...	...	...	...	...	...	...	...	...	...
K12	85.5	8.2	85	85.9	4.98	84	78.4	4.61	84	77.5	4.64	0.913	0.902	0.37	-0.03
K13	82.6	-24.4	106	86.1	6.41	106	80.3	6.52	106	79.6	6.26	0.933	0.925	-0.11	0.26
K14	85.9	-8.1	95	86.3	5.07	95	79.3	5.34	95	78.6	5.28	0.919	0.911	-0.27	0.06
K15	72.9	-53.0	126	90.2	5.52	126	81.8	4.31	125	81.7	7.32	0.907	0.906	1.21	-3.01
K16	66.3	-67.8	136	94.8	5.95	135	86.6	6.90	135	85.9	6.70	0.914	0.906	-0.95	0.20
K17	53.6	80.8	34	96.9	5.49	33	88.0	6.90	34	87.4	6.51	0.908	0.902	-1.41	0.39
K18	64.5	81.7	38	104.1	5.00	39	98.4	6.18	39	97.7	6.00	0.945	0.939	-1.19	0.18
K19	-10.8	-103.9	-174	104.4	5.44	-174	96.4	6.47	-174	95.4	6.18	0.923	0.914	-1.03	0.29
K20	-82.9	70.8	-50	109.0	5.53	-50	101.5	5.28	-50	100.5	4.94	0.931	0.922	0.25	0.34
K21	-107.6	-18.6	-100	109.2	5.28	-100	99.1	3.69	...	...	...	0.908	...	1.59	...
K22	-95.5	60.1	-58	112.8	4.79	-57	107.0	7.04	...	...	...	0.949	...	-2.25	...
K23	76.5	83.7	42	113.4	4.84	...	...	...	...	...	...	...	...	...	...
K24	73.3	89.9	39	116.0	5.43	39	105.1	5.82	38	102.3	5.51	0.906	0.882	-0.39	0.31
K25	108.0	42.8	68	116.1	5.68	68	106.0	7.89	...	...	...	0.913	...	-2.21	...
K26	97.3	77.4	51	124.3	5.88	...	...	...	...	...	...	...	...	...	...
K27	124.0	-14.9	97	124.9	5.36	97	114.8	6.78	97	113.1	6.30	0.919	0.906	-1.42	0.48
K28	-110.1	61.2	-61	126.0	5.21	-61	115.9	5.79	-61	114.4	5.59	0.920	0.908	-0.58	0.20
K29	123.3	37.6	73	128.9	4.78	73	116.9	7.10	73	116.0	6.66	0.907	0.900	-2.32	0.44
K30	122.5	46.9	69	131.2	5.48	70	119.5	6.79	69	118.8	7.40	0.911	0.905	-1.31	-0.61

3.4 Expansion of the Nova Shell

A comparison of the knot positions between 1994 and 1995 by Shara et al. (1997) did not show any expansion of the shell around T Pyx. With our new observations, however, we have a much longer time baseline, which gives the knots more time to travel and therefore makes it easier to measure any expansion that may be occurring. A quick measure of the radial positions of the knots in 1995 and 2007 shows an obvious expansion. A visual example of this can be seen in Figure 3.3, which shows sections of the 1995 and 2007 images that have identical scales, positions (relative to T Pyx), and angular sizes. The knots in the bottom section, from 2007, are clearly farther from T Pyx (the bright star to the left) than the knots in the top section, from 1995, which demonstrates unequivocally that the shell is expanding. Additionally, the right-most knots appear to have moved farther than the knots closer in to T Pyx, which provides the first evidence that the expansion is homologous, wherein the increase in radial distance is proportional to the radial distance itself.

This conclusion of homologous expansion could in principle be compromised by incorrect knot selection in three different ways. First, if we selected knots in the 1995 image to correspond with our 2007 knots based on where we thought they *ought* to be, we would introduce (and confirm) a bias. Second, the 1995 image has many more knots than the 2007 one; if we incorrectly picked from among the possible 1995 knots when matching to the 2007 knots, we would introduce a potentially-large systematic error. Third, the knots appear to vary in brightness between epochs, so a "twinkling" or "Christmas tree light" effect could lead us to unintentionally pick knots which are actually neighbors, not the same knot. Fortunately, the knot density in both images is sufficiently low that these potential problems are not significant, and we are confident that our match-ups between 1995 and 2007 are in fact correct.

We quantified this in a formal and unbiased manner by performing a cross-correlation analysis between all three images. We took each 2007 knot position and constructed a series of positions for which the radial distance was increased by a factor F, where F varied from

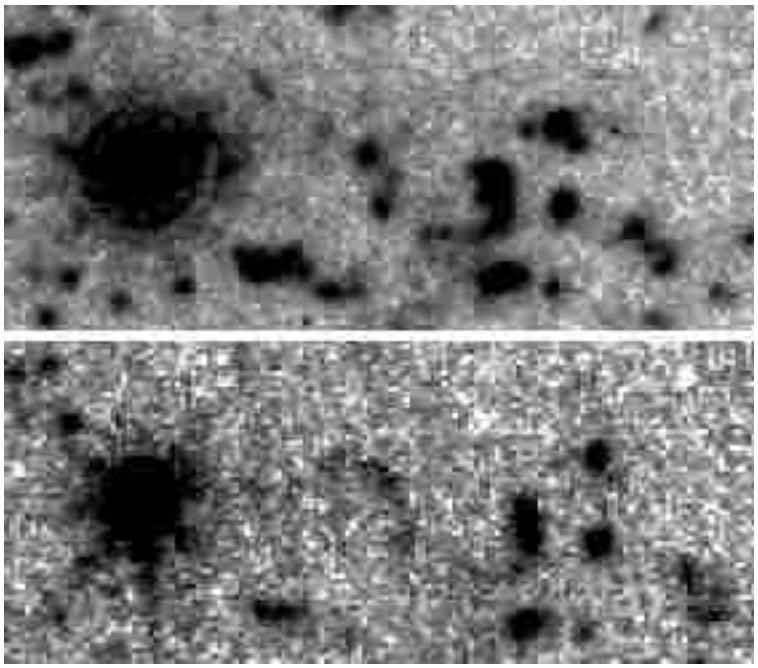

Figure 3.3 Shell Expansion in T Pyx. This figure shows sections of the 1995 (top) and 2007 (bottom) *HST* WFPC2 images. The sections are identically scaled, cropped, and positioned, and they have identical angular sizes. The knots in the bottom section are clearly farther from T Pyx (the large star near the left edge) than those in the top section. This visually shows that shell expansion is in fact occurring. Additionally, the knots farther from T Pyx appear to have moved a greater distance than those closer in, the first indication that the shell expansion is homologous.

0.80 to 1.20, inclusive. Using the 1995 image, we measured the total flux within a 1.0″ aperture at each of these positions. We used the same aperture to measure the flux at the actual knot position on the 2007 image. The cross-correlation is then the product of the 2007 flux with the flux at each of the 1995 positions. If there is no expansion, the cross-correlation should peak at $F = 1.00$ for each knot. If there is homologous expansion, the cross-correlation should peak at approximately the same, non-1.00, F value for each knot.

The results of this cross-correlation analysis for a representative sample of five knots can be seen in Figure 3.4. The product of the fluxes is plotted as a function of F, and they have all been normalized to their peak value. Some of the knots have multiple peaks, due to neighboring knots, but most have only one peak, and these are all close to $F = 0.91$. Figure 3.5 shows the cross-correlation summed over all 30 knots for both the 1994 and 1995 images. A single, highly significant peak can be seen around $F = 0.91$ for both cross-correlations.

The shell expansion can then be measured using four different methods. First, we take the best peak value from Figure 3.5, where the uncertainties will be on the order of the half-width at half-maximum of the peak divided by the square root of the number of knots. For 2007.5-1995.8, $F = 0.912 \pm 0.004$. For 2007.5-1994.1, $F = 0.907 \pm 0.005$. Second, we can average the peak F value for each of the individual knots. This gives $F = 0.917 \pm 0.003$ for 2007.5-1995.8 and $F = 0.905 \pm 0.003$ for 2007.5-1994.1. Third, we can use the measured radial shifts, as reported in Table 3.1. Columns 13 and 14 list R_{95}/R_{07} and R_{94}/R_{07} for each knot, where R_{9X}/R_{07} is the distance ratio between $199X$ and 2007. The average of these distance ratios is F, and the uncertainty on the average gives the uncertainty on F. From this third method, $F = 0.919 \pm 0.003$ for 2007.5-1995.8 and $F = 0.902 \pm 0.006$ for 2007.5-1994.1. Fourth, we can examine the slope of the change in the radial positions of the knots as a function of distance from T Pyx, a plot of which can be seen in Figure 3.6. Linear fits to the well-defined lines intercept the origin within a fraction of a pixel of zero, so we conclude that the rate of expansion is proportional to the radius, so the expansion is in fact homologous. The F values are one minus the slope, so $F = 0.918 \pm 0.005$ for 2007.5-1995.8

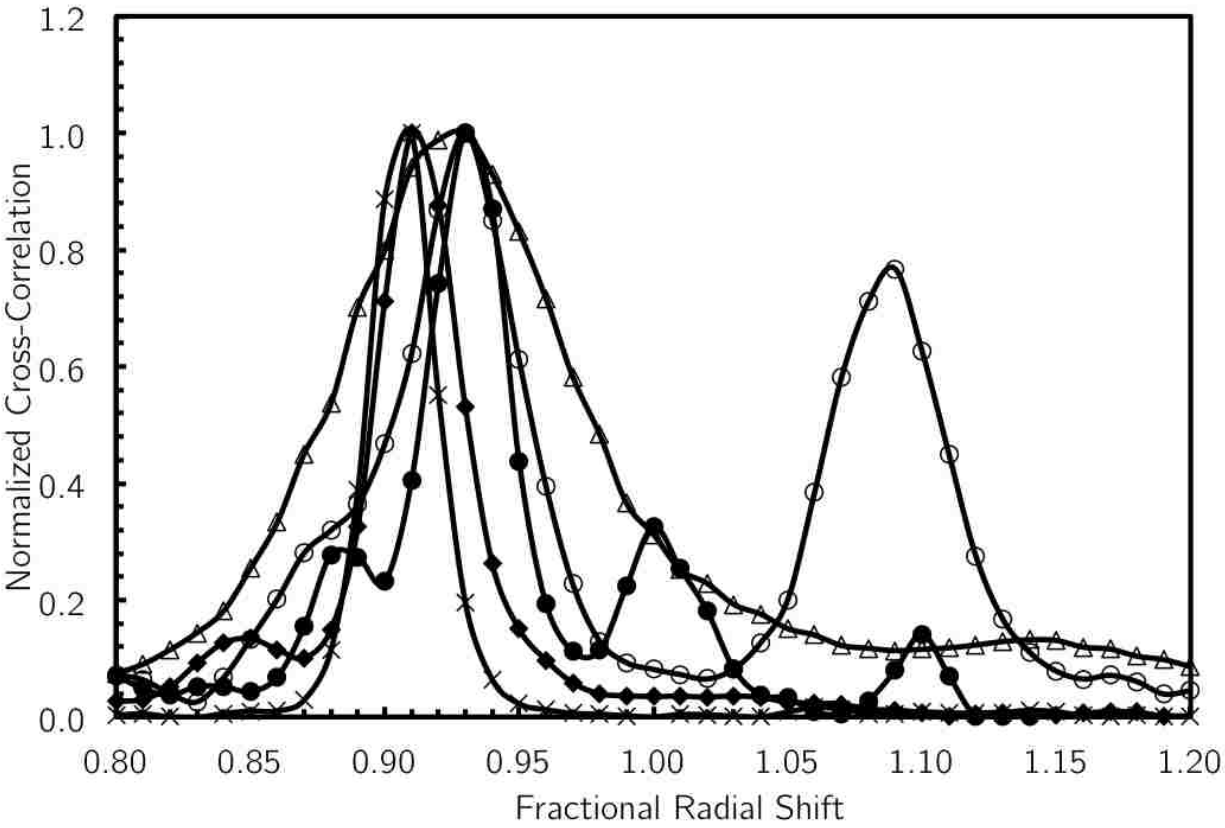

Figure 3.4 Cross-Correlation from 2007 to 1995 for Five Representative Knots. The cross-correlation is the product of the flux in a knot on the 2007 image and the flux in a shifted position on the 1995 image. The x-axis plots the fractional radial shift of the aperture on the 1995 image. The peak in the cross-correlation functions shows the fractional radial shift between the two epochs. All of the peaks occur near $F = 0.91$, which indicates that the knot selection in the 1995 image (to match up with the 2007 knots) is accurate, and that the expansion is homologous, so the radial shifts between epochs are proportional to the radial distances of the knots themselves.

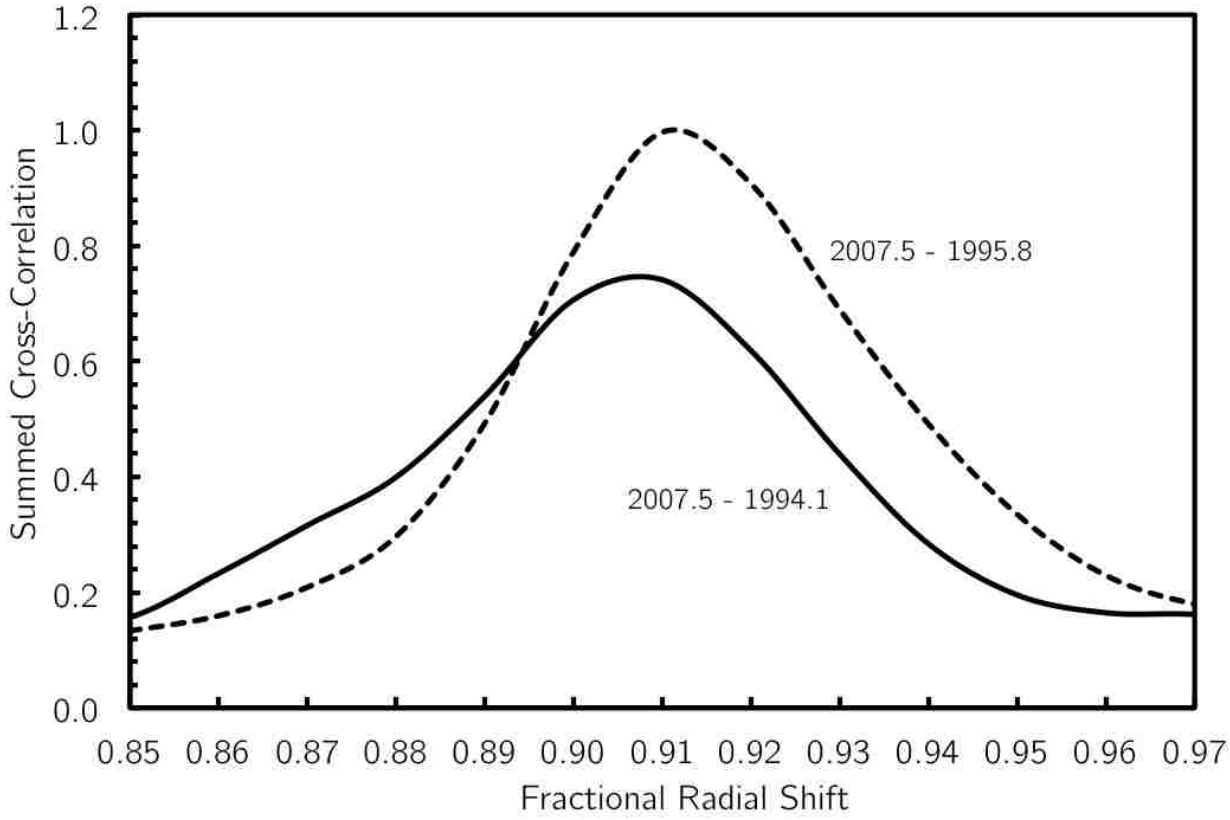

Figure 3.5 Summed Cross-Correlation for 30 Knots. The summed cross-correlation for 30 knots is shown for both the 1994 and 1995 epochs, as compared to 2007. Both epochs show a highly significant peak near $F = 0.91$; specifically, for 2007.5-1995.8, $F = 0.912 \pm 0.004$, and for 2007.5-1994.1, $F = 0.907 \pm 0.005$.

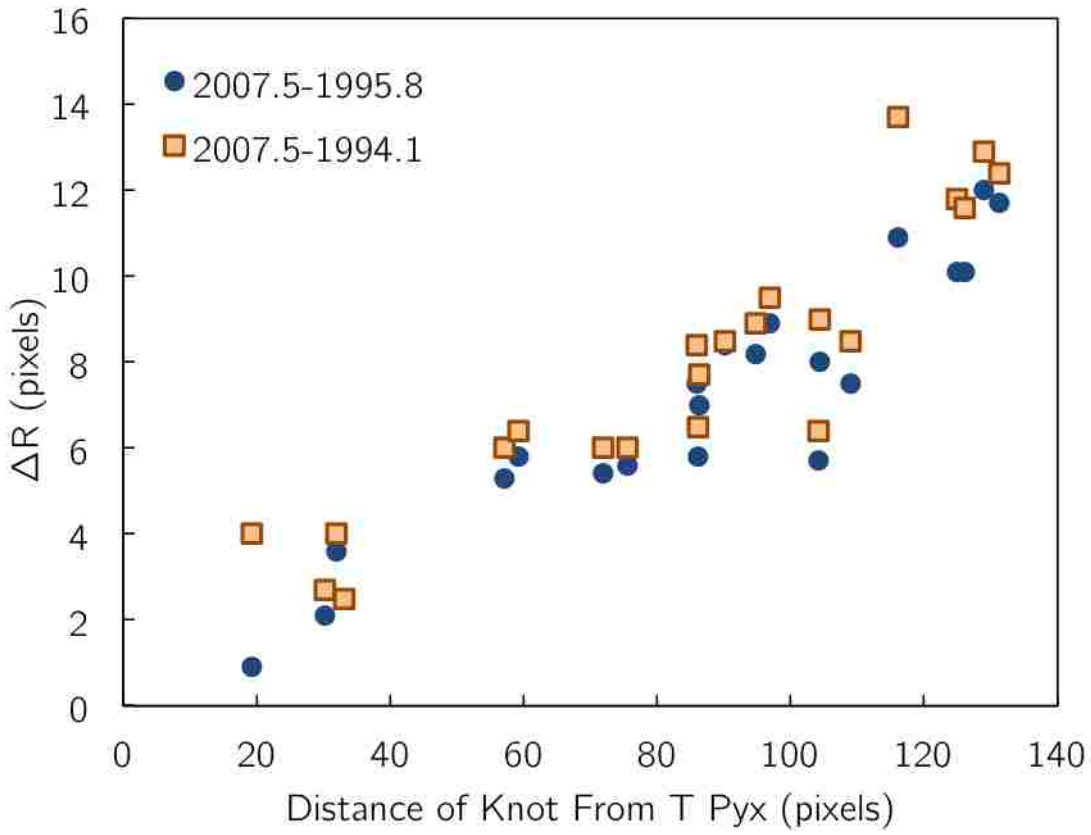

Figure 3.6 Radial shift (ΔR) vs. Distance from T Pyx. The knots farther from T Pyx expand by a greater amount than the knots closer in, showing that the shell expansion is homologous. The expansion is plotted for both 1994 to 2007 (brown squares) and 1995 to 2007 (blue circles). The linear relation is clearly observable for each epoch, with the line intercepting close to the origin, which is the signature of homologous expansion.

and $F = 0.913 \pm 0.006$ for 2007.5-1994.1. We adopt as our final F value the average of each of these four methods, and retain the RMS scatter in all four as our error on F. This gives $F = 0.917 \pm 0.003$ for 2007.5-1995.8 and $F = 0.907 \pm 0.005$ for 2007.5-1994.1.

To calculate the expansion factor of the shell and the real speed of the knots, we must know the distance to T Pyx. This distance is poorly known, as discussed by Patterson et al. (1998), Schaefer (2010), Selvelli et al. (2008), and Webbink et al. (1987), all of whom conclude that the best estimate is near 3500 pc, with average uncertainties on the order of $\pm$1000 pc, although recent observations have suggested that the distance is $\geq$ 4500 pc (Shore et al. 2011). We adopt 3500 ± 1000 pc as our distance and define for convenience d_{3500}, which is simply the true distance in pc divided by 3500 pc. Then movement over one 0.046″ pixel

on the *HST* images of T Pyx between 1995.8 and 2007.5 corresponds to a transverse velocity of $65 \cdot d_{3500}$ km s^{-1}. Presumably, the outermost knots have fully transverse motion and maximum velocity; for these knots, the average $\Delta R = 11 \pm 1$ pixels, so $V_{\rm max} = 715 \pm 65 \cdot d_{3500}$ km s^{-1}.

The average velocity of the knots is much more difficult to calculate, due to likely confusion from non-transverse motion and sub-maximal velocities. To estimate the possible velocity range, we constructed a Monte Carlo simulation of knots being ejected in random directions and with a range of velocities uniformly distributed between $V_{\rm min}$ and $V_{\rm max}$. We compared the simulation output to the observed distribution and used this to obtain $V_{\rm min} = 500 \pm 5$ km s^{-1}. The knot velocities therefore vary between $500 - 715$ km s^{-1}, so we take the reasonable average of 600 km s^{-1}.

The ejection velocity observed previously for T Pyx was 2000 km s^{-1} in 1967 (Catchpole 1969), which is significantly higher than the 600 km s^{-1} value obtained for the knots. This is because the eruption that ejected the shell/knots was significantly different from the observed RN eruptions in many ways, as we will explore in Section 3.7.

We constructed three models for shell expansion that included significant deceleration, due to (1) collisions with previously-ejected knots, (2) slow-moving gas from previous eruptions, or (3) interactions with a non-negligible ISM. None of these models can account for the relatively narrow distribution in observed knot velocities, despite widely varying knot masses. If we look at the conservation equation for each knot in each of the three deceleration models, it is only possible to get the same fractional rate of expansion if the masses are all nearly identical. For example, consider a case of scenario (1), in which a knot ejected at 2000 km s^{-1} runs into a knot moving at 300 km s^{-1}. As the mass ratio changes from 0.01 to 1.0 to 100, the final velocity changes from 320 to 1150 to 1980 km s^{-1}. This is completely inconsistent with the observations that the knots are all currently moving at very close to 600 km s^{-1} but have masses that vary by almost two orders of magnitude (Shara et al. 1997). The only model that can replicate the observed velocity distribution is one in which there

is no significant deceleration in the knots. This allows for an easy calculation of the time at which they were ejected. For an image taken ΔY years before our 2007.5 epoch, the eruption year is $2007.5 - \Delta Y(1-F)^{-1}$, with a 1σ uncertainty of $\sigma_F \Delta Y(1-F)^{-2}$. The 1994 image gives an eruption year of 1867 ± 5 and the 1995 image gives 1864 ± 7. Since these two values share half of their data (the 2007 image), they cannot simply be averaged, but instead we take a final value for the eruption year of 1866 ± 5.

3.5 Knot Brightness

A comparison of the knot brightnesses between 1994, 1995, and 2007 shows that they are not constant, but in fact both brighten and fade on a knot-by-knot basis. Some knots even "turn on" between images, e.g. K7 which is one of the brightest knots in 2007 but was not visible in either the 1994 or 1995 images. Additionally, knots were seen to turn on even between 1994 and 1995 (Shara et al. 1997). The knots appear to turn on at an average rate of one per year. There are four possible mechanisms that can power the knots: (1) the knots were ejected as ionized gas and are still glowing from the original 1866 eruption; (2) the knots are pre-existing and then flash-ionized by the light from an RN eruption, as was seen for the nova V458 Vul (Ness et al. 2009); (3) the knots are pre-existing and powered by the highly luminous, hot WD, as proposed by Knigge et al. (2000); (4) the knots are pre-existing and powered by collisions with the expanding shells from the RN eruptions, as indicated by the analysis of Contini & Prialnik (1997). The first three mechanisms are unable to produce knots that brighten between 1994, 1995, and 2007, as there were no RN eruptions during that time. The fourth mechanism is the only possibility, and does in fact produce knots that brighten or turn on during the 1990s and 2000s, as the ejecta from the 1967 eruption, moving at 2000 km s^{-1}, run into the knots from 1866, moving at speeds varying from $\sim 400 - 800$ km s^{-1}.

Some knots are also seen to fade, such as K21—Knot A in Shara et al. (1997)—which turned on between 1994 and 1995 and then faded by 1.59 mag between 1995 and 2007.

After the collisional shocks, which ionize the gas, the electrons begin to recombine and N_e declines, which causes the fading. This simple picture is complicated by varying densities within each knot and between knots, as well as velocity dispersions in the RN shells, but we can nevertheless use the relation between brightness and electron density to estimate N_e. The e-folding timescale over which the electrons recombine is $T_{\rm rec} = 100,000/N_e$. The knot brightness is proportional to $N_e N_{\rm H}$ in general, and proportional to N_e^2 for a fully ionized gas. During one $T_{\rm rec}$, N_e will decrease by a factor of 2.7, the flux will decrease by a factor of 7.4, and the magnitude will thus decrease by 2.2 mag. In general, if a knot fades by Δm in Δy years, then the electron number density is $N_e = (\Delta m/2.2 \text{ mag})(100,000 \text{ yrs}/\Delta y)$ in units of cm^{-3}. If we apply this to, e.g. K21 (with Δm $\approx$ 1.5 mag and $\Delta y = 11.7$ yrs), we find $N_e \approx 6000$ cm^{-3}, which is close to the densities estimated by Contini & Prialnik (1997) and Shara et al. (1997).

3.6 Shell Structure and Mass

Our *HST* images allow us to study the overall structure of the shell by measuring the amount of flux in annular rings centered on T Pyx. We use two different measurements, one adding up the total flux in each ring, and one taking the mode of all the pixels within the annulus to largely remove the flux contribution from the knots. For both measurements we subtracted out the constant sky background (as measured in the corners of the *HST* image, far from T Pyx) and the scattered light from T Pyx itself (measured by scaling the flux around Check in similar annular rings). These radial profiles can be seen in Figure 3.7. The profiles from the two different measurements track each other, unsurprisingly, and both peak significantly near 110 pixels (5.0″), which corresponds to the location of the majority of the slowly expanding knots. The unresolved knots in the 2007 image contribute to the smooth flux measured by the mode, which is why there is a peak there as well, even though the contribution from the resolved knots is negligible. There are a number of other, smaller peaks in both distributions, but they do not appear to be significant or representative of any shell. Monte

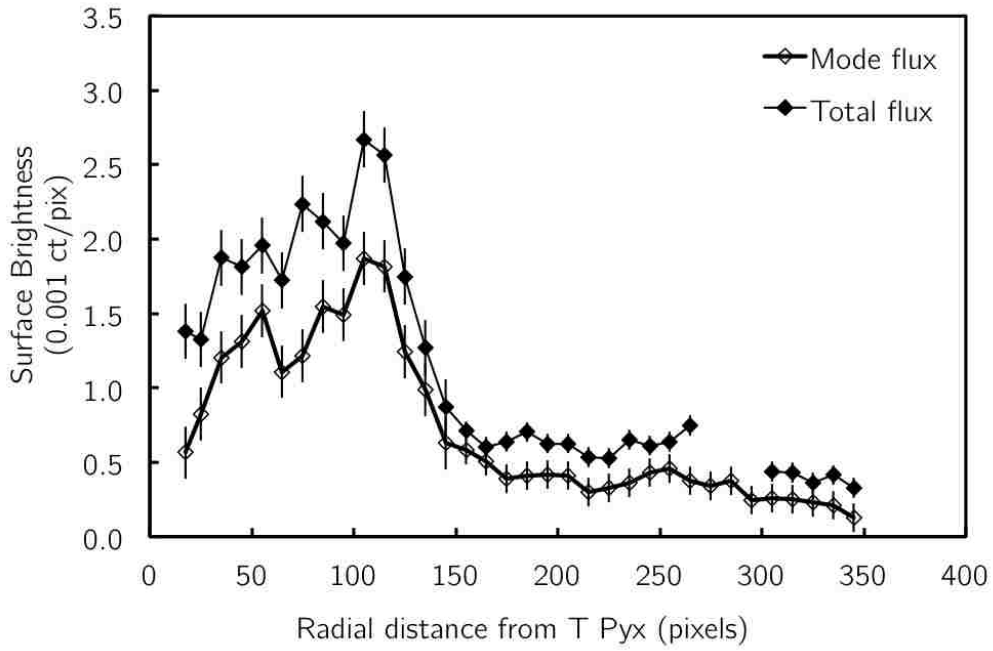

Figure 3.7 Radial Profiles of the T Pyx shell. This shows the flux in annuli surrounding T Pyx, calculated by summing the total flux (filled diamonds) and by taking the mode in each annulus (unfilled diamonds). There is a break in the total flux profile due to the presence of the check star in the annuli near 280 pixels from T Pyx. The radial profiles are dominated by the knots from the 1866 event, visible at approximately 110 pixels. An extended, faint outer halo is also visible out to at least 350 pixels.

Carlo simulations of expected radial profiles show similar such apparent peaks that vary from realization to realization, so we conclude that they are due to random shot noise.

The other significant feature seen in our radial profiles is a flux above background at distances greater than 180 pixels (8″). This flux falls off roughly linearly with distance, but shows substantial variations around this idealized model. This flux is caused by the fast-moving gas from the many RN events which has swept past the 1866 knots and reached large distances from T Pyx. As expected, the RN shells appear to have overlapped and jumbled together to present the observed mostly-smooth radial profile. It is tempting to associate the small deviations from the linear decline with shells from particular eruptions, but the confidence level of these associations is too low to be believable.

As the RN shells expand outward, they sweep past and interact with the 1866 ejecta. These fast winds blast the ejecta and break it up into the knots we currently observe via

Rayleigh-Taylor instabilities. This is unsurprising, as the knots are shaped much like those seen in planetary nebulae, known as cometary knots, which have been well studied (e.g. Capriotti & Kendall 2006) and are also due to Rayleigh-Taylor instabilities. Detailed simulations by J. Toraskar et al. have confirmed this theory; the simulated images, one of which can be seen in Figure 3.8, reproduce the observed distribution of knots and predict the presence of cometary tails.

The mass of the shell—or at least, the mass of the ionized fraction—is proportional to the emission line flux of all of the knots, but the standard method for calculating this mass (Gallagher & Starrfield 1978) is highly model-dependent and produces mass estimates with large uncertainties (Schaefer 2011). We can, however, use it to obtain an order of magnitude estimate that is still quite useful. Shara et al. (1997)'s detailed analysis of their *HST* images produced a shell mass of $1.3 \times 10^{-6} M_{\odot}$, assuming a distance of 1500 pc and $N_{\rm H} = N_e = 10^3$ cm^{-3}, where $N_{\rm H}$ and N_e are the number density of hydrogen and electrons, respectively. We updated this estimate in two ways.

First, use of the currently-accepted distance to T Pyx of 3500 pc increases the mass estimate to $7 \times 10^{-6} d_{3500}^2 M_{\odot}$. Second, with the observation of knot turn-on over the 12 year baseline from 1995 to 2007, it becomes obvious that at any given time, only a fraction of the knots are shining at their peak brightness, so only a corresponding fraction of the gas is counted. Since we have quantified the knot turn-on rate (Section 3.5) as approximately one knot per year, we can better estimate the real shell mass. We constructed a Monte Carlo simulation that creates a shell of knots (with velocity and mass distributions to match those observed) and then follows each knot as it is impacted by the RN eruptions from 1890 to 1967. This simulation allows for a comparison between the brightnesses of the knots at full ionization and the brightnesses in 1995, when some knots have either not yet turned on or have already started fading. The correction factor between the observed mass and the actual mass is 4.4 ± 0.3, where the uncertainty comes from the variations in different Monte Carlo realizations.

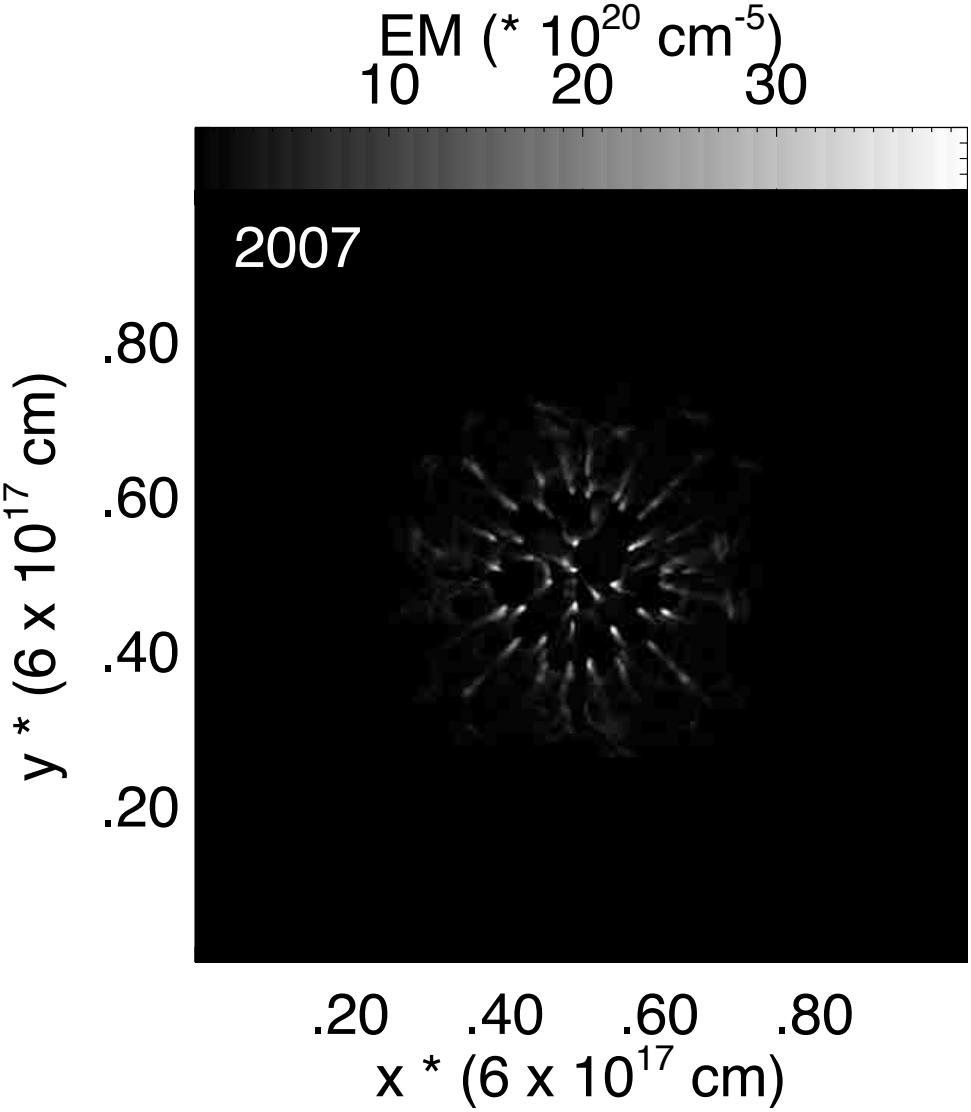

Figure 3.8 Shell Simulation. This image shows the result of a simulation of the T Pyx shell, specifically the effect of the 1967 eruption on the 1866 classical nova ejecta, as it would appear in 2007, along the axis of observation. The glowing knots are prominent, as is seen in the *HST* images (Figure 3.2). The simulation also predicts the presence of cometary tails trailing out away from T Pyx. Image Credit: J. Toraskar, M.-M. Mac Low, M. M. Shara, D. Zurek (AMNH)

With this correction factor, the shell mass estimate becomes $3.1 \times 10^{-5} d_{3500}^2 M_\odot$. Since this is highly uncertain, it is better expressed as $\sim 10^{-4.5} M_\odot$ which, despite being only order of magnitude, is enough to once again tell us that the 1866 eruption was vastly different from the RN eruptions that have since been observed. With a recurrence time of $12-24$ years and an accretion rate of $\sim 10^{-7} M_\odot$ yr^{-1}, there is literally not enough time to accumulate $\sim 10^{-4.5} M_\odot$ worth of gas, by more than an order of magnitude.

3.7 A New Model For T Pyx

We now have a collection of unusual and unexpected characteristics: a lengthening recurrence time, an accretion rate that is too high, and a knotty shell which is too massive and moving too slowly, and which has been blasted by lighter, faster shells that came later. We can combine all of these observed characteristics to construct a new model for the evolution of T Pyx.

With its high mass ($M_{\rm shell} \sim 10^{-4.5} {\rm M}_\odot$) and low velocities ($500 - 700$ km s^{-1}), the '1866' eruption was significantly different than the recently-observed RN eruptions. It was much closer in nature to a classical nova, and must have occurred after a very long time (likely $\sim 750,000$ years) during which matter accumulated on the surface of the WD. After this classical nova event, nuclear burning on the surface of the WD was ignited. Due to the unusually high-mass WD and the proximity of the companion, this nuclear burning was sustained for a longer-than-usual time period, during which it irradiated the companion, causing it to puff up and increasing the accretion rate. The supersoft X-ray source caused by the nuclear burning was not, however, completely self-sustaining, so as time wore on, the rate of nuclear burning decreased and consequently so did the accretion rate. This is visible in the long-term secular decline of T Pyx's B-band magnitude, which has fallen by 1.9 mags, which corresponds to a factor of 5.9 in flux.

The high accretion rate driven by the supersoft X-ray source pushed T Pyx into its current RN state, during which matter can build up fast enough on the WD surface to cause

the multiple RN eruptions that have been observed. The accretion rate is still higher than what it ought to be for a CV below the period gap, but it continues to fade. Eventually the accretion will fall to a level at which matter cannot pile up fast enough on the WD surface to cause any more RN eruptions. At the time we wrote the original paper on this model (Schaefer et al. 2010b), we believed that T Pyx would not undergo any more RN eruptions until at least 2225. In spectacular fashion, T Pyx proved us wrong; see Section 3.8 for further details. This does not, however, change any of the basic parameters of our new model; in fact, we even stated in the paper that the length of the RN state was somewhat uncertain, and not particularly crucial for the rest of the conclusions: "We adopt a total time in the RN state (ΔT) of two centuries, although none of our results depend significantly on this assumption".

During the RN state, however long it lasts, there are six dynamical mechanisms operating on the system, each of which works to change the orbital period. (1) Mass lost during the 1866 eruption will increase the orbital period. Schaefer & Patterson (1983) show that the orbital period change over an eruption is

$$\Delta P = A P_{\rm orb} M_{\rm shell} M_{\rm comp}^{-1} \tag{3.1}$$

where for T Pyx, $P_{\rm orb}$ = 1.83 hours, $M_{\rm shell} \sim 10^{-4.5} M_{\odot}$, $M_{\rm comp} = 0.12 M_{\odot}$ (Knigge et al. 2000; Selvelli et al. 2008), and A=2.13, where A depends on the specific angular momentum of the ejecta as well as the fraction of the ejecta captured by the companion star. This effect increases the orbital period of T Pyx by +0.0010 hours. (2) Mass lost during the RN eruptions will increase the orbital period. Again using Equation 3.1, but with $M_{\rm shell} \sim 2 \times 10^{-6} M_{\odot}$, we find that the five RN events from 1890 to 1967 increase the orbital period by +0.000064 hours each, for a total increase of +0.0005 hours. (3) The companion passing through the expanding shell from the 1866 event will decrease the orbital period. This was estimated by Kato & Hachisu (1991) and Livio (1991), but we update their estimates using our better input values to obtain an orbital period decrease of -0.000013 hours. (4) The companion passing through the expanding shell from the RN eruptions will also decrease

the orbital period. For five RN eruptions, the total period change is -0.0000012 hours. (5) Ordinary gravitational radiation will grind down the orbit, as it does in all binary systems. During the ∼200 year RN state, $q = M_{\rm comp}/M_{\rm WD} \approx 0.092$ and so we can calculate the orbital period change as

$$\Delta P = -860 G^{5/3} c^{-5} \Delta T (4/3 - q)^{-1} (M_{\rm comp} + M_{\rm WD})^{-1/3} \times M_{\rm comp} M_{\rm WD} P_{\rm orb}^{-5/3} \tag{3.2}$$

using Rappaport et al. (1982) and Frank et al. (2002). This effect causes a period decrease of roughly -0.00000011 hours. (6) Ordinary conservative mass transfer in the system will increase the orbital period. From Frank et al. (2002),

$$\Delta P = 3 P_{\rm orb} (1 - q) \Delta T \dot{M} M_{\rm comp}^{-1}. \tag{3.3}$$

During the RN state, the integral over time of $\Delta T \dot{M}$ is estimated to be $6 \times 10^{-6} M_\odot$, so this effect increases T Pyx's orbital period by +0.00025 hours.

Adding up these six contributions gives a combined total increase of +0.0013 hours to the T Pyx period. This is approximate, but still very useful. Notably only two of the six mechanisms are responsible for most of the period change: the mass loss during the 1866 eruption and the conservative mass transfer throughout the RN state, both of which act to increase the period. The 1866 mass loss has the biggest effect, so we describe it as the dynamically dominant event. As the period increases, so does the binary separation and consequently the size of the Roche lobe.

During the RN state, the companion star loses $\sim 6 \times 10^{-6} M_\odot$, which causes the radius to shrink by 5 km. The Roche lobe expands by 54 km, leaving the outer edge of the companion star 59 km from the border of the Roche lobe. Although the companion is now far inside the Roche lobe, accretion will not entirely cease because of the exponential scale height of the companion's atmosphere, $H_* = kT_*/g\mu m_{\rm H}$, where k is the Boltzmann constant, T_* is the surface temperature (∼3000 K in this case), g is the surface gravity (1.14×10^5 cm s^{-2}, μ is the mean atomic weight for the companion (∼1.4 for solar abundances), and $M_{\rm H}$ is the mass of hydrogen. The scale height of T Pyx is thus 12 km. The accretion rate is proportional

to $e^{-\Delta R/H_*}$ (Frank et al. 2002), so with $\Delta R = 59$ km and $H_* = 12$ km, we find that the accretion rate drops by a factor of 140, to around $\dot{M} = 3 \times 10^{-13} M_\odot$ yr^{-1}. This period of extremely low accretion is known as the hibernation state (Shara et al. 1986) of T Pyx. In this state, the gravitational radiation dominates over the conservative mass transfer and the overall period change is a decrease of $\dot{P} = -5.2 \times 10^{-10}$ hr yr^{-1}. This will continue until the outer edge of the companion is once again in contact with the Roche lobe. From Frank et al. (2002), $\Delta P_{\rm hib}/P = 1.5 \cdot \Delta R_{\rm Roche}/R_{\rm Roche}$ and we can then estimate the amount of time in the hibernation state as

$$\Delta T_{\rm hib} = 1.5(\Delta R_{\rm Roche}/R_{\rm Roche})(P/\dot{P}). \tag{3.4}$$

The Roche lobe must contract by 59 km, so the hibernation state will last for approximately 2.6 million years.

At the end of the hibernation state when the binary returns to contact, T Pyx will look like most other CVs below the period gap, with an accretion rate of $\dot{M} = 4 \times 10^{-11} M_\odot$ yr^{-1}, driven entirely by gravitational radiation, and a B-band magnitude of around 18.5 mag. Such a system would likely never be discovered with current observing programs. The regular CV state will last until the classical nova trigger mass accumulates on the surface of the WD and the process begins again. Nova trigger theory (Yaron et al. 2005) says that, for the $\dot{M} = 4 \times 10^{-11} M_\odot$ yr^{-1} accretion rate, the trigger mass is $3 \times 10^{-5} M_\odot$, which will take approximately 750,000 years to accumulate, assuming the accretion rate remains relatively constant (which it should). The full cycle, which can be seen in Figures 3.9 and 3.10, will take approximately 3,300,000 years.

Although we currently see T Pyx as a rare phenomenon, it is possible that there are quite a number of similar systems out there that we simply have not seen or identified, because they are in their normal CV or hibernation states. There is at least one other RN similar to T Pyx in many ways, and that is IM Nor. Very little is known about IM Nor, except that it has an orbital period of 2.45 hours, right in the middle of the CV period gap. It is unknown whether or not it has a secular decline, a shell, or any evidence for a supersoft X-ray source.

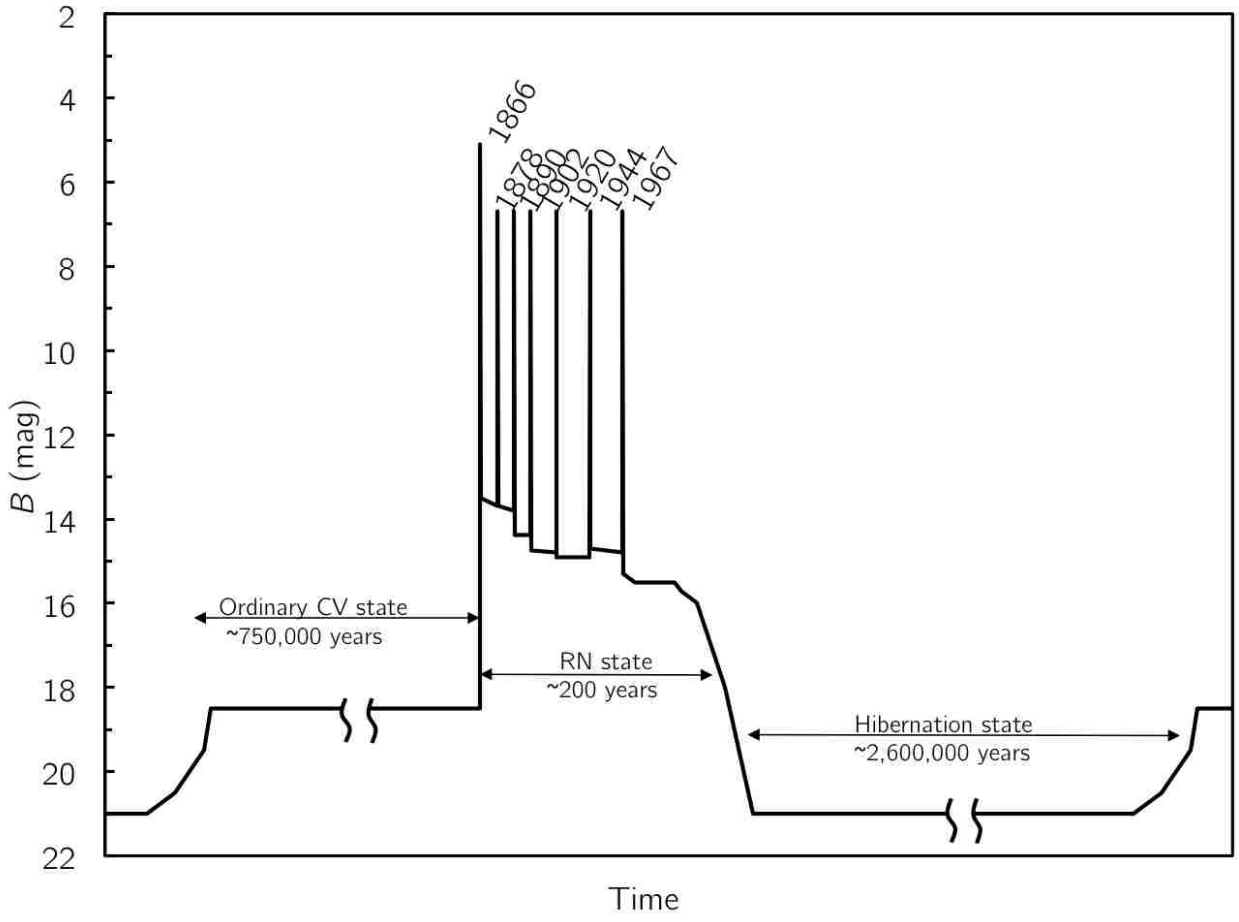

Figure 3.9 Brightness Evolution of T Pyx. This schematic plot of the B-band magnitude of T Pyx visualizes the entire evolutionary cycle, from ordinary CV state, to RN state, to hibernation state, and back again. During the ordinary CV state, the system appears to be an unexceptional interacting binary with weak accretion driven by angular momentum loss due to gravitational radiation. Once the trigger mass is accumulated, the system undergoes a classical nova eruption, such as the 1866 event of T Pyx. This eruption starts nuclear burning on the surface of the WD which produces supersoft X-rays and irradiates the companion star, increases the accretion rate, and starts the RN state. The supersoft X-ray source is not entirely self-sustaining, and as it slows, the brightness of the system fades. Eventually, accretion slows to near-zero, at which point the system becomes very faint and enters the hibernation state, which lasts for approximately 2.6 million years until gravitational radiation returns the system to contact, and it once again appears to be an ordinary CV.

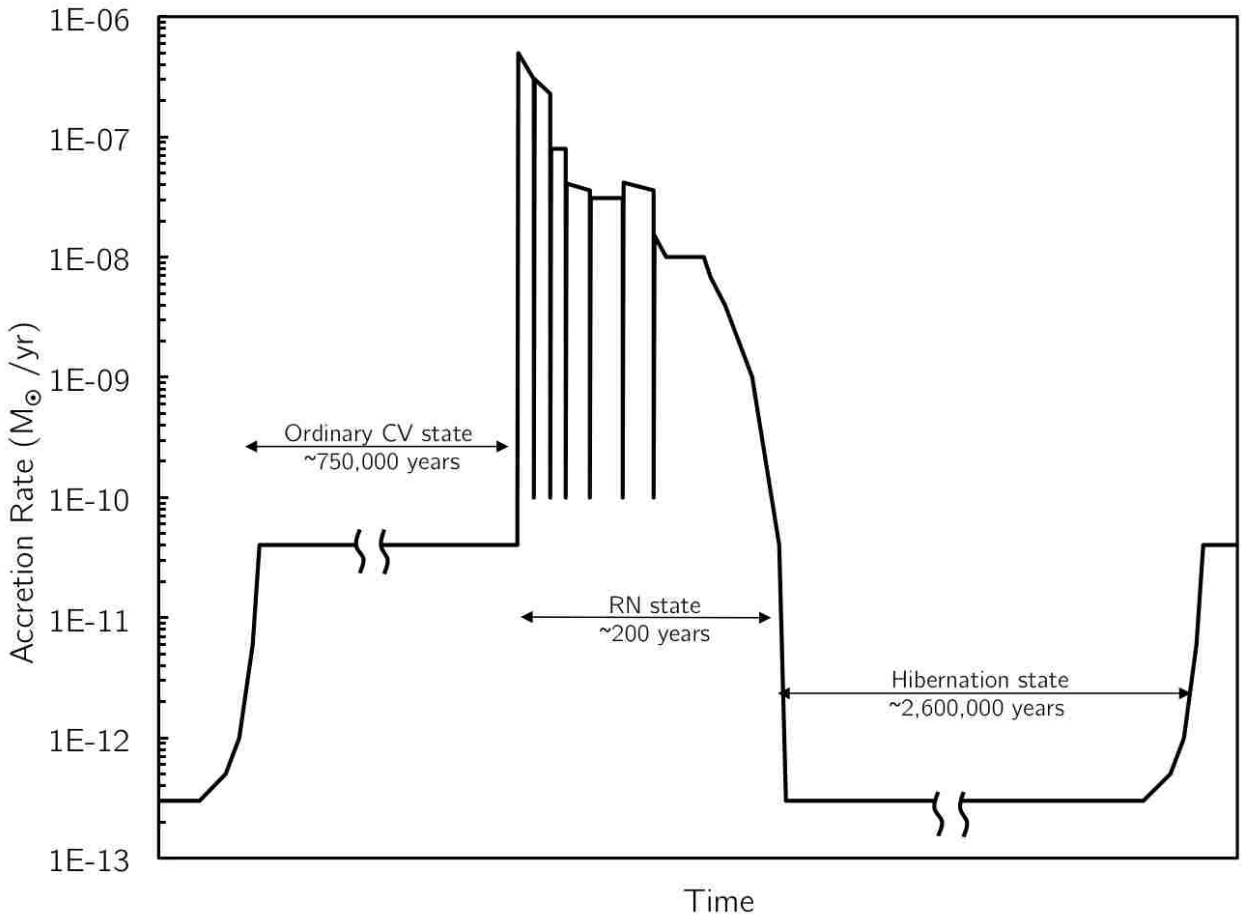

Figure 3.10 Accretion Evolution of T Pyx. Accretion is lowest during the hibernation state, when the binary is only barely in contact. Once the system returns to the ordinary CV state, the accretion is driven by gravitational radiation until triggering a classical nova event like the 1866 T Pyx eruption. The supersoft X-ray source ignited by this eruption irradiates and puffs up the companion star, driving a very high accretion rate during the RN state. Since the supersoft X-ray source is not self-sustaining, the accretion slowly falls until the system returns to hibernation.

There are a number of CNe which have been categorized by Schaefer & Collazzi (2010) as V1500 Cyg stars, named after the prototype of the class. The V1500 Cyg systems undergo CN eruptions that are very similar to the 1866 T Pyx eruption, wherein sustained nuclear burning on the surface of the WD drives a supersoft X-ray source for a number of years after the nova eruption. Although the mechanism is not yet comprehensively understood, it is believed that the V1500 Cyg systems have high magnetic fields, which funnel the accreting material towards the poles. The smaller surface onto which the material accretes is what allows the sustainment of nuclear burning. T Pyx is the only known V1500 Cyg star that went into an RN state after its CN eruption, though. The rest returned to quiescent behavior eventually, or are on track to do so now.

3.8 The Unexpected 2011 Eruption of T Pyx

On 2011 April 14, AAVSO observer M. Linnolt observed T Pyx at V=13.0, at the beginning of its rise to peak in a new, unexpected RN eruption (Waagan et al. 2011). Despite predictions by our group (Schaefer 2005; Schaefer et al. 2010b) as well as others (Selvelli et al. 2008) that T Pyx would not erupt again for many years, here was T Pyx proving us wrong, as astronomical objects are wont to do. Amateurs and professionals worldwide sprung into action, observing T Pyx at all wavelengths, eventually amassing more than 100,000 optical observations of the eruption (Schaefer 2012; see Figure 3.11 for the light curve) in addition to thorough X-ray coverage from the *Swift* X-Ray Telescope (XRT)[7] (Schwarz et al. 2011) and a large assortment of other observations.

While interesting and exciting, this was somewhat of an embarrassment for those of us who had predicted that there would not be another eruption in our lifetimes. The immediate question then is, of course, where did we go wrong, and how can we improve our models and theories to account for the observations. The key is in realizing that T Pyx is a magnetic system, like the rest of the V1500 Cyg stars, in which the accreted material is being funneled

[7]See Appendix A.4.2 for more information on the XRT

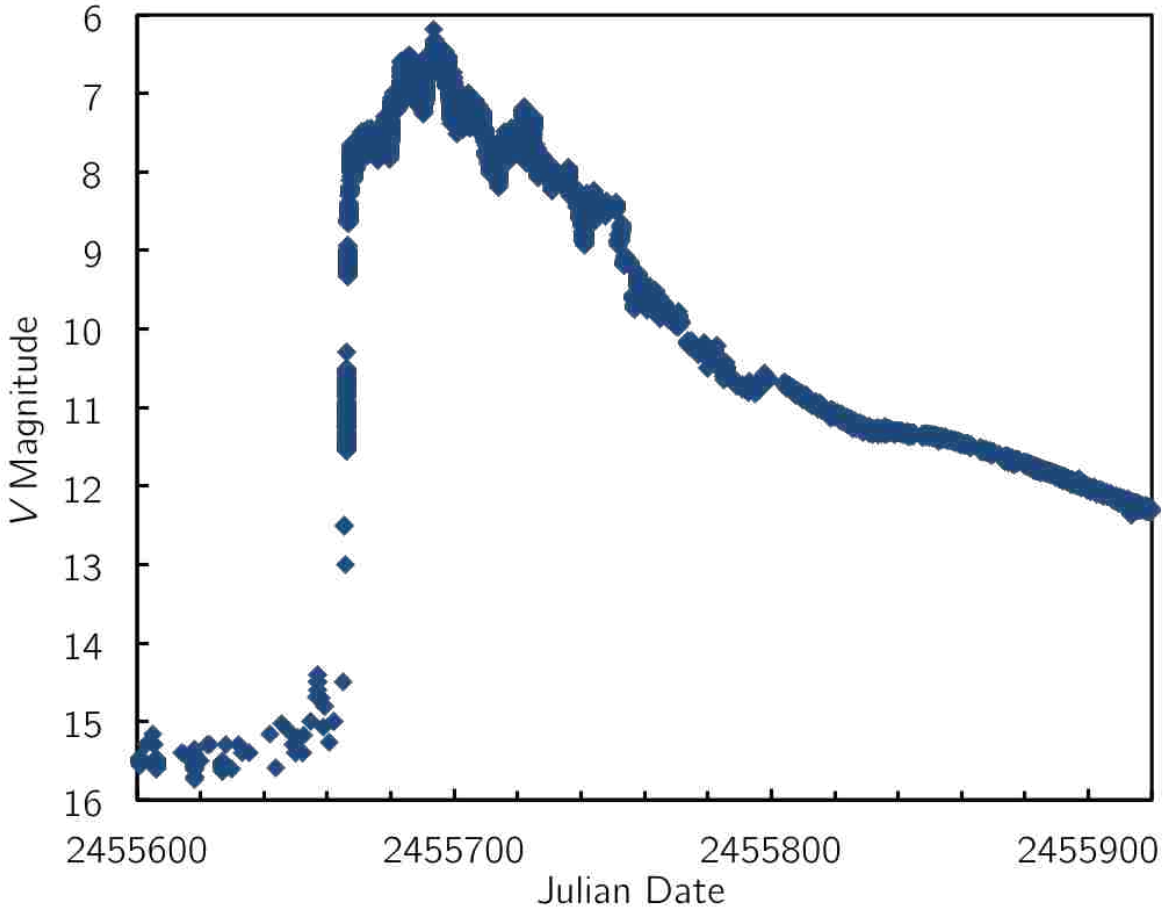

Figure 3.11 Optical Light Curve of the 2011 Eruption of T Pyx. This light curve contains more than 100,000 observations made by professional and amateur astronomers worldwide.

to the poles, and therefore T Pyx does not have an accretion disk. This changes the relation between accretion rate and B-band flux from $\dot{M} \propto F^{2.0}$, which we assumed for the preceding analysis, to $\dot{M} \propto F^{1.0}$. The key consequence of this is that the decrease by a factor of 5.7 in flux that has been observed over the past century in T Pyx corresponds not to a factor of 33 decrease in accretion rate, but instead a factor of only 5.7. Because of this, the system *was* able to accrete the trigger mass and explode in 2011. The details have not yet been completely sorted out, but empirically, $\dot{M} \propto F^{1.0}$ exactly reproduces the observed eruption cycle (Schaefer et al. 2011b). We will continue to monitor T Pyx, measuring orbital period changes (which can be used to calculate the total amount of mass ejected during the 2011 eruption) and the magnitude of the system. We anticipate that the system will continue to fade, as it has over the past 122 years, but only future observations can confirm this. If the magnitude (and thus accretion rate) remains at its current level, we can anticipate another eruption of T Pyx around 2055, but if the system continues to fade as expected, the next eruption will occur after 2055, if at all.

3.9 T Pyx as a Type Ia Supernova Progenitor

The possibility of T Pyx becoming a Type Ia supernova has been much discussed in the literature (Anupama 2002; Hachisu et al. 2008b; Knigge et al. 2000; Livio & Truran 1992; Schaefer 2005; Selvelli et al. 2008), but none of the previous discussion considered the 1866 classical nova eruption, as it had not been proposed at the time, and therefore all previous discussion is no longer relevant. It is likely that the T Pyx system does not have enough total mass to go supernova, as the best mass measurements are $M_{\rm WD} = 1.25 M_{\odot}$ and $M_{\rm comp} = 0.12 M_{\odot}$. Mass measurements are, however, notoriously unreliable, so it is worthwhile to examine the question anyway, in case the total mass of the system is in fact greater than the Chandrasekhar limit. Considering our new model, there are three key points: (1) Nova models indicate that the events such as the 1866 eruption should eject more mass than is accreted, by 15%-35% (Yaron et al. 2005), due to mixing between the accreted gas and the

outer layers of the WD. When the eruption occurs, some of the WD material is dredged up and ejected, and over time the T Pyx WD should therefore lose more mass than it accretes, even considering the accretion during the RN state. (2) Spectra of the knots indicate that they have solar abundances (Contini & Prialnik 1997; Williams 1982), which contradicts the idea that dredge-up is occurring. If there were significant dredge-up, the knots should show evidence of that in their spectra. If it is true that there is no dredge-up, then the WD should be gaining mass overall. (3) If the WD is now losing mass, and is currently near the Chandrasekhar limit, a backwards extrapolation implies that the WD was previously super-Chandrasekhar, but did not explode as an SN Ia at the time. A possible explanation for this is that the WD formed very, very near the Chandrasekhar limit and has since been slowly whittled away, although this is very unlikely.

Taken all together, these three considerations are contradictory and point to different conclusions about the eventual fate of T Pyx. Despite this, we can make estimates about the mass history of the WD, specifically during the 1866 eruption, as it is the dynamically dominant event. We adopt ranges of $1 - 10 \times 10^{-11} M_\odot$ yr^{-1} for $\dot{M}$ before the 1866 eruption and $1.2 - 1.4 M_\odot$ for $M_{\rm WD}$. For any two given values in these ranges, we can use theoretical models to calculate the trigger mass, $M_{\rm trig}$, and then the duration of the CV state is $M_{\rm trig}/\dot{M}$. With ϵ as an adjustable parameter, then the total amount of mass ejected is $\epsilon M_{\rm trig}$, where $0 < \epsilon < 1$ to ensure some ejected mass, but no dredge-up. $M_{\rm trig}$ is the total amount of mass accreted. The mass gain during a given cycle is then $(1 - \epsilon) M_{\rm trig}$.

Taking our best estimates for $M_{\rm WD}$ and $\dot{M}$, $1.23 - 1.3 M_\odot$ and $4 \times 10^{-11} M_\odot$ yr^{-1}, respectively, the time to collapse depends entirely on ϵ and rises from 6.3 to 63 billion years as ϵ goes from 0.0 to 0.9, becoming longer than the age of the universe at $\epsilon > 0.5$. We can also exclude low values of ϵ, since we know that $M_{\rm ejecta} \sim 10^{-4.5} d_{3500}^2 M_\odot$. Thus we must have some combination of low $M_{\rm WD}$ and high ϵ, which means that the time to supernova will be very long. For $M_{\rm WD} = 1.35 M_\odot$, ϵ must be > 0.35 and the time to supernova is then 9.7 billion years, but given the solar metallicity of the ejecta, a system age of 9.7 billion years is

not plausible. For $M_{\rm WD} = 1.25 M_{\odot}$, $\epsilon > 0.40$ and the time to supernova is then 22.5 billion years.

The lifetime of the T Pyx system will be on the order of the age of the universe, so the death rate of such systems must be very low. The total number of CVs in our galaxy is approximately 2 million, given that the space density of CVs is $\sim 1 \times 10^{-5}$ pc^{-3} for the disk population (Patterson 1984; Pretorius et al. 2007; Rogel et al. 2008), the effective volume of the disk is $< 10^{11}$ pc^3, and there are roughly equal numbers of CVs in the bulge and the disk (Shafter 2002). As T Pyx, with its near-Chandrasekhar mass WD, is quite unusual, we can set an upper limit on such systems of approximately 100,000. With this, the average lifetime of the systems must be $\sim$30 million years to contribute the 0.3 ± 0.2 SNe Ia that occur in our galaxy every century (Wheeler & Benetti 2000), which is far shorter than possible for T Pyx and similar systems. We can conclude that systems like T Pyx cannot provide any significant contribution to the observed SN Ia rate and are therefore not viable progenitor candidates.

4. The 2010 Eruption of U Scorpii: A Command Performance[1]

Eruptions of the recurrent nova U Scorpii have been observed in 1863, 1906, 1917, 1936, 1945, 1969, 1979, 1987, 1999, and 2010. U Sco is an exceptional system in many ways, a fact which we were able to confirm with comprehensive observational coverage during the 2010 eruption. U Sco is an eclipsing system with a 1.23 day orbital period (Schaefer 2010) and an inclination of 83° (Thoroughgood et al. 2001). In quiescence, it is at $V = 17.6$ and it rises to $V = 7.5$ at the peak of its eruption; its 2.6 day t_3 is the fastest of all of the novae. The companion star is estimated to be a G3-6 III-IV subgiant (Webbink et al. 1987) and the white dwarf mass has been estimated to be between $1.37 M_\odot$ (Hachisu et al. 2000a) and $1.55 \pm 0.24 M_\odot$ (Thoroughgood et al. 2001).

4.1 Eruption Prediction

The historical record of U Sco observations implies that eruptions occur approximately every 10 ± 2 years, with missing eruptions in 1927 and 1957, likely due to eruptions hidden in solar or lunar gaps (c.f. Sections 2.5.2 and 2.6.2 for more on RN discovery efficiencies). After the 1999 eruption, Schaefer (2005) predicted the next eruption by considering the fact that the time between eruptions scales as the inverse of the amount of mass accreted during the inter-eruption interval. The mass accretion can be tracked by looking at the B-band flux, and scaled based on B-band light curves from previous eruptions. Combining U Sco's history with its B-band magnitudes in the early 2000s, Schaefer (2005) predicted that the next eruption of U Sco should occur in 2009.3 ± 1.0. Such a precise prediction is useful, as

[1]Section 4.7 reproduced by permission of IOP Publishing Limited (Schaefer, Pagnotta, et al. 2011). The permission statement is available in Appendix B. Portions of the section have been updated and adapted to the dissertation format. I was primarily responsible for the analysis presented in Sections 4.4-4.6, 4.8-4.9, and 4.11; Sections 4.1-4.2 and 4.7 include a large amount of work done by my advisor in addition to my contributions; the data presented in Sections 4.3 and 4.10 were obtained by members of the USCO2010 collaboration.

it allows for observers to plan discovery and observing strategies in advance for maximum scientific return.

4.2 The USCO2009 Collaboration

As the time of the predicted eruption neared, we assembled a worldwide collaboration of professional and amateur astronomers to monitor U Sco, discover the eruption early, and obtain the best possible coverage of the eruption from start to finish. Since the U Sco eruption is so fast, it is crucial to discover it quickly, otherwise a significant percentage of the event, including the peak, will be missed. The skilled amateurs who are members of the American Association of Variable Star Observers (AAVSO) are the best observers to catch an eruption promptly. They have complete control over their telescope time, as the majority of them are using privately-owned telescopes, and are able to push further into morning and evening twilight than most of the professional telescopes. Because of this, we coordinated with the AAVSO to request regular monitoring of U Sco starting in 2008[2], and we also arranged for AAVSO headquarters to be a clearinghouse for the observations, tracking all of the monitoring, confirming any reported eruptions, and notifying us immediately upon receipt of confirmation. We also monitored U Sco with the ROTSE telescopes, a network of four 0.45m telescopes located one each in Australia, Turkey, Namibia, and Texas. The ROTSE telescopes are designed to do fast follow-up of Gamma-Ray Bursts (GRBs), but are available for other science observations when not searching for GRB optical afterglows. At the height of the monitoring campaign, we obtained approximately one image per hour from ROTSE. All ROTSE images are available publicly online as soon as they are taken, so we were able to check in on U Sco regularly via the ROTSE website[3].

In addition to prompt discovery, we designed our collaboration to obtain comprehensive, multi-wavelength coverage of U Sco for the duration of the eruption. We secured time on the SMARTS 1.3m telescope at CTIO to obtain optical and near-IR photometry of the entire

[2]AAVSO Alert Notice 367: http://www.aavso.org/node/1555/129
[3]http://www.rotse.net/operation/

eruption. We prepared target-of-opportunity proposals and submitted them through the *Swift* Nova-CV group which would allow us to obtain UV and X-ray photometry and spectroscopy of the eruption. Various collaborators also obtained target-of-opportunity observations on IRTF (IR photometry and spectroscopy), the SMARTS 1.5m (optical spectroscopy), and the Chandra X-Ray Observatory (X-ray photometry and spectroscopy). Additionally, we collaborated with the Center for Backyard Astrophysics (CBA) to arrange for their observers (who are distributed all over the world) to take fast time series photometry of U Sco while in eruption to supplement our nightly SMARTS observations and those of the AAVSO. In all, we would be able to cover the entire energy spectrum over which U Sco was expected to be observable.

The predicted eruption time, 2009.3, came and went without any signs of unusual activity from U Sco. In late October, U Sco entered solar conjunction, and our biggest fear was that it would erupt during the time it was behind the sun. Thankfully, as it once again became visible in late December, it was observed to be still at minimum, and we knew that we had not missed the eruption. The monitoring resumed at that point, as we were still within the 1σ error bars of the Schaefer (2005) prediction and could expect an eruption any day.

4.3 The USCO2010 Eruption

The 2010 eruption of U Sco was discovered independently by Barbara G. Harris and Sean Dvorak as part of the intense monitoring campaign described in the previous section (Schaefer et al. 2010a,c; Simonson & MacRobert 2010). Harris and Dvorak are both AAVSO observers in Florida who have their own private telescopes. Harris, from New Smyrna Beach, FL, had been diligently observing U Sco every morning since it had come out of solar conjunction; in fact, in December of 2009 she was the first person to report a post-conjuction magnitude, reassuring us that U Sco had not in fact erupted while it was behind the sun. On the morning of the 28th, she had planned to sleep in, but after her dog insisted on being let out, she decided to take a few images of U Sco using her 16" Schmidt-Cassegrain telescope and

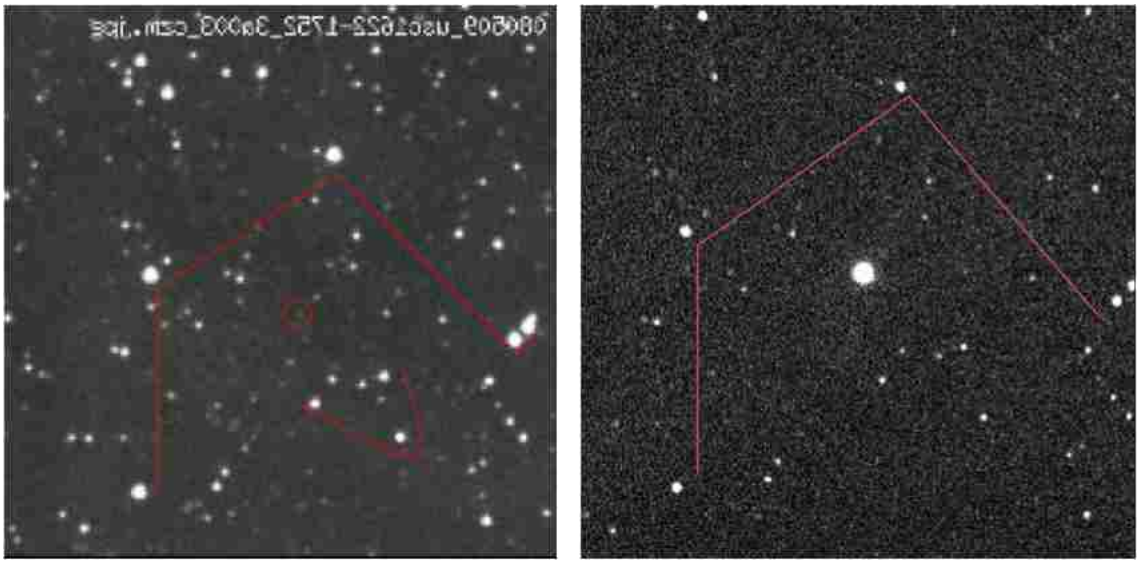

Figure 4.1 U Sco in Quiescence (left) and Near Peak (right). The pre-eruption image on the left is from one of the 0.45m ROTSE telescopes and shows the appearance of the U Sco field in quiescence; U Sco is the faint star inside the red circle near the center of the field. The image on the right is Barbara G. Harris's discovery image, taken a few hours after the eruption peaked at $V = 7.5$ mag; U Sco is the very bright star right near the center of the image. The red lines on both images mark nearby, bright asterisms (star patterns) that can be used to locate U Sco.

CCD camera just in case. The bright, overexposed star in the center of the field surprised her. She double-checked the position, took another exposure to confirm, and then immediately notified both the AAVSO and our group at LSU. Figure 4.1 shows a comparison between a pre-eruption image from one of the ROTSE 0.45m telescopes (on the left) and Harris's discovery image (on the right).

At the same time, in Clermont, FL, Shawn Dvorak woke up early to go to the gym and checked U Sco before leaving. At first, he believed he was pointing at the wrong field, but quickly realized he was in fact seeing the eruption. He immediately began taking a series of short exposures, to avoid saturation of the bright U Sco, pushing as far as possible into the morning sunrise.

The discovery triggered a worldwide invocation of both pre-planned (target-of-opportunity) and serendipitous observing programs. We notified all members of the collaboration as soon as possible, via telephone and email, and they responded in spectacular fashion. U Sco was

observed in all wavelengths from radio to X-ray during the 2010 eruption, with detections from IR to soft X-rays, by our collaboration of professionals and amateurs. The $BRVIJHK$ observations by myself using the CTIO 1.3m and $UBVRIy$ observations by G. Handler using the SAAO 0.5m form the backbone of our optical/near-IR light curve. The regular monitoring by the *Swift* XRT and UVOT instruments provide the majority of the UV and X-ray light curve. Each of these will be discussed in detail in the following sections. Additionally, U Sco was observed by all of the other X-ray satellites (Chandra, XMM-Newton (Ness et al. 2012), INTEGRAL (Manousakis et al. 2010), Suzaku, and MAXI); with ground-based IR from Mt. Abu (Ashok et al. 2010; Das et al. 2010), the SAAO 0.75m, and IRTF; and in radio with the Australian Telescope Compact Array and the Giant Metrewave Radio Telescope.

Because of the intense monitoring campaign we were able to obtain a thorough pre-eruption light curve with 815 magnitudes and 16 useful limits. The latest pre-eruption detection was made by B. G. Harris on JD 2455223.9473. M. Linnolt placed a visual limit of >16.5 mag from Hawaii on JD 2455224.1271, and the last pre-eruption observation was taken by Y. Watanabe, an amateur, on JD 2455224.3438, placing U Sco at $V > 9.2$. This comprehensive coverage allowed us to definitively show that U Sco does not have any pre-eruption rise or dip, such as the rise seen in V533 Her (Robinson 1975; Collazzi et al. 2009) or the dip in T CrB (Schaefer 2010). Fast variations are seen throughout the pre-eruption light curve, but they are all due to usual CV flickering and do not show any overall rise or dip trend (Schaefer et al. 2010c).

4.4 Multi-Wavelength Light Curve

We obtained nightly $BVRIJHK$ photometry of U Sco using the ANDICAM[4] CCD on the SMARTS 1.3m telescope at CTIO. All observations were queue scheduled from Lousiana, via the established SMARTS system. During the first few weeks after the eruption, the exposure times were adjusted daily to get the deepest possible exposure (to include multiple

[4]See Appendix A.2.1 for more details on ANDICAM.

comparison stars) without saturating U Sco itself. The actual observations were taken by the CTIO telescope operators, reduced early the next morning by S. Tourtellotte at Yale, and then uploaded to the SMARTS servers for us to download and examine. These nightly observations began the night after the eruption was discovered (HJD 2455225.8) and ended more than six months later (HJD 2455409.6) to ensure the eruption was followed in its entirety. Most previous eruptions of U Sco (and essentially all other RNe) have very little late-time coverage, once the 'exciting' part of the eruption has ended; we specifically designed the SMARTS campaign to cover U Sco's eruption completely.

The other source of regular, long-term, professional optical/near-IR observations for U Sco was G. Handler, an Austrian astronomer who serendipitously had a month-long run on the 0.5m Telescope at the South African Astronomical Observatory (SAAO) near Sutherland, South Africa. Handler observed U Sco in $UBVRIby$ nightly from HJD 2455225.6 until 2455249.6.

Figure 4.2 shows the combined SMARTS+SAAO $UBVRIJHK$ light curve for the entire eruption of U Sco. The U-band filter was available exclusively at SAAO, so there is only about a month of U-band data. Also, as U Sco returned to quiescence, the detection in the near-IR bands (JHK) became less and less significant, so the near-IR coverage does not last as long as the optical ($BVRI$) coverage. Table C.1 in Appendix C presents the data that went into Figure 4.2.

The eruption began on JD 2455224.32 ± 0.12, peaked on JD 2455224.69 ± 0.07 at $V = 7.5$ mag (Schaefer et al. 2010c), and returned to quiescence on day 67 after peak. There are four main parts of the light curve: the initial fast decline (days 0-15), the first plateau (days 15-32), the subsequent decline (days 32-41), and the second plateau (days 41-54), which was followed by a jittery return to quiescence. 2010 marks the first time a U Sco eruption has been followed past day 30, and is therefore also the first time the second plateau has been seen (Pagnotta et al. 2010). This is one of the two new phenomena discovered during this eruption that do not yet have theoretical explanations. The first plateau is attributed to the

turn-on of the supersoft X-ray source, however the X-rays had turned off at the time of the second plateau, so cannot explain its appearance.

4.5 *Swift* Observations

Through our accepted target-of-opportunity program, we obtained regular *Swift* UVOT and XRT[5] observations of U Sco. *Swift* observed U Sco from HJD 2455228.42 until 2455287.98 in $w1$ (2600 Å) and $w2$ (1928 Å) with UVOT and with XRT, which is sensitive from 0.2-10 keV. The $w1$ and $w2$ light curves can be seen in Figure 4.3 and are nearly identical. In general, the UV light curve has a very similar shape to that of the optical/near-IR light curve, which can be seen in Figure 4.4, where the $w1$ light curve is plotted along with the idealized V-band light curve, which will be described in Section 4.7. The UV observations show the system eclipses on the orbital period, as can be seen in Figure 4.4.

The XRT light curve can be seen in Figure 4.5, again compared to the idealized V-band light curve. The shape of the XRT curve is strikingly different from that of the V-band. The X-rays turn on at around day 14, which is the time at which the expanding nova shell becomes optically thin and we are able to see down to the inner binary, where the source of the X-rays is located. At the same time, the eclipses become visible again and the first optical plateau starts. This is not a coincidence, as it is the reprocessing of the X-ray light by the accretion disk which causes the plateau (Hachisu et al. 2008c). The eclipses are also visible in the *Swift* X-ray light curve, although they are not as prominent as in optical, and have a somewhat different shape. This was explored in detail with targeted XMM-Newton eclipse mapping observations, which showed deep X-ray dips early in the eruption before the eclipses returned to a normal shape by day 35 (Ness et al. 2012).

[5]See Appendix A.4 for more information on UVOT and XRT.

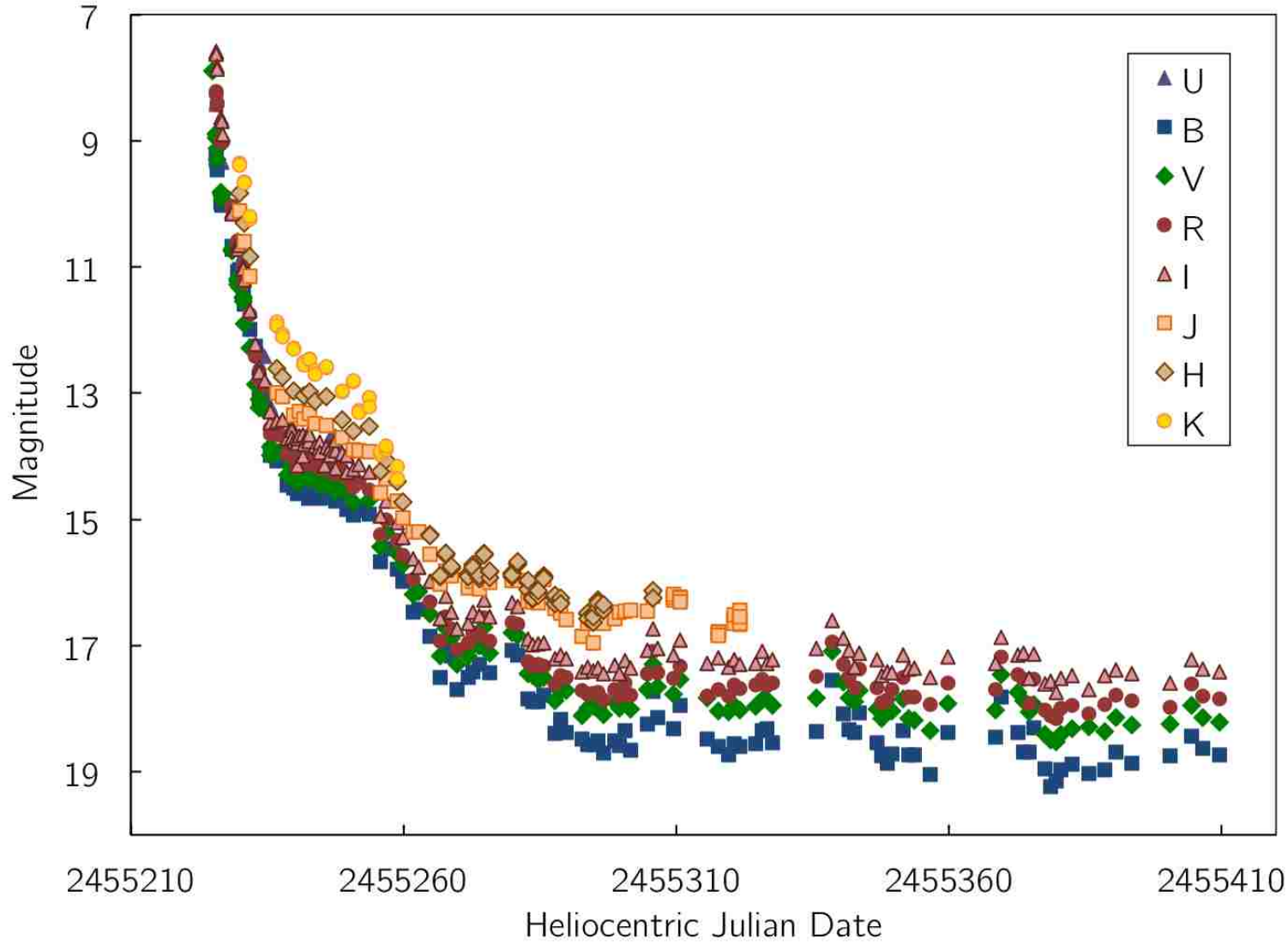

Figure 4.2 U Sco $UBVRIJHK$ Light Curve from the SMARTS 1.3m and SAAO 0.5m Telescopes for phases 0.1-0.9. The observations within a tenth of a phase of eclipse have been removed to show the overall trend of the light curve. The eruption light curve can be divided into four main parts: the initial fast decline (days 0-15), the first plateau (days 15-32), the subsequent decline (days 32-41), and the second plateau (days 41-54). U Sco returned to quiescence on day +67. This marks the first time that U Sco has been followed past day 30, and therefore the first time the second plateau has been seen (Pagnotta et al. 2010).

4.6 Universal Decline Law

Hachisu & Kato (2006) introduced a universal decline law for novae that can be used to predict the turn-on and turn-off of supersoft X-ray flux as well as estimate the mass of the WD. Their template light curve has a slope of $F \sim t^{-1.75}$ shortly after peak, where F is flux (measured in magnitudes) and t is time (in days), and a slope of $F \sim t^{-3.5}$ in the later part of the eruption light curve. It is best to look at the narrow Stromgren y-band light curve for this, because it is free of contamination from strong emission lines. We therefore arranged for as many Stromgren y observations of U Sco as possible. This is difficult because Stromgren y is no longer a common filter, but we were able to obtain some Stromgren y coverage from G. Handler on the SAAO 0.5m, A. Landolt on the KPNO 2.1m, J. Clem on the CTIO 1.0m, S. Kiyota using his personal 0.25m Schmidt-Cassegrain telescope, and H. Maehara using the Kwasan Observatory 0.25m. The full Stromgren y light curve can be seen in Figure 4.6. Figure 4.7 shows the best fit power laws for the Stromgren y data (using only the data from phases 0.1 to 0.9 to avoid the eclipses), with indices of -1.70 for the first power law and -3.08 for the second. However, since the coverage is somewhat sparse, the break time is not well defined. To remedy this, we also fit the V-band data, shown in Figure 4.8, which gives power law indices of -1.72 and -3.34 for the first and second power laws, respectively. Despite the fact that V is a broad-band filter which includes some contaminating emission line fluxes, it is reasonable to fit the V-band data as well because V and Stromgren y track each other almost identically, as shown in Figure 4.9. Our results are consistent with the predictions of Hachisu & Kato (2006).

For some novae, the break time can be used to determine the composition of the WD, whether it is carbon-oxygen or oxygen-neon-magnesium. Unfortunately for our case with U Sco, the models do not yet account for WDs very near to the Chandrasekhar limit, nor are they fully capable of dealing with RNe (I. Hachisu 2010, private communication), so we are unable to use this method to determine the type of WD in the U Sco system.

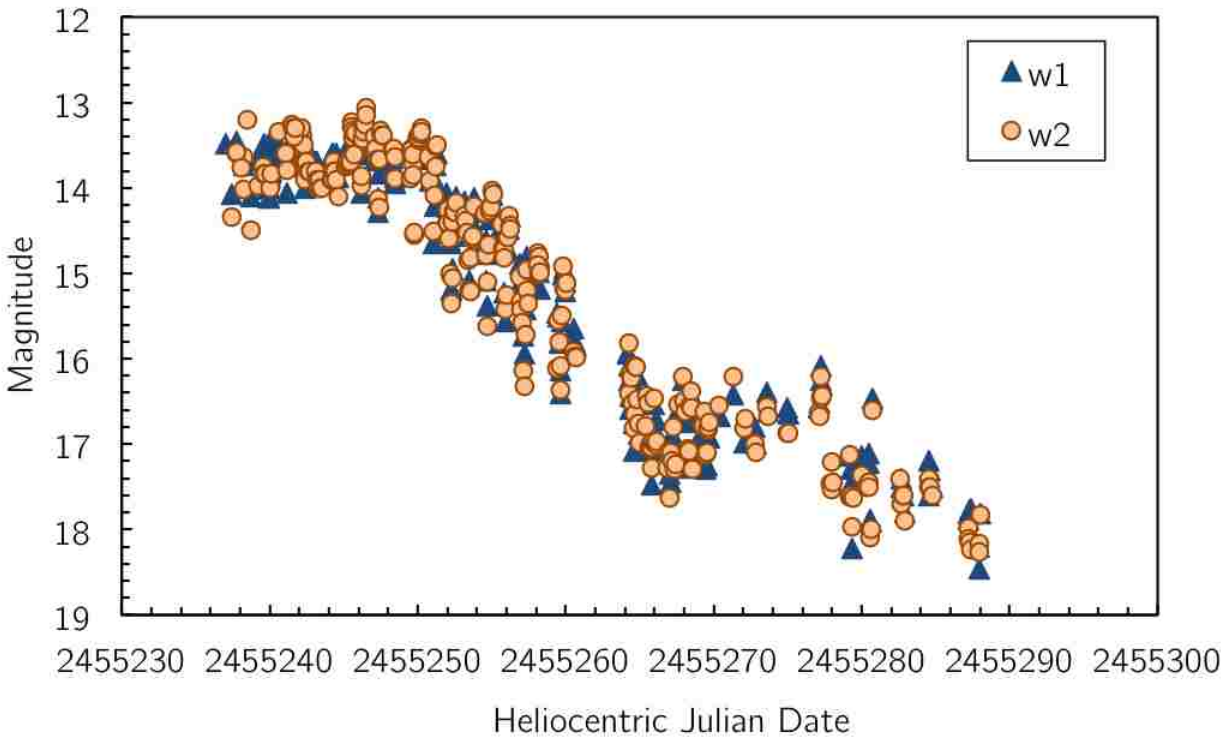

Figure 4.3 UVOT Light Curve. The *Swift* UVOT light curve in two UV filters, $w1$ at 2600 Å and $w2$ at 1928 Å. The two curves are nearly identical, with significant overlap. It is particularly useful to obtain UV observations of nova eruptions, since the majority of the energy is released in the UV regime.

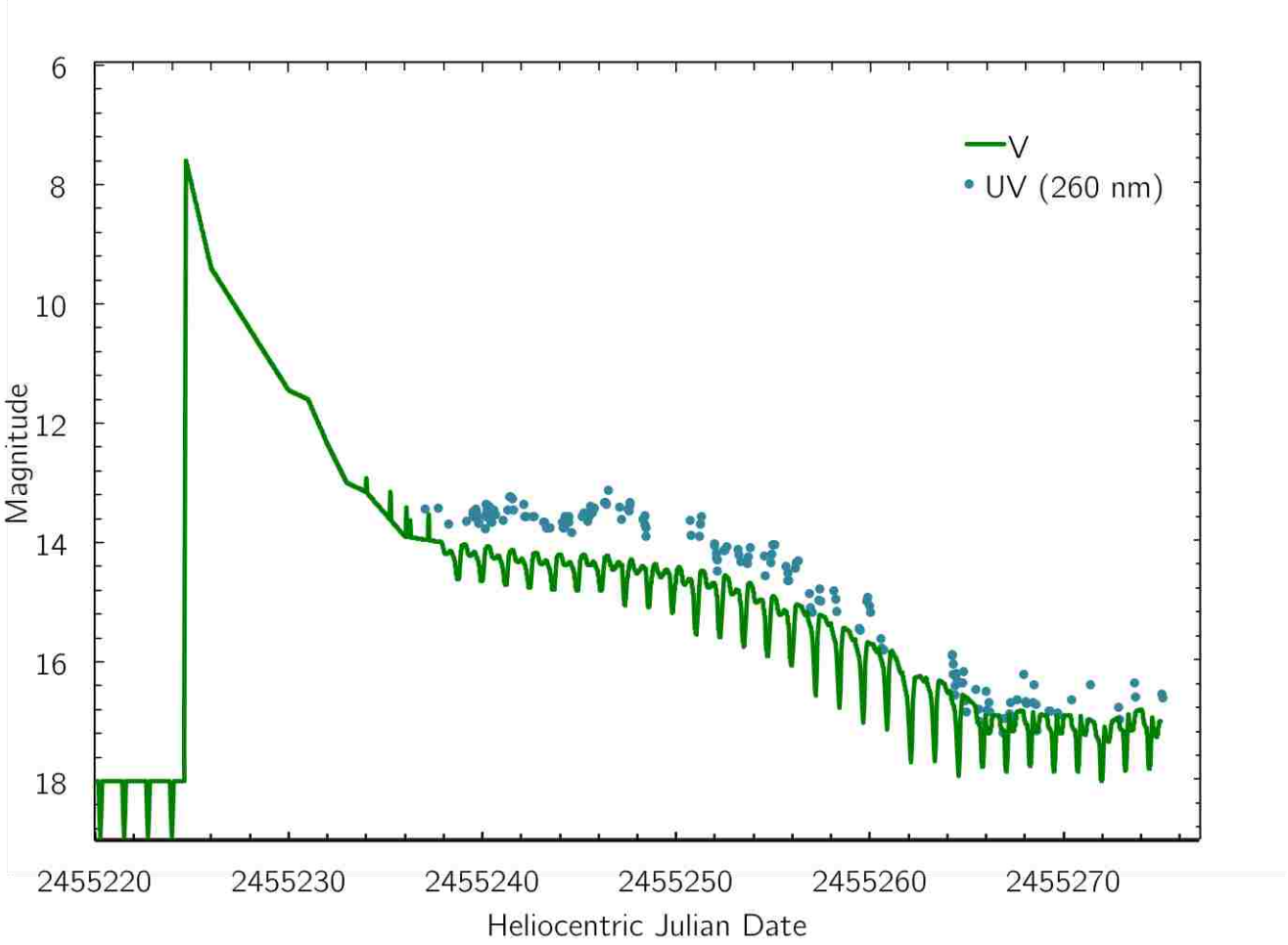

Figure 4.4 *Swift* $w1$+V-Band Light Curve. This figure shows the *Swift* UVOT $w1$ band overlaid on the idealized V-band light curve (Section 4.7). The shape of the UV light curve closely tracks that of the optical, with the UV also showing eclipses on U Sco's orbital period.

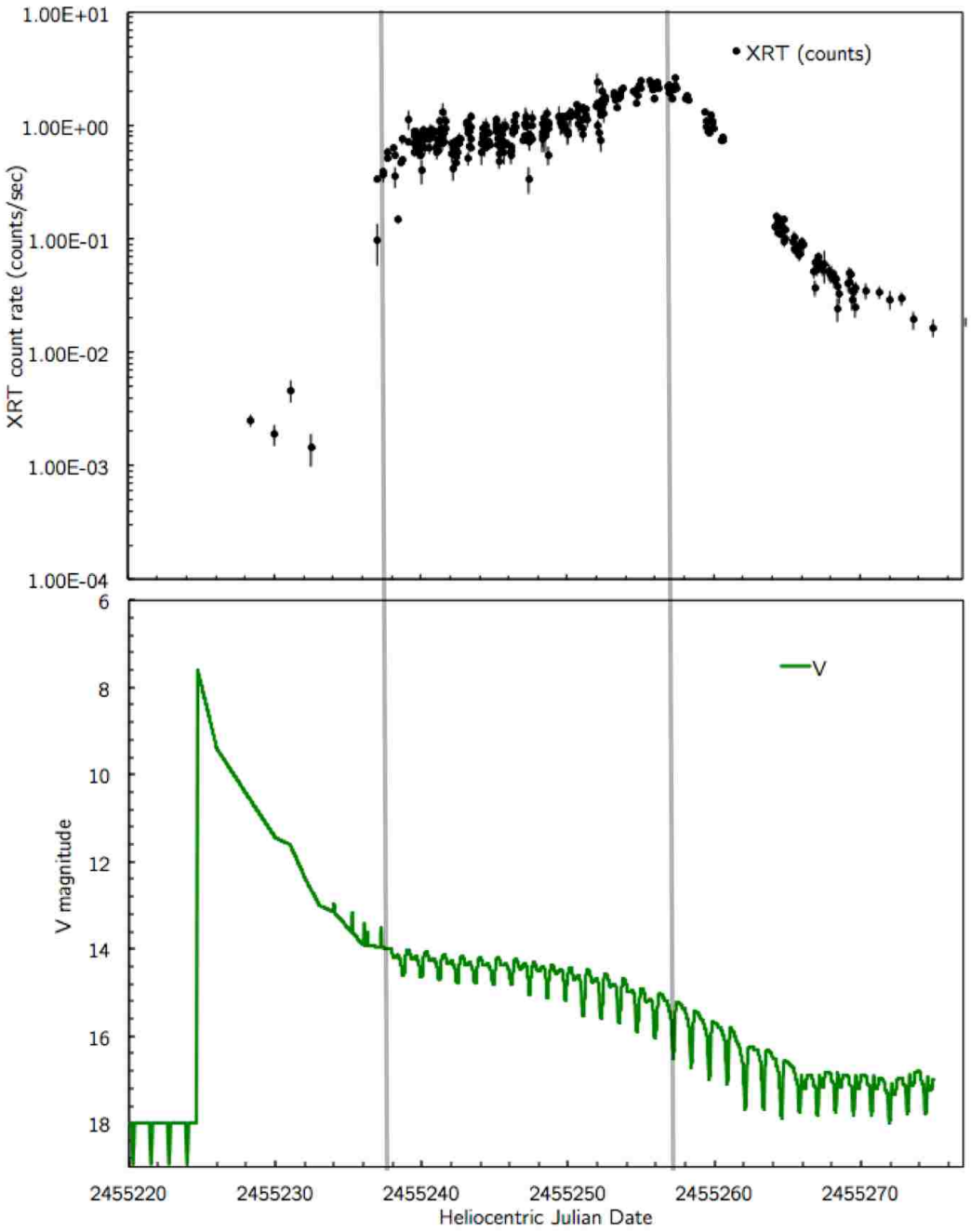

Figure 4.5 *Swift* XRT+V-Band Light Curve. The *Swift* XRT light curve (top) compared to the idealized V-band light curve (bottom, Section 4.7). The X-rays brighten drastically at around day 14. At the same time, the optical plateau begins and the eclipses become visible once again. These three effects all start when the expanding nova shell becomes optically thin and we can once again see down to the underlying binary system. The X-ray turn-on and peak are marked with vertical lines.

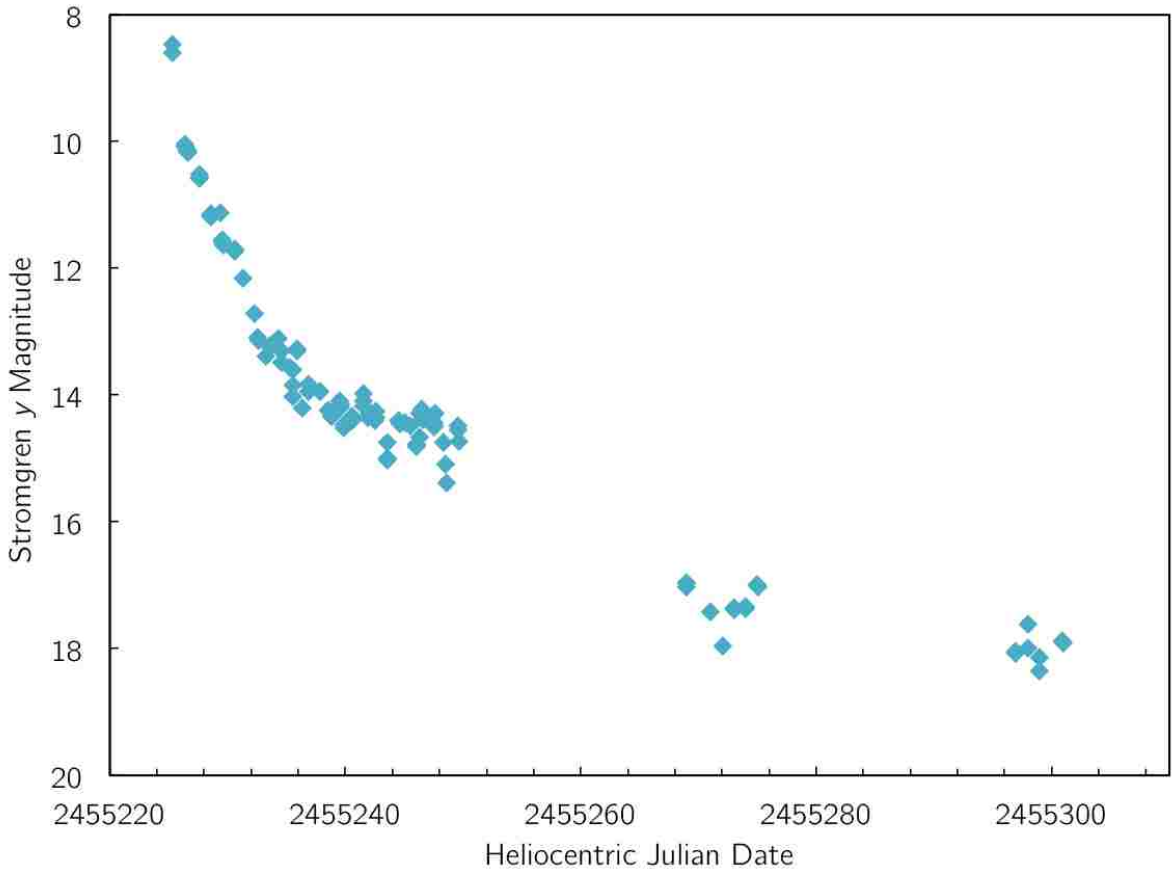

Figure 4.6 Stromgren y Light Curve. Stromgren y-band observations of U Sco during the 2010 eruption from G. Handler on the SAAO 0.5m, A. Landolt on the KPNO 2.1m, J. Clem on the CTIO 1.0m, S. Kiyota using his personal 0.25m Schmidt-Cassegrain telescope, and H. Maehara using the Kwasan Observatory 0.25m. This filter is no longer available at most telescopes, so we were unable to get complete coverage throughout the eruption, but we were able to get some epochs. Stromgren y is a narrow bandpass which is free from contamination by bright emission lines and is therefore ideal for testing Hachisu & Kato (2006)'s universal decline law (Figure 4.7).

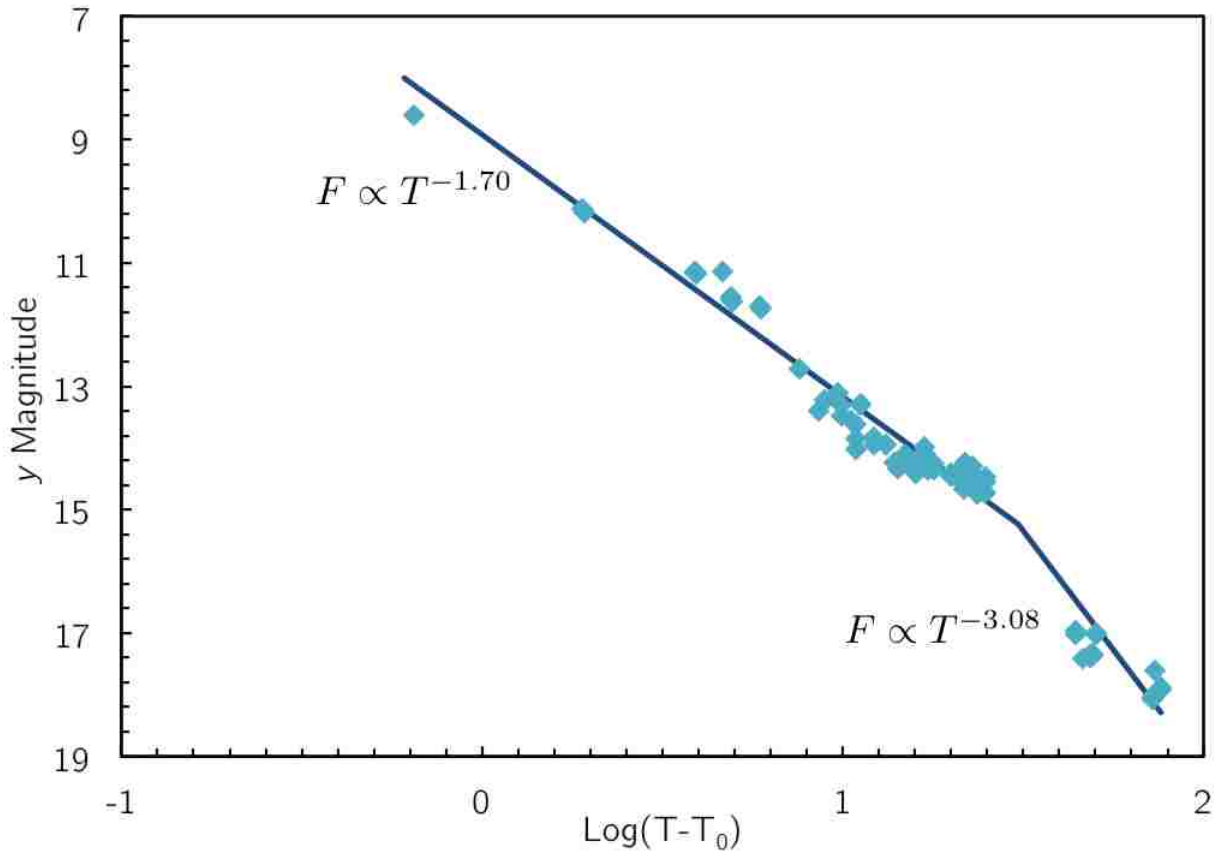

Figure 4.7 Stromgren y Universal Decline Law. Stromgren y light curve (phases 0.1 to 0.9) of the U Sco 2010 eruption and the best fit power laws to the data. The first power law has a best fit index of -1.70, and the second has a best fit power law index of -3.08. These are consistent with the predictions of Hachisu & Kato (2006), which give template fits of -1.75 and -3.5 for the first and second power laws, respectively.

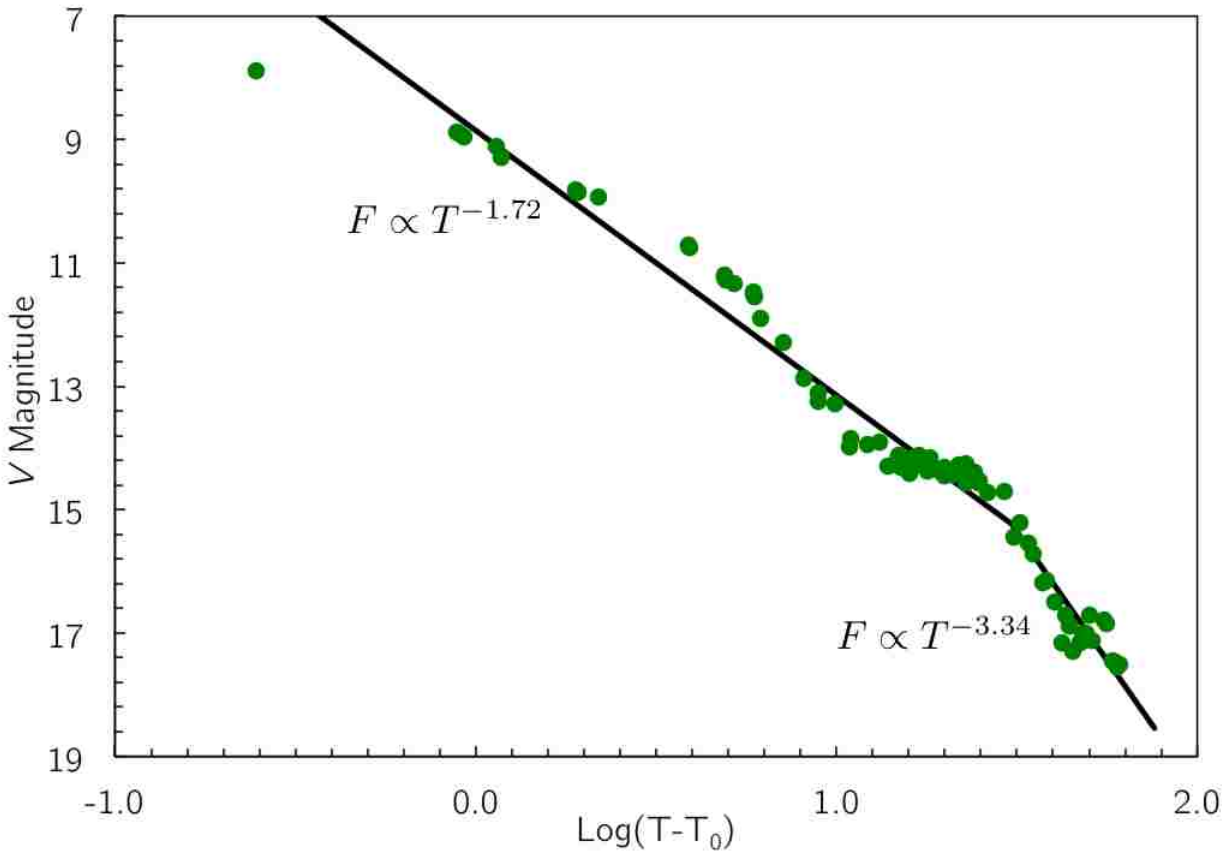

Figure 4.8 V-Band Universal Decline Law. We also fit power laws to the V-band light curve, which give best fit indices of -1.72 and -3.34 for the first and second parts of the light curve, respectively. Again this is consistent with the predictions of Hachisu & Kato (2006). Although V-band does have potential emission line contamination, Figure 4.9 shows that it tracks well with Stromgren y and therefore the power law fits are still useful.

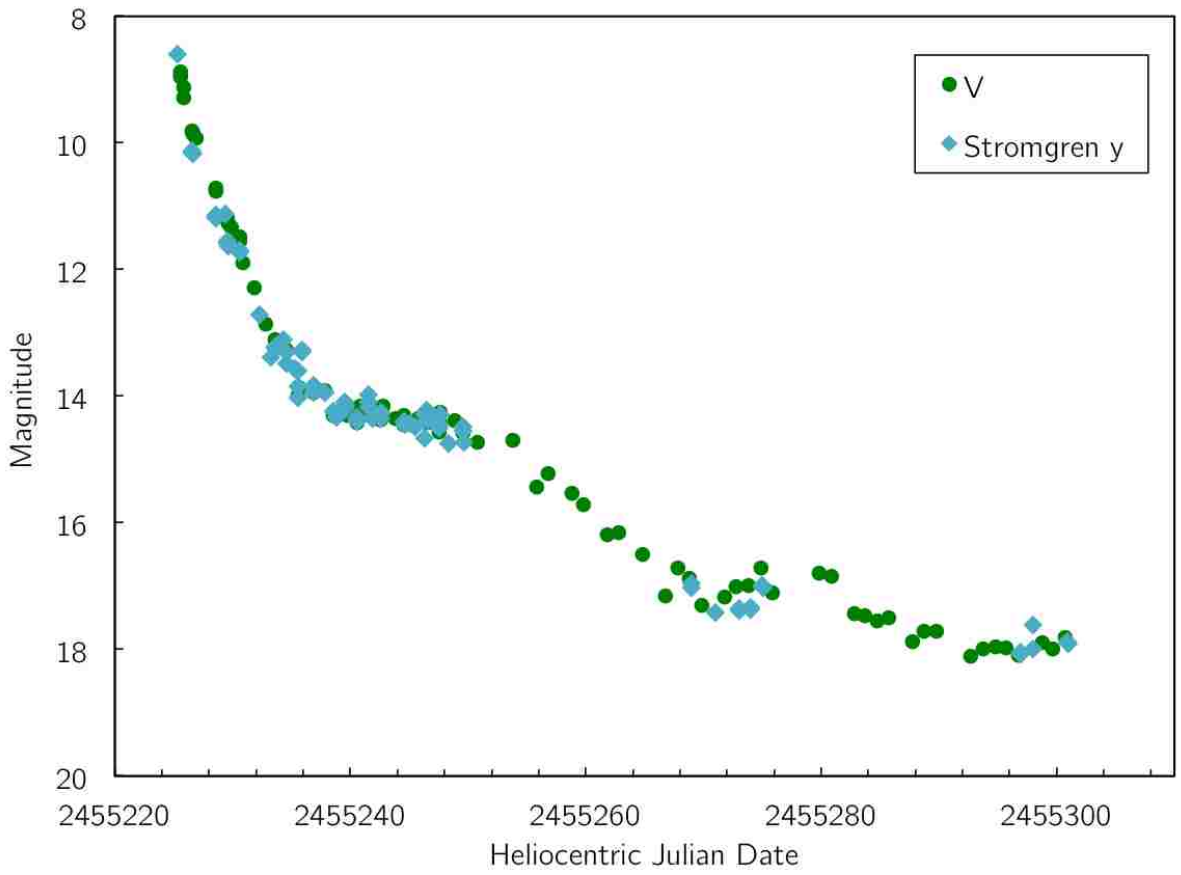

Figure 4.9 Stromgren y vs. V-Band. This comparison of the Stromgren y and V-band light curves shows that they are nearly identical, despite the extra emission line flux in the V-band. For this reason, we are confident that it is reasonable to fit the V-band light curve with the power laws as displayed in Figure 4.8 to test the predictions of Hachisu & Kato (2006)'s universal decline law.

4.7 Fast Time Series Observations

Our fast time series observations came from programs prepared long before the eruption, including networks of AAVSO and CBA observers. We made no attempt to get telescope time on large telescopes as these would be essentially useless, because they would saturate the bright stars and the amount of available time would be negligible. Instead, we obtained many long sets of fast time series photometry on telescopes with apertures from 0.2m to 2.0m. The smaller telescopes were of use only during the fast decline and first plateau phases, while our larger telescopes worked well throughout. By having many telescopes distributed widely in longitude, we covered a large fraction of each U Sco orbit throughout the entire eruption, despite U Sco being visible for only around one hour from each site at the beginning of the eruption. (By the end of the eruption, as U Sco moved farther away from the Sun in the morning sky, we could get 6 hour runs from any of our southern sites.) In the end, we obtained 36,776 magnitudes, with an average of 2.6 minutes between observations throughout the entire 67 days of the eruption.

A full list of observers, sites, telescopes, and filters is given in Table 4.1. For the photometry in this section, we are concentrating on the essentially V-band magnitudes, and this is where we have the 36,776 measures. All of these magnitudes were taken either with CCDs covered by a Johnson V-band filter or with CCDs running with no filter. In all cases, these magnitudes were derived with standard aperture photometry on fully processed images as differential photometry with respect to calibrated comparison stars nearby on the same image. The comparison stars are all well calibrated in B and V bands through either the sequences published in Henden & Honeycutt (1997) or Schaefer (2010).

Table 4.1. USCO2010 V-Band Observations

Observer	Site	Telescope	Filters	Start-Stop (HJD-2455000)	$N_{\rm mags}$	Offset (mag)
Harris	New Smyrna Beach, Floriday	0.4m Schmidt-Cass.	V	224.9-283.9	87	0.05
Dvorak	Clermont, Florida	0.25m Schmidt-Cass.	V	224.9-259.9	424	-0.15
Revnivtsev	Earth orbit	INTEGRAL OMC	V	225.4-234.4	133	0
Handler	Sutherland, South Africa	0.5m SAAO	V (and UBRIby)	225.5-249.5	55	0
Worters	Sutherland, South Africa	1m SAAO	V	225.6-236.6	2650	0
Munari[a]	Verona, Italy	0.3m Schmidt-Cass.	V (and BRI)	225.6-264.6	12	0
Pagnotta	Cerro Tololo, Chile	SMARTS 1.3m	V (and BRIJHK)	225.8-295.7	59	0
Stockdale	Hazelwood, Australia	0.28m Schmidt-Cass.	V	226.2-268.3	2640	0
Tan	Perth, Australia	0.24m Schmidt-Cass.	V	226.3-263.3	337	-0.07
Stein	Las Cruces, New Mexico	0.35m Schmidt-Cass.	V	226.9-261.0	1968	0.07
Krajci and Henden	Cloudcroft, New Mexico	0.28m Schmidt-Cass.	V	226.9-292.0	1284	0
Monard	Pretoria, South Africa	0.3m Schmidt-Cass.	Unfiltered	228.5-228.6	279	0
Sjoberg	Mayhill, New Mexico	0.36m Schmidt-Cass.	BV	229.9-262.9	665	-0.03
Maehara	Kyoto, Japan	0.25m Kwasan Obs.	Unfiltered	231.3-275.2	1198	0
Allen	Blenheim, New Zealand	0.4m Cassegrain	Unfiltered	234.1-260.2	1396	-0.45
Richards	Melbourne, Australia	0.4m Ritchey-Chretien	Unfiltered	235.2-259.2	1086	-0.45
Gomez	Madrid, Spain	0.2m Newtonian	V	237.7-247.7	65	0 and -0.33
LaCluyze and Reichart	Cerro Tololo, Chile	Two PROMPT 0.41m	UBVRI	240.8-292.8	11543	0
Krajci	Cloudcroft, New Mexico	0.35m Schmidt-Cass.	VR	241.9-296.0	2078	0.25 and -0.5
Oksanen	San Pedro de Atacama, Chile	0.5m Cass.	Unfiltered	243.7-424.7	7065	-0.32
Roberts	Harrison, Arkansas	0.4m Schmidt-Cass.	V	243.8-255.0	746	-0.01
McCormick	Aukland, New Zealand	0.35m Schmidt-Cass.	Unfiltered	248.1-249.1	300	-0.3
Mentz	Sutherland, South Africa	1m SAAO	V	248.5-248.6	190	0
Darnley	La Palma, Canary Islands	2m Liverpool Telescope	V	252.6-259.7	91	0
Sefako	Sutherland, South Africa	1m SAAO	V	259.5-259.6	137	0
Rea	Nelson, New Zealand	0.3m Schmidt-Cass.	Unfiltered	260.1-260.2	120	0
Schaefer	Cerro Tololo, Chile	SMARTS 0.9m	I	334.6-387.7	119	0
Lepine and Shara	Kitt Peak, Arizona	2.4m MDM	I	382.6-382.7	49	0

[a]Munari et al. (2010)

This same calibration was applied to the unfiltered images, with the resulting magnitude for U Sco being close to the V-band magnitude system, but with a systematic offset that varied from observer to observer. U Sco does not change its colors greatly throughout the eruption (Pagnotta et al. 2010), so this systematic offset should be nearly constant for a given observer. Indeed, we find that we can reconcile every observer to the Johnson V-magnitude system by taking a constant offset. This offset is determined for each observer by direct comparison with simultaneous observations from a fully calibrated observer. The uncertainty in these measured offsets is roughly ± 0.04 mag. The offsets for all observers are presented in the last column of Table 4.1.

We also had collaborators who used the PROMPT 0.41m telescopes on Cerro Tololo in Chile to obtain quasi-simultaneous $UBVRI$ time series from the start of the plateau until after the end of the eruption. This allows us to see the specific color variations throughout the decline, the eclipses, and the later dips. (All other observers only took colors once or twice a night, and it is difficult to reconstruct the fast color changes from such data. Only the PROMPT data have both colors and fast time series.) One PROMPT telescope regularly cycled between B, V, R, then I images (all 40 s exposures), while another PROMPT telescope simultaneously took long series of U images (all 80 s exposures). These were calibrated by differential photometry with respect to nearby stars of known magnitude. The average $U-B$ and $B-V$ colors are somewhat more red than measured with other detectors, so we think that there must be significant uncorrected color terms associated with having a nonstandard effective bandpass. Fortunately, such color corrections will be essentially a constant, so the shape of the color curves will be correct. In all, we have 11,543 PROMPT magnitudes in $UBVRI$.

After the end of the first plateau, the nova brightness became faint enough that some of our telescopes had observing cadences (typically one-minute integrations) that produced high statistical noise. We need to have photometric accuracy better than the size of the significant variations ($\sim$0.1 mag), and indeed most of our data have statistical error bars of

<0.03 mag. The solution for the post-plateau time series with too optimistic cadences is to bin the data together. This binning is performed as a weighted average. The result is a substantial reduction in the scatter of the light curve, at a cost of some time resolution. With our better data, we have never seen variations with time scales of faster than ten minutes or so. So our bin sizes are either 1.4, 2.9, 5.8, or 11.5 minutes. With this binning, our 36,776 magnitudes are consolidated into 16,995 magnitudes.

The statistical uncertainty for individual observations is often calculated by the photometry program. In cases where this is not reported, we adopt a typical value of 0.01 mag. The uncertainties for the binned magnitudes come from the usual propagation of errors for a weighted average.

The time associated with each magnitude is halfway between the start and stop time of each image. These have been converted to Julian Dates, and then the heliocentric corrections have been applied. For magnitudes binned in time, we take the average time of all input images.

The orbital phase for each observation is taken from our very well determined ephemeris for the eclipse minima during quiescence. This ephemeris for the Heliocentric Julian Date of the middle of the eclipses in quiescence is

$$HJD = 2451234.5387 + N \times 1.23054695. \tag{4.1}$$

This is based on 45 eclipse times from 2001 to 2009, covering more than 2600 orbits. The curvature in the observed $O-C$ curve is consistent with zero and the sudden period change at the time of the eruption is irrelevant for the ephemeris during the eruption, so this ephemeris is applicable during the eruption.

Figure 4.10 shows the overall V-band light curve for the eruption. We see the fast fall (from days 0-12), a transition time interval (days 12-15), the onset of eclipses (around day 15), the first plateau (days 15-32), the fall after the first plateau (days 32-41), the second plateau (days 41-54), the jittery fall after the second plateau (days 54-67), and the end of

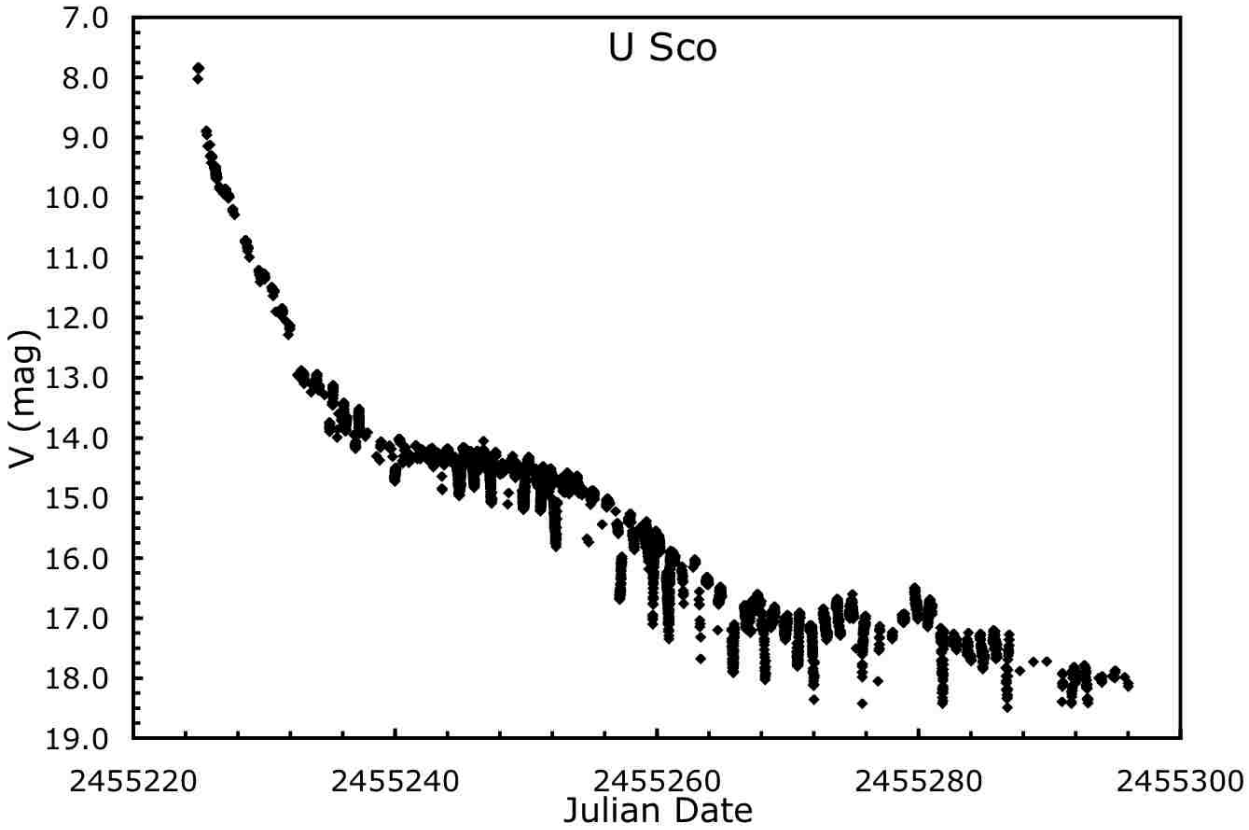

Figure 4.10 U Sco Fast Time Series Light Curve. This light curve is based on 36,776 V-band magnitudes, with complete coverage throughout the entire 67 days of the eruption at a rate of one magnitude every 2.6 minutes. We see the very fast decline, the startup of eclipses when the first plateau begins, and a second late plateau just above the quiescent level.

the eruption with the return to the quiescent level (day 67). The exact boundaries between these phases are uncertain by 1-2 days.

No other nova eruption at the time had ever had anywhere near as good a light curve. Indeed, relatively few nova eruptions have even had full coverage from peak to the return to quiescence (Strope et al. 2010). U Sco not only has *complete* coverage, but also we have magnitudes an average of once every 2.6 minutes throughout the eruption. This was, at the time, completely unprecedented.

We took all 36,776 V-band magnitudes and used them to create an idealized light curve of the 2010 eruption, which can be seen in Figure 4.11. We smoothly extrapolate between points and fill in the eclipses that were missed due to the fact that U Sco was only visible for

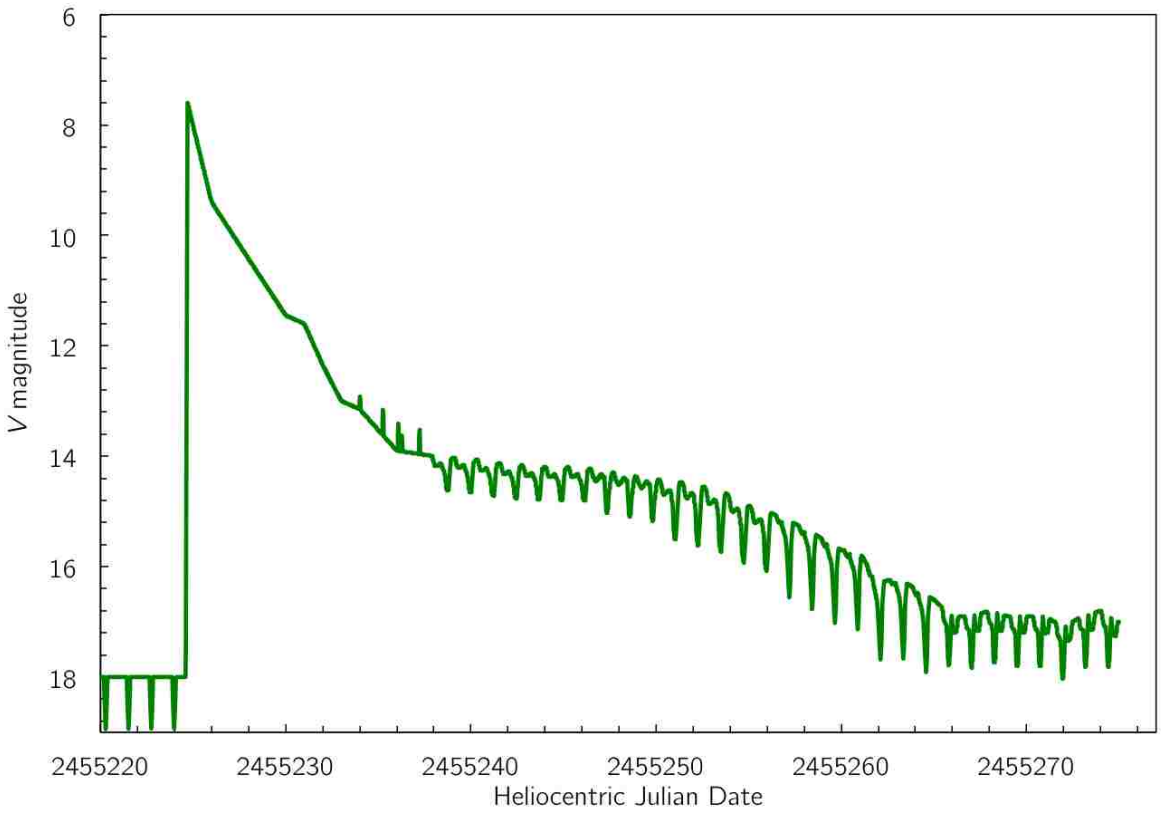

Figure 4.11 U Sco Idealized Light Curve. This idealized V-band light curve of the 2010 eruption of U Sco is created from the 36,776 V-band observations made during the course of the two month eruption. We have smoothed the data and extrapolated between data points. We also filled in the eclipses that were missed due to the short morning visibility of U Sco during much of the eruption. This idealized light curve is useful for easily visualizing the various parts of the light curve such as the initial fast decline and the plateaus.

a few hours from any given location. We also smoothed over some of the late flickering for clarity. We note that some early fast flares were likely missed, again due to short visibility windows, so the only ones present on this idealized curve are the four that were actually observed (Pagnotta et al. 2010).

4.7.1 Detrended and Phased Light Curve

To pull out the light curve for the eclipses and other fast phenomena, we must remove the overall trend visible in Figure 4.10. To do this, we have established a trend line which essentially runs across the upper envelope of the light curve to avoid the eclipses. The trend

line is a multiply-broken line passing through the light curve at phase 0.25, and is presented in Table 4.2. The first column gives the Heliocentic Julian Date for each normal point, the second column gives the time since the start of the eruption (i.e., HJD-2455224.32), the third column gives the V-band magnitude at that time, and the fourth column gives a variety of comments for the associated time. For times between these normal points, the trend line is given by simple linear interpolation.

Magnitudes from this trend line ($V_{\rm trend}$) are then subtracted from the observed magnitudes (V) to get the detrended magnitudes ($V - V_{\rm trend}$). This detrending is important for the timing of eclipses, as an eclipse superposed on a falling light curve will have its time of minimum biased to later time. This detrending is also important as it gives us the ability to superpose phased light curves from successive orbital periods.

The phased and detrended light curve is constructed by plotting $V - V_{trend}$ versus the orbital phase. The eruption can be divided up into intervals during which the light curve is largely stationary. Figures 4.12−4.19 present the detrended and phased light curves for each of these intervals. These figures have identical magnitude scales for easy comparison, and they doubly display the data (each point is given twice, once with its phase and once with 1.0 plus the phase) to allow the eclipse to be readily visible around phase 1.0 without break.

For days 0−9 (Figure 4.12), the steeply falling light curve is flattened out, so we see a nearly constant detrended light curve. Some of the scatter could be due to imperfect detrending. But some of the variations, like the short rise and falls seen around phases 0.02 and 0.33 (duplicated at phases 1.02 and 1.33), are significant and intrinsic to the nova. The amplitudes are about 0.1 mag with durations of 0.04−0.06 in phase (1.2−2.1 hours), with these two events from days 8−9 (with peaks at HJD 2455232.979 and 2455234.013).

For days 9−15 (Figure 4.13), the light curve is in a transition interval, as the fast decline slows to a stop at the start of the first plateau phase. The light curve displays large amplitude short flares far above the trend line. Three of these flares have visible peaks (at HJD

Table 4.2. Trend Line for Eruption Light Curve

HJD	$T - T_0$ (days)	$V_{\rm trend}$ (mag)	Comments
2455224.32	0.00	18.00	Eruption start (T_0)
2455224.69	0.37	7.60	Peak
2455226	1.68	9.40	$t_2 = 1.7$ days
2455228	3.68	10.43	$t_3 = 3.6$ days
2455230	5.68	11.45	...
2455231	6.68	11.70	...
2455232	7.68	12.35	...
2455233	8.68	13.00	Start of early flares
2455234	9.68	13.15	Short 0.5 mag flares
2455236	11.68	13.90	Short 0.5 mag flares
2455238	13.68	14.00	Onset of plateau, X-rays, eclipses
2455240	15.68	14.05	...
2455242	17.68	14.15	...
2455244	19.68	14.20	...
2455246	21.68	14.20	...
2455248	23.68	14.30	Onset of flickering
2455250	25.68	14.40	Onset of secondary eclipses
2455252	27.68	14.50	...
2455254	29.68	14.70	...
2455255	30.68	14.90	...
2455256	31.68	15.00	End of plateau, sec. eclipses
2455258	33.68	15.30	...
2455259	34.68	15.50	...
2455260	35.68	15.70	...
2455261	36.68	15.75	...
2455262	37.68	16.00	...
2455263	38.68	16.10	...
2455264	39.68	16.40	...
2455265	40.68	16.60	...
2455266	41.68	16.90	Onset of optical dips, plateau
2455267	42.68	16.80	...
2455268	43.68	16.70	...
2455269	44.68	16.90	...
2455271	46.68	16.90	...
2455272	47.68	17.20	...
2455273	48.68	16.80	...
2455274	49.68	16.70	...
2455275	50.68	16.80	...
2455276	51.68	16.90	...
2455278	53.68	16.90	End of second plateau
2455279	54.68	17.00	...
2455280	55.68	16.60	...
2455281	56.68	16.80	...
2455283	58.68	17.45	...
2455285	60.68	17.30	End of optical dips
2455287	62.68	17.20	...
2455288	63.68	18.10	...
2455289	64.68	17.60	...
2455291	66.68	18.00	End of eruption
2455301	76.68	18.00	...

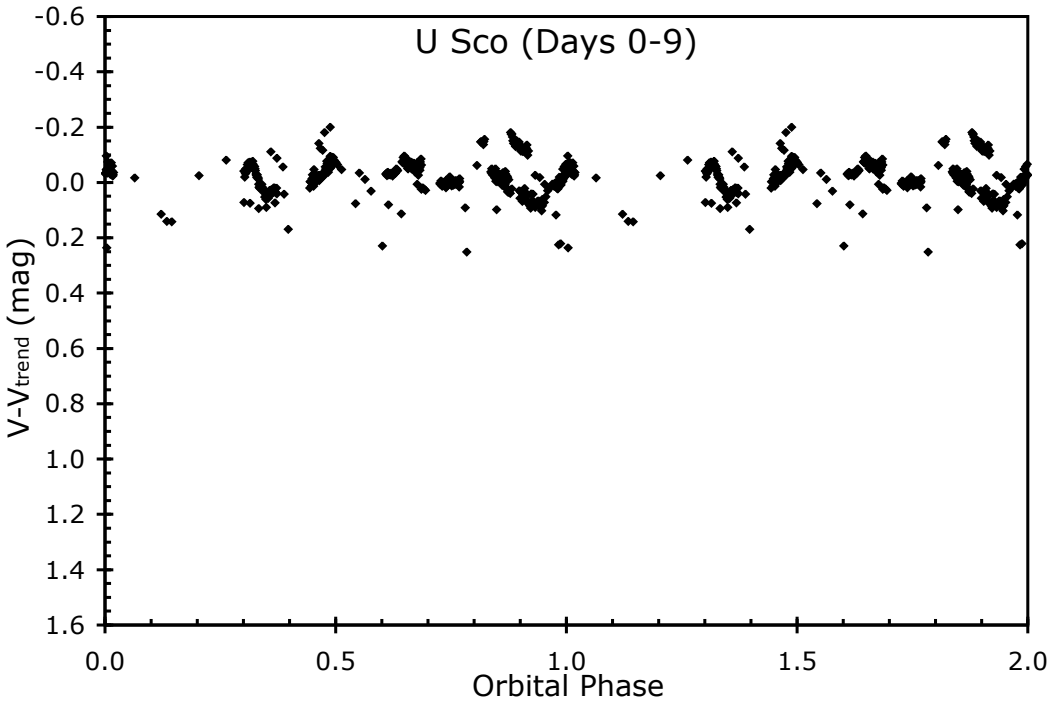

Figure 4.12 Detrended Phased Light Curve for Days 0−9. Figures 4.12−4.19 show the $V - V_{trend}$ magnitudes plotted (with a doubling of phase) for a series of time intervals throughout the eruption. For this figure (covering days 0−9), the initial fast decline is relatively smooth, so the detrended light curve appears flat with no significant variations with orbital phase.

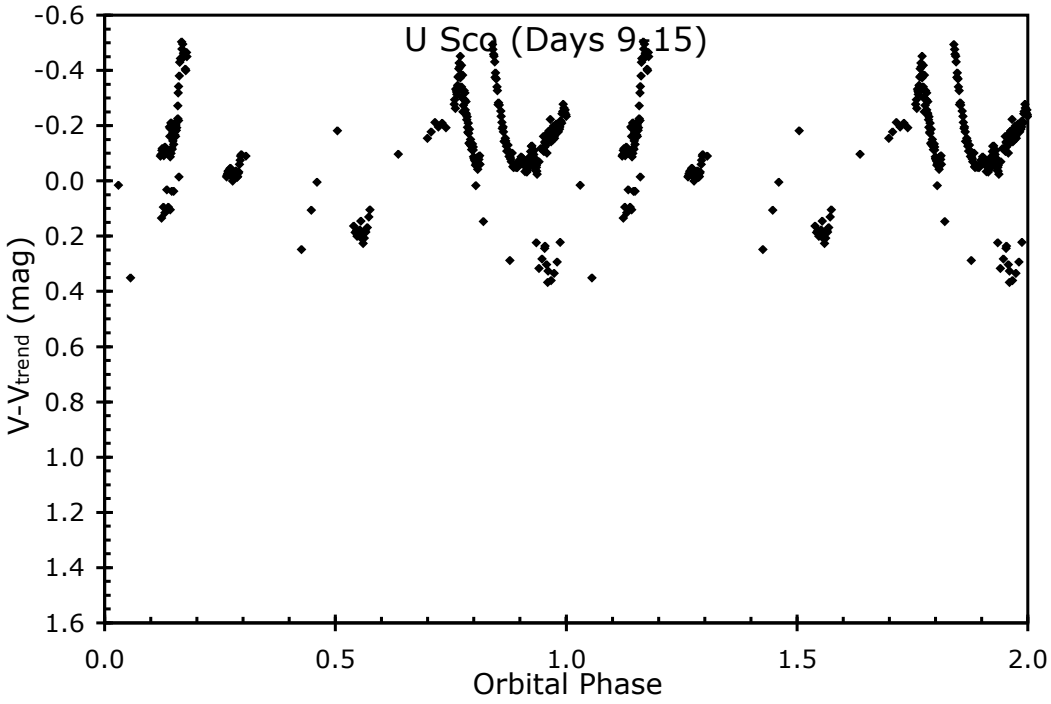

Figure 4.13 Days 9−15. We see random flares with amplitudes of half a magnitude and durations of half an hour. These flares can only come from small regions of the shell which suddenly brighten with a luminosity rivaling that of the entire shell. The cause of these flares is currently unknown.

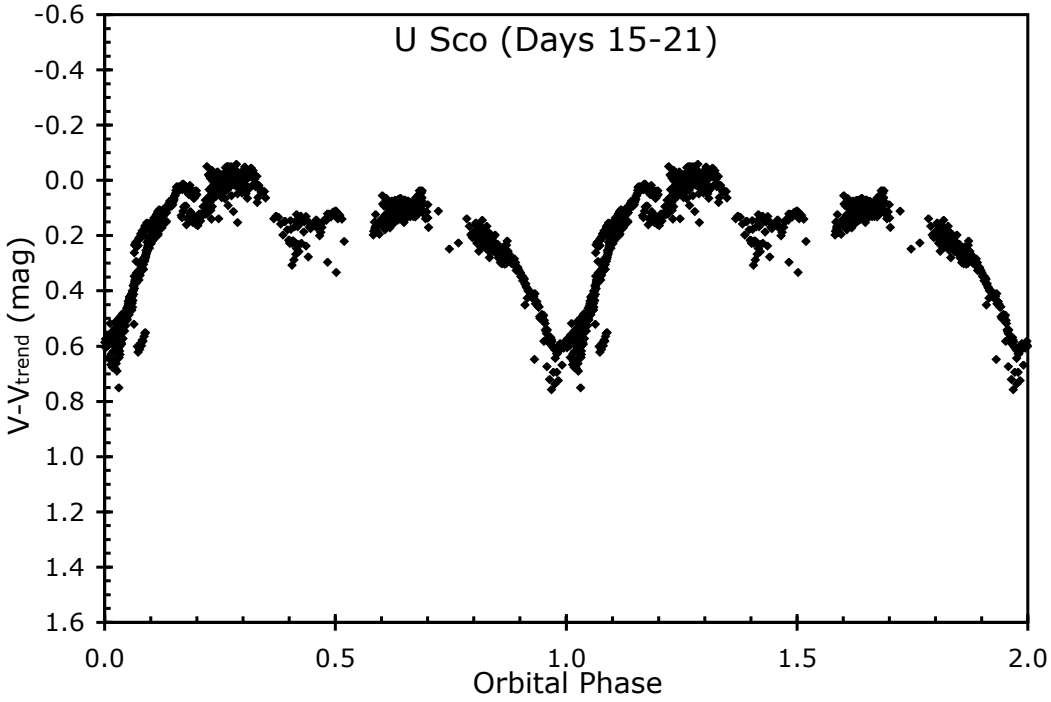

Figure 4.14 Days 15−21. The eclipses suddenly appear sometime between days 12.0 and 15.6. Coincident with this is the sudden turn-on of the supersoft X-ray source, and the start of the plateau. All three phenomena are explained by the outer shell thinning enough so that the inner binary system is visible. The soft X-ray photons from near the surface of the WD can escape, the reprocessing of some of the X-ray flux provides the extra light that causes the plateau in the overall light curve, and the eclipses can be seen.

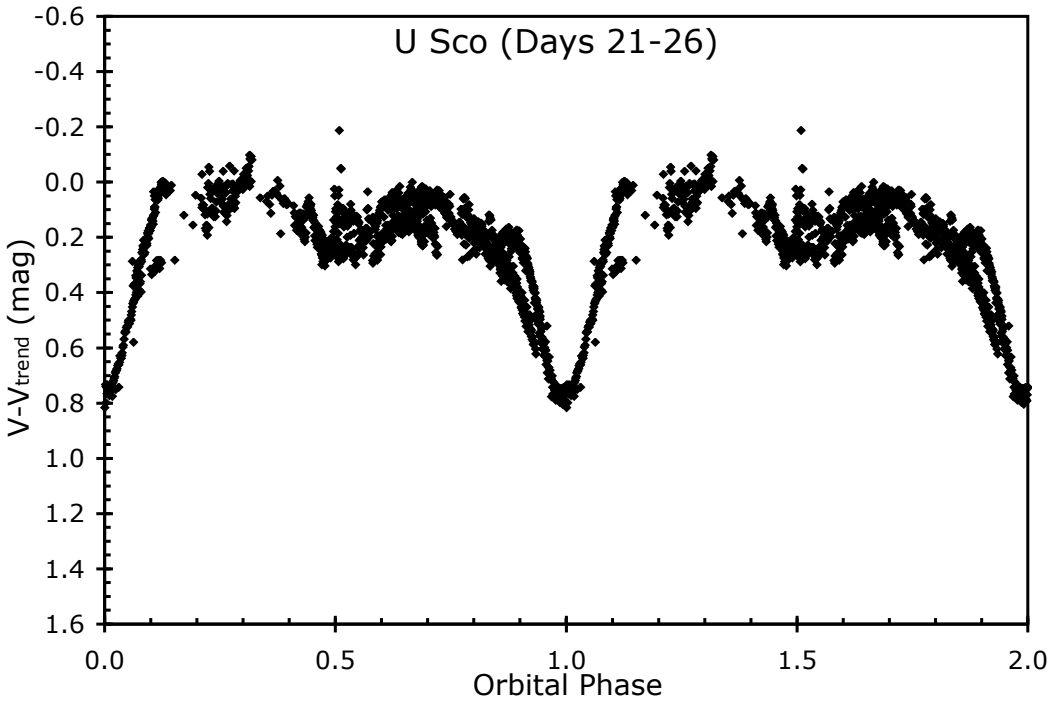

Figure 4.15 Days 21−26. The eclipses deepen and and become slightly shorter in duration in comparison with the previous week. From days 15−26, the light curve shows a curious asymmetry between the elongations at phase 0.25 and 0.75. This asymmetry could be caused by the illumination of the inner side of the accretion stream ahead of the companion star. Eclipse mapping shows that all of the optical light is configured as an apparently uniform sphere with radius $4.1R_{\odot}$, which can only be the emission from the usual nova wind being driven off the WD by the continuing nuclear burning near its surface.

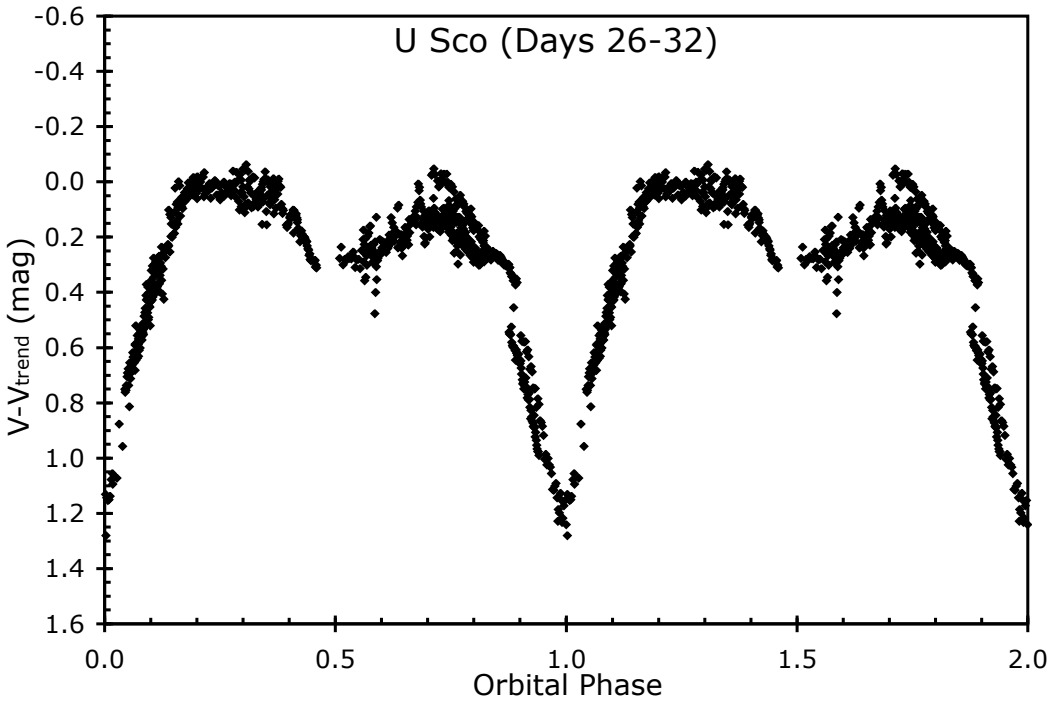

Figure 4.16 Days 26−32. The eclipses become even deeper and broader, and the secondary eclipse is apparent. The asymmetry between phases 0.25 and 0.75 has become less prominent. Eclipse mapping shows that the configuration of the optical light source has changed completely, with there now being no light coming from away from the orbital plane (so the wind is no longer contributing much optical light), but rather the optical light is coming from a large optical disk with radius roughly $3.4 R_{\odot}$ and that is faint in the center (Schaefer et al. 2011a). This shows that the accretion disk has been re-established but has not yet had time to work material into its central region.

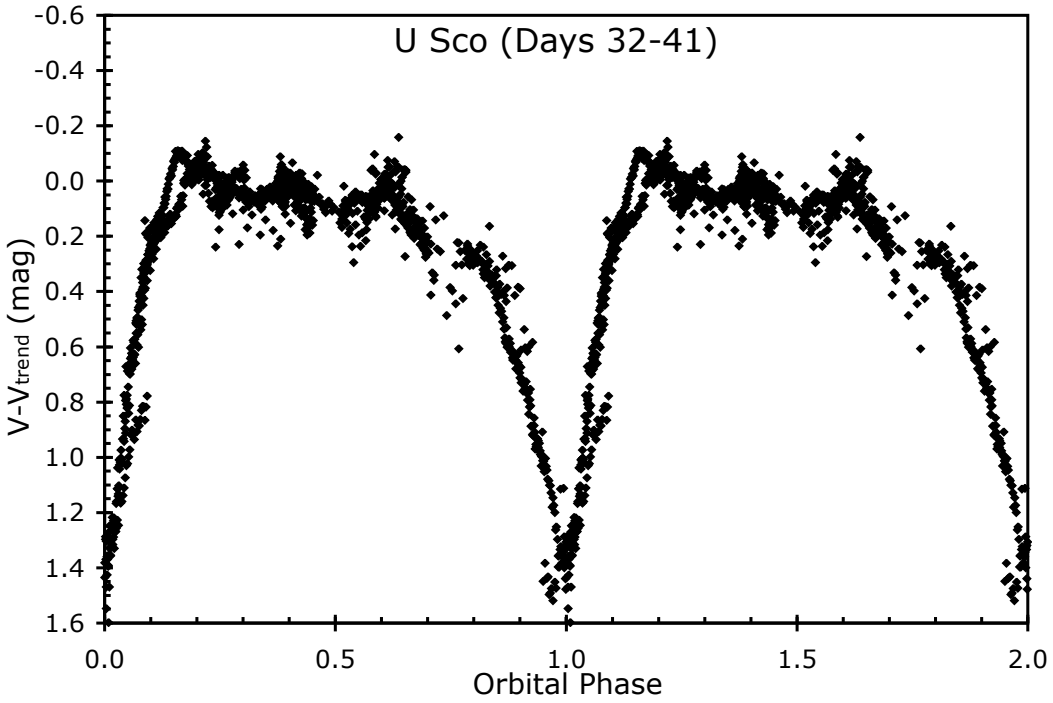

Figure 4.17 Days 32−41. The eclipses get very deep, with the 1.4 mag amplitude implying that the companion star (2.66 AU in radius) is covering up 75% of the system's light. Eclipse mapping shows that the central light source is consistent with a centrally-bright disk with radius around $2.2R_{\odot}$, which is similar to the quiescent state (Schaefer et al. 2011a). However, some of the egresses are a bit wider than in quiescence, indicating some residual material outside the stabilizing disk. The system has suddenly stopped showing the secondary eclipse, despite this being so prominent from days 26−32. The light curve shows two asymmetries, a steady fading by a quarter of a magnitude from phase 0.25 to 0.75, and a slow ingress relative to the egress. Both asymmetries can be explained by material in the accretion stream and near the usual hot spot position providing occultation of the inner light source as well as a bright inner edge best visible just after eclipse.

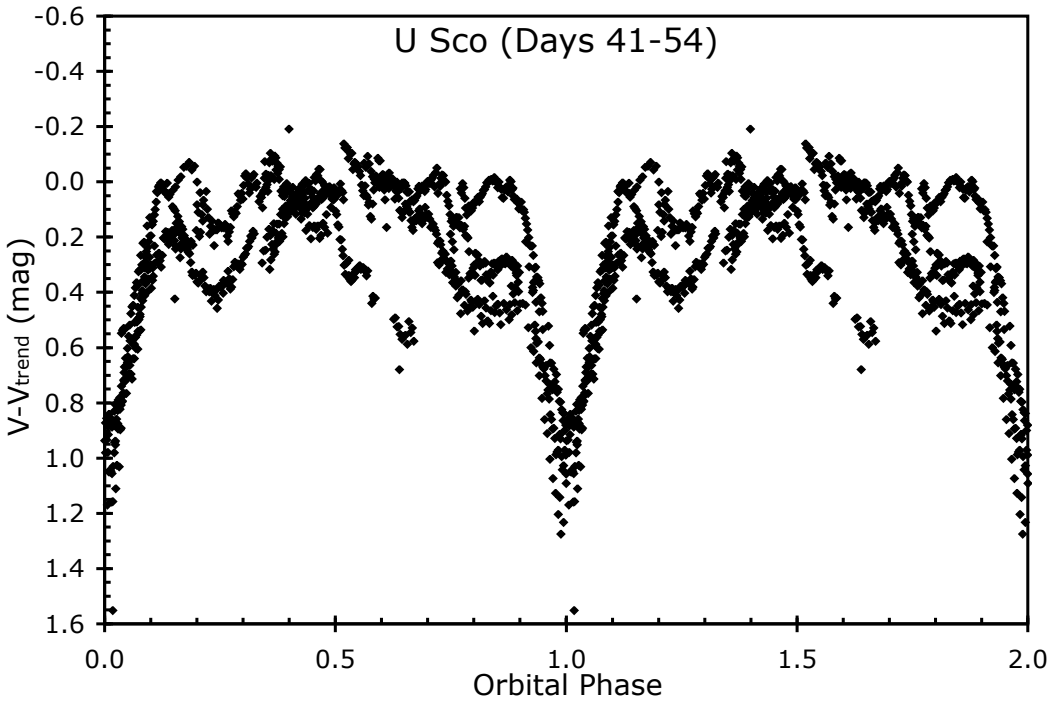

Figure 4.18 Days 41−54. The stunning change during this epoch is that the out-of-eclipse intervals show deep dips that vary greatly from orbit to orbit. These dips get as deep as 0.6 mag with typical durations of 0.2 in phase. This phenomenon has no precedent in novae at any time, and here we propose that these dips are analogous to the dips in low mass X-ray binaries. The secondary eclipse and the light curve asymmetries have disappeared, although this could well be confused by the dips. The primary eclipses have a depth of 1.0 mag, while the duration has shortened greatly to 0.20 in phase. In contrast to the previous days, the ingress is substantially faster than the egress.

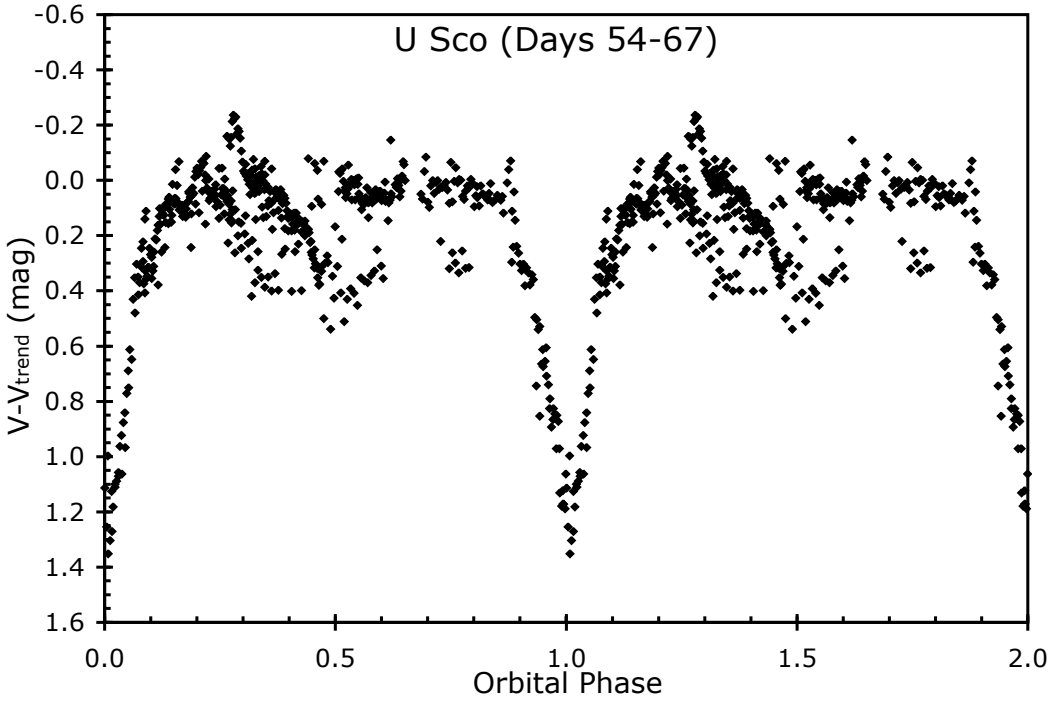

Figure 4.19 Days 54−67. This light curve has similar properties to the one during the interval from days 41−54, but we have kept them separate in two figures so that some of the runs from individual nights can be distinguished. The eclipse looks slightly deeper (1.1 mag), somewhat longer in duration (0.27 in phase), and nearly symmetric in shape. The key feature of this light curve is the continued presence of deep and broad dips that occur apparently randomly in phase.

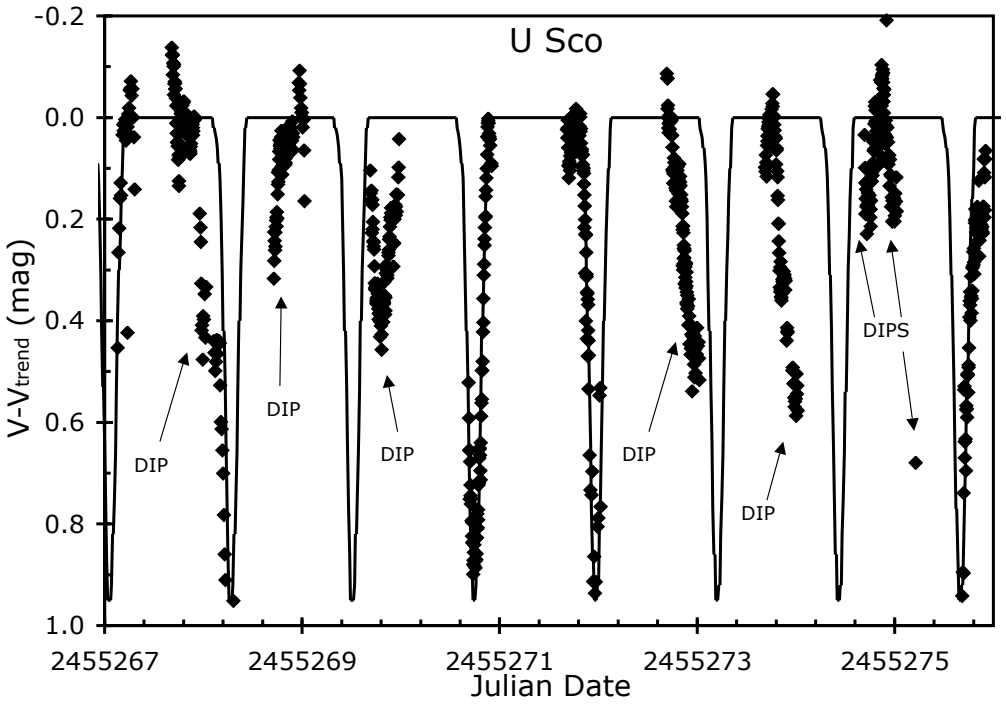

Figure 4.20 Optical Dips. From days 41−61, the detrended light curve shows deep dips at apparently random phases, which indicates that they cannot be associated with the regular primary eclipses caused by the secondary star. This plot shows the light curve template (Figure 4.11) plus all our observed magnitudes from JD 2455267.0 to 2455276.0 (roughly days 43−52). The optical light source is fairly small and centered on the WD (as demonstrated by the depth and timing of the primary eclipses), so the dips can only be eclipses caused by occulters spread around the WD. U Sco has an inclination of roughly 80−84°, so our line of sight to the bright central source is just skimming over the top of the disk, such that a small increase in the height of the disk rim will dim the entire system for a small range of phases. Raised rims are expected during the re-establishment of the disk, as the accretion stream moves around. This optical dipping is unique among novae, although low mass X-ray binary systems with neutron stars are often seen to have X-ray dips.

2455235.253, 2455236.080, and 2455237.225), all with a peak of 0.5 mag above the trend line, and all with rise or fall times of 0.02−0.04 in phase (0.6−1.2 hours). The peak times show no correlation with orbital phase. The cause of these early flares is currently unknown. At the time of the flares, the nova shell is optically thick to the central binary system, as shown by the lack of eclipses or supersoft X-ray flux. On day 10, for an expansion velocity of 5,000 km s^{-1}, the shell has a radius of 4 light-hours. With this, the flares (which must be smaller than, and likely much smaller than, 0.6−1.2 light hours in size) must involve a small fraction of the shell. So the picture we get is a small region in the shell producing roughly the same luminosity as the rest of the shell, but only for an hour or so.

For days 15−21 (Figure 4.14), the light curve shows the first part of the plateau phase. We see a full eclipse plus asymmetric structure outside of the eclipse. On day 12.0 there is certainly no eclipse, on day 14.5 we have several isolated magnitudes that might be from a low amplitude eclipse, and on day 15.6 there is certainly a well formed eclipse. So eclipses reappear sometime in the 3-orbit interval from days 12.0−15.6. The amplitude is 0.6 mag, the total duration is around 0.29 in phase (8.7 hours), and the shape varies somewhat over the interval. The sudden appearance of eclipses shows us that the nova shell and wind has rapidly become optically thin (or at least translucent) all the way from the inner binary system out to infinity. The sudden and sharp turn-on of the supersoft X-ray source on days 12−14 (Schlegel et al. 2010) also shows that the optical depth to the binary became small at this time. This same time is when the early fast decline stops and the plateau phase begins, which is caused by the reprocessing of some of the X-ray flux by the accretion disk, providing extra optical light that we observe as the plateau. At phase 0.5 (and phase 1.5 in the figure), we see what looks like a secondary eclipse with an amplitude of 0.20 mag. This light curve has a striking asymmetry in that the brightness level at phase 0.25 is 0.08 mag brighter than at phase 0.75. This requires that some structure in the binary breaks the symmetry of the line between the two stars. The shell, the two stars, and the wind from the WD will all respect this symmetry from orbit to orbit, so the only apparent way to break the

symmetry is with additional material such as the gas coming off the companion star as part of the forming accretion stream. With the accretion stream leading the companion star, the brightness asymmetry could be caused by the hot region around the WD illuminating the inner edge of the accretion stream.

For days 21−26 (Figure 4.15), the light curve shows the core time interval of the first plateau phase, with the supersoft X-ray source shining brightly. The eclipse deepens to 0.80 mag, and the duration might be somewhat shortened (0.25 in phase). The light curve shows apparent variations in shape.

For days 26−32 (Figure 4.16), the light curve covers the last part of the first plateau, during which time the supersoft X-ray source is peaking in luminosity. The eclipse deepens to 1.1 mag, while the total duration increases to something like 0.37 in phase. The secondary eclipse remains prominent. To have a secondary eclipse while the nova is bright, we must have the companion star greatly brighter than normal, and this is likely due to the illumination of the inner edge of the star by the luminosity from near the WD. A secondary eclipse also implies something near the WD doing the eclipsing (since the WD itself is too small to cause an eclipse), so the occulter must be the optically thick inner parts of the wind being driven off the WD by the supersoft X-ray source or a just-forming accretion disk. The brightness at phase 0.75 apparently varies, but at least on occasion is nearly equal to that at phase 0.25.

For days 32−41 (Figure 4.17), the light curve is in a fast decline from the first plateau, covering a time when the supersoft X-ray source is rapidly turning off. The eclipse deepens to 1.4 mag, and the total duration remains nearly the same at 0.36 phase. The eclipse is definitely asymmetric, as the ingress crosses 0.4 mag at phase -0.15 while the egress crosses 0.4 mag at phase +0.08. This asymmetry could be caused by material in the accretion stream which is in front of the companion star. This same material would also be illuminated on its inner side and provide extra light around phase 0.25, causing the obvious asymmetry outside of eclipse. We see that the secondary eclipse (so obvious in previous days) has now vanished.

For days 41−54 (Figure 4.18), the light curve covers the second plateau. We see deep

and broad dips scattered apparently randomly from phase 0.25 to 0.85. These dips are a completely new phenomenon for novae. The bulk of the light is coming from near the WD (as demonstrated by the deep primary eclipse), so the dips can only be eclipses of this source. The variability in time and phase demonstrates that the eclipses are not associated with the secondary star. Eclipses that occur at phases of 0.25, 0.55, 0.65, 0.80, and 0.85 can only come from an accretion disk. The disk was certainly blown away by the initial eruption, so the disk is being re-established as the accretion stream orbits the WD colliding with itself. The inclination of U Sco is $\sim 80-84^{\circ}$ (Hachisu et al. 2000a,b; Thoroughgood et al. 2001), so the line of sight to the WD passes just above the disk; any high spot in the edge of the disk will cause an eclipse of the central source. The chaotic disk edge will have fast-changing collision regions at any azimuth, so the high edges of the disk can produce eclipses that appear and disappear at any orbital phase. We name this new phenomenon optical dips, with U Sco being an optical dipper. This name is taken from an analogous phenomenon seen in low mass X-ray binaries that have an inclination of $\sim 80^{\circ}$ which show X-ray dips and are known as X-ray dippers (Walter et al. 1981, 1982; White & Swank 1982; Frank et al. 1987; Balman 2009). Our explanation for the optical dips has a good precedent from the X-ray dips, and there is no other reasonable explanation for how eclipses can occur at such a wide range of phases.

For days 54−67 (Figure 4.19), the light curve covers the decline from the second plateau until the return to quiescence. We see that the optical dips, which can be seen in an unfolded light curve in Figure 4.20, continue. The phases of the three optical dips covered are 0.40, 0.50, and 0.75, with depths of 0.4 mag. The primary eclipse is deep with amplitude 1.1 mag, fairly symmetric in shape, and has a duration of 0.25 in phase. With this, the U Sco light curve returns to its normal quiescent magnitude and shape, so the eruption is over.

4.8 Spectral Energy Distribution

A primary reason for the comprehensive multi-wavelength coverage of U Sco was to obtain the data needed to create spectral energy distributions (SEDs) for the entire eruption. Using primarily the SMARTS 1.3m, SAA0 0.5m, and Swift observations, we can create daily SEDs, a sampling of which can be seen in Figure 4.21; the full listing of daily flux values (in Jy) can be found in Table 4.3. These SEDs run from UVOT $w2$ (193 nm) to K-band (2200 nm) and cover a large range of the spectrum over which energy is released in the eruption. The vast majority of energy is released in the UV, so the UVOT coverage is crucial for obtaining an accurate SED, although it is likely that it does not go far enough blueward and we could be missing a significant portion of the flux. There is unfortunately no way to obtain that part of the spectrum at this time, but what we do have is reasonable and useful. I have extracted a few serendipitous Wide-field Infrared Survey Explorer (WISE) far-IR observations of U Sco on days 28 and 29 of the eruption (in bands $W1$ and $W2$, at 3.4 μ and 4.6 μ, respectively), however I have chosen not to include them in this set of SEDs, as the contribution to the flux is negligible and the extrapolation to other days is very uncertain.

4.9 Masses

The SEDs described in Section 4.8 are particularly important because they can be used to calculate the total amount of energy radiated during the eruption, $E_{\rm rad}$. To get this quantity, we numerically integrate under the SED curve each day (after subtracting out the quiescent level) to get the luminosity and then sum up all of the luminosities to obtain the total $E_{\rm rad}$. The daily luminosities (with the quiescent level subtracted out) in each band as well as the total for each day can be seen in Table 4.4. For U Sco, $E_{\rm rad} = 6.82 \times 10^{44}$ ergs. Following Shara et al. (2010), we can use this $E_{\rm rad}$ to obtain the total amount of mass ejected, $m_{\rm ej}$, as

$$m_{\rm ej} = 6 \times 10^{-18} E_{\rm rad} \tag{4.2}$$

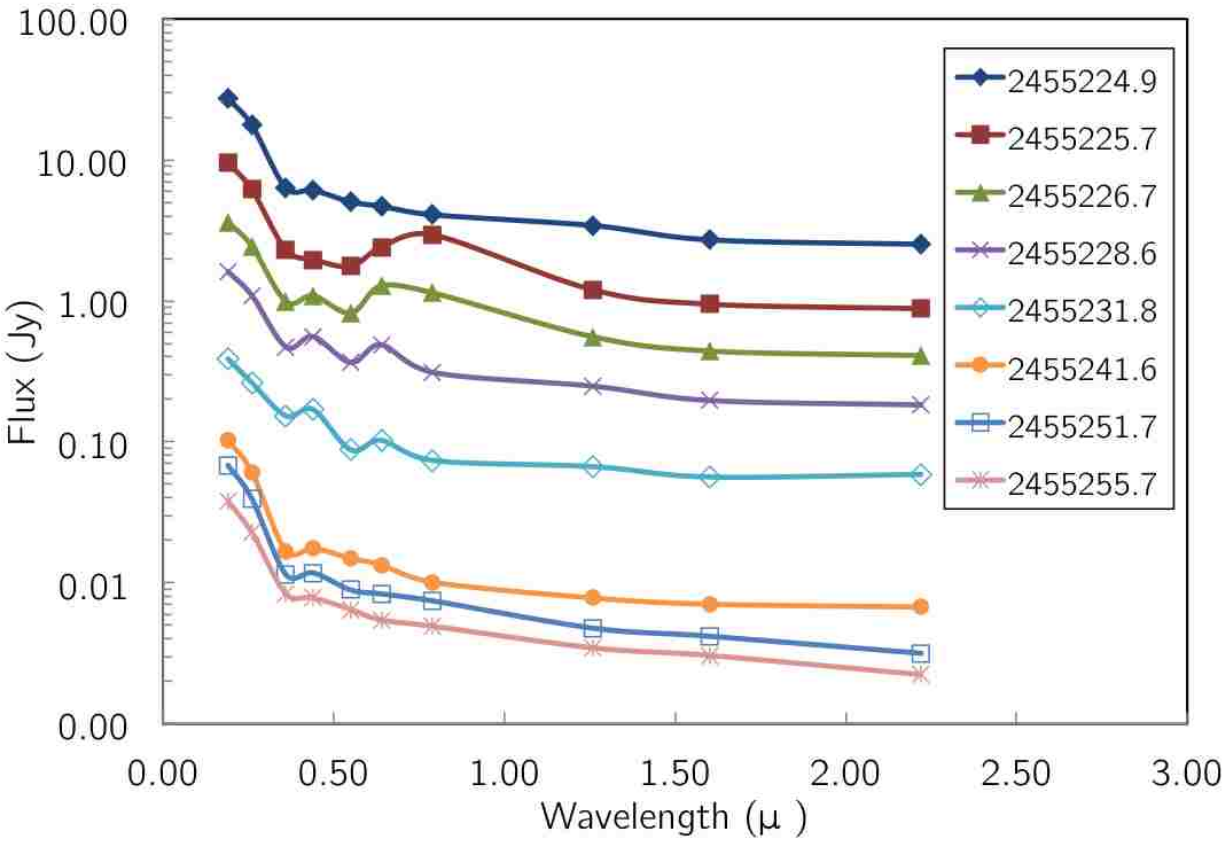

Figure 4.21 Spectral Energy Distributions (SEDs) for selected days during the 2010 eruption of U Sco. The wavelength range extends from UVOT's $w2$ filter (193 nm) to K-band (2200 nm). The majority of the energy is released near the short end of the spectrum, so the UVOT coverage was particularly important.

Table 4.3. Daily U Sco Fluxes (in Jy)

HJD	*Swift w2*	*Swift w1*	*U*	*B*	*V*	*R*	*I*	*J*	*H*	*K*
2455224.9	27.158	17.677	6.347	6.090	5.043	4.683	4.084	3.422	2.713	2.520
2455225.7	9.500	6.184	2.304	1.964	1.764	2.410	2.942	1.197	0.949	0.881
2455226.7	3.620	2.453	0.991	1.088	0.820	1.285	1.141	0.556	0.441	0.410
2455227.6	2.419	1.640	0.684	0.780	0.548	0.793	0.596	0.372	0.295	0.274
2455228.6	1.617	1.096	0.472	0.558	0.366	0.489	0.311	0.248	0.197	0.183
2455229.7	1.000	0.678	0.305	0.388	0.226	0.290	0.190	0.174	0.143	0.129
2455230.7	0.726	0.492	0.248	0.288	0.164	0.191	0.133	0.111	0.093	0.099
2455231.8	0.389	0.264	0.153	0.170	0.088	0.103	0.074	0.067	0.056	0.059
2455232.8	0.227	0.154	0.094	0.133	0.051	0.055	0.045	0.047	0.041	0.043
2455233.6	0.172	0.116	0.058	0.069	0.039	0.041	0.031	0.034	0.029	0.032
2455234.6	0.155	0.105	0.057	0.061	0.035	0.035	0.026	0.024	0.021	0.023
2455235.6	0.086	0.058	0.027	0.028	0.019	0.018	0.015	0.017	0.015	0.017
2455236.8	0.084	0.057	0.022	0.024	0.019	0.017	0.014	0.012	0.011	0.012
2455237.8	0.080	0.058	0.018	0.026	0.019	0.017	0.015	0.011	0.009	0.010
2455238.4	0.075	0.046	0.015	0.017	0.013	0.013	0.011	0.010	0.009	0.009
2455239.6	0.063	0.052	0.018	0.018	0.015	0.014	0.012	0.008	0.008	0.008
2455240.5	0.080	0.054	0.015	0.016	0.013	0.012	0.010	0.009	0.007	0.008
2455241.6	0.103	0.061	0.017	0.018	0.015	0.013	0.010	0.008	0.007	0.007
2455242.5	0.084	0.054	0.016	0.016	0.013	0.012	0.011	0.009	0.007	0.007
2455243.5	0.058	0.044	0.015	0.016	0.013	0.011	0.010	0.007	0.006	0.006
2455244.4	0.061	0.047	0.014	0.015	0.012	0.011	0.010	0.007	0.007	0.006
2455245.6	0.085	0.054	0.013	0.015	0.012	0.011	0.008	0.007	0.007	0.006
2455246.5	0.107	0.067	0.017	0.016	0.013	0.011	0.009	0.007	0.006	0.006
2455247.5	0.094	0.058	0.015	0.015	0.012	0.011	0.009	0.006	0.005	0.005
2455248.6	0.080	0.046	0.014	0.015	0.012	0.010	0.009	0.006	0.005	0.004
2455249.6	0.076	0.045	0.013	0.012	0.010	0.009	0.008	0.005	0.004	0.005
2455250.5	0.089	0.043	0.011	0.011	0.009	0.008	0.007	0.005	0.004	0.005
2455251.7	0.068	0.040	0.011	0.012	0.009	0.008	0.007	0.005	0.004	0.003
2455252.3	0.039	0.028	0.012	0.011	0.009	0.008	0.007	0.005	0.004	0.003
2455253.6	0.036	0.028	0.012	0.011	0.009	0.007	0.007	0.005	0.004	0.004
2455254.8	0.043	0.027	0.010	0.009	0.008	0.006	0.006	0.004	0.004	0.003
2455255.7	0.038	0.023	0.008	0.008	0.006	0.005	0.005	0.003	0.003	0.002
2455256.7	0.028	0.018	0.007	0.007	0.005	0.005	0.004	0.003	0.003	0.002
2455257.3	0.017	0.016	0.006	0.006	0.005	0.004	0.004	0.002	0.002	0.001
2455258.5	0.024	0.014	0.005	0.005	0.004	0.003	0.003	0.002	0.002	0.001
2455259.7	0.015	0.012	0.004	0.004	0.003	0.003	0.002	0.001	0.001	0.002
2455260.5	0.011	0.008	0.003	0.003	0.003	0.002	0.002	0.001	0.001	0.001
2455261.9	0.009	0.007	0.003	0.002	0.002	0.002	0.002	0.001	0.001	0.001
2455262.8	0.010	0.007	0.003	0.003	0.002	0.001	0.001	0.001	0.001	0.001
2455263.7	0.009	0.007	0.002	0.002	0.002	0.001	0.001	0.001	0.001	0.001
2455264.6	0.006	0.004	0.002	0.002	0.001	0.001	0.001	0.001	0.001	0.001
2455265.6	0.004	0.003	0.001	0.001	0.001	0.001	0.001	0.000	0.000	0.000
2455266.6	0.003	0.002	0.001	0.001	0.001	0.000	0.000	0.000	0.000	0.000
2455267.6	0.004	0.003	0.002	0.001	0.001	0.001	0.001	0.000	0.000	0.000
2455268.6	0.004	0.003	0.001	0.001	0.001	0.001	0.001	0.000	0.000	0.000
2455269.6	0.004	0.002	0.001	0.001	0.000	0.000	0.000	0.000	0.000	0.000
2455270.4	0.005	0.003	0.001	0.001	0.000	0.000	0.000	0.000	0.000	0.000
2455271.7	0.007	0.004	0.001	0.001	0.001	0.000	0.000	0.000	0.000	0.000
2455272.8	0.003	0.002	0.001	0.001	0.001	0.001	0.001	0.000	0.000	0.000
2455273.8	0.005	0.003	0.001	0.001	0.001	0.001	0.000	0.000	0.000	0.000
2455274.9	0.004	0.003	0.002	0.001	0.001	0.001	0.001	0.000	0.000	0.000
2455275.6	0.004	0.003	0.001	0.001	0.001	0.000	0.000	0.000	0.000	0.000
2455276.5	0.004	0.003	0.001	0.001	0.001	0.000	0.000	0.000	0.000	0.000
2455277.3	0.004	0.004	0.001	0.001	0.001	0.000	0.000	0.000	0.000	0.000
2455278.5	0.003	0.003	0.001	0.001	0.001	0.000	0.000	0.000	0.000	0.000
2455279.7	0.003	0.002	0.001	0.001	0.001	0.001	0.001	0.000	0.000	0.000
2455280.7	0.003	0.002	0.001	0.001	0.001	0.001	0.001	0.000	0.000	0.000
2455281.7	0.002	0.002	0.001	0.001	0.001	0.000	0.000	0.000	0.000	0.000
2455282.8	0.002	0.001	0.001	0.000	0.000	0.000	0.000	0.000	0.000	0.000
2455283.7	0.002	0.001	0.001	0.000	0.000	0.000	0.000	0.000	0.000	0.000
2455284.7	0.002	0.001	0.001	0.000	0.000	0.000	0.000	0.000	0.000	0.000
2455285.7	0.001	0.001	0.001	0.000	0.000	0.000	0.000	0.000	0.000	0.000
2455286.6	0.001	0.001	0.000	0.000	0.000	0.000	0.000	0.000	0.000	0.000
2455287.5	0.001	0.001	0.000	0.000	0.000	0.000	0.000	0.000	0.000	0.000
2455288.7	0.002	0.002	0.000	0.000	0.000	0.000	0.000	0.000	0.000	0.000
2455289.8	0.002	0.002	0.000	0.000	0.000	0.000	0.000	0.000	0.000	0.000
2455290.7	0.002	0.001	0.000	0.000	0.000	0.000	0.000	0.000	0.000	0.000
2455291.7	0.002	0.001	0.000	0.000	0.000	0.000	0.000	0.000	0.000	0.000
2455292.7	0.001	0.001	0.000	0.000	0.000	0.000	0.000	0.000	0.000	0.000
2455293.7	0.002	0.001	0.000	0.000	0.000	0.000	0.000	0.000	0.000	0.000

where $m_{\rm ej}$ is measured in gm and $E_{\rm rad}$ in erg. With this, we find that the total mass ejected during the 2010 eruption is $m_{\rm ej} = 4.09 \times 10^{27}$ gm $= 2.05 \times 10^{-6} M_{\odot}$. It is difficult to place error bars on this measurement, as the uncertainties are not well defined, but we can make a good estimate. The majority of the radiated energy comes out right at the peak of the eruption in the UV regime. *Swift* was not observing at that time, so the UVOT $w1$ and $w2$ values just after peak are extrapolated from the V-band measurement and model predictions. To estimate the error on the $m_{\rm ej}$ measurement, we vary the first extrapolated $w2$ value by one standard deviation of the $<V - w2>$ values for times at which both were measured. This gives 1σ error bars of $+0.26 \times 10^{-6} M_{\odot}$ and $-0.18 \times 10^{-6} M_{\odot}$. We thus conclude that $m_{\rm ej} = 2.05^{+0.26}_{-0.18} \times 10^{-6} M_{\odot}$. This is consistent with the (highly-uncertain) measurements from previous eruptions, such as $m_{\rm ej} \sim 10^{-7} M_{\odot}$ from Anupama & Dewangan (2000).

This is crucial for determining whether or not U Sco and the other similar RNe can become a Type Ia supernovae. For the WD to reach the Chandrasekhar limit and explode, it must have a net mass gain over its lifetime. We can compare the $m_{\rm ej}$ measurement with the total amount of mass accreted during the time preceding the eruption, $m_{\rm acc}$, to determine the overall mass change of the WD. Although in principle it is straightforward to measure the accreted mass by considering the B-band flux, in reality there are a number of uncertainties. The following values have been proposed for the yearly accretion rate of U Sco, all in units of $M_{\odot}$: $< 0.3 \times 10^{-6}$ (Shen & Bildsten 2007), 0.1×10^{-6} (Duschl et al. 1990), 0.8×10^{-6} (Hachisu et al. 2000a), 1.1×10^{-6} (Starrfield et al. 1988), and 0.1×10^{-6} (Kato 1990). $\dot{M}$ is therefore likely in the range of $0.1 - 0.3 \times 10^{-6} M_{\odot}$ yr^{-1}. For an average recurrence time of 10 years, this means that $m_{\rm acc}$ is therefore in the range $1 - 3 \times 10^{-6} M_{\odot}$. Unfortunately there is too much uncertainty in this value to definitively state whether or not the U Sco WD is gaining mass —it could go either way.

Table 4.4. Daily U Sco Luminosities

HJD	*Swift w2*	*Swift w1*	*U*	*B*	*V*	*R*	*I*	*J*	*H*	*K*	$L_{\rm total}$
2455224.9	2.96E+39	1.13E+39	2.58E+38	1.51E+38	9.24E+37	6.67E+37	8.10E+37	5.66E+37	2.40E+37	2.15E+37	4.84E+39
2455225.7	1.04E+39	3.97E+38	9.36E+37	4.86E+37	3.23E+37	3.44E+37	5.84E+37	1.98E+37	8.40E+36	7.53E+36	1.74E+39
2455226.7	3.95E+38	1.57E+38	4.02E+37	2.69E+37	1.50E+37	1.83E+37	2.26E+37	9.20E+36	3.91E+36	3.50E+36	6.92E+38
2455227.6	2.64E+38	1.05E+38	2.78E+37	1.93E+37	1.00E+37	1.13E+37	1.18E+37	6.15E+36	2.61E+36	2.34E+36	4.60E+38
2455228.6	1.76E+38	7.03E+37	1.92E+37	1.38E+37	6.71E+36	6.97E+36	6.18E+36	4.11E+36	1.74E+36	1.56E+36	3.07E+38
2455229.7	1.09E+38	4.35E+37	1.24E+37	9.62E+36	4.15E+36	4.14E+36	3.78E+36	2.88E+36	1.27E+36	1.10E+36	1.92E+38
2455230.7	7.91E+37	3.15E+37	1.01E+37	7.14E+36	3.01E+36	2.73E+36	2.65E+36	1.84E+36	8.21E+35	8.42E+35	1.40E+38
2455231.8	4.24E+37	1.69E+37	6.21E+36	4.20E+36	1.61E+36	1.46E+36	1.47E+36	1.10E+36	5.00E+35	5.02E+35	7.64E+37
2455232.8	2.47E+37	9.86E+36	3.83E+36	3.29E+36	9.35E+35	7.87E+35	8.97E+35	7.83E+35	3.60E+35	3.68E+35	4.58E+37
2455233.6	1.87E+37	7.47E+36	2.36E+36	1.71E+36	7.07E+35	5.88E+35	6.14E+35	5.54E+35	2.59E+35	2.69E+35	3.32E+37
2455234.6	1.69E+37	6.75E+36	2.31E+36	1.51E+36	6.39E+35	5.03E+35	5.24E+35	3.92E+35	1.86E+35	1.97E+35	3.00E+37
2455235.6	9.35E+36	3.73E+36	1.08E+36	6.82E+35	3.49E+35	2.61E+35	3.04E+35	2.77E+35	1.33E+35	1.44E+35	1.63E+37
2455236.8	9.13E+36	3.64E+36	8.99E+35	6.05E+35	3.41E+35	2.47E+35	2.87E+35	1.94E+35	9.50E+34	1.05E+35	1.55E+37
2455237.8	8.68E+36	3.74E+36	7.48E+35	6.40E+35	3.55E+35	2.42E+35	2.92E+35	1.84E+35	8.38E+34	8.80E+34	1.51E+37
2455238.4	8.15E+36	2.94E+36	6.22E+35	4.22E+35	2.43E+35	1.87E+35	2.19E+35	1.59E+35	7.53E+34	7.95E+34	1.31E+37
2455239.6	6.82E+36	3.34E+36	7.26E+35	4.52E+35	2.71E+35	1.97E+35	2.37E+35	1.38E+35	6.76E+34	7.18E+34	1.23E+37
2455240.5	8.68E+36	3.45E+36	6.04E+35	4.03E+35	2.41E+35	1.67E+35	1.97E+35	1.46E+35	6.50E+34	6.43E+34	1.40E+37
2455241.6	1.12E+37	3.93E+36	6.82E+35	4.35E+35	2.74E+35	1.91E+35	2.00E+35	1.29E+35	6.25E+34	5.75E+34	1.72E+37
2455242.5	9.11E+36	3.44E+36	6.31E+35	3.98E+35	2.43E+35	1.70E+35	2.26E+35	1.42E+35	6.63E+34	6.14E+34	1.45E+37
2455243.5	6.32E+36	2.84E+36	6.09E+35	3.98E+35	2.33E+35	1.60E+35	1.97E+35	1.20E+35	5.74E+34	5.01E+34	1.10E+37
2455244.4	6.69E+36	2.99E+36	5.88E+35	3.71E+35	2.23E+35	1.55E+35	1.93E+35	1.19E+35	5.97E+34	5.21E+34	1.14E+37
2455245.6	9.25E+36	3.45E+36	5.15E+35	3.65E+35	2.21E+35	1.51E+35	1.68E+35	1.18E+35	6.21E+34	5.41E+34	1.44E+37
2455246.5	1.17E+37	4.27E+36	6.73E+35	4.03E+35	2.33E+35	1.63E+35	1.84E+35	1.10E+35	5.50E+34	4.79E+34	1.79E+37
2455247.5	1.03E+37	3.71E+36	5.96E+35	3.72E+35	2.19E+35	1.55E+35	1.79E+35	1.04E+35	4.87E+34	4.23E+34	1.57E+37
2455248.6	8.75E+36	2.95E+36	5.67E+35	3.72E+35	2.24E+35	1.43E+35	1.77E+35	9.75E+34	4.30E+34	3.74E+34	1.34E+37
2455249.6	8.25E+36	2.85E+36	5.39E+35	2.98E+35	1.92E+35	1.30E+35	1.50E+35	8.81E+34	3.95E+34	4.03E+34	1.26E+37
2455250.5	9.75E+36	2.76E+36	4.63E+35	2.71E+35	1.62E+35	1.11E+35	1.37E+35	7.95E+34	3.62E+34	4.34E+34	1.38E+37
2455251.7	7.45E+36	2.54E+36	4.66E+35	2.92E+35	1.63E+35	1.19E+35	1.48E+35	7.89E+34	3.70E+34	2.70E+34	1.13E+37
2455252.3	4.27E+36	1.82E+36	4.69E+35	2.84E+35	1.64E+35	1.12E+35	1.39E+35	7.81E+34	3.79E+34	2.92E+34	7.40E+36
2455253.6	3.96E+36	1.80E+36	4.72E+35	2.76E+35	1.66E+35	1.06E+35	1.31E+35	7.72E+34	3.87E+34	3.15E+34	7.06E+36
2455254.8	4.63E+36	1.72E+36	4.01E+35	2.32E+35	1.40E+35	9.08E+34	1.13E+35	6.66E+34	3.24E+34	2.46E+34	7.45E+36
2455255.7	4.13E+36	1.46E+36	3.41E+35	1.94E+35	1.18E+35	7.76E+34	9.77E+34	5.72E+34	2.71E+34	1.91E+34	6.52E+36
2455256.7	3.02E+36	1.15E+36	2.89E+35	1.63E+35	9.99E+34	6.63E+34	8.41E+34	4.90E+34	2.25E+34	1.47E+34	4.97E+36
2455257.3	1.88E+36	1.02E+36	2.48E+35	1.39E+35	8.51E+34	5.63E+34	7.04E+34	4.03E+34	1.87E+34	1.18E+34	3.57E+36
2455258.5	2.58E+36	8.94E+35	2.12E+35	1.19E+35	7.23E+34	4.76E+34	5.88E+34	3.28E+34	1.54E+34	9.40E+33	4.04E+36
2455259.7	1.62E+36	7.43E+35	1.77E+35	9.76E+34	5.96E+34	3.72E+34	4.57E+34	2.41E+34	1.06E+34	1.30E+34	2.83E+36
2455260.5	1.16E+36	5.00E+35	1.40E+35	7.63E+34	4.63E+34	3.01E+34	3.79E+34	2.09E+34	9.27E+33	9.93E+33	2.03E+36
2455261.9	1.00E+36	4.23E+35	1.10E+35	5.92E+34	3.56E+34	2.42E+34	3.13E+34	1.80E+34	8.10E+33	7.44E+33	1.72E+36
2455262.8	1.04E+36	4.41E+35	1.15E+35	6.21E+34	3.73E+34	2.11E+34	2.70E+34	1.79E+34	7.04E+33	7.83E+33	1.78E+36
2455263.7	1.03E+36	4.36E+35	9.55E+34	4.93E+34	3.04E+34	1.83E+34	2.35E+34	1.39E+34	6.08E+33	6.23E+33	1.71E+36
2455264.6	6.53E+35	2.54E+35	7.92E+34	3.87E+34	2.46E+34	1.58E+34	2.04E+34	1.05E+34	5.21E+33	4.87E+33	1.11E+36
2455265.6	4.79E+35	1.72E+35	5.51E+34	2.62E+34	1.59E+34	1.03E+34	1.36E+34	6.69E+33	2.97E+33	2.86E+33	7.85E+35
2455266.6	3.14E+35	1.40E+35	3.73E+34	1.70E+34	9.55E+33	6.14E+33	8.46E+33	3.62E+33	1.31E+33	1.37E+33	5.39E+35
2455267.6	4.02E+35	1.66E+35	6.25E+34	2.98E+34	1.86E+34	1.14E+34	1.47E+34	6.35E+33	3.11E+33	3.48E+33	7.18E+35
2455268.6	4.48E+35	1.65E+35	5.18E+34	2.65E+34	1.48E+34	8.59E+33	1.02E+34	5.34E+33	1.92E+33	2.59E+33	7.35E+35
2455269.6	4.22E+35	1.46E+35	3.10E+34	1.26E+34	7.30E+33	4.78E+33	6.08E+33	4.53E+33	1.74E+33	8.45E+32	6.37E+35
2455270.4	5.27E+35	1.81E+35	3.38E+34	1.47E+34	8.31E+33	5.26E+33	6.72E+33	3.76E+33	1.56E+33	1.08E+33	7.83E+35
2455271.7	7.37E+35	2.34E+35	3.68E+34	1.71E+34	9.39E+33	5.76E+33	7.39E+33	3.04E+33	1.40E+33	1.33E+33	1.05E+36
2455272.8	3.60E+35	1.44E+35	4.47E+34	1.93E+34	1.22E+34	7.69E+33	1.01E+34	4.14E+33	1.98E+33	1.99E+33	6.06E+35
2455273.8	4.94E+35	2.14E+35	4.52E+34	2.24E+34	1.24E+34	7.33E+33	9.05E+33	2.84E+33	1.27E+33	2.04E+33	8.11E+35
2455274.9	3.86E+35	2.03E+35	6.30E+34	3.18E+34	1.88E+34	1.13E+34	1.35E+34	5.47E+33	3.11E+33	3.52E+33	7.40E+35
2455275.6	3.84E+35	1.93E+35	3.93E+34	1.89E+34	1.03E+34	6.23E+33	8.91E+33	3.93E+33	1.49E+33	1.54E+33	6.67E+35
2455276.5	4.03E+35	2.20E+35	4.34E+34	2.13E+34	1.18E+34	7.07E+33	9.78E+33	4.03E+33	1.47E+33	1.88E+33	7.23E+35
2455277.3	4.23E+35	2.50E+35	4.24E+34	2.07E+34	1.14E+34	6.85E+33	9.56E+33	4.01E+33	1.48E+33	1.80E+33	7.71E+35
2455278.5	3.54E+35	1.69E+35	4.26E+34	2.08E+34	1.15E+34	6.91E+33	9.61E+33	4.01E+33	1.48E+33	1.82E+33	6.22E+35
2455279.7	2.96E+35	1.13E+35	5.78E+34	2.98E+34	1.69E+34	9.95E+33	1.26E+34	4.36E+33	1.41E+33	3.08E+33	5.45E+35
2455280.7	2.85E+35	1.35E+35	5.42E+34	2.70E+34	1.56E+34	9.68E+33	1.16E+34	4.41E+33	2.28E+33	2.79E+33	5.48E+35
2455281.7	2.20E+35	9.88E+34	3.80E+34	1.71E+34	9.80E+33	5.88E+33	7.43E+33	2.52E+33	1.49E+33	1.43E+33	4.03E+35
2455282.8	1.68E+35	7.14E+34	2.56E+34	9.93E+33	5.38E+33	2.98E+33	4.14E+33	8.98E+32	8.01E+32	3.98E+32	2.89E+35
2455283.7	1.82E+35	7.81E+34	2.47E+34	9.12E+33	5.03E+33	2.38E+33	3.15E+33	7.38E+32	2.44E+31	3.18E+32	3.05E+35
2455284.7	1.97E+35	8.52E+34	2.21E+34	9.22E+33	4.10E+33	2.56E+33	3.35E+33	6.76E+32	2.91E+32	1.01E+32	3.24E+35
2455285.7	1.56E+35	7.34E+34	2.34E+34	1.09E+34	4.58E+33	2.34E+33	3.50E+33	4.50E+33	1.26E+33	2.12E+32	2.80E+35
2455286.6	1.22E+35	6.30E+34	1.77E+34	5.99E+33	2.54E+33	1.31E+33	2.22E+33	1.99E+33	5.59E+32	0.00E+00	2.17E+35
2455287.5	9.34E+34	5.39E+34	1.29E+34	2.29E+33	8.20E+32	3.94E+32	1.09E+33	0.00E+00	0.00E+00	0.00E+00	1.65E+35
2455288.7	2.42E+35	9.75E+34	1.68E+34	4.82E+33	2.21E+33	1.24E+33	1.69E+33	0.00E+00	0.00E+00	0.00E+00	3.66E+35
2455289.8	2.44E+35	9.83E+34	1.70E+34	2.50E+33	2.28E+33	1.00E+33	1.14E+33	0.00E+00	0.00E+00	0.00E+00	3.66E+35
2455290.7	2.11E+35	8.52E+34	1.35E+34	2.13E+33	1.04E+33	5.72E+32	5.53E+32	0.00E+00	0.00E+00	0.00E+00	3.14E+35
2455291.7	1.82E+35	7.37E+34	1.05E+34	1.78E+33	0.00E+00	1.66E+32	3.01E+19	0.00E+00	0.00E+00	0.00E+00	2.68E+35
2455292.7	1.57E+35	6.35E+34	7.73E+33	1.44E+33	0.00E+00	0.00E+00	0.00E+00	0.00E+00	0.00E+00	0.00E+00	2.29E+35
2455293.7	1.80E+35	7.27E+34	1.02E+34	5.84E+32	0.00E+00	0.00E+00	4.47E+31	0.00E+00	0.00E+00	0.00E+00	2.63E+35

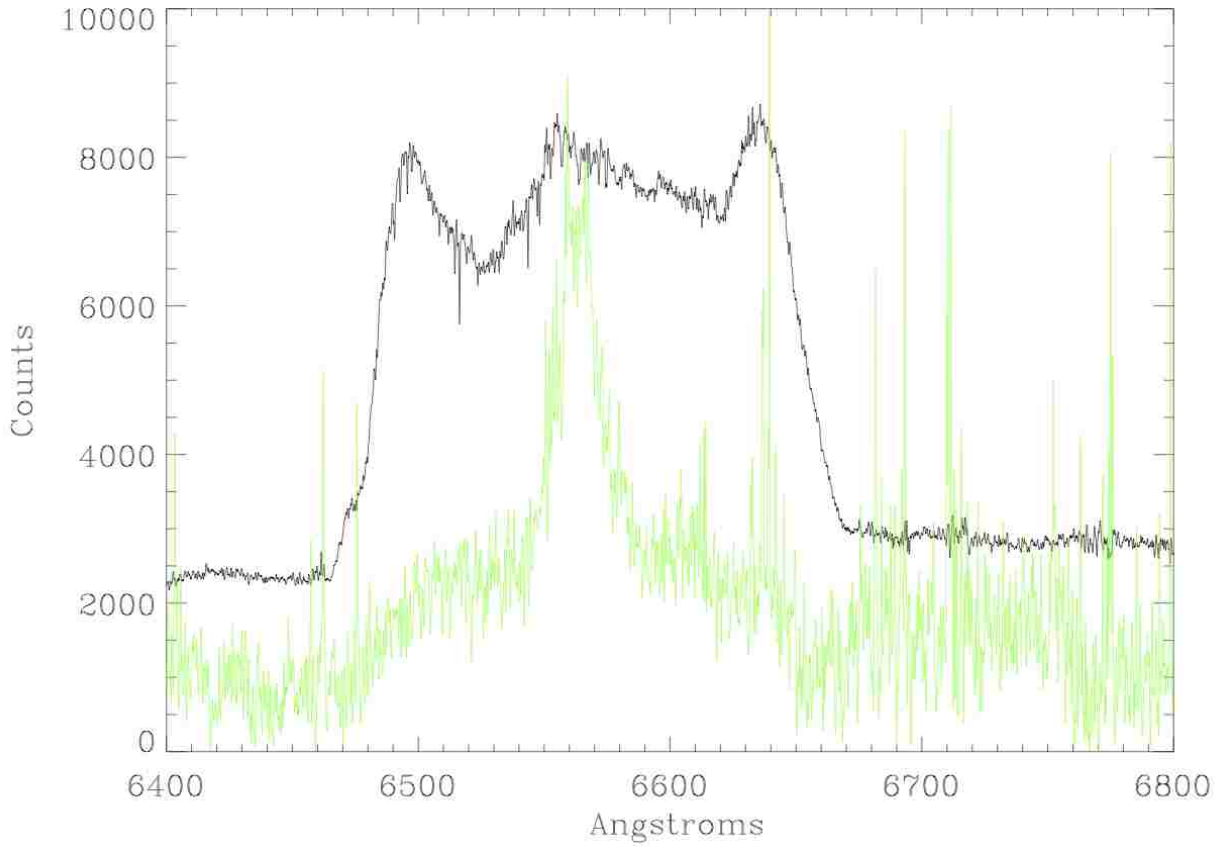

Figure 4.22 U Sco Early Spectrum. Sample spectrum from F. Walter's observations on the SMARTS 1.5m telescope at CTIO that shows the distinct triple-peaked structure in the Hα lines. The black spectrum is from 2010 January 29; the green spectrum is from 2010 February 5 and has been multiplied by a factor of 15. The triple-peaked features are seen early on in known and suspected recurrent novae and fade within a few weeks. Image Credit: F. Walter

4.10 Spectra of the 2010 Eruption

In addition to the large amount of photometry collected during the eruption, collaboration members also took spectra of U Sco throughout the eruption. The primary contributor to the U Sco spectroscopy was F. Walter, using the SMARTS 1.5m telescope at CTIO. His spectra were taken from 2010 January 28 (the night after the eruption was discovered) until 2010 April 21. The early spectra show the unusual triple-peaked Balmer lines (Section 2.2.7) nicely; a sample spectrum can be seen in Figure 4.22. The cause of this line structure is still not well understood, but it appears to be associated with RNe.

In addition to giving us information about the expansion velocities and energetics of the system, the spectra can potentially tell us about the composition of the underlying WD. Mason (2011) obtained late time spectra of U Sco using the medium-resolution X-Shooter spectrograph on the Very Large Telescope in Chile. Her observations were on days 45, 73, and 104 after peak and were specifically aimed at measuring abundances in the ejecta. Theory (Yaron et al. 2005) indicates that the abundances should be nearly-solar, and that there should not be any WD dredge-up, but the observations are murkier. The spectra from Mason (2011) show a remarkably high amount of neon at late times, and this is confirmed by the late time CTIO spectra (F. Walter 2012, private communication). Although the interpretation is not yet final, this indicates first that there is dredge-up occurring during the nova eruption and second that the underlying WD is an oxygen-neon-magnesium WD, not carbon-oxygen. Both of these facts, if true, mean that U Sco can never become a Type Ia supernova, because dredge-up means that the WD is losing mass overall and because only carbon-oxygen WDs can explode as SNe Ia. This issue needs more study and better models before the answer is definitive.

4.11 Implications

In all, the U Sco 2010 eruption was a resounding success. It erupted on time as predicted (within the 1σ error bars), was discovered early on, and was comprehensively observed at all wavelengths by a worldwide collaboration of professional and amateur astronomers. The optical photometry discovered three new phenomena: early fast flares, late optical dips (Section 4.7 and Schaefer et al. 2011a), and the second plateau (Section 4.4 and Pagnotta et al. 2010). The first two phenomena would never have been discovered without the fast time series observations from the highly skilled AAVSO and CBA amateurs. At this point only the late optical dips have any reasonable theoretical explanation. As a result of our excellent coverage, we were able to construct daily spectral energy distributions covering the UV, optical, and near-IR wavelengths, use them to calculate the total radiated energy,

and from that derive the total amount of mass ejected, $m_{\rm ej} = 2.05^{+0.26}_{-0.18} \times 10^{-6} M_{\odot}$. This is the best yet estimate for $m_{\rm ej}$, and the first time that an eruption was covered well enough to use the Shara et al. (2010) method. Unfortunately, the estimate of the total amount of mass accreted during the preceding years is not precise enough to determine whether the WD is gaining or losing mass in the long run. If, however, the Mason (2011) results and interpretation, which indicate an underlying oxygen-neon-magnesium WD, turn out to be true, we will be forced to conclude that U Sco can never become a Type Ia supernova due to its lack of the required carbon-oxygen WD and the fact that there is dredge-up of WD material during the eruption. We look forward to the upcoming years, when observers and theorists alike will be able to use our unprecedented data set to solve some of the mysteries that have been surrounding novae for years and answer the new questions raised by this eruption.

5. Supernova Remnants in the Large Magellanic Cloud: A Treasure Hunt[1]

5.1 Type Ia Supernova Progenitors

As discussed in Sections 1.2 and 1.3, Type Ia supernovae are a critical component of many areas of modern astrophysics, including stellar evolution and cosmology. It is widely accepted that the detonation is caused by the thermonuclear explosion of a carbon-oxygen white dwarf that has reached the Chandresekhar mass limit. A variety of stellar systems have been proposed as progenitors. These progenitor candidates can be divided into two classes, the double-degenerates (Tutukov & Yungelson 1981; van Kerkwijk et al. 2010), and the single-degenerates (Iben & Tutukov 1984; Whelan & Iben 1973), based on whether the system has one or two WDs. After considering the full array of WD binaries (Branch et al. 1995; Parthasarathy et al. 2007), reasonable SD progenitor models include the recurrent novae, symbiotic stars, supersoft X-ray sources, helium stars, and spin-up/spin-down systems (Hachisu & Kato 2001; Hachisu et al. 1999b,a; Langer et al. 2000; Wang et al. 2009; Justham 2011; Di Stefano et al. 2011). There is plausible evidence that the observed SN Ia events could arise from multiple progenitor channels (Maoz & Mannucci 2011).

For many decades the progenitor question has gone unanswered; over the last 15 years, the use of SNe Ia as cosmology tools has elevated the importance of this problem (c.f. Blandford et al. 2010). The progenitor problem can be approached from many directions. The recent nearby supernova SN 2011fe has had modest limits placed (Li et al. 2011) on its pre-eruption progenitor magnitude (M_V must be fainter than -1), but this limit can only reject the most

[1]Sections 5.1, 5.2, and 5.4 reproduced by permission of the Nature Publishing Group (Schaefer & Pagnotta 2012); Section 5.5 reproduced by permission of IOP Publishing Limited (Edwards, Pagnotta, & Schaefer 2012). The permission statements are available in Appendix B. Portions of the sections have been updated and adapted to the dissertation format. I was primarily responsible for the data analysis that went into this chapter; Sections 5.4.2 and 5.4.3 include a large amount of work done by my advisor in addition to my contributions; Section 5.5 includes a large amount of work done by Z. I. Edwards (our summer 2011 REU student) in addition to my contributions.

luminous red giant companion stars in a symbiotic system. Limits based on death rates of progenitor candidates from population synthesis models have uncertainties that are too large to have any real utility in deciding between candidates. The recent claim to eliminate all SD models (Gilfanov & Bogdán 2010), based on the supersoft X-ray flux from elliptical galaxies, has been broadly rejected for many strong reasons (Di Stefano 2010b; Hachisu et al. 2010; Lipunov et al. 2011; Meng & Yang 2011; Orio et al. 2010). The lack of even a small amount of hydrogen in SN Ia spectra (e.g. Leonard 2007) would appear to reject all SD candidates, but this result is ambiguous because detailed models show that the hydrogen will not be visible (Marietta et al. 2000), and some events have been seen to have hydrogen (Branch et al. 1983; Hamuy et al. 2003; but see Livio & Riess 2003). In all, there has been no decisive evidence proving or disproving any one progenitor candidate or class, and our community is roughly evenly divided in opinions.

5.2 Type Ia Supernova Leftovers

A promising method (Ruiz-Lapuente 1997; Canal et al. 2001) to distinguish between candidates is to look for the former companion star near the center of nearby supernova remnants, because the various progenitor classes have different types of companion stars that survive the explosion. Symbiotic progenitors must leave behind a red giant star in the middle of the SNR, while a helium star progenitor must leave the luminous helium star near the SNR center. An RN progenitor must leave either a red giant or subgiant. (As discussed in Chapter 3 and Schaefer et al. (2010b), RNe such as T Pyx which have main-sequence or dwarf companions cannot become SNe Ia because the dynamically-dominant event—the CN eruption that sparks the RN state—expels greatly more mass than is accreted during the lifetime of the system and therefore the WD cannot ever reach or exceed the Chandrasekhar limit. Thus we do not need to consider the case of small main-sequence or dwarf ex-companions.) In these two cases (symbiotics and RNe) the identity of the leftover ex-companion is clear. The other three cases (supersoft X-ray sources, helium stars, and spin-up/spin-down systems),

with their potential low-mass, low-luminosity ex-companions, must be considered in more detail.

Persistent supersoft X-ray sources are "binaries containing white dwarfs which can accrete matter from a more massive and possibly slightly evolved companion" (Di Stefano & Nelson 1996). Their orbital periods range from 0.14 to 3.5 days, with the shorter period systems having too little total mass to allow the WD to reach the Chandrasekhar limit. The fast accretion onto the WD (which is required to power the steady hydrogen burning that produces the persistent supersoft X-ray light) is driven by the Roche lobe shrinking faster than the companion star (van den Heuvel et al. 1992), which requires a mass ratio of >5/6 (Frank et al. 2002). For the WD to be near the Chandrasekhar limit, this requires that the companion star be more massive than $1.16 M_{\odot}$. Such a star will necessarily be at least as luminous as a normal $1.16 M_{\odot}$ main-sequence star, for which the absolute magnitude is $M_V = +4.2$. This result has been confirmed by very detailed models (Langer et al. 2000). With the LMC distance modulus of 18.50, the star would appear brighter than V=22.7 mag.

Progenitor models have been proposed wherein the companion star has been stripped of most of its outer envelope, so we consider whether these can produce low-luminosity ex-companion stars. One such model is that of helium star companions, red giants stripped of their outer hydrogen envelope, with the remaining helium envelope providing the mass accreted onto the white dwarf. But the donor star still has the same energy generation as in the core of the original red giant, so the luminosity is still 1000 to 10,000 times that of the Sun and the temperatures are around 80,000 K (Wang et al. 2009). This compact star will suffer relatively little mass loss during the supernova explosion (Pan et al. 2010). The absolute magnitude of such a star will be roughly $M_{\rm V} = +2$ or brighter (including bolometric corrections), so any such ex-companion in the LMC will appear as V=20.5 mag or brighter.

The spin-up/spin-down model (Justham 2011; Di Stefano et al. 2011) posits a red giant donor star that spins up the WD so that its rotation will support a mass greatly exceeding the Chandrasekhar limit, until the donor's envelope is exhausted and the donor star shrinks

to a small, hot core, while the white dwarf takes a longer time to redistribute or lose angular momentum to allow for the ignition of the supernova event. (The published model is for a red giant or possibly a subgiant companion, but in principle this could be extended to main-sequence stars. The name 'spin-up/spin-down' refers to the progenitor model, but it can also refer to the physical process where the WD spins up and then spins down. The spin-up process is inevitable and previously ignored; the spin-down process and SN ignition will only occur in this model in the small-chance case that the companion star turns off the accretion when the WD is above the Chandrasekhar mass.) The result will be a relatively small ex-companion star with little surface material blown off by the supernova (Pan et al. 2010). Again, the core of the red giant star will have the same luminosity as before the explosion. The time from the cessation of the accretion (after which the companion's exhausted envelope shrinks on the fast Kelvin-Helmholtz time scale) until the supernova event occurs is governed by the growth rate for r-mode instabilities that will redistribute or remove angular momentum from the WD. Calculations of this growth rate (Lindblom 1999) for the relevant conditions give time scales of 10^3 to 10^5 years (Yoon & Langer 2005). During this time, the luminosity of the companion will change little, so that a typical luminosity is $50L_{\odot}$, which for the given temperature of 6000 K corresponds to V=19.0 mag in the LMC (Di Stefano et al. 2011). So any ex-companion from a spin-up/spin-down progenitor in the LMC must appear bright at roughly $V = 19$.

We can also consider the idea within a spin-up/spin-down scenario where the companion is a main-sequence star that might somehow get to low luminosity before the explosion. At the start of this scenario, the only means for the WD to spin up and gain mass is for the accretion rate to be very high, which can only be when the mass ratio is >5/6. Then, as the mass of the main-sequence companion falls below $1.16M_{\odot}$ (with $M_{\rm V} = +4.2$), the accretion rate will largely turn off. The hallmark of the spin-up/spin-down idea is that the delay from the end of spin-up to the explosion allows for the companion to shrink (to minimize the hydrogen contamination of the subsequent supernova shell as well as to minimize the Kasen

(2010) effect). But the $1.16 M_{\odot}$ star will be unchanging on any interesting time scale. The system will still have a relatively low accretion rate (driven by angular momentum loss due to magnetic braking) that will very slowly reduce the mass of the companion from $1.16 M_{\odot}$ (with $M_{\rm V} = +4.2$) down to $\sim 0.5 M_{\odot}$ (with $M_{\rm V} = +8.4$). The time required for ordinary magnetic braking to grind down the companion star is roughly 5×10^9 years (Andronov & Pinsonneault 2004). Indeed, the timescale for the companion star to start evolving off the main-sequence is likely faster, in which case its luminosity will be brightening. In all, the spin-up/spin-down model with a main-sequence star cannot produce a low luminosity ex-companion star because the companion star will be at $M_{\rm V} = +4.2$ when the fast accretion stops and it will still be at $M_{\rm V} = +4.2$ when the explosion happens, which corresponds to an apparent magnitude of $M_{\rm V} = 22.7$ in the LMC.

In summary, all the reasonable SD systems either have evolved luminous companions or main-sequence companions greater than one solar mass. Systems with low-mass main-sequence stars (the cataclysmic variables like T Pyx) are rejected both because they cannot maintain the high required accretion rate necessary to avoid hydrogen flashes (which makes the WD lose mass over the long term) and because the number density and death rate of these systems are much too low (Schaefer et al. 2010b and Section 3.9) to account for the observed rate of SNe Ia (Branch et al. 1995).

We also consider the possibility that the supernova explosion itself could modify and dim the companion star significantly. For the cases where the companion star has a moderate or high surface gravity (the main-sequence stars in supersoft progenitors, helium donor stars, and the cores in spin-up/spin-down progenitors), the stripping of the envelope will be minimal and the ex-companion star will have much the same luminosity 400 years after the supernova as it does pre-explosion (Marietta et al. 2000; Pan et al. 2010; Podsiadlowski 2003). Detailed calculations for the subgiant case show that usually the ex-companion star will be up to two orders of magnitude more luminous (due to the deposited energy), although in the unexpected case of low energy deposition, the ex-companion can be as much as ten times less

Table 5.1. Candidate Progenitor Classes

Candidate Progenitor	P_{orb} (days)	$v_{ex-comp}$ (km s^{-1})	Surviving Companion	M_V (mag)	V range in LMC (mag)
Double-degenerate			None		
Recurrent Nova	0.6-520	50-350	Red Giant or Subgiant	-2.5 to +3.5	16-22
Symbiotic Star	245-5700	50-250	Red Giant	-2.5 to +0.5	16-19
Persistent Supersoft X-ray Source	0.14-4.0	170-390	Subgiant or $> 1.16 M_\odot$ MS	+0.5 to +4.2	19-22.7
Helium Star Donor	0.04-160	50-350	Red Giant or Subgiant Core	-0.5 to +2.0	18-20.5
Spin-Up/Spin-Down	245-5700	50-250	Red Giant or Subgiant Core	-0.5 to +4.2	18-22.7

luminous due to internal energy going into expanding the surviving envelope (Podsiadlowski 2003). In all these cases, the stellar core is still producing energy at the same rates, so the luminosity cannot change greatly.

In conclusion, there are no published SD models for which the ex-companion star will be significantly less luminous than $M_V = +4.2$ (V=22.7 mag in the LMC). The DD model predicts that there will be no ex-companion star, as both WDs are destroyed in the SN explosion. A summary of all possible ex-companion stars can be seen in Table 5.1. Thus, by looking near the center of a Type Ia SNR, the existence and nature of any ex-companion star will distinguish the progenitor system.

This method can only be applied to SNRs which definitely came from SNe Ia. In our galaxy, only Tycho's SNR (SN 1572) and the remnant from SN 1006 are confidently known to be from SNe Ia (Krause et al. 2008; Schaefer 1996). Ruiz-Lapuente et al. (2004) looked near the center of the Tycho remnant and identified a G2 IV subgiant star, which they called Star G, near the center as the ex-companion based on its high proper motion at the right distance. If this identification is confirmed, it would immediately rule out the DD and symbiotic channels, pointing to an RN progenitor. Unfortunately, various properties are still being disputed (Ihara et al. 2007; Kerzendorf et al. 2009; González Hernández et al. 2009). González Hernández et al. (2009) performed a detailed analysis of hundreds of metal absorption lines to find that nickel and cobalt are anomalously over-abundant in the atmosphere of Star G. If confirmed, this would strongly point to Star G having contamination from SN ejecta. For now, the case is unresolved, although we are inclined to think that Star G is the ex-companion star based on the González Hernández et al. (2009) paper. For the case of SN

1006, a red giant ex-companion star can be ruled out (Ruiz-Lapuente et al. 2011). A major challenge is that galactic SNRs have large uncertainties in distances, high extinction, and crowded fields.

5.3 Type Ia Supernova Remnants in the Large Magellanic Cloud

To break this impasse, we have looked at four SNRs in the Large Magellanic Cloud (LMC), a satellite galaxy of our own Milky Way. The LMC has three main advantages over galactic searches: (1) the distance to the LMC is well known, with a distance modulus of 18.50 ± 0.10 mag (Freedman et al. 2001; Schaefer 2008); (2) the extinction has been thoroughly mapped and is generally low (Zaritsky et al. 2004); and (3) the star fields are on average less crowded than those in the Milky Way.

Four SNRs in the LMC have been proven to have come from SNe Ia: SNR 0505-67.9, SNR 0509-67.5, SNR 0509-68.7, and SNR 0519-69.0. Hughes et al. (1995, 1998) have typed each of these remnants as SNe Ia based on X-ray spectroscopy, and Rest et al. (2005, 2008) have identified light echoes from three of them (SNR 0509-67.5, SNR 0509-68.7, and SNR 0519-69.0) which confirm the Ia identification as well as allow for sub-typing of each SN, since the echo light comes from the original explosion, so a spectrum can be obtained. SNR 0509-67.5 was a 1991T (overluminous) subclass (Rest et al. 2008), while SNR 0509-68.7 and SNR 0519-69.0 were normal Ia events (A. Rest 2010, private communication). Table 5.2 gives a brief summary of the properties of each of the four remnants, and Figure 5.1 shows a Chandra X-ray image of each remnant. The following sections will examine each of the four remnants in detail.

5.4 SNR 0509-67.5

We first consider the case of SNR 0509-67.5, which was an SN Ia of the 1991T subclass 400 ± 50 years ago (Hughes et al. 1995; Rest et al. 2005, 2008; Badenes et al. 2009). There

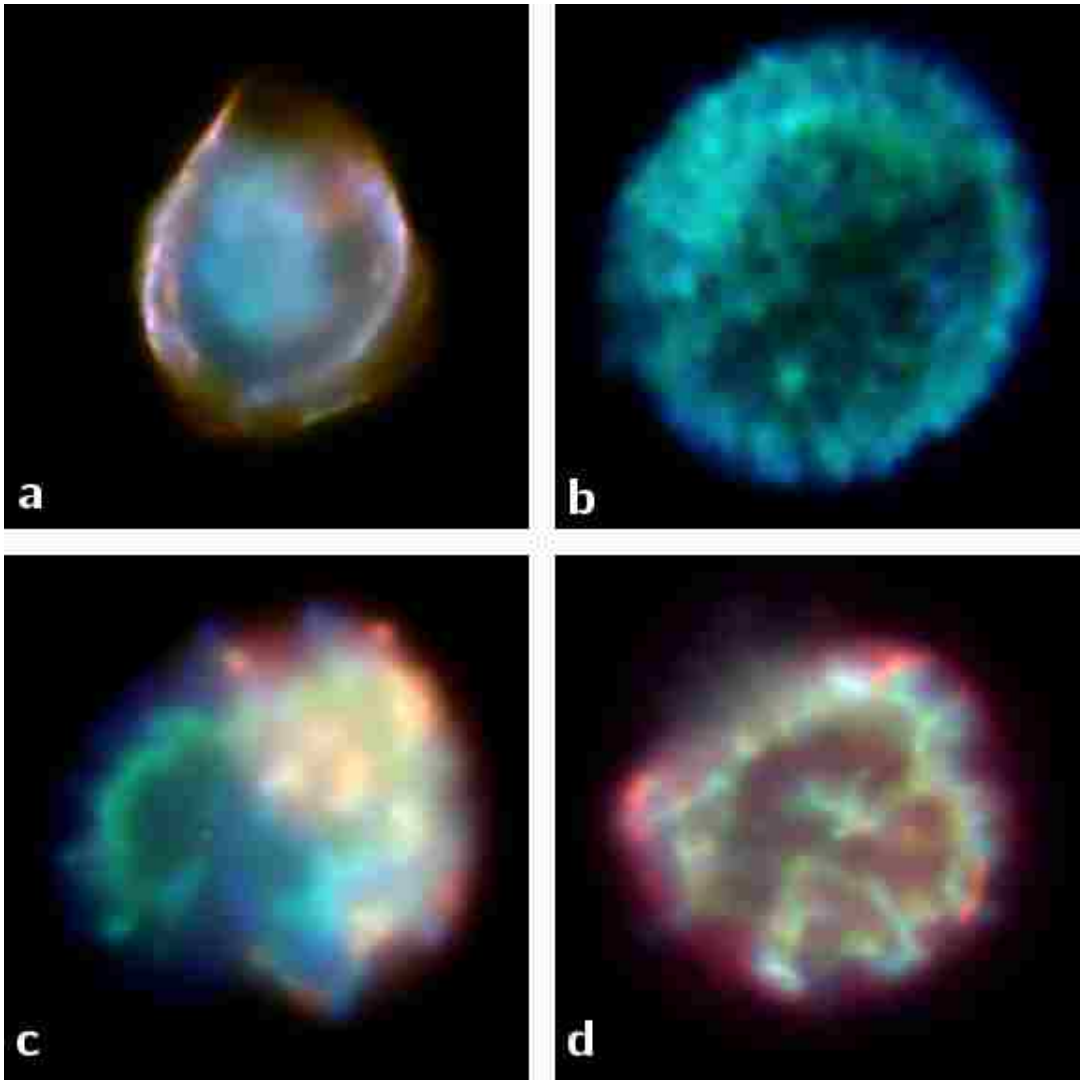

Figure 5.1 Chandra X-ray Images of the Four Type Ia Supernova Remnants in the Large Magellanic Cloud: (a) SNR 0505-67.9, (b) SNR 0509-67.5, (c) SNR 0509-68.7, and (d) SNR 0519-69.0. We looked for ex-companion stars in the center of each of these remnants to identify the progenitor systems of each supernova. For one remnant (SNR 0509-67.5, image b), we are able to definitively identify the progenitor as a double-degenerate (double white dwarf) system. For the other three, we can place constraints on the possible progenitors; future observations will improve those constraints. Image Credit: Chandra Supernova Remnant Catalog (http://hea-www.harvard.edu/ChandraSNR/), NASA/CXC/SAO

Table 5.2. Four Type Ia Supernova Remnants in the LMC

Remnant	Size	Age (years)
0505-67.9 (DEM L71)	72" × 72"	4360 ± 290
0509-67.5	29.2" × 32.0"	400 ± 50
0509-68.7 (N103B)	39" × 42"	860
0519-69.0	45" × 45"	600 ± 200

are a number of public *HST* observations of SNR 0509-67.5, namely a set of Hα observations from WFPC2[2] in 2008 (original observing program #11015, PI J. P. Hughes, Rutgers[3]) and a set of BVI images from WFC3[4] in late 2010 (original observing program #12326, PI K. S. Noll, STScI/Hubble Heritage[5]).

We downloaded the full public domain data sets from the STScI archive. There are 12 total Hα (F656N) observations, however 8 of them have data quality flags due to a WF4 anomaly causing a gain error and streaks on the image, so we only used the 4 data sets without any warnings: U9UE0201M, U9UE0205M, U9UE0209M, U9UE020CM. This gives a total combined exposure time of 5000 sec. We combined them using MultiDrizzle (Fruchter et al. 2009) as instructed by the WFPC2 Drizzling Cookbook[6] and obtained good results with the default values. The BVI images (F475W, F555W, F814W) from WFC3 have exposure times of 1010 sec, 696 sec, and 800 sec, respectively; they were also processed using MultiDrizzle. We performed aperture photometry on the stars in all images using IRAF's *apphot* task and then converted the BVI instrumental mags to calibrated mags using the zeropoints in Kalirai et al. (2009). Table 5.3 gives V and I magnitudes for the twelve stars nearest the center (where Θ is the angular distance from the center of the remnant to the star), as well as three other interesting stars in the field.

To make the final combined image, seen in Figure 5.2, we combined the the Hα and BVI

[2]See Appendix A.3.2 for more information on WFPC2.
[3]http://archive.stsci.edu/proposal_search.php?id=11015&mission=hst
[4]See Appendix A.3.3 for more information on WFC3.
[5]http://archive.stsci.edu/proposal_search.php?id=12326&mission=hst
[6]http://www.stsci.edu/hst/wfpc2/analysis/WFPC2_drizzle_4ditherWF.html

Table 5.3. Stars Near the Center of SNR 0509-67.5

Star	RA (J2000)	Dec (J2000)	Θ (″	V (mag)	I (mag)	Comments
A	05:09:30.960	-67:31:16.28	1.7	26.08 ± 0.11	24.50 ± 0.08	Nearest to error ellipse
B	05:09:30.701	-67:31:18.75	1.7	24.82 ± 0.04	23.61 ± 0.04	
C	05:09:30.753	-67:31:16.63	1.9	26.30 ± 0.13	24.77 ± 0.09	
D	05:09:30.916	-67:31:19.91	2	24.02 ± 0.03	22.98 ± 0.03	
E	05:09:30.660	-67:31:19.07	2.1	23.99 ± 0.02	23.05 ± 0.03	
F	05:09:30.824	-67:31:16.03	2.1	23.30 ± 0.02	22.53 ± 0.02	
G	05:09:31.212	-67:31:16.30	2.2	25.36 ± 0.06	23.76 ± 0.04	
H	05:09:30.712	-67:31:16.01	2.5	22.87 ± 0.01	22.06 ± 0.02	
I	05:09:30.581	-67:31:16.74	2.6	26.57 ± 0.15	24.72 ± 0.08	
J	05:09:31.454	-67:31:17.21	2.9	25.84 ± 0.09	24.43 ± 0.07	
K	05:09:30.824	-67:31:15.20	2.9	22.55 ± 0.01	21.86 ± 0.01	Nearest V>22.7
L	05:09:31.299	-67:31:15.72	2.9	20.56 ± 0.01	20.07 ± 0.01	
M	05:09:31.837	-67:31:19.61	5.2	24.26 ± 0.03	21.00 ± 0.01	Very red star
N	05:09:31.604	-67:31:22.54	5.8	20.92 ± 0.01	19.87 ± 0.01	Nearest subgiant
O	05:09:31.586	-67:31:11.49	7.4	18.75 ± 0.01	17.68 ± 0.01	Nearest red giant

images using the IRAF task *imarith* to retain the sharply-defined edges of the shell present in the Hα images without losing the stars in the BVI field. Figure 5.2 is labeled with all of the stars from Table 5.3 and shows the final error circle, which will be described in Section 5.4.2.

5.4.1 Finding the Center of SNR 0509-67.5

Any ex-companion star should appear near the geometric center of the shell. The shell of SNR 0509-67.5 is nearly symmetric and smooth, making this a good case for measuring an accurate center position. But the shell center cannot be measured perfectly, and different measures will yield different centers. Here, we report on three independent methods to determine the geometric center. Importantly, these methods use different gases in different positions of the shell.

The first method defines the center based on the outer edge of the Hα shell. The procedure is to take a baseline cut through the shell, noting the very edges, take the perpendicular bisector of this segment, noting the very edges, and then take the remnant center measurement to be the middle of this perpendicular segment. A total of nine such centers are obtained for baselines tilted at 10° intervals, to sample the entire edge of the shell. The nine centers are then averaged to get a combined center, and the RMS scatter of these nine

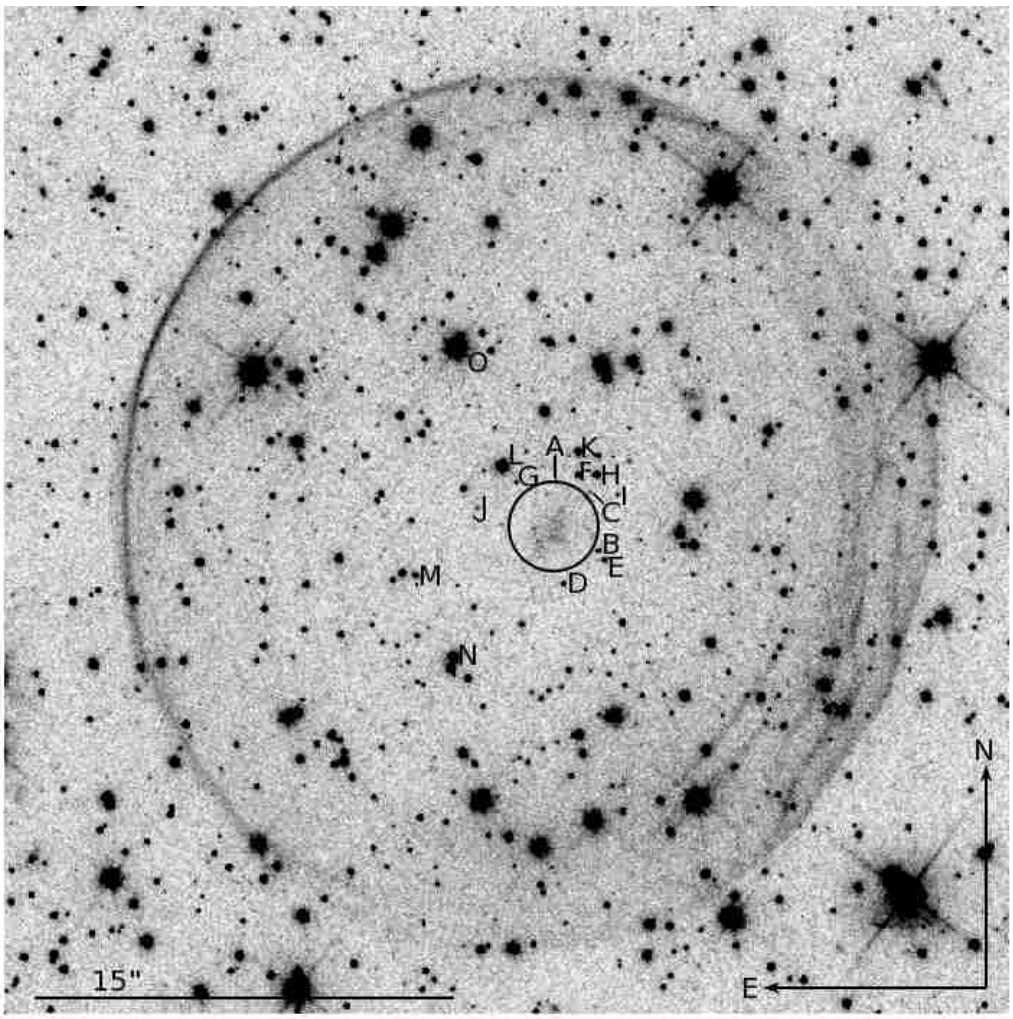

Figure 5.2 SNR 0509-67.5 and the Extreme 99.73% Error Circle. This image is a combination of *HST* observations in four different filters: 5000 sec in Hα, 1010 sec in B, 696 sec in V, and 800 sec in I. The smooth Hα shell is easily visible. The 1.43$''$ error circle is drawn in the center of the remnant and represents the 99.73% containment region for the most extreme ex-companion case: minimum possible mass main-sequence star, maximum possible velocity, highest uncertainty on the location of the center, and oldest possible remnant age. There are no stars within this error circle to a limiting magnitude of $V = 26.9$ mag, which corresponds to an absolute magnitude of $M_V = +8.4$ mag in the LMC. All published single-degenerate progenitor models indicate that any leftover ex-companion star would be more luminous than $M_V = +4.2$ mag, or brighter than $V = 22.7$ in the LMC. Since there are no stars of that brightness in the extreme central error circle, we can exclude all possible single-degenerate models and are left to conclude that SNR 0509-67.5 must have come from a double-degenerate (double white dwarf) system. There is a faint nebulosity in the error circle; it is likely a background galaxy (see Section 5.4.3 for more details) and, importantly, it is not capable of hiding any stars behind it.

Table 5.4. Positions in SNR 0509-67.5

Position	Center RA (J2000)	Center Dec (J2000)	$\sigma_{\rm short}$	$\sigma_{\rm long}$
Hα center for 0° cross (ΔRA= $-0.08''$, $\Delta\delta = 0.00''$)	05:09:31.159	-67:31:17.17	...	...
Hα center for 10° cross (ΔRA= $0.01''$, $\Delta\delta = -0.21''$)	05:09:31.143	-67:31:17.38	...	...
Hα center for 20° cross (ΔRA= $0.09''$, $\Delta\delta = -0.22''$)	05:09:31.128	-67:31:17.39	...	...
Hα center for 30° cross (ΔRA= $0.27''$, $\Delta\delta = 0.08''$)	05:09:31.098	-67:31:17.09	...	...
Hα center for 40° cross (ΔRA= $0.31''$, $\Delta\delta = 0.38''$)	05:09:31.091	-67:31:16.79	...	...
Hα center for 50° cross (ΔRA= $0.27''$, $\Delta\delta = 0.66''$)	05:09:31.098	-67:31:16.51	...	...
Hα center for 60° cross (ΔRA= $-0.24''$, $\Delta\delta = -0.19''$)	05:09:31.187	-67:31:17.36	...	...
Hα center for 70° cross (ΔRA= $-0.26''$, $\Delta\delta = -0.19''$)	05:09:31.190	-67:31:17.36	...	...
Hα center for 80° cross (ΔRA= $-0.35''$, $\Delta\delta = -0.27''$)	05:09:31.206	-67:31:17.44	...	...
Combined center of Hα edge (method 1)	05:09:31.144	-67:31:17.17	$0.18''$	$0.37''$
Center of X-ray edge (method 2)	05:09:31.195	-67:31:17.11	$0.26''$	$0.26''$
Minimum of Hα interior light (method 3)	05:09:31.342	-67:31:18.34	$0.54''$	$0.60''$
Geometric center of shell (methods 1-3)	05:09:31.208	-67:31:17.48	$0.14''$	$0.20''$
Site of supernova explosion	05:09:30.976	-67:31:17.90	$0.20''$	$0.21''$
Ex-companion star, red giant proper motion	05:09:30.976	-67:31:17.90	$0.74''$	$0.74''$
Ex-companion star, subgiant proper motin	05:09:30.976	-67:31:17.90	$1.06''$	$1.06''$
Ex-companion star, main-sequence proper motion	05:09:30.976	-67:31:17.90	$1.17''$	$1.17''$
Ex-companion star, extreme 99.73% proper motion	05:09:30.976	-67:31:17.90	$1.43''$	$1.43''$

positions is a measure of the 1σ accuracy of this combined center position. For the nine tilted baselines, Table 5.4 specifies the offsets from the combined center in terms of right ascension (ΔRA) and declination ($\Delta\delta$), expressed in arcseconds. In practice, this procedure is iterated once to avoid any sensitivity to the initial assumed center. All 36 measured edge positions define the shell radius as a function of angle from north. This radius function is closely a sine wave, except for the deviation associated with the moderately extended wispy filament towards the northwest edge of the shell. A χ^2 fit gives a radius of $16.0''$ along the long axis (oriented to $18^\circ \pm 3^\circ$ west of north) and a radius of $14.6''$ along the short axis. The ratio of the short axis to the long axis is 0.913±0.009. The error ellipses are quoted in the direction of these long and short axes. The center and uncertainties from this first method are presented in Table 5.4.

The second method defines the center based on the outer edge of the X-ray shell. For this, we have used three *Chandra* images (Warren & Hughes 2004) from May 2000, in which the remnant was imaged separately in the light of three emission lines: O (0.45-0.7 keV), Fe L (0.7-1.4 keV), and Si (1.5-2 keV). The procedure for finding the center of the three X-ray images is the same as the first method, with the three resultant centers being closely

consistent and averaged together to get one combined center based on the edge of the X-ray shell. The uncertainty in this position is characterized by the RMS scatter (in the direction of the long and short axes) of the individual centers. Table 5.4 gives this position and error ellipse.

The third method uses the faint Hα light in the remnant's central region. This interior light, far inside the outer filaments, is visibly faintest near the geometric center. This is simply the thin shell seen nearly perpendicular to its surface (instead of being seen edge-on near the edge of the remnant, which creates the thin filaments). For a thin shell of radius $R_{\rm shell}$, the brightness falls off with distance R from the remnant's center as $I_{\rm background} + I_{\rm center} \times [1 - (R/R_{\rm shell})^2]^{-0.5}$, where $I_{\rm center}$ is the central brightness. We measure the brightness of 20×20 pixel tiles in the interior of the shell (looking at the median values, to minimize the effect of the stars), and then fit them to this brightness model. (We have also made model fits where $R_{\rm shell}$ is allowed to vary as an ellipse, with essentially identical resulting centers.) We used 71 tiles within 110 pixels of the center (iteratively determined) for which the maximum pixel value in the tile was $<$0.001 counts per second. The uncertainty on each tile brightness was taken to be the RMS scatter of tiles outside the remnant, while the average for these tiles was taken to be the background brightness $I_{\rm background}$. We use a χ^2 fit to determine the best center, and the 1σ error bars along the long and short axes are determined by the point at which the χ^2 value has risen by unity above its minimum. Our best fit model has a χ^2 of 61.3 (for 67 degrees of freedom). We get the same results (to within the 1σ error bar) if we use different tile sizes, different radial cutoffs, and different star rejection thresholds. Our best fit center and the 1σ errors along the two axes are presented in Table 5.4.

We now have three independent geometric centers for the shell; each measure is based on a different gas or region. The first method is based on the relatively cold gas around the visible edge, the second method is based on the very hot gas around the edge, and the third method is based on the relatively cold gas near the middle. We have combined these three independent positions as a weighted average. Our final result for the geometric center of the

shell is J2000 05:09:31.208, -67:31:17.48 with 1σ uncertainties of $0.14''$ and $0.20''$ in the short and long axes respectively.

5.4.2 Finding the Offset for SNR 0509-67.5

Any ex-companion star is unlikely to appear at the exact geometric center of the remnant for several reasons, including the proper motion of the star away from the site of the explosion, the possibly asymmetric ejection of material so that the geometric center of the observed shell is offset from the site of the explosion, and the possibly asymmetric distribution of gas in the interstellar medium that slows the shell expansion in some direction more than in the opposite direction, resulting in an offset between the observed geometric center of the shell and the site of the explosion. Explosion sites have not been directly measured for any SNe Ia, so we must evaluate the expected sizes of these offsets from the physics of the situation. (There are extensive measures of the offsets of neutron stars from core collapse supernovae (Rothschild & Lingenfelter 1996), but the physical setting is greatly different from the SN Ia case, so this experience has no utility for understanding the offset of our LMC remnants.)

The proper motion of the ex-companion star (with respect to the center of mass of the original binary system) will come from both the kick given to the star by the supernova ejecta and the orbital velocity at the time of the explosion. The kicks onto the companion from the supernova ejecta will always be relatively small (Canal et al. 2001; Marietta et al. 2000; Pan et al. 2010). For companions filling their Roche lobe, the orbital velocity will depend primarily on the stellar radius. Canal et al. (2001) calculated average post-explosion velocities for expected conditions, with the conclusion that the ex-companions should be moving at around 480, 250, and 100 km s^{-1} for main-sequence, subgiant, and red giant companions, respectively. For the red giant and subgiant cases, the proper motion is relatively small and all such stars are far outside the SNR 0509-67.5 error ellipses. The only critical case is when we push to the smallest possible mass main-sequence star, which produces the largest possible error ellipse (see Figure 5.2). The smallest mass main-sequence star that can be a companion star for an SN Ia is a $1.16M_{\odot}$ star in a supersoft system (see Section

5.2). The 480 km s^{-1} velocity from Canal et al. (2001) is for a $0.6M_{\odot}$ star, and the proper motion gets smaller as the companion mass increases. For a $1.16M_{\odot}$ main-sequence companion star filling its Roche lobe around a $1.4M_{\odot}$ WD, the orbital period will be 10.6 hours, the orbital velocity of the companion star will be 208 km s^{-1}, and the WD orbital velocity will be 173 km s^{-1}. The supernova explosion will provide a kick to the companion star of 86 km s^{-1} in the direction perpendicular to the orbital motion (Marietta et al. 2000). The relative velocity of the WD (which will be the origin for the frame of the expanding shell) and the companion star will be 390 km s^{-1}. Going to higher mass main-sequence stars will only make for a smaller velocity. So for all viable progenitor models, the velocity of the ex-companion with respect to the original geometric center of the remnant will be 390 km s^{-1} or less. For an LMC distance modulus of 18.50 ± 0.10, the extreme case (390 km s^{-1} in a tangential direction) results in a total proper motion of 0.0016 $''$/year. For the 400 ± 50 year age of SNR 0509-67.5, any ex-companion star must be within $0.66'' \pm 0.08''$ of the site of the explosion.

Largely, the thermonuclear burning of the WD is spherically symmetric, so any asymmetries will be small. Observationally, asymmetries can be measured by polarization studies, where normal SNe Ia have small polarization in the spectral continuum (up to 0.2%−0.3%), which is consistent with an ellipsoidal shape where the minor-to-major axis ratio is 0.9 (Wang et al. 2003, 2007; Wang & Wheeler 2008). The asphericity might be smaller if the polarization is caused by dense clumps occulting part of the photosphere (Kasen et al. 2003). The observed axis ratio for SNR 0509-67.5 is 0.913 ± 0.009. If this asphericity is dipolar in shape (e.g., oblate or prolate), then the geometric center of the shell will correspond to the original position of the binary. The shell center will be offset only if there is some appreciable monopolar component (e.g., where the north pole is ejected with higher velocity than the south pole). Even for monopolar asymmetries, the apparent offset will generally be smaller than the maximal value due to projection effects, and such offsets will be near zero for cases where the monopolar axis is near the line of sight. In theory, an off-center detonation in the

white dwarf might result in asymmetric distributions of density and composition, and this will create apparent velocity differences (as viewed from opposite directions) as the photosphere recedes at differing rates (Maeda et al. 2010). This scenario is apparently confirmed by strong correlation of the velocity gradients (with high and low groups) and the bulk velocities at late times (with redshifted and blueshifted groups) (Maeda et al. 2010), as well as by the lopsided distribution of opacity in the sub-luminous SN Ia S And (Fesen et al. 2007). The model predicts late-time velocity differences (between hemispheres) of less than 10%, but this is mainly an effect of different photospheric depths, and it is unclear whether the off-center detonation translates into an offset of the geometric center of the shell. From these considerations, the maximum offset of the geometric center of the shell from the original explosion position is roughly 10% of the radius.

A global gradient in the density of the interstellar medium across the shell will result in the remnant having different radii in different directions, causing an apparent offset of the geometric center from the site of the original explosion. SNe Ia are generally in low density environments, so this effect is likely to be small. Indeed, *Spitzer* observations show no significant background flux around SNR 0509-67.5 (Williams et al. 2011), while extinction maps show no significant gradients across the remnants (Schlegel et al. 1998). Badenes et al. (2009) characterize SNR 0509-67.5 as being "in a very homogenous region".

A measure of both asymmetry offsets can be obtained from the observed ellipticity of the shell. In the case of either a lopsided high ejecta velocity or a low interstellar medium density in some direction, the out-of-round shape is due to the shell having a large radius in that direction (f times the radius in other directions, with $f > 1$). In this case, the observed short-to-long axial ratio will be $2/(1 + f)$, while the offset between the site of the explosion and the observed shell center will be $0.5(f - 1)R_{\rm shell}$ in one direction or the other along the long axis. In the case of either a lopsided low ejecta velocity or a high interstellar medium density in some direction, the out-of-round shape is due to the shell having a small radius in that direction (with $f < 1$). With this, the observed short-to-long axial ratio will

be $(1 + f)/2$, while the offset will be $0.5(1 - f)R_{\rm shell}$ in one direction or the other along the short axis. In all four cases (high/low ejection velocity or high/low interstellar medium density in some direction), if the direction is not perpendicular to the line of sight, then the foreshortening of the offset will be evident in the reduction in the ellipticity of the shell.

The case of SN 1006 provides an example of how our method accurately recovers the site of the original explosion. This thousand year old galactic remnant is nicely symmetrical, with a small ellipticity. The long axis is along the NNE-SSW line and the ratio of the short axis to the long axis is 0.90. From this, we get $f = 1.22$ and a fractional offset of 11%. If we knew only the shape of the shell, we would not know the direction of this 11% offset between the geometric center and the site of the explosion. (High ejecta velocity or low ISM density in one quadrant will result in an offset that is 11% either towards the NNE or the SSW, while low ejecta velocity or high ISM density in one quadrant will result in an offset that is 11% towards the ESE or WNW.) For SN 1006, this ambiguity can be resolved using absorption spectroscopy of five background sources, where the results show that the supernova ejected high velocity material towards the NNE quadrant (Winkler et al. 2005). In the three-dimensional analysis, the geometric center is offset by roughly 20% of the shell radius; when projected onto the sky, this corresponds to an offset of only roughly 10% of the shell's angular radius. With this, the direction ambiguity is resolved such that the offset from the observed geometric center to the explosion site is 11% towards the SSE. The good agreement between the offset from our analysis (based on the observed ellipticity of the shell) and the full three-dimensional analysis is heartening. However, we see that we must have a means to break the direction ambiguity, as otherwise we have a substantially larger error ellipse.

For the case of SNR 0509-67.5, we can cleanly choose between the four alternative offset possibilities and determine the offset and direction. The *Spitzer* 24μ image (Figure 5.3) shows the pre-existing and swept-up dust from the surrounding interstellar medium, and there is an excess of swept-up material in the quadrant centered towards the WSW short

axis (Borkowski et al. 2006). The swept-up material towards the NNW, the ENE, and the SSE axes is identical (as seen in the dust brightnesses in those directions), and is significantly lower than the amount in the WSW direction. This explains why the short axis of the shell is in that direction. This is supported by an analysis of the X-ray line widths where the shock velocity in the SW quadrant (5000 km s^{-1}) is somewhat lower than for the NE quadrant (6000 km s^{-1}), with the slow-down towards the SW happening relatively recently (Helder et al. 2010). So the case of high interstellar density in one direction (to the WSW) is known, and this results in an offset from the geometric center to the explosion site towards the WSW. For an axial ratio of 0.913 ± 0.009, we have $f = 0.826 \pm 0.018$ and an offset of $1.39'' \pm 0.14''$. The uncertainty in the direction of the short axis ($\pm 3°$) makes for an uncertainty of the offset position of $0.07''$ in the direction of the long axis of the shell. With this offset and its added uncertainty, our measured position for the site of the supernova event is J2000 05:09:30.976, -67:31:17.90 with 1σ uncertainties of $0.21''$and $0.20''$ in the long and short axes respectively.

The true difference between the observed geometric center and the position of the ex-companion star will arise from the proper motion of the ex-companion (relative to the WD and including the kick from the supernova), the uncertainty in measuring the geometric center of the remnant, and the offset of the geometric center from the site of the supernova due to the relatively high density of the interstellar medium towards the WSW. A complication arises because the distribution of the offsets from proper motion is not Gaussian shaped (rather, it is edge dominated), so the size of the ellipse for the position of the ex-companion star cannot be simply expressed with a Gaussian sigma. To account for this, we have constructed Monte Carlo simulations of the various mechanisms, including the random orientation of the proper motion, the random error in the age of the supernova remnant, and the Gaussian random error in measuring the geometric center of the shell. We report the long and short radii for ellipses (oriented with the axes in the same direction as the shell) such that 99.73% (i.e., 3σ) of the realizations are within the ellipse. Since the possible proper motions have a circularly symmetric distribution and the position for the site of the

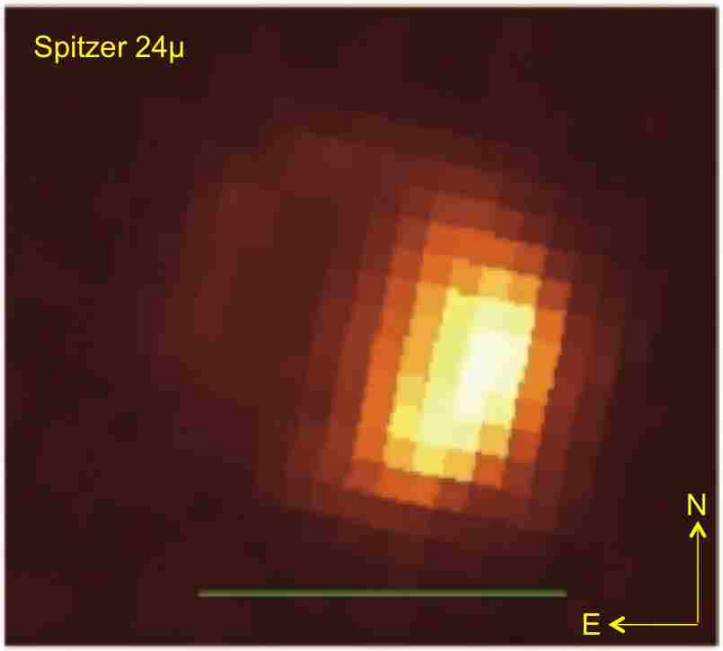

Figure 5.3 24μ *Spitzer* Infrared Image of SNR 0509-67.5. The remnant is very bright in IR in the south-southwest corner, indicating an excess of dust in that quadrant. We know that this dust must be pre-existing, because Type Ia supernovae do not create dust in their explosions. This pre-existing dust slows down the expanding shell and causes the observed deformation of the remnant. We use this knowledge to calculate the direction of the offset and are therefore able to derive the actual supernova explosion site in relation to the geometric center of the remnant. Image credit: Borkowski et al. (2006)

supernova event has nearly identical uncertainties in the two axes, we can make an accurate simplification that the final error ellipses are error circles. These error circles will depend on the probability level for containing the ex-companion (e.g., 99.73%) and on the adopted proper motion of the ex-companion star (typically 100 km s^{-1} for red giants, 250 km s^{-1} for subgiants, and 390 km s^{-1} for main-sequence stars). The 99.73% error circle radii are $0.74''$ for red giants, $1.06''$ for subgiants, and $1.17''$ for main-sequence stars. For the most conservative case (a $1.16 M_{\odot}$ main-sequence companion and a 550 year old remnant), the 3σ error circle is $1.43''$ in radius. Thus, our main result is that any ex-companion star of SNR 0509-67.5 must be within $1.43''$ of 05:09:30.976, -67:31:17.90 (J2000). This maximal error circle is drawn on the combined Hα+BVI image in Figure 5.2.

A combination of fortuitous circumstances allows for our small error circle (roughly 10% of the shell radius). First, the supernova is quite young (400±50 years), so the companion star has not had much time to move far from the site of the explosion. Second, the shell is nicely symmetrical, and this allows us to accurately determine the geometric center. Third, the *Spitzer* images demonstrate that the shell's ellipticity is caused by a somewhat denser interstellar medium in one quadrant, which resolves the direction of the offset. In all, the maximum radius of our error circle is $1.43''$. The ex-companion can lie at this extreme only for the case where it is a main-sequence star, it has the lowest acceptable mass ($1.16 M_{\odot}$), the age of the remnant is pushed to its 3σ high value (550 years), the velocity of the companion star is entirely perpendicular to the line of sight, and the measurement errors on the geometric center are at their 3σ extreme. Without such extreme assumptions all occurring together, a main-sequence ex-companion has a two-thirds chance of being in the innermost $0.7''$ of our error circle.

5.4.3 The Contents of the SNR 0509-67.5 Central Region

The error circle is completely empty of all visible point sources down to the deep limits of *HST*. Importantly, there are no red giant or subgiant stars in or near the circle. (Red giants and subgiants can be confidently recognized by their position above the main-sequence in

the color-magnitude diagram.) The nearest red giant (star O in Figure 5.2) is 7.4″ from the center, while the nearest subgiant star (star N) is 5.8″ from the center. The nearest star brighter than $V = 22.7$ mag (star K), that is, the nearest possible ex-companion of any type, is 2.9″ from the center.

The center of our error ellipse contains a nebula that might or might not be a background galaxy. The integrated magnitude for the nebula is $V = 23.32 \pm 0.07$ and $I = 20.95 \pm 0.02$, with a red color. The nebula appears faint in the Hα image, so this is not simply some shard of the outer shell. This nebula has an extended area roughly $2.1'' \times 1.4''$, with a central bright core plus 3−6 knots within this contiguous area, as well as ∼6 isolated, faint, and extended knots outside the main nebula. The center of this nebula is 0.2″ from our best estimate of the position of the supernova explosion. The contiguous region has a maximal distance from the central core of 1.3″, while the farthest of the isolated knots is 2.0″ from the center.

There can be no point source hidden by this nebulosity to the stated limit of $V = 26.9$ mag. To give specific numbers, the V-band image has the brightness in the brightest 3×3 pixel box for the brightest knot equal to 0.15 e/pixel/sec above the background, whereas star A ($V = 26.08$, see Table 5.3) has its brightest 3×3 box equal to 0.33 e/pixel/second above background, which puts the brightest knot at $V = 26.9$. All the knots are definitely extended. No significant source with a point spread function rises above the nebula.

The obvious conclusion is that this nebula is a background galaxy of no relevance to the supernova. The mottled shape and color are like other galaxies at moderate redshift as seen by *HST*. This is reinforced by the presence of four other similarly red and extended galaxies just outside the supernova shell.

Nevertheless, this nebula is strikingly centered at the site of the explosion, and this is suggestive of a connection. With five such objects (red and extended) in the 4500 square arcsecond field of view, the probability of a red nebula appearing inside our 1.60″ radius error circle (with area 8.0 square arcseconds) is 0.9%, although such a posteriori calculations are always problematic. If the nebula is associated with the supernova, then this might represent

very low velocity ejecta left far behind by all the other ejected mass. An alternative idea is that the nebula comes from a double-degenerate progenitor system where the low mass WD is disrupted by the high mass WD, forming a sort of WD accretion disk. The high mass WD accretes from this disk until reaching the Chandrasekhar limit and exploding, leaving behind a potentially large amount of WD material; the remaining accretion disk material would fly away at typical orbital velocities (Piersanti et al. 2003). For the observed nebula, the size and age yields a characteristic velocity for the contiguous region equal to 800 km s^{-1}, while the farthest isolated knot would have a velocity of 1200 km s^{-1} or more. We know of no precedent for such low-velocity material. A possible way to distinguish the likely galaxy identity from the ejecta possibility is to get a spectrum of the nebula, where any ejecta should be bright in emission lines. We have recently obtained Gemini GMOS spectra which may allow us to distinguish between these different possibilities.

Our new limit can be compared to the expected presence of ex-companion stars for the various single-degenerate models (see Table 5.1). There is no red giant star in or near the error circle, and this is strongly inconsistent with the symbiotic progenitor model. There is no red giant or sub-giant star in or near the error circle, and this is strongly inconsistent with the recurrent nova, helium star, and spin-up/spin-down progenitor models. There is no star brighter than $V = 22.7$ mag in or near the error circle, and this is strongly inconsistent with the supersoft X-ray source progenitor model. The lack of any possible ex-companion star to $M_V = +8.4$ mag rules out all published single-degenerate progenitor models. With all single-degenerate models eliminated, the only remaining progenitor model for SNR 0509-67.5 is the double-degenerate model.

5.5 SNR 0519-69.0

The second remnant we examined was SNR 0519-69.0. The light echo shows the supernova spectrum to be that of a normal SN Ia, with an age of 600 ± 200 years (Rest et al. 2005; A.

Rest 2010, private communication). We used the same techniques as in Section 5.4 on SNR 0519-69.0, applied to archival V-band and Hα HST images.

The case of SNR 0519-69.0 is not as optimal as for SNR 0509-67.5, because the SNR is older and more irregular in outline (leading to a substantially larger central error ellipse) and the star density is higher (so the error circle is not empty of stars). The next three subsections detail the size and position of the central error circle, the contents of that region, and the severe constraints on any possible progenitor model. In short, we demonstrate that SNR 0519-69.0 does not have any post-main-sequence ex-companion star, and this rejects the symbiotic, recurrent nova, helium star, and spin-up/spin-down SD models.

5.5.1 Finding the Center of SNR 0519-69.0

We have used public domain images of SNR 0519-69.0 from both *HST* and from the Chandra X-Ray Observatory. The *HST* images were taken with the ACS[7] in April 2011 (original observing program #12017, PI J. P. Hughes, Rutgers[8]). F658N (Hα) and F550M (V-band) observations were taken for a total of 4757 sec and 750 sec, respectively. The data were processed and combined using the standard PyRAF procedures and were analyzed using the IRAF *phot* package. The combined Hα and V image is presented in Figure 5.4. The *Chandra* X-ray observations in June 2000 had a total exposure of 40.6 ks (PI S. S. Holt), with images available in three energy bands: 0.3−0.72 keV, 0.72−1.05 keV, and 1.05−10 keV (Williams et al. 2011).

The geometric center of the SNR was measured by two methods, both using the same procedure, but operating off different data sets corresponding to gas at greatly different temperatures. We constructed nine sets of perpendicular bisectors from edge to edge across the remnant, each tilted approximately 10° from the previous set. The center measurement from each set was retained and averaged together to obtain the geometric center. The RMS scatter of the nine measurements is a good estimate of the measurement uncertainty. Table

[7]See Appendix A.3.1 for more information on ACS.
[8]http://archive.stsci.edu/proposal_search.php?id=12017&mission=hst

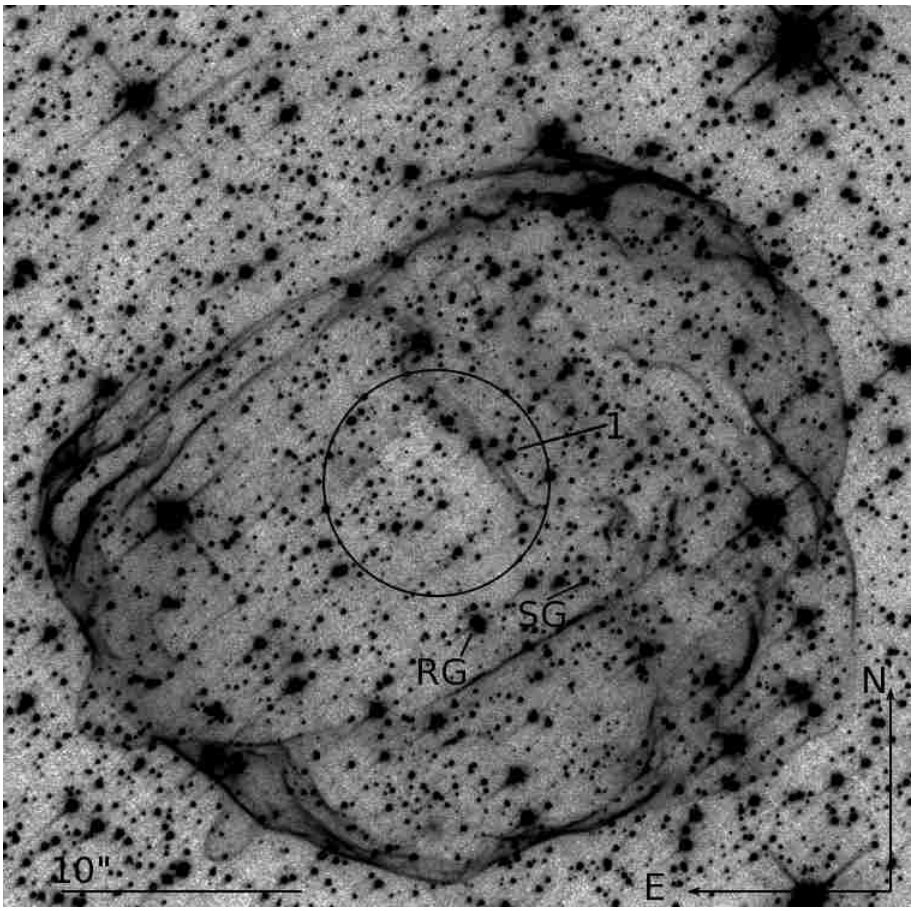

Figure 5.4 *HST* Image of SNR 0519-69.0. The *HST* picture (a combination of the V-band and Hα images) of SNR 0519-69.0 is shown here, with a circle marking the central region of the remnant. The center of this region is calculated from the entire edge of the shell as viewed in Hα and X-ray light. Note that the northeast quadrant of the shell has a faint circular arc outside the prominent arc cutting across the inside of the remnant. Any ex-companion star can be offset from the center due to its original orbital velocity, a kick from the supernova, and ordinary measurement uncertainties in positioning the center, with a $4.7''$ radius circle containing all possible ex-companions at the 99.73% containment probability level. This central region contains 27 main-sequence stars brighter than $V = 22.7$, and any one of these could be an ex-companion star from a supersoft X-ray source progenitor system. The central region does not contain any red giants or subgiants, and this eliminates all the single-degenerate models that require a post-main-sequence companion, including the symbiotic, recurrent nova, helium donor star, and spin-up/spin-down models. Only two published models remain, so the Type Ia supernova that created SNR 0519-69.0 must have come from either a double-degenerate system or a supersoft X-ray source. The star marked 1 is the brightest main-sequence star in the central region, and the nearest red giant and subgiant (both outside the central region) are labeled RG and SG, respectively.

Table 5.5. Positions in SNR 0519-69.0

Position	RA (J2000)	Dec. (J2000)	Radius ($''$)	Confidence
Geometric center in Hα	05:19:34.80	-69:02:06.46	0.7	1σ
Geometric center in X-ray	05:19:34.87	-69:02:07.38	0.7	1σ
Combined geometric center of SNR	05:19:34.83	-69:02:06.92	0.9	1σ
Site of explosion	05:19:34.83	-69:02:06.92	1.3	1σ
Red Giant ex-companion	05:19:34.83	-69:02:06.92	4.3	3σ
Subgiant ex-companion	05:19:34.83	-69:02:06.92	4.5	3σ
Main-sequence ex-companion	05:19:34.83	-69:02:06.92	4.7	3σ

5.5 presents the geometric centers for both the Hα shell and the X-ray shell. These two positions differ by $0.5''$ from the average, which is a measure of the systematic uncertainty from any one position by this method. The two centers have similar measurement uncertainty, and we know of no reason to prefer one over the other, so the overall best estimate of the geometric center is taken to be a straight average of the two positions: 05:19:34:83, -69:02:06.92 (J2000). The uncertainty in this best geometric center comes from the addition in quadrature of the measurement error ($0.7''$) and the systematic uncertainty ($0.5''$), for a total of $0.9''$.

5.5.2 Finding the Offset of SNR 0519-69.0

The offset from the geometric center to the explosion site arises from asymmetries in the ejection velocity and the surrounding interstellar medium. As described in Section 5.4.2, the ejection velocity asymmetries are expected to be small, less than 10%, while any bipolar component of the ejection will produce zero offset. Asymmetric bubbles or clumps of gas or dust surrounding the expanding shell will produce an offset. In all of these cases, the mechanism that causes the offset will also deform the edges of the shell, causing an out-of-round axis ratio. We can derive the offset from the measured axis ratio, but unfortunately the *direction* of the offset depends on knowing the cause of the deformation. For SNR0519-69.0, the shell is closely round with no apparent deformation. The edges of the shell display minor small-scale bumps, but such will lead to no significant offset. The *Spitzer* 24μ infrared image shows the swept up and heated dust grains (Williams et al. 2011), with three broad

brightenings evenly distributed around the edge of SNR 0519-69.0, showing no apparent association with asymmetries, so it appears that there are no systematic variations that deform one quadrant of the shell or cause any significant offset. A substantial qualification on this statement is that one quadrant of the remnant (towards the northeast), has a faint and thin outer arc, with a much brighter inner arc that looks like it has run into some relatively dense region of the gas and dust. The outer edge, however, is closely circular, so the best evidence is that the outer edge is not affected by either type of asymmetry, hence there is a near zero offset between the geometric center and the site of the explosion. This conclusion will have some 1σ uncertainty attached to it, and we take this to be close to the RMS variation in the outer radius of the remnant, which is 5% of the radius of the SNR (i.e., $0.9''$). When combined with the measured position of the geometric center, we get the position of the explosion with an uncertainty of $0.9''$ added in quadrature with $0.9''$, to get a total uncertainty of $1.3''$.

The position of any ex-companion star will be offset from the explosion site due to the proper motion of the star. The orbital velocity of the companion will depend on its mass and size (because it is filling its Roche lobe). The kick velocity onto the companion will be perpendicular to the orbital velocity, and will depend substantially on the size and closeness of the companion. These effects have been calculated by Canal et al. (2001); Marietta et al. (2000); Pan et al. (2010) and above in Section 5.4.2. For red giant and subgiant companions, the orbital velocities and kick velocities will be relatively small, 100 and 250 km s^{-1}, respectively. For main-sequence companion stars, it is critical to realize that all models require the star to be more massive than $1.16 M_{\odot}$, as this is the limit required to drive fast accretion onto the white dwarf (Section 5.2; Langer et al. 2000). With this limit on the mass, the orbital velocity (relative to the WD) plus the kick velocity require the relative space velocity of any main-sequence progenitor companion to be 390 km s^{-1} or less. For a distance modulus to the LMC of 18.50 ± 0.10 mag (Freedman et al. 2001; Schaefer 2008), a velocity of 390 km s^{-1} over a time interval of 600 ± 200 years corresponds to a

maximum proper motion of $1.0 \pm 0.3''$. The proper motion will be $0.25 \pm 0.08''$ and $0.6 \pm 0.2''$ for red giants and subgiants, respectively.

The size of the final error circle depends on the class of the companion and the confidence level required to be contained within the circle. The distribution of the uncertainties for the geometric center and the offset to the explosion site are Gaussian, but the distribution for the proper motion is edge dominated, so a convolution is needed to express the final distribution for the position of any ex-companion. We report the error circle radii for which 99.73% (i.e., 3σ) of the ex-companion stars will be contained. We calculate that for the minimal mass main-sequence star, the 99.73% error radius is $4.7''$. For subgiants and red giants, the error circles are $4.5''$ and $4.3''$ respectively.

5.5.3 The Contents of the SNR 0519-69.0 Central Region

We have just two bands for our *HST* images, V (F550M) and Hα (F658N). For each of the stars in the two images, we have performed aperture photometry with the standard *HST* ACS zeros. The limiting magnitude is $V = 26.05$ to the 5σ detection threshold. We calculate a non-standard color, $V-$ Hα. For all 127 stars within the $4.7''$ error radius, we have tabulated the *HST* astrometry and photometry in Table 5.6. We have added two stars of interest outside the error circle, the nearest red giant (labeled RG in Table 5.6 and Figure 5.4) and the nearest subgiant (labeled SG). The brightest star in the error circle (labeled 1) is listed next in the table, followed by the rest of the stars within the circle, listed in order of their angular distance from the center (Θ).

Table 5.6. Stars Inside Central Error Circle for SNR 0519-69.0

Star	RA (J2000)	Dec. (J2000)	Θ ($''$)	V (mag)	$V-$Hα (mag)	Comments
RG	05:09:34.261	-69:02:05.74	3.3	19.69 ± 0.00	-0.01 ± 0.01	Brightest star in circle
SG	05:09:34.521	-69:02:12.70	6.0	19.13 ± 0.00	0.47 ± 0.00	Nearest Red Giant
1	05:09:33.680	-69:02:10.97	7.4	20.78 ± 0.01	0.35 ± 0.01	Nearest possible subgiant
2	05:09:34.850	-69:02:06.83	0.1	23.37 ± 0.02	0.37 ± 0.04	...
3	05:09:34.787	-69:02:06.69	0.4	25.67 ± 0.15	...	...
4	05:09:34.801	-69:02:07.27	0.4	25.22 ± 0.10	0.68 ± 0.16	...
5	05:09:34.884	-69:02:07.57	0.7	23.97 ± 0.03	0.56 ± 0.06	...
6	05:09:34.967	-69:02:06.82	0.7	23.47 ± 0.03	0.43 ± 0.05	...
7	05:09:34.954	-69:02:07.32	0.8	22.09 ± 0.01	0.16 ± 0.02	V<22.7 MS star
8	05:09:34.791	-69:02:07.80	0.9	20.54 ± 0.01	0.04 ± 0.01	V<22.7 MS star
9	05:09:35.020	-69:02:06.66	1.0	24.32 ± 0.05	0.46 ± 0.10	...
10	05:09:34.967	-69:02:06.11	1.1	22.62 ± 0.01	0.39 ± 0.03	V<22.7 MS star
11	05:09:35.058	-69:02:06.70	1.2	24.95 ± 0.08	0.37 ± 0.18	...
12	05:09:34.773	-69:02:05.72	1.2	24.23 ± 0.04	0.36 ± 0.12	...
13	05:09:34.600	-69:02:07.38	1.3	25.13 ± 0.10	0.83 ± 0.17	...
14	05:09:34.821	-69:02:05.41	1.5	21.97 ± 0.01	0.30 ± 0.02	V<22.7 MS star
15	05:09:35.088	-69:02:07.80	1.6	24.77 ± 0.06	0.57 ± 0.12	...
16	05:09:35.068	-69:02:05.60	1.8	24.52 ± 0.06	...	...
17	05:09:34.629	-69:02:05.43	1.9	25.70 ± 0.15	...	...
18	05:09:34.973	-69:02:08.68	1.9	21.07 ± 0.01	0.59 ± 0.01	V<22.7 MS star
19	05:09:35.198	-69:02:07.36	2.0	24.95 ± 0.07	0.57 ± 0.16	...
20	05:09:35.196	-69:02:06.39	2.0	26.03 ± 0.19	...	...
21	05:09:34.850	-69:02:08.95	2.0	25.37 ± 0.11	0.78 ± 0.17	...
22	05:09:35.129	-69:02:08.22	2.0	24.00 ± 0.03	0.60 ± 0.06	...
23	05:09:35.068	-69:02:08.58	2.1	24.86 ± 0.07	0.67 ± 0.12	...
24	05:09:35.189	-69:02:07.94	2.2	25.15 ± 0.08	0.29 ± 0.21	...
25	05:09:35.250	-69:02:06.80	2.2	23.52 ± 0.03	0.23 ± 0.06	...
26	05:09:34.486	-69:02:05.66	2.3	23.57 ± 0.03	1.02 ± 0.04	...
27	05:09:34.726	-69:02:04.72	2.3	24.02 ± 0.04	0.75 ± 0.08	...
28	05:09:34.529	-69:02:05.29	2.3	20.19 ± 0.00	0.13 ± 0.01	V<22.7 MS star
29	05:09:35.053	-69:02:04.90	2.3	23.82 ± 0.03	0.68 ± 0.06	...
30	05:09:34.683	-69:02:04.74	2.3	23.92 ± 0.03	0.80 ± 0.07	...
31	05:09:35.007	-69:02:09.07	2.3	26.02 ± 0.19	...	...
32	05:09:34.836	-69:02:04.53	2.4	24.85 ± 0.07	0.64 ± 0.16	...
33	05:09:35.145	-69:02:08.75	2.5	20.61 ± 0.01	0.14 ± 0.01	V<22.7 MS star
34	05:09:34.428	-69:02:08.09	2.5	24.75 ± 0.07	0.71 ± 0.13	...
35	05:09:34.412	-69:02:05.90	2.5	25.19 ± 0.09	1.37 ± 0.13	...
36	05:09:34.768	-69:02:04.38	2.6	21.98 ± 0.01	0.55 ± 0.02	V<22.7 MS star
37	05:09:35.286	-69:02:06.05	2.6	24.60 ± 0.06	0.66 ± 0.11	...
38	05:09:34.457	-69:02:08.55	2.6	25.05 ± 0.08	0.82 ± 0.15	...
39	05:09:34.584	-69:02:09.15	2.6	25.0 ± 0.1	1.7 ± 0.1	...
40	05:09:35.312	-69:02:07.42	2.6	23.31 ± 0.02	0.48 ± 0.04	...
41	05:09:34.728	-69:02:04.34	2.6	21.14 ± 0.01	0.52 ± 0.01	V<22.7 MS star
42	05:09:34.540	-69:02:09.05	2.7	25.8 ± 0.1	1.8 ± 0.1	...
43	05:09:34.759	-69:02:09.55	2.7	24.77 ± 0.06	0.93 ± 0.09	...
44	05:09:34.789	-69:02:04.20	2.7	23.9 ± 0.1	2.4	...
45	05:09:35.345	-69:02:06.93	2.7	22.20 ± 0.01	0.39 ± 0.02	V<22.7 MS star
46	05:09:35.290	-69:02:08.18	2.7	24.22 ± 0.04	0.32 ± 0.10	...
47	05:09:34.568	-69:02:09.28	2.8	23.94 ± 0.03	0.69 ± 0.05	...
48	05:09:34.345	-69:02:06.08	2.8	23.28 ± 0.02	0.75 ± 0.04	...
49	05:09:34.460	-69:02:08.84	2.8	24.38 ± 0.05	0.63 ± 0.09	...
50	05:09:35.336	-69:02:07.72	2.8	25.10 ± 0.09	0.70 ± 0.16	...
51	05:09:35.254	-69:02:08.75	2.9	21.91 ± 0.01	0.08 ± 0.02	V<22.7 MS star
52	05:09:34.337	-69:02:05.71	2.9	25.1 ± 0.1	...	...
53	05:09:34.387	-69:02:05.23	2.9	20.56 ± 0.01	0.17 ± 0.01	V<22.7 MS star
54	05:09:34.924	-69:02:04.00	3.0	24.83 ± 0.07	0.76 ± 0.14	...
55	05:09:34.686	-69:02:04.06	3.0	24.55 ± 0.06	1.12 ± 0.10	...
56	05:09:34.663	-69:02:09.77	3.0	20.45 ± 0.00	0.11 ± 0.01	V<22.7 MS star

Table 5.6—Continued

Star	RA (J2000)	Dec. (J2000)	Θ (″)	V (mag)	$V-$Hα (mag)	Comments
57	05:09:34.267	-69:02:07.22	3.1	24.60 ± 0.06	1.23 ± 0.09	...
58	05:09:35.342	-69:02:05.51	3.1	23.99 ± 0.03	0.70 ± 0.06	...
59	05:09:35.400	-69:02:07.57	3.1	25.66 ± 0.14	...	...
60	05:09:35.427	-69:02:07.78	3.3	25.51 ± 0.13	...	...
61	05:09:34.859	-69:02:03.62	3.3	21.17 ± 0.01	0.34 ± 0.01	V<22.7 MS star
62	05:09:34.217	-69:02:06.37	3.4	25.06 ± 0.08	...	...
63	05:09:35.327	-69:02:04.82	3.4	24.81 ± 0.06	0.93 ± 0.11	...
64	05:09:35.405	-69:02:08.47	3.4	23.13 ± 0.02	0.24 ± 0.04	...
65	05:09:34.759	-69:02:10.38	3.5	24.93 ± 0.07	0.95 ± 0.10	...
66	05:09:35.415	-69:02:05.32	3.5	23.06 ± 0.02	0.51 ± 0.03	...
67	05:09:34.511	-69:02:09.98	3.5	22.89 ± 0.02	0.38 ± 0.03	...
68	05:09:35.002	-69:02:03.51	3.5	24.2 ± 0.1	1.0 ± 0.2	...
69	05:09:35.459	-69:02:08.06	3.5	22.71 ± 0.02	0.42 ± 0.03	...
70	05:09:34.959	-69:02:03.44	3.5	22.26 ± 0.01	0.46 ± 0.02	V<22.7 MS star
71	05:09:35.153	-69:02:03.79	3.6	22.33 ± 0.01	0.46 ± 0.02	V<22.7 MS star
72	05:09:34.907	-69:02:03.35	3.6	24.27 ± 0.05	1.10 ± 0.08	...
73	05:09:34.260	-69:02:05.07	3.6	22.06 ± 0.01	0.40 ± 0.02	V<22.7 MS star
74	05:09:35.486	-69:02:06.01	3.6	22.96 ± 0.02	0.56 ± 0.03	...
75	05:09:34.202	-69:02:08.27	3.7	24.06 ± 0.04	0.57 ± 0.07	...
76	05:09:35.376	-69:02:09.19	3.7	24.86 ± 0.07	0.49 ± 0.13	...
77	05:09:35.209	-69:02:10.04	3.7	24.18 ± 0.04	0.43 ± 0.08	...
78	05:09:35.298	-69:02:09.70	3.7	24.07 ± 0.04	0.56 ± 0.06	...
79	05:09:35.508	-69:02:07.86	3.7	24.81 ± 0.07	0.33 ± 0.17	...
80	05:09:35.064	-69:02:03.37	3.8	22.37 ± 0.01	0.32 ± 0.03	V<22.7 MS star
81	05:09:34.148	-69:02:07.71	3.8	24.17 ± 0.04	1.35 ± 0.05	...
82	05:09:34.167	-69:02:08.12	3.8	24.31 ± 0.05	0.60 ± 0.09	...
83	05:09:34.362	-69:02:04.03	3.8	24.43 ± 0.05	0.77 ± 0.10	...
84	05:09:34.880	-69:02:03.06	3.9	22.04 ± 0.01	0.43 ± 0.02	V<22.7 MS star
85	05:09:35.313	-69:02:04.00	3.9	25.30 ± 0.11	0.74 ± 0.21	...
86	05:09:34.143	-69:02:05.77	3.9	24.15 ± 0.04	0.32 ± 0.11	...
87	05:09:35.322	-69:02:09.84	3.9	23.43 ± 0.03	0.47 ± 0.04	...
88	05:09:35.257	-69:02:10.12	3.9	25.23 ± 0.10	0.91 ± 0.14	...
89	05:09:35.368	-69:02:04.24	3.9	24.49 ± 0.05	0.64 ± 0.10	...
90	05:09:34.229	-69:02:04.72	3.9	23.49 ± 0.03	0.56 ± 0.05	...
91	05:09:34.158	-69:02:05.07	4.1	24.06 ± 0.04	0.50 ± 0.09	...
92	05:09:35.480	-69:02:04.76	4.1	24.23 ± 0.04	0.40 ± 0.09	...
93	05:09:34.157	-69:02:08.76	4.1	20.36 ± 0.00	0.12 ± 0.01	V<22.7 MS star
94	05:09:34.258	-69:02:04.23	4.1	24.80 ± 0.07	0.45 ± 0.17	...
95	05:09:35.336	-69:02:03.80	4.1	25.23 ± 0.10	0.69 ± 0.20	...
96	05:09:35.042	-69:02:10.92	4.2	25.15 ± 0.09	...	...
97	05:09:35.579	-69:02:05.65	4.2	24.19 ± 0.04	0.92 ± 0.06	...
98	05:09:35.382	-69:02:09.96	4.2	24.37 ± 0.05	0.66 ± 0.08	...
99	05:09:34.217	-69:02:04.26	4.3	24.4 ± 0.1	0.5 ± 0.2	...
100	05:09:34.944	-69:02:11.14	4.3	23.40 ± 0.02	0.43 ± 0.04	...
101	05:09:34.669	-69:02:11.11	4.3	25.13 ± 0.09	0.93 ± 0.13	...
102	05:09:34.211	-69:02:04.22	4.3	24.4 ± 0.1	0.5 ± 0.2	...
103	05:09:34.034	-69:02:06.90	4.3	24.32 ± 0.05	0.63 ± 0.10	...
104	05:09:35.417	-69:02:03.94	4.3	21.82 ± 0.01	0.32 ± 0.02	V<22.7 MS star
105	05:09:34.168	-69:02:09.33	4.3	22.44 ± 0.01	0.38 ± 0.02	V<22.7 MS star
106	05:09:34.829	-69:02:02.59	4.3	25.68 ± 0.16	1.38 ± 0.23	...
107	05:09:34.046	-69:02:07.89	4.3	24.79 ± 0.06	1.18 ± 0.09	...
108	05:09:35.587	-69:02:08.60	4.4	23.18 ± 0.02	0.45 ± 0.04	...
109	05:09:35.492	-69:02:04.31	4.4	20.46 ± 0.00	-0.03 ± 0.01	V<22.7 MS star
110	05:09:35.251	-69:02:10.70	4.4	25.35 ± 0.11	0.72 ± 0.18	...
111	05:09:34.641	-69:02:02.63	4.4	22.92 ± 0.02	0.49 ± 0.04	...
112	05:09:34.586	-69:02:02.70	4.4	25.85 ± 0.19	...	...
113	05:09:35.401	-69:02:10.17	4.4	24.85 ± 0.07	0.97 ± 0.10	...
114	05:09:35.089	-69:02:02.61	4.5	25.14 ± 0.10	1.35 ± 0.14	...

Table 5.6—Continued

Star	RA (J2000)	Dec. (J2000)	Θ ($''$)	V (mag)	$V-$Hα (mag)	Comments
115	05:09:35.656	-69:02:05.77	4.6	22.18 ± 0.01	0.50 ± 0.02	V<22.7 MS star
116	05:09:34.653	-69:02:11.38	4.6	25.00 ± 0.08	0.43 ± 0.16	...
117	05:09:35.009	-69:02:11.40	4.6	25.25 ± 0.09	0.97 ± 0.13	...
118	05:09:33.997	-69:02:07.92	4.6	23.62 ± 0.03	0.55 ± 0.05	...
119	05:09:34.894	-69:02:11.53	4.6	23.30 ± 0.02	0.34 ± 0.04	...
120	05:09:35.638	-69:02:05.19	4.6	24.85 ± 0.06	0.88 ± 0.11	...
121	05:09:35.391	-69:02:03.32	4.7	22.21 ± 0.01	0.35 ± 0.02	V<22.7 MS star
122	05:09:35.053	-69:02:02.39	4.7	23.55 ± 0.03	0.88 ± 0.05	...
123	05:09:35.689	-69:02:07.98	4.7	20.85 ± 0.01	-0.10 ± 0.01	V<22.7 MS star
124	05:09:35.583	-69:02:09.39	4.7	23.96 ± 0.03	0.57 ± 0.06	...
125	05:09:34.040	-69:02:04.92	4.7	24.92 ± 0.08	0.30 ± 0.21	...
126	05:09:34.187	-69:02:10.11	4.7	23.91 ± 0.03	0.50 ± 0.07	...
127	05:09:35.704	-69:02:06.17	4.7	24.22 ± 0.04	0.63 ± 0.07	...

We have constructed a color-magnitude diagram with the V and $V-$Hα magnitudes, which can be seen in Figure 5.5. This can be converted to an HR diagram with the distance modulus to the LMC of 18.50 ± 0.10. Unfortunately, this HR diagram uses nonstandard colors, as this is all that is currently available from *HST*. The wavelength separation between the two bands is not as large as desired, and this makes for relatively small separation between subgiants and main-sequence stars. The exposure times (12.5 minutes in V and 79 minutes in Hα) along with the narrow bandpass for Hα make for relatively poor photon statistics at the faint end. Nevertheless, the *HST* HR diagram for SNR 0519-69.0 shows a clear main-sequence, red clump, and red giant branch. This allows for simple identification of each star by its luminosity class. As always, there are difficulties with distinguishing subgiant stars positioned near the main-sequence, and we expect that ordinary measurement errors will shift some of the many main-sequence stars out towards the subgiant region on the HR diagram.

The contents of the central region include 127 stars, of which 27 are main-sequence stars brighter than $V = 22.7$, which could be ex-companion stars for the supersoft X-ray source progenitor model. Thus, there are 27 candidate ex-companion stars. The other 100 stars in the central region are main-sequence stars that are fainter than the required $V = 22.7$, therefore not possible ex-companions. Importantly, the stars in the central region do not include any post-main-sequence stars. That is, there are no red giants or subgiants within

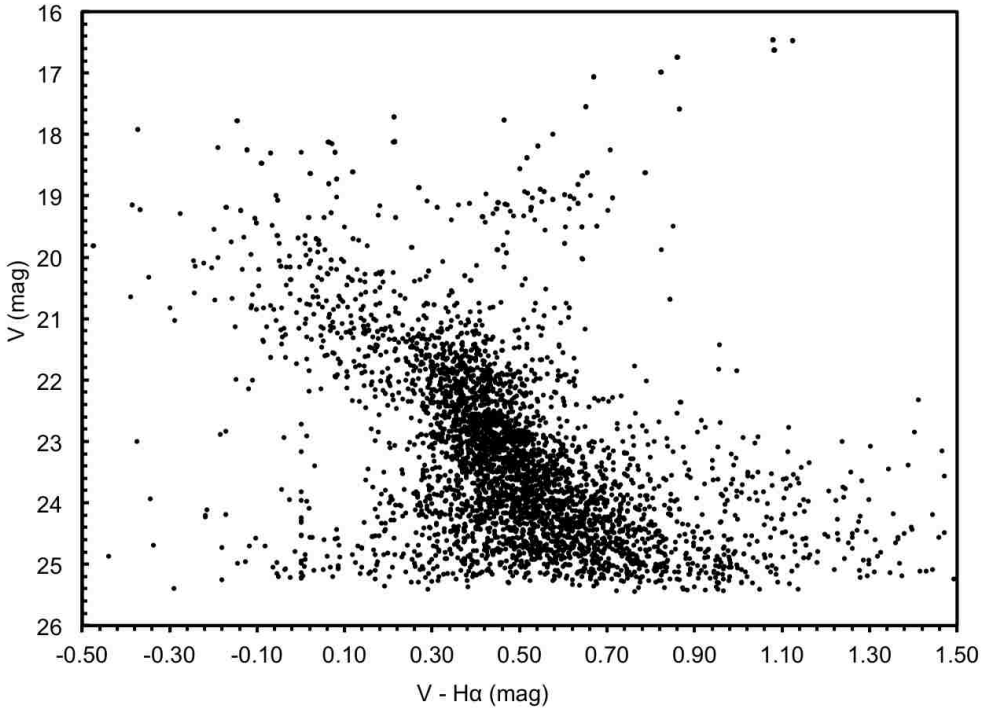

Figure 5.5 $V - \mathrm{H}\alpha$ Color-Magnitude Diagram for SNR 0519-69.0. This $V - \mathrm{H}\alpha$ color-magnitude diagram can be used to identify post-main-sequence stars in the field of SNR 0519-69.0. The $V - \mathrm{H}\alpha$ color index, constructed with the currently-available *HST* images, is unusual, but still shows a clear main-sequence, red clump, and red giant branch.

the 4.7″ error circle. The nearest red giant and subgiant are 6.0″ and 7.4″ from the center, respectively. There is no chance for any progenitor model that has a red giant or subgiant donor star.

The detection or exclusion of ex-companion stars near the center of Type Ia supernova remnants can provide decisive information about the progenitor. For SNR 0519-69.0, the 99.73% error circle contains no post-main-sequence stars, which eliminates the symbiotic, recurrent nova, helium star, and spin-up/spin-down progenitor models. Among the published single-degenerate models, only the supersoft X-ray source model is possible for SNR 0519-69.0. A double-degenerate system has no ex-companion star, so this model is also fully consistent with our images. Thus, for SNR 0519-69.0, the only possible progenitors are a supersoft X-ray source or a double-degenerate.

We note that Badenes et al. (2007) have examined SNR 0519-69.0 for evidence of a large cavity in the circumstellar region that would be carved out by fast, optically thick outflows that occur in the accretion wind scenario proposed for supersoft X-ray sources (Hachisu et al. 1996). They found that the dynamics of the ejecta from SNR 0519-69.0 are inconsistent with the predictions. If the accretion wind scenario is in fact the only possible method for obtaining an SN Ia from a supersoft X-ray source, then the lack of a cavity would exclude the supersoft X-ray source progenitor class for SNR 0519-69.0 and we would be left with the double-degenerate model as the only viable progenitor. Like SNR 0509-67.5, which has been shown to be a double-degenerate, SNR 0519-69.0 also comes from a region with a low star formation history, which slightly favors a delayed progenitor (Badenes et al. 2009).

SNR 0509-67.5 already has a decisive result, where the entire central region is empty of any point source to $V = 26.9$ ($M_{\rm V} = +8.4$), so that all published single-degenerate models are eliminated, and only the double-degenerate model remains. While the SNR 0519-69.0 limits are not as tight (because the supernova is older and the remnant is in an area with much higher star density), nevertheless the result is important as it rules out all but two

Table 5.7. Positions in SNR 0509-68.7

Position	RA (J2000)	Dec. (J2000)	Radius ($''$)	Confidence
Geometric center in Radio	05:08:59.65	-68:43:35.6	0.7	1σ
Geometric center in X-ray	05:08:59.59	-68:43:35.3	0.7	1σ
Combined geometric center of SNR	05:08:59.62	-68:43:35.5	0.5	1σ
Site of explosion	05:08:59.62	-68:43:35.5	0.5	1σ
Main-sequence ex-companion	05:08:59.62	-68:43:35.5	4.4	3σ

possible progenitor classes for this particular supernova, the supersoft X-ray sources and the double-degenerates.

5.6 SNR 0509-68.7

The third LMC Ia SNR we consider is SNR 0509-68.7 (N103B). Again, this remnant has X-ray spectra (Hughes et al. 1995) and light echo observations (Rest et al. 2005; A. Rest 2010, private communication) confirming the Ia nature of the supernova that caused the remnant.

We obtained Gemini GMOS[9] imagery of SNR 0509-68.7 because there were no useful images in the *HST* archive. Only half of the remnant is bright in Hα, as can be seen in Figure 5.6, so we could not use it to locate the geometric center of the remnant. Instead, we used radio (Dickel & Milne 1995) and X-ray images (Figure 5.1c, Lewis et al. 2003; obtained via the Chandra SNR Catalog[10]) and the perpendicular bisector method described in Section 5.4.1 to locate the geometric center. Table 5.7 presents the geometric centers, as well as the explosion site and the distance any possible ex-companion stars could have traveled.

We note that the shell is almost perfectly round in radio and X-ray, with only small out-of-roundness likely caused by random variations. This implies that the explosion site should be at the same location as the geometric center, so we include no formal offset between the two locations, and therefore the explosion site is 05:08:59.62, -68:43:35.5 (J2000). As for SNR 0519-69.0 (Section 5.5.2), the 1σ uncertainty on this is approximately equal to the

[9]See Appendix A.2.2 for more information on GMOS.
[10]http://hea-www.harvard.edu/ChandraSNR/

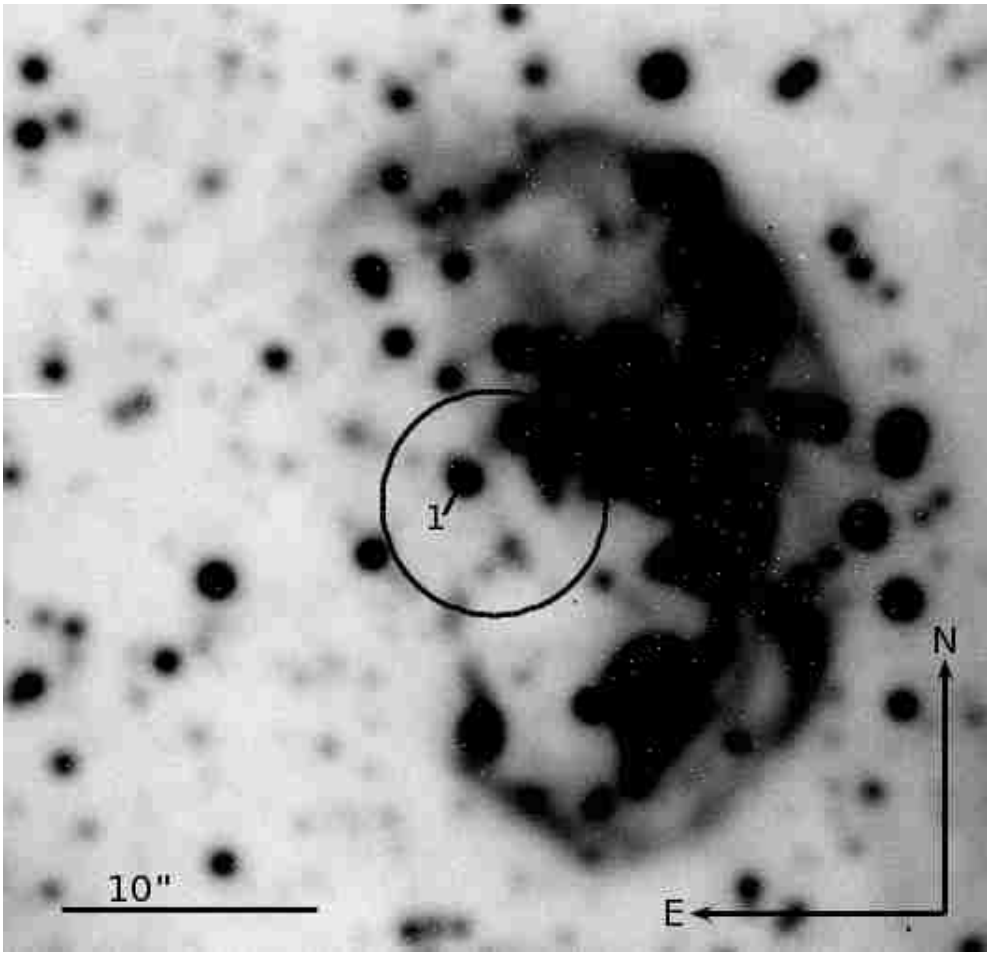

Figure 5.6 Gemini Image of SNR 0509-68.7. This Hα image of SNR 0509-68.7 was taken by the GMOS imager on the 8.1m Gemini South Telescope. The 4.4″ 99.73% containment central region is marked. The biggest and brightest star in the center of the remnant, marked as star 1, is a red giant, and therefore a possible ex-companion from a recurrent nova or symbiotic system. Additionally, there are seven other main-sequence stars inside the error circle that are bright enough to be ex-companions from supersoft X-ray sources. Future GMOS spectroscopy should allow us to identify which of the central stars are likely to be the actual ex-companion, if any.

Table 5.8. Stars Inside Central Error Circle for SNR 0509-68.7

Star	RA (J2000)	Dec. (J2000)	Θ ($''$)	g' (mag)	$g'-i'$ (mag)	Comments
1	05:08:59.824	-68:43:34.54	1.5	18.98 ± 0.00	0.92 ± 0.00	Red Giant
2	05:08:59.482	-68:43:37.30	1.9	19.52 ± 0.01	-0.03 ± 0.01	...
3	05:08:59.675	-68:43:38.12	2.6	20.04 ± 0.01	-0.39 ± 0.02	...
4	05:08:59.110	-68:43:33.52	3.4	22.94 ± 0.12	0.91 ± 0.14	...
5	05:09:00.193	-68:43:33.85	3.5	21.01 ± 0.02	-0.08 ± 0.03	...
6	05:08:58.964	-68:43:34.89	3.6	19.95 ± 0.03	-0.90 ± 0.04	Very Blue, Red Giant Core?
7	05:08:59.868	-68:43:39.22	4.0	20.29 ± 0.01	-0.09 ± 0.02	...
8	05:08:59.294	-68:43:31.97	4.0	22.53 ± 0.07	0.15 ± 0.11	...
9	05:08:59.196	-68:43:38.78	4.0	22.11 ± 0.03	0.46 ± 0.04	...

RMS of the shell radii, which is $0.9''$ for both radio and X-ray, so this is added into the total uncertainty on the site of the eruption.

There are eight possible ex-companion stars located within the central error region of SNR 0509-68.7. The bright central star is clearly a red giant, based on its location on the $g'-i'$ color-magnitude diagram, which can be seen in Figure 5.7, and there are seven main-sequence stars bright enough to have come from supersoft X-ray source binaries. The stars located within the central error region are highlighted with blue diamonds in Figure 5.7 and listed in Table 5.8. Any of these eight stars could be the ex-companion, which means that all SD and DD models are currently possible for SNR 0509-68.7. Further observations of these stars with upcoming Gemini GMOS spectroscopy will hopefully allow us to identify which star, if any, is the ex-companion. In particular we will look for unusually high radial and/or rotational velocities, which would indicate that the star was formerly part of a tight binary.

5.7 SNR 0505-67.9

The final SN Ia remnant in the LMC is SNR 0505-67.9 (DEM L71). There are no light echoes for this 4360-year old remnant, but X-ray spectra show that it is Balmer-dominated and has enhanced Fe abundances, both of which indicate that it is from an SN Ia (Hughes et al. 1998). There are no *HST* observations of this remnant, so we obtained Gemini South

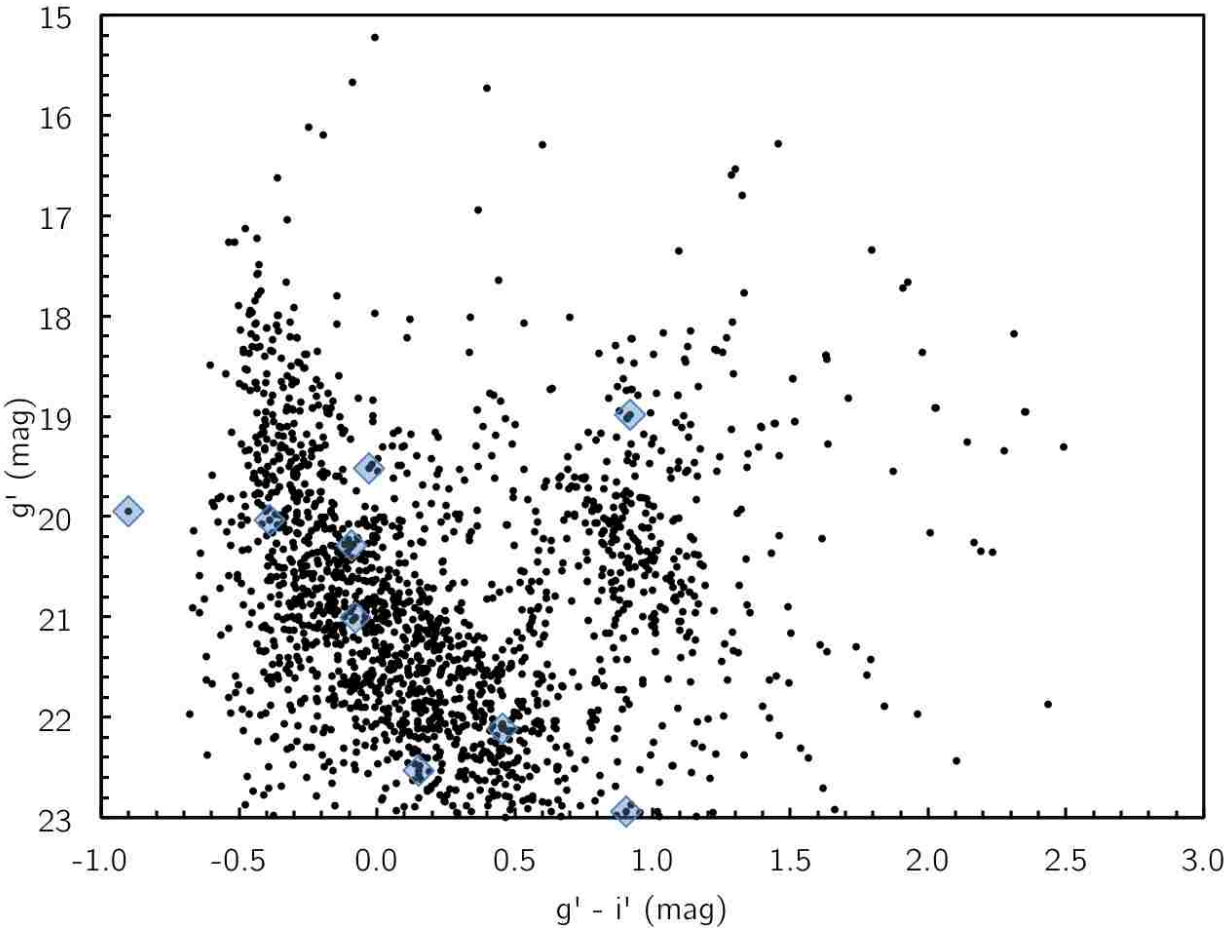

Figure 5.7 $g' - i'$ Color-Magnitude Diagram for SNR 0509-68.7. This $g' - i'$ color-magnitude diagram constructed from our Gemini GMOS observations can be used to identify post-main-sequence stars in the field of SNR 0509-68.7. The stars located within the central region of the supernova remnant are highlighted with blue diamonds. There is one clear red giant as well as seven possible main-sequence ex-companions that are bright enough to have come from supersoft X-ray sources.

Table 5.9. Positions in SNR 0505-67.9

Position	RA (J2000)	Dec. (J2000)	Radius ($''$)	Confidence
Geometric center in Hα	05:05:41.77	-67:52:42.5	0.7	1σ
Geometric center in X-ray (0.7-1.1 keV), extreme outer edge	05:05:41.89	-67:52:42.1	2.0	1σ
Geometric center in X-ray (0.7-1.1 keV), rim of outer shell	05:05:42.27	-67:52:40.3	2.0	1σ
Geometric center in X-ray (0.7-1.1 keV), edge of inner region	05:05:42.46	-67:52:37.7	1.0	1σ
Geometric center in X-ray (0.7-1.1 keV), central minimum	05:05:43.00	-67:52:38.9	2.0	1σ
Combined geometric center of SNR	05:05:42.71	-67:52:43.5	3.2	1σ
Site of explosion	05:05:42.71	-67:52:43.5	3.2	1σ
Main-sequence ex-companion	05:05:42.71	-67:52:43.5	15.8	3σ

GMOS[11] imagery. The GMOS image, with the central error region marked, can be seen in Figure 5.8.

We used both our GMOS Hα images in combination with Chandra X-ray images (Hughes et al. 2003; Rakowski et al. 2003, obtained via the Chandra SNR Catalog[12]) to identify the geometric center of the remnant. For the X-ray images, we used four different gas regions to locate the center: the extreme outer edge, the rim of the outer shell, the edge of the inner region, and the central minimum. These regions can be seen in the Chandra X-ray true-color image shown in Figure 5.1a. All of the center measurements can be seen in Table 5.9. The final explosion site is 05:05:42.71, -67:52:43.5 (J2000).

SNR 0505-67.9 is the oldest of our remnants by far, at 4360 ± 290 years. During this time, any ex-companion star could have moved a great distance, so the final 99.73% containment circle is very large, at $15.8''$. Because of this, there are quite a lot of stars located within the central region, including red giants, subgiants, and main-sequence stars bright enough to have come from supersoft X-ray sources. The color-magnitude diagram for all of the stars in the SNR 0505-67.9 field can be seen in Figure 5.9; the stars located within the central error circle are highlighted with blue diamonds and listed in Table 5.10. Like SNR 0509-68.7, this is another case in which all SD and DD progenitors are still possibilities. With future Gemini GMOS spectra, we will hopefully be able to identify the true ex-companion, based on unusual features such as high radial and/or rotational velocities.

[11]See Appendix A.2.2 for more information on GMOS.
[12]http://hea-www.harvard.edu/ChandraSNR/

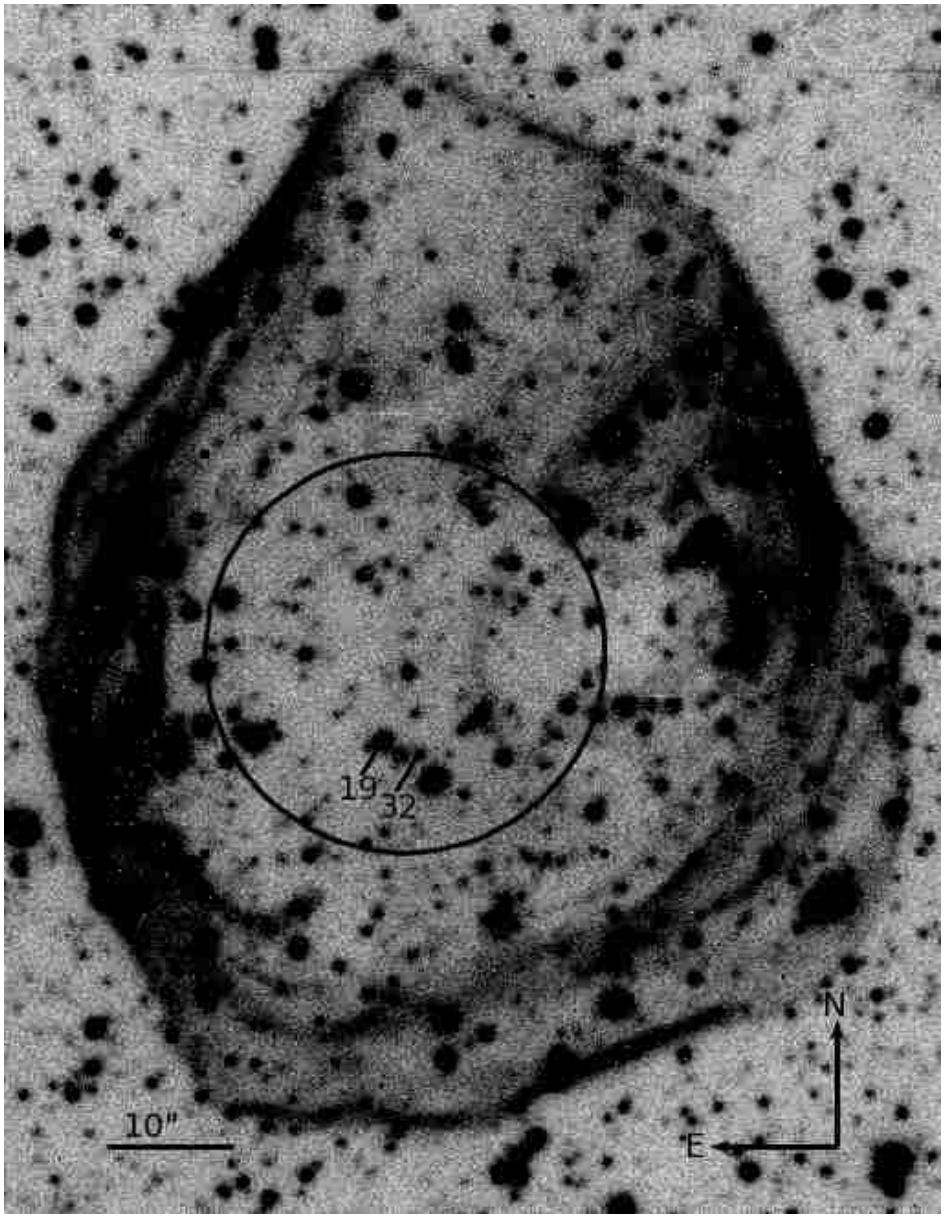

Figure 5.8 Gemini Image of SNR 0505-67.9. This Hα image of SNR 0505-67.9 was taken by the GMOS imager on the 8.1m Gemini South Telescope. The 15.8″ 99.73% containment central region is marked. The error circle is very large because the remnant is so old (4360 years), and therefore it contains a lot of possible ex-companion stars. Stars 19 and 32 are marked; star 19 is the nearest red giant, and star 32 is the nearest subgiant. Future GMOS spectroscopy should allow us to identify which of the central stars are likely to be the actual ex-companion, if any.

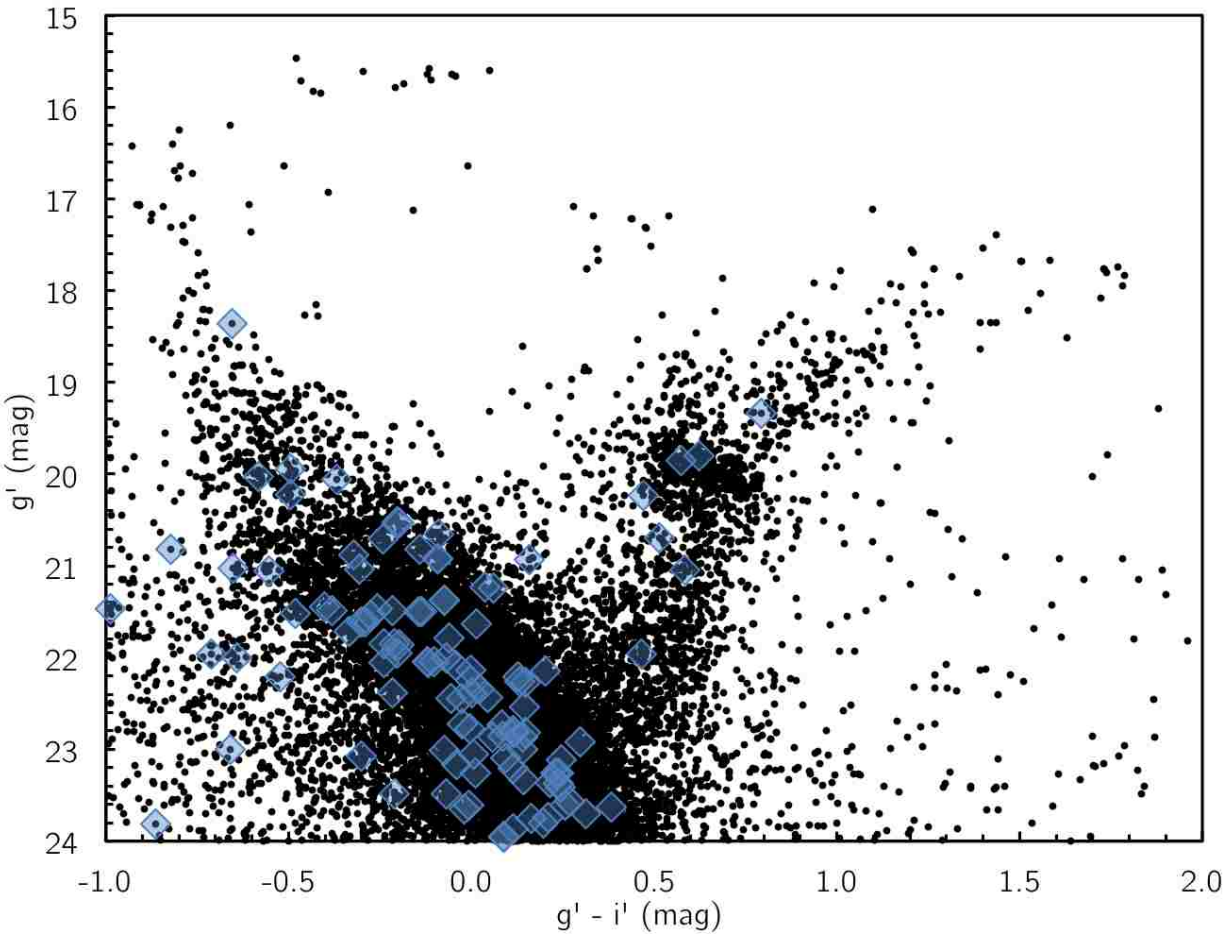

Figure 5.9 $g' - i'$ Color-Magnitude Diagram for SNR 0505-67.9. This $g' - i'$ color-magnitude diagram constructed from our Gemini GMOS observations can be used to identify post-main-sequence stars in the field of SNR 0505-67.9. The stars located within the central region of the supernova remnant are highlighted with blue diamonds. There are many possible ex-companion stars of all different types (main-sequence, subgiant, and red giant). Future GMOS spectroscopy should help us to identify the true ex-companion.

Table 5.10. Stars Inside Central Error Circle for SNR 0505-67.9

Star	RA (J2000)	Dec. (J2000)	Θ ($''$)	g' (mag)	$g' - i'$ (mag)	Comments
1	05:05:42.656	-67:52:41.97	1.5	22.45 ± 0.01	-0.03 ± 0.02	...
2	05:05:42.700	-67:52:45.18	1.7	20.66 ± 0.00	-0.09 ± 0.01	...
3	05:05:42.941	-67:52:45.35	2.3	22.86 ± 0.02	0.14 ± 0.03	...
4	05:05:42.185	-67:52:42.17	3.2	23.26 ± 0.03	0.23 ± 0.04	...
5	05:05:42.524	-67:52:40.10	3.5	23.12 ± 0.02	0.25 ± 0.03	...
6	05:05:42.019	-67:52:44.64	4.0	23.61 ± 0.03	0.26 ± 0.05	...
7	05:05:42.586	-67:52:48.29	4.9	21.78 ± 0.01	-0.06 ± 0.01	...
8	05:05:42.726	-67:52:38.50	5.0	24.10 ± 0.08	-0.02 ± 0.14	...
9	05:05:43.496	-67:52:46.10	5.2	22.82 ± 0.02	0.15 ± 0.03	...
10	05:05:41.984	-67:52:39.90	5.4	24.62 ± 0.09	0.09 ± 0.15	...
11	05:05:42.064	-67:52:39.31	5.5	23.26 ± 0.03	0.24 ± 0.04	...
12	05:05:43.097	-67:52:38.26	5.7	22.38 ± 0.02	0.00 ± 0.03	...
13	05:05:41.892	-67:52:46.96	5.8	22.77 ± 0.02	0.00 ± 0.03	...
14	05:05:43.481	-67:52:47.47	5.9	23.05 ± 0.02	0.01 ± 0.04	...
15	05:05:43.764	-67:52:43.76	6.0	23.57 ± 0.03	0.27 ± 0.05	...
16	05:05:42.718	-67:52:36.80	6.7	22.14 ± 0.02	0.00 ± 0.02	...
17	05:05:43.300	-67:52:37.26	7.1	20.52 ± 0.00	-0.20 ± 0.01	...
18	05:05:41.470	-67:52:41.74	7.2	22.45 ± 0.01	-0.06 ± 0.02	...
19	05:05:43.038	-67:52:50.40	7.2	20.23 ± 0.00	0.47 ± 0.01	Red Giant
20	05:05:43.678	-67:52:48.10	7.2	22.43 ± 0.01	0.04 ± 0.02	...
21	05:05:42.149	-67:52:36.95	7.2	23.87 ± 0.05	0.12 ± 0.07	...
22	05:05:42.966	-67:52:36.33	7.3	22.86 ± 0.04	0.09 ± 0.05	...
23	05:05:43.962	-67:52:40.98	7.5	23.37 ± 0.03	0.24 ± 0.04	...
24	05:05:43.201	-67:52:36.45	7.6	20.53 ± 0.00	-0.20 ± 0.01	...
25	05:05:41.374	-67:52:42.38	7.6	23.26 ± 0.03	0.01 ± 0.04	...
26	05:05:41.836	-67:52:37.58	7.6	23.96 ± 0.06	0.09 ± 0.09	...
27	05:05:41.681	-67:52:38.32	7.7	22.05 ± 0.01	-0.10 ± 0.02	...
28	05:05:41.805	-67:52:49.31	7.7	20.22 ± 0.00	-0.49 ± 0.01	...
29	05:05:41.651	-67:52:48.54	7.8	20.71 ± 0.01	-0.24 ± 0.01	...
30	05:05:43.193	-67:52:50.96	8.0	21.50 ± 0.01	-0.14 ± 0.01	...
31	05:05:44.136	-67:52:43.65	8.1	20.93 ± 0.01	0.16 ± 0.01	Possible Subgiant
32	05:05:42.540	-67:52:51.64	8.2	21.96 ± 0.02	0.47 ± 0.03	Subgiant
33	05:05:44.132	-67:52:45.14	8.2	22.73 ± 0.02	0.08 ± 0.02	...
34	05:05:41.213	-67:52:43.37	8.4	23.81 ± 0.04	0.20 ± 0.06	...
35	05:05:42.825	-67:52:51.87	8.4	20.82 ± 0.01	-0.14 ± 0.01	...
36	05:05:41.410	-67:52:39.16	8.5	22.21 ± 0.02	-0.52 ± 0.05	...
37	05:05:41.377	-67:52:39.27	8.6	22.01 ± 0.02	-0.64 ± 0.04	...
38	05:05:42.102	-67:52:35.49	8.7	23.95 ± 0.06	0.09 ± 0.10	...
39	05:05:42.375	-67:52:34.85	8.8	22.06 ± 0.01	-0.24 ± 0.02	...
40	05:05:42.062	-67:52:51.51	8.8	22.92 ± 0.03	0.30 ± 0.04	...
41	05:05:41.365	-67:52:38.38	9.1	22.05 ± 0.02	-0.12 ± 0.03	...
42	05:05:41.161	-67:52:39.92	9.4	22.09 ± 0.02	-0.04 ± 0.03	...
43	05:05:44.227	-67:52:47.40	9.5	24.91 ± 0.12	0.49 ± 0.16	...
44	05:05:44.286	-67:52:39.83	9.7	22.00 ± 0.01	-0.07 ± 0.02	...
45	05:05:43.878	-67:52:36.17	9.9	24.71 ± 0.08	0.38 ± 0.11	...
46	05:05:44.479	-67:52:42.53	10.1	22.54 ± 0.02	0.15 ± 0.02	...
47	05:05:44.232	-67:52:38.11	10.2	23.75 ± 0.04	0.16 ± 0.07	...
48	05:05:43.048	-67:52:53.46	10.2	23.37 ± 0.03	0.21 ± 0.05	...
49	05:05:41.071	-67:52:39.08	10.2	22.04 ± 0.02	-0.12 ± 0.03	...
50	05:05:41.409	-67:52:36.33	10.2	21.64 ± 0.01	0.02 ± 0.01	...
51	05:05:42.318	-67:52:53.63	10.4	19.33 ± 0.00	0.79 ± 0.00	Red Giant
52	05:05:44.411	-67:52:39.44	10.5	22.35 ± 0.01	0.02 ± 0.02	...
53	05:05:43.030	-67:52:33.17	10.5	21.49 ± 0.01	-0.22 ± 0.01	...
54	05:05:44.025	-67:52:50.83	10.5	24.71 ± 0.10	-0.05 ± 0.16	...
55	05:05:41.081	-67:52:48.83	10.6	24.08 ± 0.06	0.45 ± 0.07	...
56	05:05:44.480	-67:52:39.58	10.8	22.38 ± 0.01	-0.22 ± 0.03	...
57	05:05:41.223	-67:52:36.42	10.9	21.04 ± 0.01	0.58 ± 0.01	Red Giant
58	05:05:40.805	-67:52:45.95	11.0	24.47 ± 0.07	0.16 ± 0.11	...

Table 5.10—Continued

Star	RA (J2000)	Dec. (J2000)	Θ ($''$)	g' (mag)	$g'-i'$ (mag)	Comments
59	05:05:41.353	-67:52:51.99	11.4	20.06 ± 0.00	-0.37 ± 0.00	...
60	05:05:41.967	-67:52:32.49	11.7	23.07 ± 0.03	-0.30 ± 0.06	...
61	05:05:40.884	-67:52:37.60	11.8	21.25 ± 0.01	0.06 ± 0.01	...
62	05:05:44.807	-67:52:42.39	11.9	23.70 ± 0.05	0.31 ± 0.07	...
63	05:05:44.468	-67:52:36.85	12.0	25.27 ± 0.15	0.65 ± 0.19	...
64	05:05:44.154	-67:52:52.23	12.0	22.72 ± 0.02	-0.03 ± 0.02	...
65	05:05:43.909	-67:52:33.59	12.0	21.61 ± 0.01	-0.30 ± 0.01	...
66	05:05:41.872	-67:52:54.62	12.1	21.54 ± 0.01	-0.28 ± 0.01	...
67	05:05:42.489	-67:52:31.22	12.3	23.00 ± 0.02	-0.66 ± 0.05	...
68	05:05:41.623	-67:52:32.71	12.4	21.03 ± 0.01	-0.31 ± 0.01	...
69	05:05:44.837	-67:52:46.77	12.5	22.87 ± 0.03	0.06 ± 0.04	...
70	05:05:40.571	-67:52:39.96	12.5	21.95 ± 0.01	-0.2 ± 0.02	...
71	05:05:42.334	-67:52:31.06	12.6	23.00 ± 0.02	0.14 ± 0.03	...
72	05:05:41.702	-67:52:32.18	12.6	20.89 ± 0.01	-0.32 ± 0.02	...
73	05:05:42.767	-67:52:30.81	12.7	23.49 ± 0.03	-0.21 ± 0.06	...
74	05:05:44.315	-67:52:34.57	12.7	23.65 ± 0.04	-0.02 ± 0.07	...
75	05:05:40.693	-67:52:49.37	12.8	22.26 ± 0.02	0.13 ± 0.02	...
76	05:05:43.392	-67:52:31.15	12.9	19.85 ± 0.00	0.57 ± 0.00	Red Giant
77	05:05:43.953	-67:52:32.64	12.9	21.61 ± 0.01	-0.29 ± 0.01	...
78	05:05:43.806	-67:52:54.91	13.0	23.01 ± 0.02	-0.07 ± 0.04	...
79	05:05:41.477	-67:52:32.37	13.1	21.03 ± 0.01	-0.65 ± 0.01	...
80	05:05:40.510	-67:52:39.25	13.1	21.96 ± 0.01	-0.71 ± 0.03	...
81	05:05:40.406	-67:52:41.40	13.1	24.48 ± 0.09	0.03 ± 0.16	...
82	05:05:41.846	-67:52:31.10	13.3	19.94 ± 0.00	-0.49 ± 0.01	...
83	05:05:41.898	-67:52:56.01	13.3	23.17 ± 0.03	-0.04 ± 0.05	...
84	05:05:40.580	-67:52:49.42	13.4	22.21 ± 0.02	0.13 ± 0.02	...
85	05:05:40.451	-67:52:47.83	13.4	20.02 ± 0.00	-0.58 ± 0.01	...
86	05:05:44.286	-67:52:33.43	13.4	21.86 ± 0.01	-0.2 ± 0.02	...
87	05:05:44.754	-67:52:50.33	13.5	20.82 ± 0.01	-0.82 ± 0.01	...
88	05:05:42.554	-67:52:56.99	13.6	23.41 ± 0.03	0.24 ± 0.05	...
89	05:05:41.559	-67:52:31.51	13.6	21.52 ± 0.02	-0.48 ± 0.04	...
90	05:05:40.580	-67:52:49.88	13.6	22.27 ± 0.02	0.15 ± 0.02	...
91	05:05:40.976	-67:52:52.97	13.6	24.21 ± 0.09	-0.17 ± 0.16	...
92	05:05:44.805	-67:52:50.16	13.6	21.06 ± 0.01	-0.56 ± 0.01	...
93	05:05:44.140	-67:52:54.42	13.6	23.74 ± 0.05	0.21 ± 0.07	...
94	05:05:43.193	-67:52:56.89	13.7	23.81 ± 0.05	-0.86 ± 0.18	...
95	05:05:45.056	-67:52:47.53	13.9	20.92 ± 0.01	-0.09 ± 0.01	...
96	05:05:41.533	-67:52:55.79	14.0	24.17 ± 0.05	0.53 ± 0.07	...
97	05:05:40.551	-67:52:36.52	14.0	23.33 ± 0.04	0.14 ± 0.06	...
98	05:05:44.857	-67:52:50.41	14.0	18.36 ± 0.00	-0.66 ± 0.00	...
99	05:05:45.192	-67:52:42.98	14.1	21.23 ± 0.01	0.04 ± 0.01	...
100	05:05:44.339	-67:52:32.77	14.1	21.85 ± 0.01	-0.21 ± 0.02	...
101	05:05:40.737	-67:52:52.27	14.2	21.85 ± 0.01	-0.24 ± 0.02	...
102	05:05:40.862	-67:52:33.71	14.3	23.63 ± 0.03	0.38 ± 0.05	...
103	05:05:40.417	-67:52:37.40	14.3	23.49 ± 0.05	-0.07 ± 0.08	...
104	05:05:42.989	-67:52:57.78	14.4	21.45 ± 0.01	-0.40 ± 0.02	...
105	05:05:40.155	-67:52:44.92	14.5	21.49 ± 0.02	-0.38 ± 0.03	...
106	05:05:41.245	-67:52:31.56	14.5	23.60 ± 0.04	-0.01 ± 0.06	...
107	05:05:40.165	-67:52:46.14	14.6	21.50 ± 0.02	-0.14 ± 0.03	...
108	05:05:43.808	-67:52:30.28	14.6	22.81 ± 0.02	0.12 ± 0.03	...
109	05:05:41.068	-67:52:54.86	14.7	23.09 ± 0.02	0.09 ± 0.03	...
110	05:05:42.655	-67:52:58.19	14.7	24.13 ± 0.08	0.17 ± 0.11	...
111	05:05:45.160	-67:52:48.43	14.7	20.92 ± 0.01	-0.09 ± 0.01	...
112	05:05:45.264	-67:52:39.39	15.0	19.80 ± 0.00	0.62 ± 0.00	Red Giant
113	05:05:44.076	-67:52:56.48	15.1	21.47 ± 0.01	-0.26 ± 0.02	...
114	05:05:44.076	-67:52:56.48	15.1	21.47 ± 0.01	-0.99 ± 0.02	...
115	05:05:40.067	-67:52:40.55	15.2	20.70 ± 0.00	0.52 ± 0.00	Red Giant
116	05:05:41.520	-67:52:29.76	15.2	22.15 ± 0.02	0.20 ± 0.03	...

Table 5.10—Continued

Star	RA (J2000)	Dec. (J2000)	Θ ($''$)	g' (mag)	$g'-i'$ (mag)	Comments
117	05:05:43.513	-67:52:28.91	15.3	22.80 ± 0.03	0.12 ± 0.04	...
118	05:05:43.158	-67:52:58.62	15.4	21.37 ± 0.01	-0.07 ± 0.01	...
119	05:05:45.451	-67:52:43.19	15.5	21.71 ± 0.01	-0.33 ± 0.02	...
120	05:05:43.281	-67:52:58.72	15.6	21.37 ± 0.01	-0.07 ± 0.01	...
121	05:05:39.931	-67:52:44.68	15.7	22.26 ± 0.02	0.00 ± 0.03	...
122	05:05:40.292	-67:52:35.58	15.7	24.06 ± 0.08	0.33 ± 0.10	...
123	05:05:40.863	-67:52:55.37	15.8	23.21 ± 0.03	0.11 ± 0.04	...

5.8 Implications

Considering all the local SNe Ia, we appear to have a mix of progenitors. LMC SNR 0509-67.5 certainly came from a DD progenitor (Section 5.4 and Schaefer & Pagnotta 2012). SN 1572 (Tycho's SN) likely has a subgiant companion, which indicates a recurrent nova or supersoft X-ray source progenitor (Ruiz-Lapuente et al. 2004). For the rest of the local SNe Ia, we can only place limits, some stricter than others, at this time. Red giant and subgiant companions have been excluded for SN 1006 (Ruiz-Lapuente et al. 2011) and possibly for SN 2011fe (Bloom et al. 2012; Li et al. 2011; Nugent et al. 2011), although this is still under debate. For LMC SNR 0519-69.0, we have shown that we can definitively exclude red giants and subgiants, but have possible main-sequence companion stars (Section 5.5 and Edwards et al. 2012). For the other two LMC SNRs, SNR 0509-68.7 and SNR 0505-67.9, we have a number of possible ex-companion stars in the central error regions (Sections 5.6 and 5.7). A summary of the current progenitor possibilities is presented in Figure 5.10.

If we knew it to be true that all SNe Ia came from identical progenitor systems, we could extrapolate the DD progenitor result from SNR 0509-67.5 to the entire SNe Ia population. However, we do not know this to be true. In fact, there is strong evidence that there may be multiple channels that lead to the observed SN Ia population. Brandt et al. (2010) examined a set of 101 SNe Ia from the Sloan Digital Sky Survey (all with $z \lesssim 0.3$) and found a striking distinction between low- and high-stretch SNe, with the high-stretch SNe coming from a younger population ($\lesssim$400 Myr between the birth of the progenitor system and the explosion, known as the delay time) and low-stretch SNe coming from a much

	Double-Degenerate	Single-Degenerate		
Supernova	White Dwarf?	Main Sequence?	Subgiant?	Red Giant?
LMC SNR 0509-67.5	✓	✗	✗	✗
LMC SNR 0519-69.0	?	?	✗	✗
LMC SNR 0505-67.9	?	?	?	?
LMC SNR 0509-68.7	?	?	?	?
SN 1006	?	?	✗	✗
SN 1572 (Tycho)	?	✗	✓?	✗
SN 2011fe	?	✓?	✗?	✗

Figure 5.10 Comparison of Local Type Ia Supernova Progenitors. The LMC SNR results are ours, SN 1006 is from (Ruiz-Lapuente et al. 2011), SN 1572 (Tycho) is from Ruiz-Lapuente et al. (2004), and SN 2011fe is from Bloom et al. (2012), Li et al. (2011), and Nugent et al. (2011). A "?" alone indicates a possible companion of that type; when combined with a check or an "x" it indicates uncertainty on the result. We appear to have a mix of different progenitors for the local Type Ia supernovae, which is not unsurprising given the recent strong indications of multiple progenitor channels.

older population ($\gtrsim$2.4 Gyr delay time). They find that intermediate-age progenitors do not contribute significantly to either the low- or high-stretch populations. (They define $s = 0.92$ to be the dividing line between low- and high-stretch SNe.) No single progenitor model is able to reproduce the observed stretches and delay times in their sample.

Greggio (2010) constructed model delay time distributions which show that if there is a dual progenitor channel (a situation which is neither ruled out nor favored by her model), the early-type galaxies (with short delay times) should have a uniform progenitor class consisting of DDs almost (if not entirely) exclusively, while later-type galaxies should have SD and DD events at approximately equal rates. It is worth noting, however, that Maoz & Mannucci (2011) find nearly the opposite, that DD events should dominate both short- and long-delay times, with SDs contributing only at short-delay times, i.e., in early-type galaxies, where the observational uncertainties are greatest. Although the results of delay time distribution studies are currently not in agreement, it is clear that a dual progenitor channel is not only possible, but very probable.

Because of this, it is not surprising that we seem to be finding both SD and DD progenitors in our local neighborhood, especially given the Greggio (2010) result. Although we do, for the first time ever, have a definitive identification of an SN Ia progenitor, it is unlikely that we can extend this to the entire SN Ia population. Therefore, it is important to investigate the possible SD ex-companions in the other local Ia SNRs, with the goal of quantifying the percentage of SD vs. DD progenitors and possibly linking the different progenitor types to local star formation histories.

6. Conclusions

I have described herein a number of projects I have worked on over the last five years relating to recurrent novae and Type Ia supernovae, and the connection between the two types of systems. Type Ia supernovae have been one of the hottest topics in modern astrophysics since they were used to discover the acceleration of the expansion of the Universe, driven by the mysterious Dark Energy. This discovery upended our understanding of the Universe in which we live and won the 2011 Nobel Prize in Physics for the leaders of the two teams who made it. But despite their broad importance, we still do not know *where* Type Ia supernovae come from. Although we are quite confident that the exploding star itself must be a carbon-oxygen white dwarf, the identity of the companion star has remained elusive, until now.

Many exceptional scientists have worked for decades on this problem. To paraphrase Isaac Newton, we have seen farther by standing on the shoulders of giants. In particular, we adopted the techniques of Ruiz-Lapuente et al. (2004) and extended them to our satellite galaxy, the Large Magellanic Cloud. Hughes et al. (1995) and Rest et al. (2005, 2008) had previously identified four Type Ia supernova remnants in the LMC, so we set off to see what type of leftover ex-companion stars we could find. The first remnant we examined, SNR 0509-67.5, presented us with an ideal case: a cleanly-defined, nearly-symmetric, young remnant located above the bar of the galaxy, in a region with low average star densities. It also, fortuitously, had recently been observed by the Hubble Space Telescope in multiple filters, and these images were publicly available. Our results were startling, even to us: there are no ex-companion stars, to deep *HST* limits, in the center of the remnant, even after accounting for all uncertainties and the most extreme possible motion of any given ex-companion. If this supernova had come from a single-degenerate system, we would see the ex-companion star in the central region, but there are no stars there. We therefore conclude that SNR

0509-67.5 must have come from a double-degenerate system. This is the first time anyone has been able to unambiguously identify the progenitor system of a Type Ia supernova.

This definitive result is not, however, a solution to the entire progenitor problem. If we were absolutely certain that all Type Ia supernovae came from the same type of progenitor, we could extrapolate this result to the entire population and then use this answer to better calibrate observed Type Ia supernova luminosities and thus better constrain the mysterious Dark Energy that we think pervades our universe and acts to fling everything apart at a faster and faster rate. The reality is, of course, not quite that simple. There is tantalizing evidence from a variety of sources that there are multiple progenitor channels contributing to the observed Type Ia population, not the least of which is the result of similar treasure hunting excursions in the other local Type Ia supernova remnants.

The remnant of Tycho's Supernova (SN 1572) has been observed and analyzed in detail by multiple teams. The subgiant star near the center named Star G has been identified as the ex-companion star by Ruiz-Lapuente et al. (2004), which points to a recurrent nova progenitor similar to U Sco. Although the result has been much disputed (Ihara et al. 2007; Kerzendorf et al. 2009; González Hernández et al. 2009), we are inclined to believe the original results, especially if the unusually high heavy element abundances reported by González Hernández et al. (2009) are confirmed. The other Type Ia remnant in our galaxy is that of SN 1006. Study of this remnant is still ongoing, but Ruiz-Lapuente et al. (2011) have ruled out red giant companion stars and will continue to examine the area until an answer is found. Most red giants can also be ruled out for the nearby SN 2011fe, which exploded in M101, the Pinwheel Galaxy, in late 2011 (Li et al. 2011).

As part of our study, we examined the three other Type Ia remnants in the LMC. For SNR 0519-69.0, we can rule out all but two possible progenitor systems, the double-degenerates and the supersoft X-ray sources. For the other two remnants, SNR 0505-67.9 and SNR 0509-68.7, we have multiple possible ex-companions, including subgiants and red giants. Future observations may be able to identify the true ex-companion from among the possibilities.

Namely, our upcoming spectroscopy with GMOS on Gemini South will show us whether any of the stars have unusually high radial or rotation velocities. Future higher-resolution spectra can be used to look for the heavy element abundances González Hernández et al. (2009) found in Tycho G, abundances which indicate the star was right next to the exploding white dwarf and therefore blasted by its expanding shell.

Putting all of these local results together, we have one confirmed double-degenerate, one likely subgiant ex-companion, and many possibilities for the rest of the nearby remnants. It is therefore important to continue to study the possible single-degenerate progenitor systems. I have focused heavily on recurrent novae, both as interesting systems in their own right and as good progenitor candidates. As described in the Introduction, there are three main questions which must be answered to determine whether or not recurrent novae are dominant, or even viable, progenitors: are there enough recurrent novae in our galaxy to provide the observed Type Ia supernova rate; do the white dwarfs in the systems gain mass over their lifetimes so that they can eventually reach the Chandrasekhar limit and explode; and are they carbon-oxygen white dwarfs, as required by theory and simulations?

To answer the first question, we investigated the demographics of the recurrent nova population in detail. Collecting all known information about the classical and recurrent novae allows us to identify a number of likely recurrent novae for which only one eruption has been discovered so far, causing them to be listed incorrectly as classical novae. The strongest recurrent nova candidates show multiple indicators of a short recurrence time, without any contraindications, and are deserving of further study to search for previous eruptions. These systems are V1721 Aql, DE Cir, CP Cru, KT Eri, V838 Her, V2672 Oph, V4160 Sgr, V4643 Sgr, V4739 Sgr, and V477 Sct. Previous eruptions can be discovered by searching the astronomical plate archives; it was by doing this that I found that an eruption had been recorded in June 1900 for our strongest candidate, V2487 Oph, which had previously been known only to erupt in 1998. V2487 Oph is now the tenth known

galactic recurrent nova, and is likely to erupt again soon, possibly as early as 2016. We will be watching.

We also used our study of the nova population to quantitatively estimate how many recurrent novae are currently masquerading as classical novae. Three independent methods give us recurrent nova fractions of 12% ± 3%, 24% ± 4%, and 35%. Although there are potentially large uncertainties, we can say for sure that the fraction of hidden recurrent novae is significant, on the order of 25%, and thus roughly 100 of the classical novae in our catalogs are in actuality recurrent. The big implication of this is that yes, there *are* enough recurrent novae in our galaxy to produce a significant fraction (∼50%) of the observed Type Ia supernovae.

To answer the second question, regarding whether or not the white dwarfs gain mass, we looked at two specific recurrent novae, T Pyx and U Sco. The unusual knots in the T Pyx shell allowed us to accurately measure the shell expansion and estimate the amount of mass it contains by comparing our recent *HST* observations with those of Shara et al. (1997). Both of these quantities, $v_{\rm exp} \approx 600$ km s^{-1} and $M_{\rm shell} \approx 3.1 \times 10^{-5} d_{3500}^2 M_\odot$, are completely inconsistent with the recurrent nova eruptions of T Pyx; the velocity is much too low, and the mass is much too high. Combining this with the long-term decline in brightness T Pyx has shown over the past 120 years, we developed a new model for the system which includes a classical nova eruption in ∼1866 that ejects the massive, slow-moving shell and also sparks the recurrent nova state which we are now observing. This state will be short-lived, however, as the brightness—and thus accretion rate—of T Pyx continues to fall and the time between eruptions lengthens. Eventually T Pyx will enter a state of hibernation which will last for approximately 2.6 million years, before gravitational radiation returns it to a normal cataclysmic variable state and the cycle begins again. Importantly, the classical nova eruption ejects more mass than the white dwarf accretes during the rest of its lifetime, so it can never grow to reach the Chandrasekhar limit. We conclude that T Pyx, and likely also the similar recurrent nova IM Nor, can never explode as a Type Ia supernova.

If T Pyx is the unique member of an already unusual class, U Sco is the poster child for how a recurrent nova should behave. Eruptions occur on time as predicted, with all of the hallmarks of a recurrent nova: fast eruption, small amplitude, plateau-shaped light curve, high expansion velocities, high excitation lines early on, and triple-peaked spectral lines. We took advantage of its regularity to assemble a worldwide collaboration of professional and amateur astronomers to discover and comprehensively observe the 2010 eruption. It was the best-observed nova eruption in history, observed in all wavelengths from radio to hard X-ray, with detections from infrared to soft X-ray. We obtained the comprehensive coverage we needed and used it to discover three new phenomena: early fast flares, late optical dips, and a second plateau in the light curve. Currently, only the late optical dips have any level of theoretical explanation. We were also able to create daily spectral energy distributions from which we could obtain the best-yet estimate of the amount of mass ejected during the eruption, $m_{\rm ej} = 2.05^{+0.26}_{-0.18} \times 10^{-6} M_{\odot}$. Unfortunately, the estimates of the amount of mass accreted during the inter-eruption time interval are not precise enough to tell us whether the white dwarf in U Sco is gaining mass, but future measurements may be able to shed light on this.

To answer the third question, regarding the composition of the white dwarfs in recurrent novae, we again look to U Sco and to the many spectra obtained by our collaboration members. Initial results from Mason (2011) indicate that there *is* dredge-up occurring during the U Sco eruptions (contrary to previous theory) and that the U Sco white dwarf has high neon abundances, indicating that it is an oxygen-neon-magnesium white dwarf instead of the carbon-oxygen composition needed if it is to explode as a Type Ia supernova. The neon detections are confirmed by F. Walter (2012, private communication). At this point, however, the theory and models are not quite sophisticated enough to confirm the interpretations, so we hold off on sounding the death knell for recurrent novae as Type Ia supernova progenitors. Current studies are working to improve the interpretations as well as investigate the spectra

of the other recurrent novae to see if they show high neon abundances as well. It is possible that only some fraction of the recurrent novae have oxygen-neon-magnesium white dwarfs.

In all, we still have a conflicted situation, but we are in a significantly better position today than even just a few years ago. We know that some fraction of the Type Ia supernovae must come from double-degenerate systems, because we have shown that at least one definitely did. Both theory and observations, however, indicate that there may be two dominant progenitor channels. If this is true, we favor recurrent novae for the second channel. Our demographics studies have shown that yes, there are plenty of recurrent novae in our galaxy to contribute significantly to the observed Type Ia supernova rate, even accounting for the T Pyx-like systems that will not go supernova. Although we are unable to say for sure whether the white dwarf in U Sco is gaining mass, the white dwarf in the recurrent nova CI Aql is, so we are confident that this is a reasonable assumption for similar systems (Schaefer 2011). If, however, it is shown that most or all of the recurrent novae do in fact have oxygen-neon-magnesium white dwarfs, we will have to rethink this conclusion, but for now it is reasonable to consider recurrent novae to be the other half of the Type Ia supernova progenitors.

Bibliography

Aikman, G. C. L., Hilditch, R. W., & Younger, F. 1973, PASP, 85, 756

Amanullah, R., et al. 2010, ApJ, 716, 712

Andronov, N., & Pinsonneault, M. H. 2004, ApJ, 614, 326

Anupama, G. C. 2002, in American Institute of Physics Conference Series, Vol. 637, Classical Nova Explosions, ed. M. Hernanz & J. José, 32–41

Anupama, G. C., & Dewangan, G. C. 2000, AJ, 119, 1359

Ashok, N. M., Das, R. K., & Banerjee, D. P. K. 2010, Central Bureau Electronic Telegrams, 2153, 1

Austin, S. J., Schwarz, G., Starrfield, S., & Wagner, R. M. 1994, IAUC, 5993, 1

Ayani, K. 2004, IAUC, 8443, 2

Ayani, K., & Kawabata, T. 2001, IAUC, 7589, 2

Ayani, K., & Kawabata, Y. 2005, IAUC, 8501, 3

Ayani, K., Murakami, N., Hata, K., Tanaka, A., Tachibana, M., & Kanda, A. 2009, Central Bureau Electronic Telegrams, 1911, 1

Baade, W., & Zwicky, F. 1934, Physical Review, 46, 76

Badenes, C., Harris, J., Zaritsky, D., & Prieto, J. L. 2009, ApJ, 700, 727

Badenes, C., Hughes, J. P., Bravo, E., & Langer, N. 2007, ApJ, 662, 472

Baggett, S., et al. 2002, HST WFPC2 Data Handbook, ed. B. Mobasher, Vol. 4.0 (Baltimore: STScI)

Balman, Ş. 2009, AJ, 138, 50

Barbon, R., & Rosino, L. 1989, IAUC, 4862, 1

Blandford, R., et al. 2010, New Worlds, New Horizons in Astronomy and Astrophysics (National Academies Press)

Bloch, M., Dufay, J., Fehrenbach, C., & Mao Lin, T. 1946, Annales d'Astrophysique, 9, 157

Bloom, J. S., et al. 2012, ApJLett, 744, L17

Bode, M. F., Harman, D. J., O'Brien, T. J., Bond, H. E., Starrfield, S., Darnley, M. J., Evans, A., & Eyres, S. P. S. 2007, ApJLett, 665, L63

Borkowski, K. J., et al. 2006, ApJLett, 642, L141

Branch, D., Lacy, C. H., McCall, M. L., Sutherland, P. G., Uomoto, A., Wheeler, J. C., & Wills, B. J. 1983, ApJ, 270, 123

Branch, D., Livio, M., Yungelson, L. R., Boffi, F. R., & Baron, E. 1995, PASP, 107, 1019

Brandt, T. D., Tojeiro, R., Aubourg, É., Heavens, A., Jimenez, R., & Strauss, M. A. 2010, AJ, 140, 804

Brosch, N., & Leibowitz, E. M. 1981, IAUC, 3596, 2

Brown, N. J., Yamaoka, H., West, J. D., & Liller, W. 2003, IAUC, 8204, 1

Brown, S. J., Mills, O. F., Osborn, W., & Hoette, V. 2010, Journal of the American Association of Variable Star Observers (JAAVSO), 38, 176

Bruch, A. 1982, PASP, 94, 916

Burlak, M. A., & Henden, A. A. 2008, Astronomy Letters, 34, 241

Canal, R., Méndez, J., & Ruiz-Lapuente, P. 2001, ApJLett, 550, L53

Capriotti, E. R., & Kendall, A. D. 2006, ApJ, 642, 923

Catchpole, R. M. 1969, MNRAS, 142, 119

Chandrasekhar, S. 1931, ApJ, 74, 81

—. 1934, The Observatory, 57, 373

Chen, W., Shrader, C. R., & Livio, M. 1997, ApJ, 491, 312

Collazzi, A. C., Schaefer, B. E., Xiao, L., Pagnotta, A., Kroll, P., Löchel, K., & Henden, A. A. 2009, AJ, 138, 1846

Conley, A., et al. 2011, ApJS, 192, 1

Contini, M., & Prialnik, D. 1997, ApJ, 475, 803

Crampton, D., Fisher, W. A., & Cowley, A. P. 1986, ApJ, 300, 788

Darnley, M. J., Ribeiro, V. A. R. M., Bode, M. F., & Munari, U. 2011, A&A, 530, A70

Das, R. K., Banerjee, D. P. K., & Ashok, N. M. 2010, Central Bureau Electronic Telegrams, 2157, 1

della Valle, M. 1993, IAUC, 5870, 1

della Valle, M., & Benetti, S. 1997, IAUC, 6532, 2

della Valle, M., Cristiani, S., & Lissandrini, C. 1993, IAUC, 5863, 1

della Valle, M., & Livio, M. 1996, ApJ, 473, 240

della Valle, M., Pizzella, A., & Bernardi, M. 1998, IAUC, 6848, 1

della Valle, M., & Smette, A. 1992, IAUC, 5529, 1

della Valle, M., Turatto, M., Cutispoto, G., Moneti, A., Zelinger, W., & Giraud, E. 1991, IAUC, 5223, 1

Di Stefano, R. 2010a, ApJ, 712, 728

—. 2010b, ApJ, 719, 474

Di Stefano, R., & Nelson, L. A. 1996, in Lecture Notes in Physics, Berlin Springer Verlag, Vol. 472, Supersoft X-Ray Sources, ed. J. Greiner, 3

Di Stefano, R., Voss, R., & Claeys, J. S. W. 2011, ApJLett, 738, L1+

Diaz, M. P., & Bruch, A. 1997, A&A, 322, 807

Dickel, J. R., & Milne, D. K. 1995, AJ, 109, 200

Domínguez, I., Höflich, P., & Straniero, O. 2001, ApJ, 557, 279

Downes, R. A., Webbink, R. F., Shara, M. M., Ritter, H., Kolb, U., & Duerbeck, H. W. 2001, PASP, 113, 764

Dressel, L., Wong, M. H., Pavlovsky, C., Long, K. S., Bond, H. E., & Quijano, J. K. 2011, Wide Field Camera 3 Instrument Handbook, Vol. 4.0 (Baltimore: STScI)

Duerbeck, H. W. 1987, in RS Ophiuchi (1985) and the Recurrent Nova Phenomenon, ed. M. F. Bode, 99

Duerbeck, H. W. 1988, A&A, 197, 148

Duerbeck, H. W., & Augusteijn, T. 1989, IAUC, 4838, 1

Duerbeck, H. W., & Grebel, E. K. 1993, MNRAS, 265, L9

Duerbeck, H. W., & Seitter, W. C. 1979, The Messenger, 17, 1

Duerbeck, H. W., Sterken, C., & Fu, J. N. 2002, IAUC, 7974, 1

Dufay, J., Bloch, M., Bertaud, C., & Dufay, M. 1964a, Annales d'Astrophysique, 27, 555

Dufay, J., Bloch, M., & Chalonge, D. 1964b, Annales d'Astrophysique, 27, 539

Duschl, W. J., Livio, M., & Truran, J. W. 1990, ApJ, 360, 232

Ederoclite, A., et al. 2006, A&A, 459, 875

Edwards, Z. I., Pagnotta, A., & Schaefer, B. E. 2012, ApJLett, 747, L19

Eisenstein, D. J., et al. 2005, ApJ, 633, 560

Feast, M. W., Evans, T. L., Mattei, J. A., & Snyder, L. F. 1991, IAUC, 5233, 2

Fesen, R. A., Höflich, P. A., Hamilton, A. J. S., Hammell, M. C., Gerardy, C. L., Khokhlov, A. M., & Wheeler, J. C. 2007, ApJ, 658, 396

Filippenko, A. V., Leonard, D. C., Modjaz, M., & Eastman, R. G. 1998, IAUC, 6943, 1

Fontanille, J.-P. 2007, JRASC, 101, 11

Frank, J., King, A., & Raine, D. J. 2002, Accretion Power in Astrophysics: Third Edition (Cambridge University Press)

Frank, J., King, A. R., & Lasota, J.-P. 1987, A&A, 178, 137

Freedman, W. L., et al. 2001, ApJ, 553, 47

Fruchter, A., Sosey, M., Hack, W., Dressel, L., Koekemoer, A. M., Mack, J., Mutchler, M., & Pirzkal, N. 2009, The MultiDrizzle Handbook, Vol. 3.0 (Baltimore: STScI)

Fujii, M. 1998, IAUC, 7037, 2

—. 2001, IAUC, 7651, 2

Fujii, M., Kato, T., Takao, A., Haseda, K., & Nakajima, K. 2002, IAUC, 7882, 3

Fujii, M., & Kawakita, H. 1997, IAUC, 6678, 1

Fujii, M., & Yamaoka, H. 2005, IAUC, 8617, 3

Gallagher, J., Skiff, B., & Wagner, R. M. 1987, IAUC, 4501, 1

Gallagher, J. S., & Starrfield, S. 1978, ARA&A, 16, 171

Garnavich, P., Howell, E., & Soderberg, A. 1999, IAUC, 7154, 2

Gilfanov, M., & Bogdán, Á. 2010, Nature, 463, 924

Gonzaga, S., Pavlovsky, C., Koekemoer, A., & Mack, J. 2011, ACS Data Handbook, Vol. 6.0 (Baltimore: STScI)

González Hernández, J. I., Ruiz-Lapuente, P., Filippenko, A. V., Foley, R. J., Gal-Yam, A., & Simon, J. D. 2009, ApJ, 691, 1

Gosset, E. 2002, IAUC, 7887, 2

Greggio, L. 2010, MNRAS, 406, 22

Hachisu, I., & Kato, M. 2001, ApJ, 558, 323

—. 2004, ApJLett, 612, L57

—. 2005, ApJ, 631, 1094

—. 2006, ApJS, 167, 59

—. 2007, ApJ, 662, 552

—. 2009, ApJLett, 694, L103

—. 2010, ApJ, 709, 680

Hachisu, I., Kato, M., & Cassatella, A. 2008a, ApJ, 687, 1236

Hachisu, I., Kato, M., Kato, T., & Matsumoto, K. 2000a, ApJLett, 528, L97

Hachisu, I., Kato, M., Kato, T., & Matsumoto, K. 2002, in Astronomical Society of the Pacific Conference Series, Vol. 261, The Physics of Cataclysmic Variables and Related Objects, ed. B. T. Gänsicke, K. Beuermann, & K. Reinsch, 629

Hachisu, I., Kato, M., Kato, T., Matsumoto, K., & Nomoto, K. 2000b, ApJLett, 534, L189

Hachisu, I., Kato, M., & Nomoto, K. 1996, ApJLett, 470, L97

—. 1999a, ApJ, 522, 487

—. 2008b, ApJLett, 683, L127

—. 2010, ApJLett, 724, L212

Hachisu, I., Kato, M., Nomoto, K., & Umeda, H. 1999b, ApJ, 519, 314

Hachisu, I., et al. 2008c, in Astronomical Society of the Pacific Conference Series, Vol. 401, Astronomical Society of the Pacific Conference Series, ed. A. Evans, M. F. Bode, T. J. O'Brien, & M. J. Darnley, 206

Hacke, G. 1987, Information Bulletin on Variable Stars, 2979, 1

Hamuy, M., Phillips, M. M., Suntzeff, N. B., Schommer, R. A., Maza, J., & Aviles, R. 1996, AJ, 112, 2391

Hamuy, M., et al. 2003, Nature, 424, 651

Hanzl, D. 1998, IAUC, 6976, 3

Harrison, T. E. 1992, MNRAS, 259, 17P

—. 1996, PASP, 108, 1112

Harrison, T. E., Johnson, J. J., & Spyromilio, J. 1993, AJ, 105, 320

Helder, E. A., Kosenko, D., & Vink, J. 2010, ApJLett, 719, L140

Helton, L. A., Woodward, C. E., Vanlandingham, K., & Schwarz, G. J. 2008a, IAUC, 8989, 2

—. 2008b, Central Bureau Electronic Telegrams, 1379, 1

Henden, A. A., & Honeycutt, R. K. 1997, PASP, 109, 441

Henize, K. G., & McLaughlin, D. B. 1951, AJ, 56, 74

Hernanz, M., & Sala, G. 2002, Science, 298, 393

Hoard, D. W., Wachter, S., Clark, L. L., & Bowers, T. P. 2002, ApJ, 565, 511

Horne, K., & Schneider, D. P. 1989, ApJ, 343, 888

Hounsell, R., Darnley, M. J., Bode, M. F., Harman, D. J., Helton, L. A., & Schwarz, G. J. 2011, A&A, 530, A81

Hounsell, R., et al. 2010, The Astronomer's Telegram, 2558, 1

Hughes, J. P., Ghavamian, P., Rakowski, C. E., & Slane, P. O. 2003, ApJLett, 582, L95

Hughes, J. P., Hayashi, I., & Koyama, K. 1998, ApJ, 505, 732

Hughes, J. P., et al. 1995, ApJLett, 444, L81

Iben, Jr., I., & Tutukov, A. V. 1984, ApJS, 54, 335

Ihara, Y., Ozaki, J., Doi, M., Shigeyama, T., Kashikawa, N., Komiyama, K., & Hattori, T. 2007, PASJ, 59, 811

Iijima, T. 2001, IAUC, 7666, 2

—. 2006, A&A, 451, 563

Iijima, T., & Cassatella, A. 2010, A&A, 516, A54

Iijima, T., & Nakanishi, H. 2008, A&A, 482, 865

Iijima, T., et al. 1991, IAUC, 5236, 1

Jablonski, F., Braga, J., & Gilmore, A. C. 1991, IAUC, 5262, 2

Joy, A. H. 1961, ApJ, 133, 493

Jurdana-Šepić, R., Ribeiro, V. A. R. M., Darnley, M. J., Munari, U., & Bode, M. F. 2012, A&A, 537, A34

Justham, S. 2011, ApJLett, 730, L34+

Kalirai, J. S., et al. 2009, WFC3 SMOV Proposal 11450: The Photometric Performance and Calibration of WFC3/UVIS, Tech. rep., STScI

Kasen, D. 2010, ApJ, 708, 1025

Kasen, D., et al. 2003, ApJ, 593, 788

Kato, M. 1990, ApJ, 355, 277

Kato, M., & Hachisu, I. 1991, ApJ, 373, 620

—. 2003a, ApJLett, 587, L39

—. 2003b, ApJLett, 598, L107

—. 2007, ApJ, 657, 1004

—. 2011, ApJ, 743, 157

Kato, M., Hachisu, I., & Cassatella, A. 2009, ApJ, 704, 1676

Kato, T., Fujii, M., & Ayani, K. 2002a, IAUC, 7975, 2

Kato, T., Uemura, M., Haseda, K., Yamaoka, H., Takamizawa, K., Fujii, M., & Kiyota, S. 2002b, PASJ, 54, 1009

Kato, T., & Yamaoka, H. 2002, A&A, 396, 629

Kato, T., Yamaoka, H., & Kiyota, S. 2004, PASJ, 56, 83

Kawabata, K. S., Hirata, R., Ikeda, Y., Akitaya, H., Seki, M., Matsumura, M., & Okazaki, A. 2000, ApJ, 540, 429

Kenyon, S. J. 1986, The symbiotic stars (Cambridge University Press)

Kerzendorf, W. E., Schmidt, B. P., Asplund, M., Nomoto, K., Podsiadlowski, P., Frebel, A., Fesen, R. A., & Yong, D. 2009, ApJ, 701, 1665

Kingsburgh, R. L., & English, J. 1991, IAUC, 5320, 1

Kiss, L. L., Gogh, N., Vinkó, J., Furész, G., Csák, B., DeBond, H., Thomson, J. R., & Derekas, A. 2002, A&A, 384, 982

Kiss, L. L., & Thomson, J. R. 2000, A&A, 355, L9

Kiss, L. L., Thomson, J. R., Ogloza, W., Furész, G., & Sziládi, K. 2001, A&A, 366, 858

Klare, G., Krautter, J., & Wolf, B. 1980, A&A, 89, 282

Knigge, C., King, A. R., & Patterson, J. 2000, A&A, 364, L75

Krause, O., Tanaka, M., Usuda, T., Hattori, T., Goto, M., Birkmann, S., & Nomoto, K. 2008, Nature, 456, 617

Kuerster, M., & Barwig, H. 1988, A&A, 199, 201

Landolt, A. U. 2009, AJ, 137, 4186

Langer, N., Deutschmann, A., Wellstein, S., & Höflich, P. 2000, A&A, 362, 1046

Leavitt, H. S., & Pickering, E. C. 1913, Harvard College Observatory Circular, 179, 1

Leonard, D. C. 2007, ApJ, 670, 1275

Lewis, K. T., Burrows, D. N., Hughes, J. P., Slane, P. O., Garmire, G. P., & Nousek, J. A. 2003, ApJ, 582, 770

Li, W., et al. 2011, Nature, 480, 348

Liller, W., Benetti, S., Cappellaro, E., Gilmore, A. C., Nelson, P., & Stubbings, R. 1995, IAUC, 6130, 1

Liller, W., Jacques, C., Pimentel, E., Aguiar, J. G. D. S., & Shida, R. Y. 2005, IAUC, 8596, 1

Liller, W., & Jones, A. 1999, Information Bulletin on Variable Stars, 4774, 1

Liller, W., Monard, L. A. G., & Africa, S. 2003, IAUC, 8221, 1

Lindblom, L. 1999, Phys. Rev. D, 60, 064007

Lipunov, V. M., Panchenko, I. E., & Pruzhinskaya, M. V. 2011, New Astron., 16, 250

Livio, M. 1991, ApJLett, 369, L5

Livio, M., & Riess, A. G. 2003, ApJLett, 594, L93

Livio, M., & Truran, J. W. 1992, ApJ, 389, 695

Lyke, J. E., et al. 2003, AJ, 126, 993

Lynch, D. K., Rudy, R. J., Mazuk, S., & Puetter, R. C. 2000, ApJ, 541, 791

Lynch, D. K., Rudy, R. J., Venturini, C. C., Mazuk, S., & Puetter, R. C. 2001a, AJ, 122, 2013

Lynch, D. K., Russell, R. W., Bus, S. J., Golisch, W., & Harrison, T. 2004, IAUC, 8392, 3

Lynch, D. K., Russell, R. W., Rudy, R. J., Woodward, C. E., & Schwarz, G. J. 2008, IAUC, 8935, 1

Lynch, D. K., Russell, R. W., & Sitko, M. L. 2001b, AJ, 122, 3313

Maeda, K., et al. 2010, Nature, 466, 82

Manousakis, A., Revnivtsev, M., Krivonos, R., & Bozzo, E. 2010, The Astronomer's Telegram, 2412, 1

Maoz, D., & Mannucci, F. 2011, PASA

Marietta, E., Burrows, A., & Fryxell, B. 2000, ApJS, 128, 615

Marin, E., & Shafter, A. W. 2009, PASP, 121, 1090

Martini, P., Gaudi, B. S., & Wagner, R. M. 1996, IAUC, 6453, 1

Mason, E. 2011, A&A, 532, L11

Mason, P., Harrison, T. E., McNamara, B. J., & Johnson, J. J. 1997, IAUC, 6679, 2

Mayall, M. W. 1938, Harvard College Observatory Bulletin, 907, 28

Maybhate, A., Armstrong, A., Boffi, F. R., Pavlovsky, C., Gonzaga, S., Suchkov, A., & Jedrzejewski, R. 2010, ACS Instrument Handbook, Vol. 10.0 (Baltimore: STScI)

Mazuk, S., Lynch, D. K., Rudy, R. J., Venturini, C. C., Puetter, R. C., Perry, R. B., & Walp, B. 2005, IAUC, 8644, 1

McLaughlin, D. B. 1951, PASP, 63, 129

McNaught, R. H., Lee, S., Peterson, B., & Shanks, T. 1987, IAUC, 4397, 1

Meng, X.-C., & Yang, W.-M. 2011, Research in Astronomy and Astrophysics, 11, 965

Morales-Rueda, L., Still, M. D., Roche, P., Wood, J. H., & Lockley, J. J. 2002, MNRAS, 329, 597

Munari, U., Dallaporta, S., & Castellani, F. 2010, Information Bulletin on Variable Stars, 5930, 1

Munari, U., Ribeiro, V. A. R. M., Bode, M. F., & Saguner, T. 2011, MNRAS, 410, 525

Munari, U., Siviero, A., Navasardyan, H., & Dallaporta, S. 2006, A&A, 452, 567

Naik, S., Banerjee, D. P. K., & Ashok, N. M. 2009, MNRAS, 394, 1551

Naito, H., Tokimasa, N., & Yamaoka, H. 2005a, IAUC, 8484, 1

Naito, H., Tokimasa, N., Yamaoka, H., & Fujii, M. 2005b, IAUC, 8576, 2

Nakano, S., Takamizawa, K., Kushida, R., Kushida, Y., & Kato, T. 1998, IAUC, 6941, 1

Ness, J.-U., et al. 2009, AJ, 137, 4160

—. 2012, ApJ, 745, 43

Nugent, P. E., et al. 2011, Nature, 480, 344

Ohshima, O., Shimizu, M., Ayani, K., & Suzuki, M. 1995, IAUC, 6134, 2

Orio, M., Nelson, T., Bianchini, A., Di Mille, F., & Harbeck, D. 2010, ApJ, 717, 739

Orio, M., Tepedelenlioglu, E., Starrfield, S., Woodward, C. E., & Della Valle, M. 2005, ApJ, 620, 938

Pagnotta, A., Schaefer, B. E., Xiao, L., Collazzi, A. C., & Kroll, P. 2009, AJ, 138, 1230

Pagnotta, A., et al. 2010, The Astronomer's Telegram, 2507, 1

Pan, K.-C., Ricker, P. M., & Taam, R. E. 2010, ApJ, 715, 78

Panagia, N. 1985, in Lecture Notes in Physics, Berlin Springer Verlag, Vol. 224, Supernovae as Distance Indicators, ed. N. Bartel, 14–33

Parthasarathy, M., Branch, D., Jeffery, D. J., & Baron, E. 2007, NewAR, 51, 524

Patat, F., Contreras, C., Prieto, J., Altavilla, G., Benetti, S., Cappellaro, E., Pastorello, A., & Turatto, M. 2001, IAUC, 7709, 1

Patterson, J. 1984, ApJS, 54, 443

Patterson, J., et al. 1998, PASP, 110, 380

Payne-Gaposchkin, C. 1964, The galactic novae (Dover Publications)

Perlmutter, S. 2003, Physics Today, 56, 040000

Perlmutter, S., et al. 1999, ApJ, 517, 565

Perry, R. B., Venturini, C. C., Rudy, R. J., Mazuk, S., Lynch, D. K., Puetter, R. C., & Walp, B. 2005, IAUC, 8638, 1

Peters, C. S., & Thorstensen, J. R. 2006, PASP, 118, 687

Piersanti, L., Gagliardi, S., Iben, Jr., I., & Tornambé, A. 2003, ApJ, 583, 885

Podsiadlowski, P. 2003, ArXiv Astrophysics e-prints

Pojmanski, G. 2002, AcA, 52, 397

Pojmanski, G., et al. 2004, IAUC, 8369, 1

Pretorius, M. L., Knigge, C., O'Donoghue, D., Henry, J. P., Gioia, I. M., & Mullis, C. R. 2007, MNRAS, 382, 1279

Puetter, R. C., Lynch, D. K., Mazuk, S., Rudy, R. J., Venturini, C. C., & Perry, R. B. 2002, IAUC, 7938, 2

Puetter, R. C., Rudy, R. J., Lynch, D. K., Mazuk, S., Venturini, C. C., & Perry, R. B. 2004, IAUC, 8370, 3

Rajan, A., Quijano, J. K., Bushouse, H., & Deustua, S. 2010, WFC3 Data Handbook, Vol. 2.1 (Baltimore: STScI)

Rakowski, C. E., Ghavamian, P., & Hughes, J. P. 2003, ApJ, 590, 846

Rappaport, S., Joss, P. C., & Webbink, R. F. 1982, ApJ, 254, 616

Rest, A., et al. 2005, Nature, 438, 1132

—. 2008, ApJ, 680, 1137

Ribeiro, V. A. R. M., Darnley, M. J., Bode, M. F., Munari, U., Harman, D. J., Steele, I. A., & Meaburn, J. 2011, MNRAS, 412, 1701

Riess, A. G., et al. 1998, AJ, 116, 1009

Robinson, E. L. 1975, AJ, 80, 515

Rodney, S. A., et al. 2012, ArXiv e-prints

Rogel, A. B., Cohn, H. N., & Lugger, P. M. 2008, ApJ, 675, 373

Rosenbush, A. E. 1999, Astrophysics, 42, 270

Rosenbush, A. E. 2002, in American Institute of Physics Conference Series, Vol. 637, Classical Nova Explosions, ed. M. Hernanz & J. José, 294–298

Rothschild, R. E., & Lingenfelter, R. E. 1996, in American Institute of Physics Conference Series, Vol. 366, High Velocity Neutron Stars

Ruch, G., Polomski, E., Woodward, C. E., Wagner, R. M., Starrfield, S., & Brown, N. J. 2003, IAUC, 8204, 2

Rudy, R. J., Russell, R. W., Lynch, D. K., & Widths, I. 2005, IAUC, 8523, 4

Ruiz-Lapuente, P. 1997, Science, 276, 1813

Ruiz-Lapuente, P., & et al. 2011, in IAU Symposium 281: Binary Paths to Type Ia Supernova Explosions, ed. R. Di Stefano & M. Orio

Ruiz-Lapuente, P., et al. 2004, Nature, 431, 1069

Russell, R. W., Lynch, D. K., & Rudy, R. J. 2005, IAUC, 8579, 3

Sanford, R. F. 1940, PASP, 52, 35

Schaefer, B. E. 1996, ApJ, 459, 438

—. 2005, ApJLett, 621, L53

—. 2008, AJ, 135, 112

—. 2009, ApJ, 697, 721

—. 2010, ApJS, 187, 275

—. 2011, ApJ, 742, 112

Schaefer, B. E. 2012, in American Astronomical Society Meeting Abstracts, Vol. 219, American Astronomical Society Meeting Abstracts, 348.21

Schaefer, B. E., Buie, M. W., & Smith, L. T. 2008, Icarus, 197, 590

Schaefer, B. E., & Collazzi, A. C. 2010, AJ, 139, 1831

Schaefer, B. E., Harris, B. G., Dvorak, S., Templeton, M., & Linnolt, M. 2010a, IAUC, 9111, 1

Schaefer, B. E., Landolt, A. U., Vogt, N., Buckley, D., Warner, B., Walker, A. R., & Bond, H. E. 1992, ApJS, 81, 321

Schaefer, B. E., & Pagnotta, A. 2012, Nature, 481, 164

Schaefer, B. E., Pagnotta, A., & Shara, M. M. 2010b, ApJ, 708, 381

Schaefer, B. E., & Patterson, J. 1983, ApJ, 268, 710

Schaefer, B. E., et al. 2010c, AJ, 140, 925

—. 2011a, ApJ, 742, 113

—. 2011b, ArXiv e-prints

Schlegel, D. J., Finkbeiner, D. P., & Davis, M. 1998, ApJ, 500, 525

Schlegel, E. M., et al. 2010, The Astronomer's Telegram, 2430, 1

Schmeja, S., Armsdorfer, B., & Kimeswenger, S. 2000, Information Bulletin on Variable Stars, 4957, 1

Schwarz, G. J., et al. 2009, The Astronomer's Telegram, 2173, 1

—. 2011, ApJS, 197, 31

Sekiguchi, K. 1995, AP&SS, 230, 75

Sekiguchi, K., Feast, M. W., Fairall, A. P., & Winkler, H. 1989a, MNRAS, 241, 311

Sekiguchi, K., Feast, M. W., Whitelock, P. A., Overbeek, M. D., Wargau, W., & Jones, J. S. 1988, MNRAS, 234, 281

Sekiguchi, K., et al. 1989b, MNRAS, 236, 611

—. 1990, MNRAS, 246, 78

Selvelli, P., Cassatella, A., Gilmozzi, R., & González-Riestra, R. 2008, A&A, 492, 787

Shafter, A. W. 1997, ApJ, 487, 226

Shafter, A. W. 2002, in American Institute of Physics Conference Series, Vol. 637, Classical Nova Explosions, ed. M. Hernanz & J. José, 462

Shara, M. M., Livio, M., Moffat, A. F. J., & Orio, M. 1986, ApJ, 311, 163

Shara, M. M., Moffat, A. F. J., Williams, R. E., & Cohen, J. G. 1989, ApJ, 337, 720

Shara, M. M., Yaron, O., Prialnik, D., & Kovetz, A. 2010, ApJLett, 712, L143

Shara, M. M., Zurek, D. R., Williams, R. E., Prialnik, D., Gilmozzi, R., & Moffat, A. F. J. 1997, AJ, 114, 258

Shears, J., & Poyner, G. 2007, Journal of the British Astronomical Association, 117, 136

Sheffer, Y., & Krisciunas, K. 1987, IAUC, 4293, 2

Shemmer, O. 2001, IAUC, 7628, 2

Shen, K. J., & Bildsten, L. 2007, ApJ, 660, 1444

Shore, S. N., Augusteijn, T., Ederoclite, A., & Uthas, H. 2011, A&A, 533, L8

Simonson, M., & MacRobert, A. 2010, Sky & Telescope, 5, 18

Sirianni, M., et al. 2005, PASP, 117, 1049

Siviero, A., Munari, U., & Jones, A. F. 2005, Information Bulletin on Variable Stars, 5638, 1

Smith, D. A., Dhillon, V. S., & Marsh, T. R. 1998, MNRAS, 296, 465

Spergel, D. N., et al. 2007, ApJS, 170, 377

Starrfield, S., Sparks, W. M., & Shaviv, G. 1988, ApJLett, 325, L35

Steiner, J. E., Campos, R., & Cieslinski, D. 1999, IAUC, 7185, 2

Stringfellow, G. S., & Gregg, M. D. 1992, IAUC, 5635, 1

Strömgren, B., & Shapley, H. 1951, Harvard College Observatory Announcement Card, 1119, 1

Strope, R. J., Schaefer, B. E., & Henden, A. A. 2010, AJ, 140, 34

Surina, F., Bode, M. F., & Darnley, M. J. 2011, ArXiv e-prints

Szkody, P. 1994, AJ, 108, 639

Szkody, P., & Feinswog, L. 1988, ApJ, 334, 422

Thomas, H. L. 1940, Harvard College Observatory Bulletin, 912, 10

Thoroughgood, T. D., Dhillon, V. S., Littlefair, S. P., Marsh, T. R., & Smith, D. A. 2001, MNRAS, 327, 1323

Thorstensen, J. R., Peters, C. S., & Skinner, J. N. 2010, PASP, 122, 1285

Thorstensen, J. R., & Taylor, C. J. 2000, MNRAS, 312, 629

Tomov, T., Mikolajewski, M., Brozek, T., Ragan, E., Swierczynski, E., Wychudzki, P., & Galan, C. 2008, The Astronomer's Telegram, 1485, 1

Tomov, T., Moro, D., & Munari, U. 1999, IAUC, 7225, 1

Townsley, D. M. 2008, in Astronomical Society of the Pacific Conference Series, Vol. 401, Astronomical Society of the Pacific Conference Series, ed. A. Evans, M. F. Bode, T. J. O'Brien, & M. J. Darnley, 131

Tutukov, A. V., & Yungelson, L. R. 1981, Nauchnye Informatsii, 49, 3

Uomoto, A., & Kirshner, R. P. 1985, A&A, 149, L7

Uthas, H., Knigge, C., & Steeghs, D. 2010, MNRAS, 409, 237

van den Heuvel, E. P. J., Bhattacharya, D., Nomoto, K., & Rappaport, S. A. 1992, A&A, 262, 97

van Kerkwijk, M. H., Chang, P., & Justham, S. 2010, ApJLett, 722, L157

Vanlandingham, K., Wagner, R. M., & Starrfield, S. G. 2001, IAUC, 7696, 3

Venturini, C. C., Rudy, R. J., Lynch, D. K., Mazuk, S., & Puetter, R. C. 2002, AJ, 124, 3009

Vidal, N. V., & Rodgers, A. W. 1974, PASP, 86, 26

Waagan, E., Linnolt, M., & Pearce, A. 2011, IAUC, 9205, 1

Wagner, R. M., Bertram, R., & Starrfield, S. G. 1990, IAUC, 5006, 1

—. 2000, IAUC, 7363, 1

Wagner, R. M., & Starrfield, S. G. 1991, IAUC, 5243, 1

Wagner, R. M., Vandlandingham, K. M., & King, N. 1994, IAUC, 6002, 1

Walter, F. M., & Battisti, A. 2011, in Bulletin of the American Astronomical Society, Vol. 43, American Astronomical Society Meeting Abstracts #217, 338.11

Walter, F. M., Mason, K. O., Clarke, J. T., Halpern, J., Grindlay, J. E., Bowyer, S., & Henry, J. P. 1982, ApJLett, 253, L67

Walter, F. M., White, N. E., & Swank, J. 1981, IAUC, 3611, 2

Wang, B., Meng, X., Chen, X., & Han, Z. 2009, MNRAS, 395, 847

Wang, L., Baade, D., & Patat, F. 2007, Science, 315, 212

Wang, L., & Wheeler, J. C. 2008, ARA&A, 46, 433

Wang, L., et al. 2003, ApJ, 591, 1110

Warren, J. S., & Hughes, J. P. 2004, ApJ, 608, 261

Webbink, R. F., Livio, M., Truran, J. W., & Orio, M. 1987, ApJ, 314, 653

Weight, A., Evans, A., Naylor, T., Wood, J. H., & Bode, M. F. 1994, MNRAS, 266, 761

Weller, W. G., & Heathcote, S. R. 1988, IAUC, 4594, 1

Wellmann, P. 1951, ZAP, 29, 112

Wheeler, J. C., & Benetti, S. 2000, Supernovae (AIP Press), 451

Wheeler, J. C., & Levreault, R. 1985, ApJLett, 294, L17

Whelan, J., & Iben, Jr., I. 1973, ApJ, 186, 1007

White, N. E., & Swank, J. H. 1982, ApJLett, 253, L61

Whitney, B. A., & Clayton, G. C. 1989, AJ, 98, 297

Williams, B. J., et al. 2011, ApJ, 729, 65

Williams, R. E. 1982, ApJ, 261, 170

Williams, R. E. 1993, in Frontiers of Astronomy in 1990s. Proc. Workshop held in Beijing, 30 Oct-6 Nov. 1992, Ed. Li Qibin, 127-137 (1993), 127–137

Williams, R. E., Hamuy, M., Phillips, M. M., Heathcote, S. R., Wells, L., & Navarrete, M. 1991, ApJ, 376, 721

Winkler, P. F., Long, K. S., Hamilton, A. J. S., & Fesen, R. A. 2005, ApJ, 624, 189

Woudt, P. A., & Warner, B. 2003, MNRAS, 340, 1011

Wyse, A. B. 1940, Publications of Lick Observatory, 14, 93

Yamaoka, H., & Fujii, M. 2005, IAUC, 8506, 3

Yamaoka, H., Itagaki, K., & Fujii, M. 2004, IAUC, 8381, 3

Yamaoka, H., et al. 2009, IAUC, 9098, 1

Yaron, O., Prialnik, D., Shara, M. M., & Kovetz, A. 2005, ApJ, 623, 398

Yoon, S.-C., & Langer, N. 2005, A&A, 435, 967

Zaritsky, D., Harris, J., Thompson, I. B., & Grebel, E. K. 2004, AJ, 128, 1606

Appendix A: Data Reduction and Analysis

In this Appendix, I will describe some of the theory behind why data reduction is necessary (Section A.1) as well as give brief descriptions of the main instruments that were used to collect data for this dissertation. The instrument-specific descriptions are broken up into ground-based instruments (namely the ANDICAM on the SMARTS 1.3m Telescope at Cerro Tololo Inter-American Observatory [CTIO] in Chile, Section A.2.1, and the GMOS imager on the Gemini South 8.1m Telescope on Cerro Pachon in Chile, Section A.2.2), Hubble Space Telescope instruments (Section A.3), and Swift Gamma-Ray Burst Telescope instruments (Section A.4).

A.1 Data Reduction Philosophy

As light from a star or other astronomical source travels to our detectors, it undergoes various alterations for which we must account and correct. There are three main reduction steps that are used to make these corrections: biases, flats, and darks. I will describe the need for, and implementation of, each of these reduction steps in this section, specifically as they apply to ground-based optical data.

The first calibration correction is the bias, sometimes called zero, frame. All CCD detectors have a bias voltage applied to them so that even a 0.0 second exposure will not read out an image with zero counts in every pixel. Without a bias voltage, random noise could lead to a negative voltage at points on the CCD, which would cause problems since the chips use unsigned storage, i.e. assigning each pixel a number from 0 to 20,000 based on counts, instead of -10,000 to +10,000. With an overall bias voltage applied to the chip, it is possible to safely use unsigned storage which allows for a more precise, finer resolution measurement of the counts. To correct for pixel-to-pixel variations in this artificially-imposed voltage, a series of $\sim$10 bias frames is taken before each night of observing, usually during the afternoon. The biases are combined to make a master bias which is then subtracted out

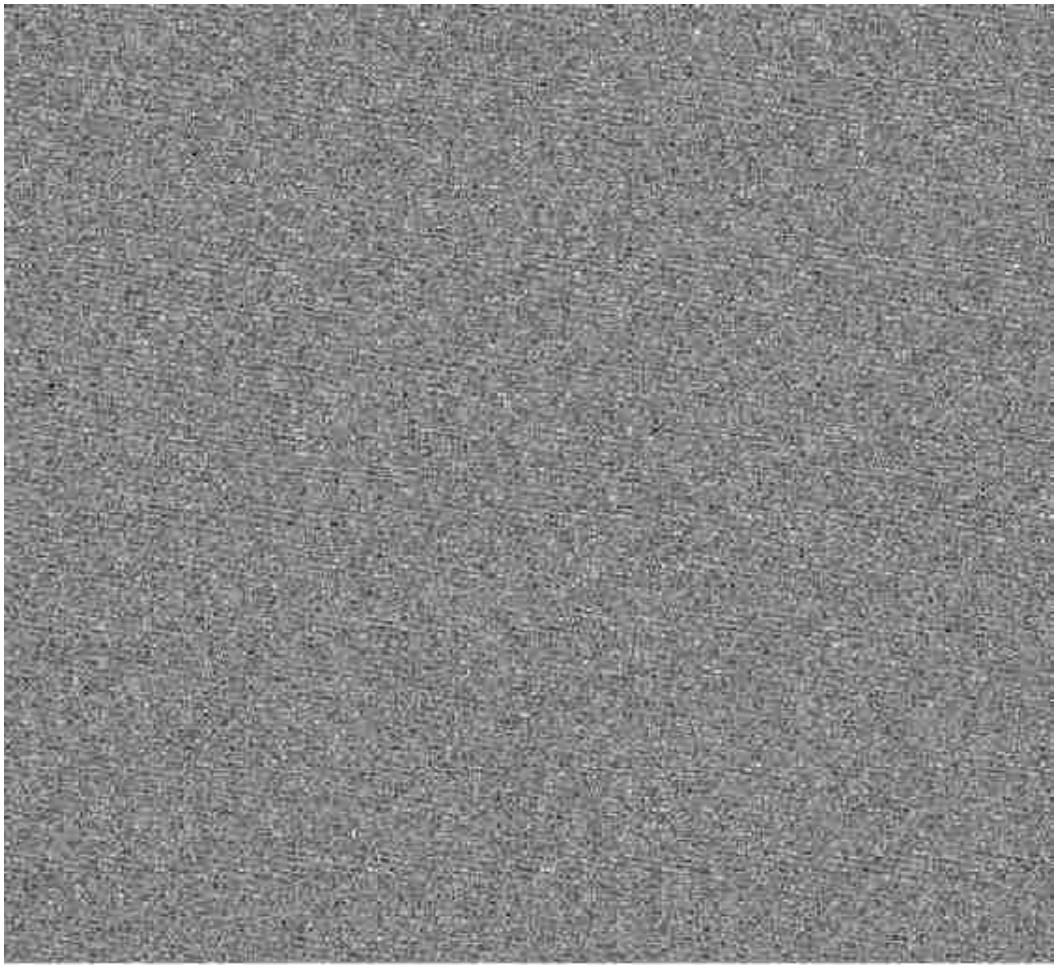

Figure A.1 Sample Master Bias. This example master bias was created with the Imaging Grism Instrument on the 2.1m (82") Otto Struve Telescope at McDonald Observatory near Fort Davis, TX, in 2009. The bias level is position-dependent, and on some instruments (e.g. the Y4KCam on the CTIO 1.0m) can change from night-to-night, so it is advisable to take a new set of biases each day during afternoon calibrations.

from all of the rest of the calibration and science images. A sample master bias, taken with the Imaging Grism Instrument (IGI) on the 2.1m (82") Otto Struve Telescope at McDonald Observatory near Fort Davis, TX, during an observing run in the summer of 2009, can be seen in Figure A.1. The bias voltage changes with position and can also change with time on a night-to-night basis, so it is important to take a new set of bias frames for each night at the telescope.

After the photons enter the telescope, they reflect off at least one mirror (often two) and usually pass through a filter as well before hitting the CCD. Both the mirror and filter can

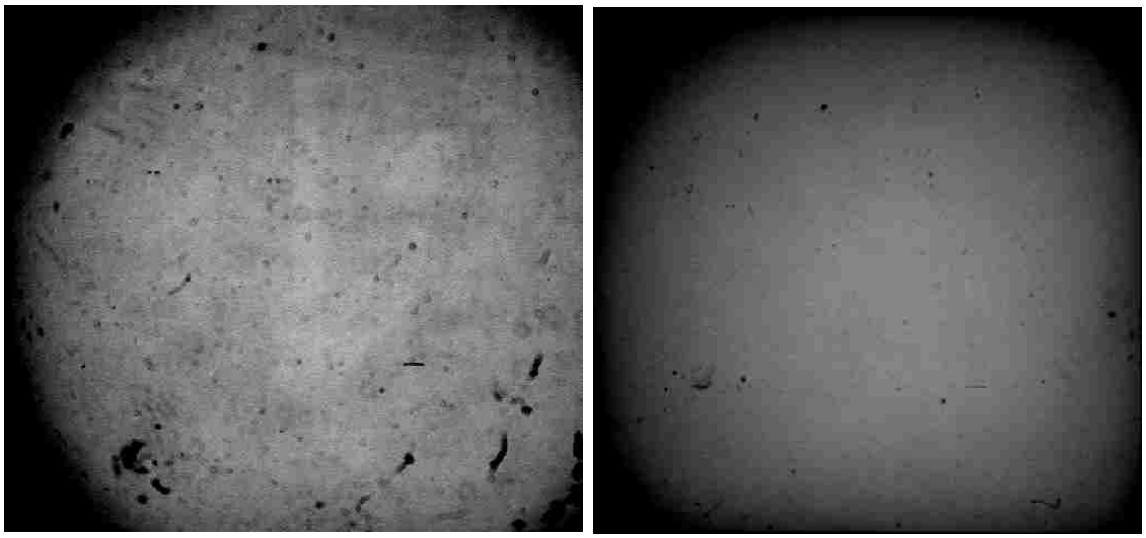

Figure A.2 Sample Flat Fields. These sample flats was taken with the Imaging Grism Instrument on the 2.1m (82") Otto Struve Telescope at McDonald Observatory near Fort Davis, TX, in 2009. The left image shows a combined V-band flat and the right image shows a combined I-band flat. Note the "dust donuts" caused by out-of-focus dust stuck to the filter glass; they are prominent in the V-band flat. Note also the significant differences between the two filters; since the flats change drastically from filter to filter, it is important to take a new set of flats in each filter that is used to obtain science data.

have aberrations that show up in the final image, such as dust particles stuck to one of the surfaces, and the sensitivity of the CCD chip can vary with position. To correct for this, the second calibration step is to take a series of flat fields, or just flats, with each filter by pointing the telescope at a uniformly-illuminated blank background, known as a flat field, and then taking $\sim$10 observations, each with an exposure length designed to create an image that is well-sampled but not saturated. Two sample flats can be seen in Figure A.2. Both flats were also taken with the IGI on the McDonald 2.1m. Many aberrations can be seen in both flats, as well as an overall vignetting effect in which the outer corners of the chip do not receive as much light as the center. The "donuts" that are particularly visible in the V-band flat (on the right) are caused by out-of-focus dust stuck to the filter. It is easy to see that flat fields can vary widely between filters, so it is crucial to take a new set of flats in each filter that is used to obtain science images. The flats are combined by filter and divided out of the science images.

There are two general methods for taking flats: dome flats and sky (or twilight) flats. Dome flats are taken—usually during the day—with the dome closed and the telescope pointed at a small white screen hung inside the dome, as can be seen in Figure A.3. The flat screen is illuminated as evenly as possible with lamps that are placed inside the dome. The voltage of the lamps can be adjusted, and the goal is to get a good exposure in each filter with a reasonable exposure time, so the voltage is usually increased for the less efficient filters such as U-band. There are two big advantages to dome flats: (1) they can be taken during the day, so they do not take away from active, "on sky" observing time, and (2) all of the variables such as exposure time and lamp voltage can be controlled and easily replicated from night to night. Sky flats are taken, as the name implies, on the sky during twilight, either in the evening just after the sun has set, in the morning just before it rises, or at both times depending on the number of flats which need to be taken and/or middle-of-the-night observing program changes. Sky flats have one main advantage over dome flats: they are usually more evenly illuminated and therefore provide a flat field which better calibrates the images. There is, however, only a short window during which they can be taken, and only if the sky is completely cloud-free at twilight. Additionally, all sky flats have some stars in them, which must be excluded to high accuracy. To fix this problem, it is recommended that each sky flat be taken of a different field on the sky, so that the stars will be removed when the flats are combined using their mode. Because of the potential difficulties of sky flats, it is advisable to get dome flats daily, just in case, and sky flats as often as available.

The final calibration correction is the dark frame. Dark current in CCDs is caused by thermal excitation of electrons in the chip, and is therefore very temperature dependent. The dominant term in the dark current varies as

$$e^{-E_{\rm g}/2kT} \tag{A.1}$$

where $E_{\rm g}$ is the energy gap for the CCD material, k is the Boltzmann constant, and T is the temperature in Kelvin (R. Hynes, LSU Class Notes, ASTR 7783). To correct for this dark current, a set of dark frames is taken. Since dark current accumulates over time, one

Figure A.3 Flat Screen for Dome Flats. This image shows the 1.0m SMARTS/YALO Telescope at CTIO pointed at the flat screen inside the dome. Note that this picture was taken during morning shut-down, not during dome flats, which is why the dome slit is open.

can take a set of darks with each exposure time that will be used for science observations or take one base set of darks and scale them by exposure time. The darks are then combined by exposure time to make master darks for each exposure and then subtracted out of each science image to remove the dark current. Most professional telescopes avoid this problem altogether, however, by cooling the CCDs to very low temperatures (e.g. 170K for the Y4KCAM CCD on the CTIO 1.0m) using liquid nitrogen, which reduces dark current to a negligible level and produces images that do not need to be dark subtracted.

Analytically, the reduction steps can be described as follows. For a given pixel, we can define the following quantities which directly correspond to the science and calibration frames that are obtained:

$$ADU = G \times (B + D \cdot T + Signal \cdot T \cdot F) \tag{A.2}$$

where ADU = recorded counts, G = gain, B = bias, D = dark current, T = exposure time,

$Signal$ = the actual signal from the source, and F = flat field variations;

$$Bias = G \cdot B \tag{A.3}$$

where $Bias$ = bias calibration frame;

$$Dark = G \times (B + D \cdot T_D) \tag{A.4}$$

where $Dark$ = dark calibration frame and T_D = exposure time of the dark; and

$$Flat = G \times (B + D \cdot T_F + S_F \cdot T_F \cdot F) \tag{A.5}$$

where $Flat$ = flat calibration frame, S_F = signal from the flat lamps, and T_F = exposure time of the flat.

We can then rearrange Equation A.2 as

$$Signal = \frac{\frac{ADU}{G} - B - D \cdot T}{T \cdot F} \tag{A.6}$$

and sub in Equations A.3-A.5 to obtain

$$Signal = \frac{ADU - Bias - (Dark - Bias)\frac{T}{T_D}}{\frac{1}{S_F T_F}\left[Flat - Bias - (Dark - Bias)\frac{T_F}{T_D}\right]} \tag{A.7}$$

where all quantities are known except for S_F which can be obtained by calibrating against known standards such as those in Landolt (2009).

A.2 Ground-Based Instruments and Photometry

A.2.1 ANDICAM

The ANDICAM (A Novel Double-Imaging CAMera) is installed on the SMARTS 1.3m Telescope at CTIO. A dichroic beamsplitter is used to send the incoming light down two different paths, one to the optical CCD detector and one to the IR detector. The 2048×2048 optical CCD is usually run with the default 2×2 binning in which it has a $\sim 6' \times 6'$ field of view (for $BVRI$ filters; the field of view is slightly smaller for the neutral density filters)[1]. The

[1] http://www.astronomy.ohio-state.edu/ANDICAM/detectors.html

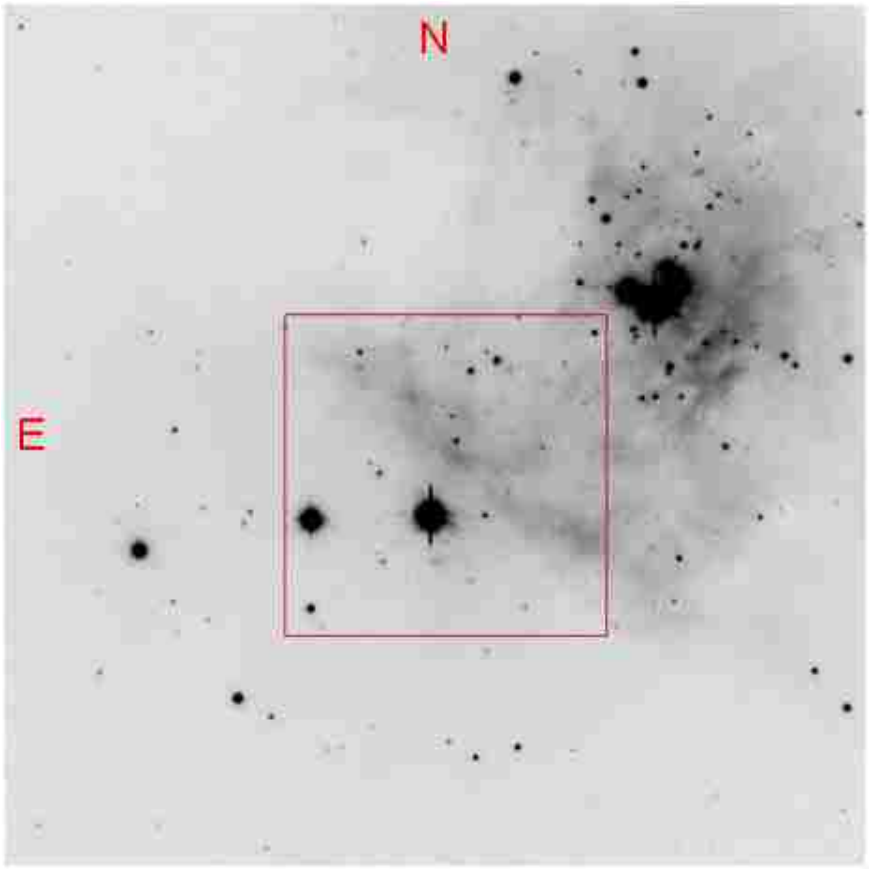

Figure A.4 ANDICAM Field of View. This figure, from the Ohio State ANDICAM website (http://www.astronomy.ohio-state.edu/ANDICAM/Images/andiCCDfov.gif) shows a comparison between the optical (full image) and IR (center red box) fields of view. The optical images have a $\sim 6' \times 6'$ field of view (in the default 2×2 binning mode) while the IR field of view is $\sim 2.4' \times 2.4'$.

IR array is 1024×1024 and is always binned 2×2 by the software after readout to better match the seeing[2]. It has a $\sim 2.4' \times 2.4'$ field of view[3]. The CCD and IR channels are at the same focal length, and the IR field is near the center of the CCD field, as illustrated in Figure A.4, where the red box in the center shows the IR field location on the full CCD field.

The ANDICAM images are all reduced by S. Tourtellotte at Yale; when we download them from the SMARTS servers, there is no need to process them further. The processing steps are standard (biases + flats) and are described in detail on the SMARTS website[4]. We

[2]http://www.astronomy.ohio-state.edu/ANDICAM/irbin.html
[3]http://www.astronomy.ohio-state.edu/ANDICAM/detectors.html
[4]http://www.astro.yale.edu/smarts/smarts13m/optprocessing.html

used ANDICAM to obtain nightly photometry of the RN U Sco during its 2010 eruption; see Section 4.4 for details.

A.2.2 GMOS

The Gemini Multi-Object Spectrographs (GMOS) are installed on the two Gemini 8.1m telescopes, one on Mauna Kea in Hawaii (GMOS-N) and one on Cerro Pachon in Chile (GMOS-S). We used GMOS-S—hereafter just GMOS, as the detectors are identical—to observe three of the four Ia SNRs in the LMC (Chapter 5). GMOS is designed for long-slit, multi-object, and integral field unit spectroscopy, but can also be used as an imager. GMOS has a selection of narrow and broad band filters; the broad band filters use the Sloan *ugriz* photometric system. The $5.5' \times 5.5'$ field of view includes two $\sim 2.8''$ gaps between chips that can be removed by dithering[5], however that was unnecessary with our observations because the middle chip contained all of the information in which we were interested. Our GMOS images were pipeline processed[6] and we were able to use them immediately as downloaded.

A.2.3 Photometry

All of the ground-based magnitudes presented in this dissertation were measured using differential photometry. Once the science images have been reduced, we use the IRAF *phot* routine to measure the instrumental magnitude of the stars in the field. Two crucial inputs are the size of the source aperture and the sky annulus. The source aperture is centered on the star and the software measures the total number of counts within that aperture. This includes the counts from both the source and the sky background. The ideal source aperture size has a radius equal to the measured FWHM of the source; this maximizes the signal while minimizing the noise contribution from the background. The sky annulus is also centered on the star but is much larger; unless the field is very crowded, the inner radius of the sky annulus should be greater than the radius of the source aperture, as shown in Figure A.5. The

[5]http://www.gemini.edu/?q=node/10007
[6]http://www.gemini.edu/sciops/instruments/gmos/data-format-and-reduction

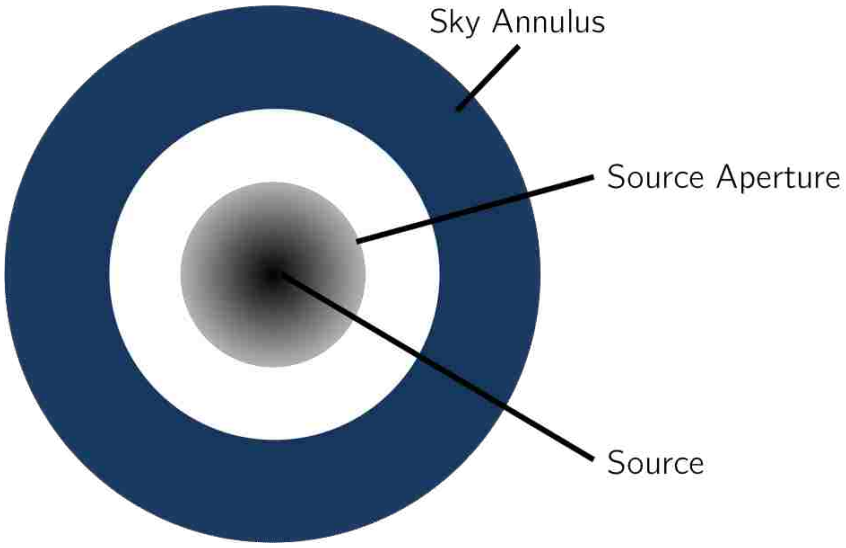

Figure A.5 Schematic of the Source Aperture and Sky Annulus Used by IRAF's *phot* Routine. The software measures the total number of counts in the source aperture and then subtracts the average sky brightness, which is measured in the sky annulus, to obtain the source counts. The source counts are then converted into an instrumental magnitude.

average sky brightness in the sky aperture is measured and subtracted from the total counts in the source aperture to give the number of counts from the source itself. An instrumental magnitude is then calculated from the source counts n as $m = m_0 - 2.5 \log n$, where m_0 is an arbitrary zeropoint set in the *phot* parameters. To ensure consistency across the years, it is highly recommended to pick an initial zeropoint and never change it. A set of sample *phot* input parameters including the basic IRAF descriptions along with my comments can be seen in Table A.1. The five blocks correspond to *phot, datapars, centerpars, fitskypars*, and *photpars*.

Table A.1. Sample IRAF *phot* Parameters

Parameter	Sample Input	IRAF Description	My Comments
image	"image.fits"	The input image(s)	The name of the image, or list of images (@list.lis) for which one wants photometry.
skyfile	""	The input sky file(s)	...
coords	"image.fits.coo.1"	The input coordinate files(s) (default: image.coo.?)	The name of the file that lists the coordinates of the stars for which one is interested in obtaining photometry.
output	"default"	The output photometry file(s) (default: image.mag.?)	The name of the file IRAF will create that lists all of the photometry measurements.
plotfile	""	The output plots metacode file	...
datapars	""	Data dependent parameters	...
centerpars	""	Centering parameters	...
fitskypars	""	Sky fitting parameters	...
photpars	""	Photometry parameters	...
interactive	no	Interactive mode ?	Set to yes to interactively pick stars instead of uploading a coordinate file.
radplots	no	Plot the radial profiles in interactive mode ?	...
icommands	""	Image cursor: [x y wcs] key [cmd]	...
gcommands	""	Graphics cursor: [x y wcs] key [cmd]	...
wcsin	)_.wcsin	The input coordinate system	...
wcsout	)_.wcsout	The output coordinate system	...
cache	)_.cache	Cache the input image pixels in memory ?	...
verify	)_.verify	Verify critical parameters in non-interactive mode ?	...
update	)_.update	Update critical parameters in non-interactive mode ?	...
verbose	)_.verbose	Print messages in non-interactive mode ?	...
graphics	)_.graphics	Graphics device	...
display	)_.display	Display device	...
mode	"ql"	...	...
scale	1	Image scale in units per pixel	...
fwhmpsf	2.5	FWHM of the PSF in scale units	Average FWHM of the stars in the field, measured with imexam before running phot.
emission	yes	Features are positive ?	...
sigma	5.	Standard deviation of background in counts	Average standard deviation of sky background, measured with imexam before running phot.
datamin	INDEF	Minimum good data value	...
datamax	INDEF	Maximum good data value	...
noise	"poisson"	Noise model	...
ccdread	""	CCD readout noise image header keyword	Keyword if available.
gain	""	CCD gain image header keyword	Keyword if available.
readnoise	4.2	CCD readout noise in electrons	Input value if there is no keyword.
epadu	2.	Gain in electrons per count	Input value if there is no keyword.
exposure	"EXPTIME"	Exposure time image header keyword	Keyword if available.
airmass	""	Airmass image header keyword	Keyword if available.
filter	""	Filter image header keyword	Keyword if available.
obstime	""	Time of observation image header keyword	Keyword if available.
itime	1.	Exposure time	Input value if there is no keyword.
xairmass	INDEF	Airmass	Input value if there is no keyword.
ifilter	INDEF	Filter	Input value if there is no keyword.
otime	INDEF	Time of observation	Input value if there is no keyword.
mode	"ql"	...	...
calgorithm	"centroid"	Centering algorithm	...
cbox	5.	Centering box width in scale units	...
cthreshold	0.	Centering threshold in sigma above background	...
minsnratio	1.	Minimum signal-to-noise ratio for centering algorithm	...
cmaxiter	10	Maximum number of iterations for centering algorithm	Reduce this value for crowded fields or nearby bright stars.
maxshift	5.	Maximum center shift in scale units	Reduce this value for crowded fields or nearby bright stars.
clean	no	Symmetry clean before centering ?	...
rclean	1.	Cleaning radius in scale units	...
rclip	2.	Clipping radius in scale units	...
kclean	3.	Rejection limit in sigma	...
mkcenter	no	Mark the computed center on display ?	...
mode	"ql"		...

Table A.1—Continued

Parameter	Sample Input	IRAF Description	My Comments
salgorithm	"centroid"	Sky fitting algorithm	...
annulus	20.	Inner radius of sky annulus in scale units	For non-crowded fields and/or bright stars, choose relatively large number.
dannulus	10.	Width of sky annulus in scale units	For non-crowded fields, choose relatively large number.
skyvalue	0.	User sky value	...
smaxiter	10	Maximum number of sky fitting iterations	...
sloclip	0.	Lower clipping factor in percent	...
shiclip	0.	Upper clipping factor in percent	...
snreject	50	Maximum number of sky fitting rejection iterations	...
sloreject	3.	Lower K-sigma rejection limit in sky sigma	...
shireject	3.	Upper K-sigma rejection limit in sky sigma	...
khist	3.	Half width of histogram in sky sigma	...
binsize	0.10000000149012	Binsize of histogram in sky sigma	...
smooth	no	Boxcar smooth the histogram	...
rgrow	0.	Region growing radius in scale units	...
mksky	no	Mark sky annuli on the display	...
mode	"ql"	...	
weighting	"constant"	Photometric weighting scheme for wphot	...
apertures	"1,2,5"	List of aperture radii in scale units	Can do a variety of apertures here and then decide which is best later by looking at errors.
zmag	25.	Zero point of magnitude scale	NEVER CHANGE THIS!
mkapert	no	Draw apertures on the display	...
mode	"ql"	...	...

This instrumental magnitude is only useful for comparing the star of interest with other stars in the same image. It can be turned into a physically meaningful quantity via differential photometry using comparison stars. The ideal comparison star is nearby, non-variable, bright but not saturated, and close in color to the star of interest. The difference between the magnitudes of the two stars can be easily calculated. This is particularly useful for variable stars. For example, to track a nova during an eruption, we can calculate the magnitude difference Δm between the nova and a nearby comparison star. In quiescence, Δm will be relatively constant, showing only small jitters due to measurement uncertainties and normal variations in the nova due to accretion. Once the eruption starts, however, Δm will increase rapidly until hitting its maximum value at the peak of the eruption, after which point it will decrease back down to the constant quiescent level. This is a perfectly adequate method for tracking the inherent magnitude changes in the variable star, but it can be improved. If the comparison stars have been calibrated using absolute photometry, the calibrated magnitude of the variable can be obtained. For example, if the variable is measured to be 0.4 mags fainter in V-band than a star that is known to be $V = 8.2$, the variable star is at $V = 8.6$.

A.3 Hubble Space Telescope

The Hubble Space Telescope (*HST*) is the flagship of NASA's Great Observatories program. It was deployed into orbit in 1990 and is still operational today. *HST* has made more than 930,000 observations of more that 30,000 different objects, and data from *HST* has been used in more than 8,700 scientific papers[7]. Since the launch, a number of servicing missions have brought astronauts to *HST* to make repairs to the telescope and instruments, as well as to install new instruments and upgrades. There are currently six active instruments on *HST*[8]. The following subsections briefly describe the three *HST* instruments I have used as part of this dissertation work.

[7] http://www.nasa.gov/mission_pages/hubble/story/index.html
[8] http://www.stsci.edu/hst/HST_overview/instruments/

A.3.1 ACS

The Advanced Camera for Surveys (ACS) was installed on *HST* during Servicing Mission 3B in 2002. ACS has three primary detectors: the Wide Field Channel (WFC), the High Resolution Channel (HRC), and the Solar Blind Channel (SBC) (Maybhate et al. 2010). We used V-band and Hα images of SNR 0519-69.0 from the ACS WFC to search for ex-companion stars near the center of the remnant; see Section 5.5 for details. The ACS WFC is a mosaic of two 4096×2048 thinned, back-illuminated CCDs which have $\sim 0.05''$/pixel resolution, for a $202'' \times 202''$ field of view (Maybhate et al. 2010).

ACS data can be obtained directly from the STScI archive in a pipeline-processed version, but we chose to reduce and process the data ourselves, as this allows for greater flexibility and ensures photometric accuracy. ACS data must be processed using the PyRAF routine MultiDrizzle, written by STScI staff scientists (Fruchter et al. 2009). The ACS Data Handbook (Gonzaga et al. 2011) outlines the basic steps that must be taken, and the MultiDrizzle Handbook (Fruchter et al. 2009) fills in the details and provides instrument-specific examples. We found that the default parameters suggested by the handbooks adequately processed our data.

The photometric zeropoints of ACS have been accurately calculated and can be used to obtain calibrated magnitudes from the processed images. The most updated ACS zeropoints are available online[9], and Sirianni et al. (2005) give the aperture corrections for each filter in their Table 5; these corrections are needed to apply the zeropoints to actual data.

A.3.2 WFPC2

The Wide Field and Planetary Camera 2 (WFPC2) was installed on *HST* during the First Servicing Mission in December 1993 and replaced by the WFC3 (see Section A.3.3) in 1999. The instrument consists of four cameras: three Wide Field Cameras (WF2, WF3, and WF4) and the Planetary Camera (PC). The WF chips are 800×800 pixels with an $80'' \times 80''$ field

[9] http://www.stsci.edu/hst/acs/analysis/zeropoints/#tablestart

of view, for a plate scale of 0.0996″ per pixel. The PC chip is also 800 × 800 pixels but has a 36″ × 36″ field of view, for a plate scale of 0.0455″ per pixel (Baggett et al. 2002).

As with ACS data, all public domain WFPC2 files can be downloaded from the STScI archive in a pipeline-processed version (with a drz.fits extension), but we chose to reduce them ourselves. WFPC2 data are also processed using STScI's MultiDrizzle routine for PyRAF (Fruchter et al. 2009). A set of "cookbooks"[10] has been produced to provide suggested parameters for drizzling images to combine them and remove aberrations such as cosmic rays. For both the T Pyx (Section 3.3) and SNR 0509-67.5 (Section 5.4) analyses, we followed the indicated cookbooks as written, obtaining good results with all the default values.

A.3.3 WFC3

The Wide Field Camera 3 (WFC3) was installed on *HST* in May 2009 during Servicing Mission 4. It has two channels, the IR Channel and the UVIS Channel. We used images of SNR 0509-67.5 taken with the UVIS Channel to search for possible ex-companions in the center of the remnant; see Section 5.4 for details. The UVIS detector consists of two thinned, back-illuminated CCDs which are each 2000 × 4000 pixels. The 0.13″ pixel size gives a 123″ × 136″ field of view (Dressel et al. 2011).

Like the ACS and WFPC2 data, WFC3 data can be downloaded in a pipeline-processed form, but again we chose to reduce all of the images ourselves using MultiDrizzle and found good results using the guidelines from the WFC3 Data Handbook (Rajan et al. 2010) and the MultiDrizzle Handbook (Fruchter et al. 2009). For WFC3, photometric zeropoints have been calculated both for infinite apertures and for apertures with a radius of 0.4″ (Kalirai et al. 2009). We used a 0.4″ radius aperture for our photometry, so no aperture corrections were needed.

[10] http://www.stsci.edu/hst/wfpc2/analysis/WFPC2_drizzle.html

A.4 Swift Gamma-Ray Burst Telescope

The Swift Gamma-Ray Burst Telescope was designed to quickly discover and thoroughly observe Gamma-Ray Bursts, some of the most powerful explosions that ever occur in our galaxy. *Swift* was launched in 2004 and is still fully operational today. The satellite holds three different telescopes, each of which cover a different portion of the electromagnetic spectrum and combine to give coverage from optical light through UV and X-rays all the way to Gamma-rays. When *Swift* is not actively observing a GRB, the instruments are used for other science observations. In conjunction with the *Swift* Nova-CV Group, we used two of the *Swift* instruments to observe U Sco during its 2010 eruption. Those two instruments are briefly described in the following subsections; see Section 4.5 for more details on our U Sco observations and results.

A.4.1 UVOT

The UltraViolet and Optical Telescope (UVOT) on *Swift* is a 0.3m modified Ritchey-Chretien telescope that has photon-counting detectors which retain the positions and timing information of each individual photon that is detected, which means that UVOT operates more like an X-ray telescope than a traditional optical telescope. UVOT has a $17' \times 17'$ field of view and is sensitive to wavelengths between 170 nm and 650 nm, which covers the optical and near-UV portion of the electromagnetic spectrum. The 11-position filter wheel allows for multi-band photometry as well as grism spectroscopy[11]

Magnitudes can be extracted from the UVOT images with the *uvotsource* tool in Xselect[12], which is part of NASA's HEASoft software package[13]. *Uvotsource* requires a source and background region to be input, as well as a working link to the CALDB calibration library. *Uvotsource* performs standard aperture photometry and returns screen output and a FITS file with the count rate, magnitude, flux density, and detection significance, among

[11]http://www.swift.psu.edu/uvot/
[12]http://heasarc.nasa.gov/docs/software/lheasoft/ftools/xselect/xselect.html
[13]http://heasarc.nasa.gov/lheasoft/

other things. The one downside of *uvotsource* is that it can only be run on one image extension (snapshot) at a time. In theory, the *uvotmaghist* tool can be used to perform photometry on every extension of a given image file, however with UVOT data there are often not enough stars in the image on which to perform aspect corrections, without with *uvotmaghist* cannot run (K. Page 2010, private communication), so *uvotsource* must be used on those extensions.

A.4.2 XRT

The X-Ray Telescope (XRT) on *Swift* is an X-ray CCD imaging spectrometer which covers the 0.2 keV to 10 keV region of the spectrum with a $23.6' \times 23.6'$ field of view. The XRT was designed to quickly and accurately pinpoint GRBs after detection and therefore has very good positioning capabilities. An aluminum/polyimide filter is located in front of the CCD to block optical light from reaching the detector. The photon-counting X-ray CCD retains information about each individual X-ray photon that is detected[14].

X-ray spectra from XRT observations can be extracted using Xselect[15] and then fit using Xspec[16], another component of the HEASoft software package[17]. Both source and background spectra can be extracted using Xselect and fed into Xspec, which can then fit both simultaneously with a wide variety of models. Figure A.6 shows a sample fit to some U Sco 2010 eruption data, with the data, models, and residuals on the left (the source spectrum is the higher curve, in black, and the background spectrum is the lower curve, in red) and the model parameters on the right. X-ray light curves can be created with Xselect and the same source and background regions used to extract the spectra by filtering on time intervals and using the *extract curve* command.

[14]http://www.swift.psu.edu/xrt/fpca.html
[15]http://heasarc.nasa.gov/docs/software/lheasoft/ftools/xselect/xselect.html
[16]http://heasarc.gsfc.nasa.gov/docs/xanadu/xspec/
[17]http://heasarc.nasa.gov/lheasoft/

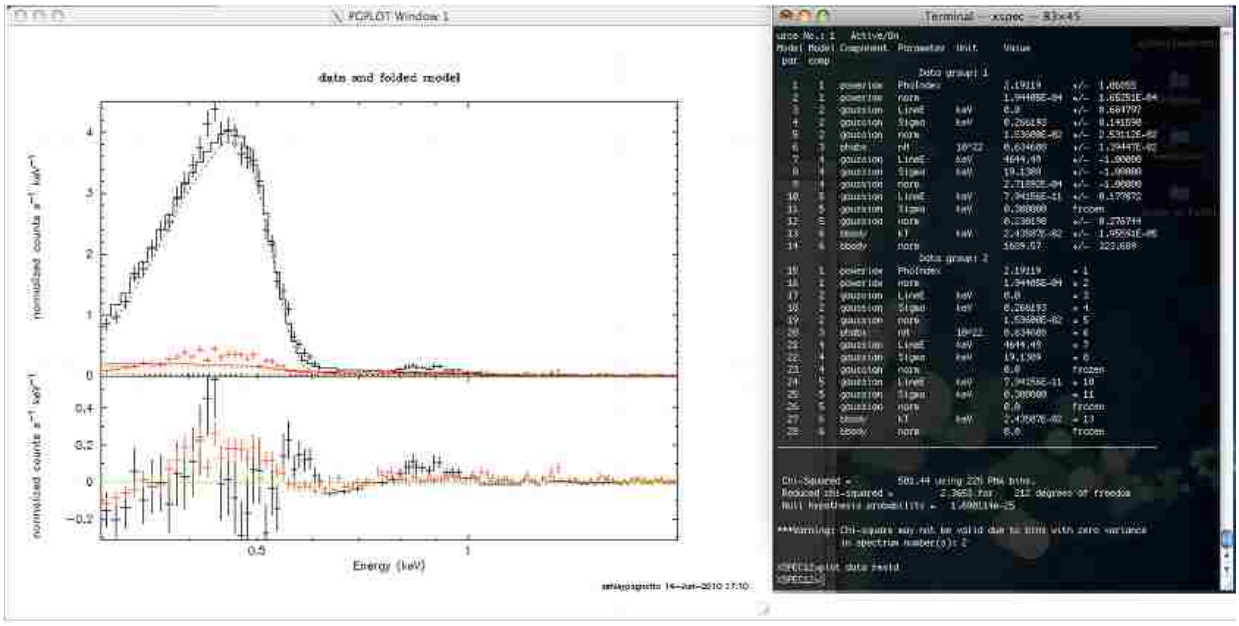

Figure A.6 Xspec Example. This figure shows a sample Xspec model fit (left), and the corresponding parameters (right), for an observation taken during the 2010 eruption of the recurrent nova U Sco. The upper (black) curve is the source spectrum; the lower (right) curve is the background spectrum, which Xspec fits simultaneously. The bottom part of the plot shows the residuals for both fits. To obtain a good fit, the parameters for the models are varied until the reduced χ^2 value is at a minimum.

Appendix B: Permission Statements

This appendix contains permission statements from IOP Publishing Limited and the Nature Publishing Group. The statements are screenshots from the publishers' websites. The IOP Publishing statement (Figure B.1) applies to Pagnotta et al. (2009) and Pagnotta & Schaefer (2012, Submitted to ApJ) in Chapter 2; Schaefer, Pagnotta, & Shara (2010) in Chapter 3; Schaefer, Pagnotta, et al. (2011) in Chapter 4; and Edwards, Pagnotta, & Schaefer (2012) in Chapter 5. The Nature Publishing Group statement (Figure B.2) applies to Schaefer & Pagnotta (2012) in Chapter 5.

Assignment of copyright form - IOP Publishing Limited

1. IOP Publishing Limited ("IOP") agrees to publish:
Manuscript Title: . . . . . **("the Article") written by**
Names of all Authors: . . . . . **("the Named Authors")**
in the following journal . . . . . **("the Journal")**

2. Transfer of Copyright Agreement
2.1 On acceptance for publication the undersigned author(s) ("Author") of the Article assigns exclusively to IOP worldwide copyright in the Article for the full term and for all media and formats in all material published as part of the Article, which expression includes but is not limited to the text, abstract, tables, figures, graphs, video abstracts and other multimedia content but excludes any other item referred to as supplementary material.

2.2 If any of the Named Authors are Government employees, on acceptance for publication the Author shall grant IOP a royalty free exclusive licence for the full term of copyright for all media and formats to do in relation to the Article all acts restricted by copyright worldwide.

2.3 On acceptance for publication the Author shall grant IOP a royalty free non-exclusive licence for the full term of copyright for all media and formats to do in relation to any supplementary material deemed to be part of the Article all acts restricted by copyright worldwide.

3. Author Rights
3.1 IOP grants the Named Authors the rights specified in 3.2 and 3.3. All such rights must be exercised for non-commercial purposes, if possible should display citation information and IOP's copyright notice, and for electronic use best efforts must be made to include a link to the on-line abstract in the Journal. Exercise of the rights in 3.3 additionally must not use the final published IOP format but the Named Author's own format (which may include amendments made following peer review).

3.2 The rights are:
3.2.1 To make copies of the Article (all or part) for teaching purposes;
3.2.2 To include the Article (all or part) in a research thesis or dissertation;
3.2.3 To make oral presentation of the Article (all or part) and to include a summary and/or highlights of it in papers distributed at such presentations or in conference proceedings; and
3.2.4 All proprietary rights other than copyright.

3.3 The additional rights are to:
3.3.1 Use the Article (all or part) without modification in personal compilations or publications of a Named Author's own works (provided not created by third party publisher);
3.3.2 Include the Article (all or part) on a Named Author's own personal web site;
3.3.3 Include the Article (all or part) on web sites of the Institution (including its repository) where a Named Author worked when research for the Article was carried out; and
3.3.4 No sooner than 12 months after publication to include the Article (all or part) on third party web sites including e-print servers, but not on other publisher's web sites.

Figure B.1 IOP Permissions. Permission statement from the Institute of Physics website, accessed on 29 February 2012: http://authors.iop.org/atom/help.nsf/0/F20EC7D4A1A670AA80256F1C0053EEFF

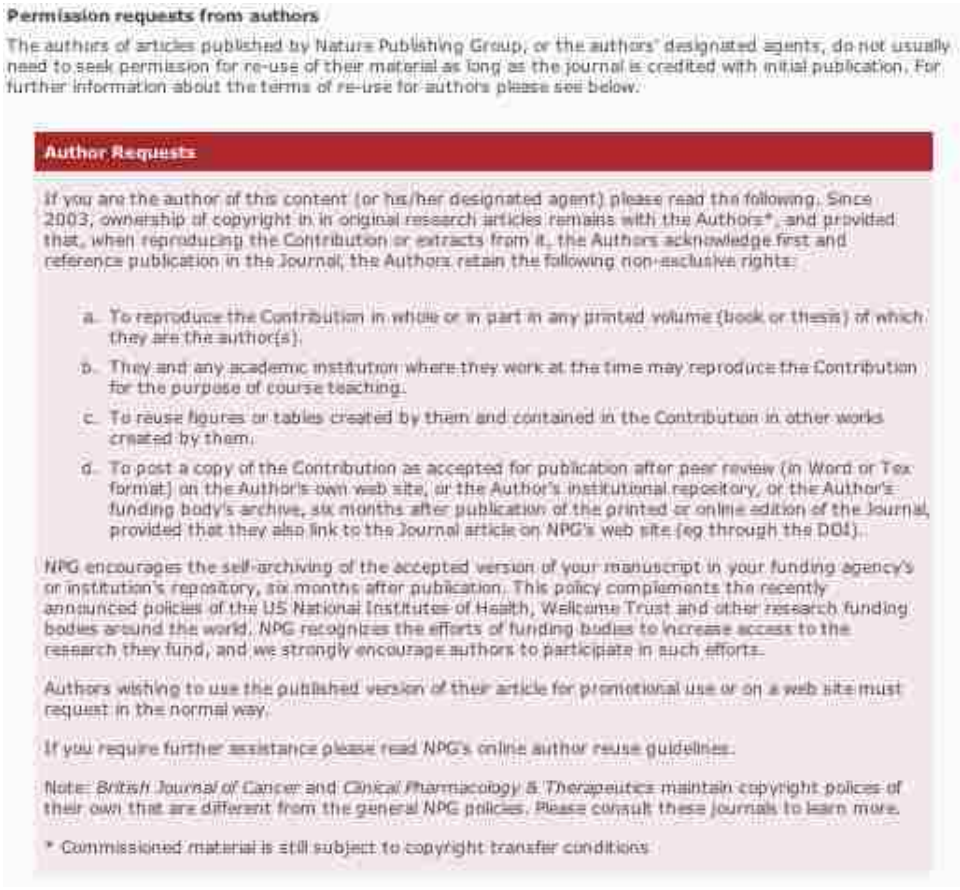

Permission requests from authors

The authors of articles published by Nature Publishing Group, or the authors' designated agents, do not usually need to seek permission for re-use of their material as long as the journal is credited with initial publication. For further information about the terms of re-use for authors please see below.

Author Requests

If you are the author of this content (or his/her designated agent) please read the following. Since 2003, ownership of copyright in in original research articles remains with the Authors*, and provided that, when reproducing the Contribution or extracts from it, the Authors acknowledge first and reference publication in the Journal, the Authors retain the following non-exclusive rights:

a. To reproduce the Contribution in whole or in part in any printed volume (book or thesis) of which they are the author(s).

b. They and any academic institution where they work at the time may reproduce the Contribution for the purpose of course teaching.

c. To reuse figures or tables created by them and contained in the Contribution in other works created by them.

d. To post a copy of the Contribution as accepted for publication after peer review (in Word or Tex format) on the Author's own web site, or the Author's institutional repository, or the Author's funding body's archive, six months after publication of the printed or online edition of the Journal, provided that they also link to the Journal article on NPG's web site (eg through the DOI).

NPG encourages the self-archiving of the accepted version of your manuscript in your funding agency's or institution's repository, six months after publication. This policy complements the recently announced policies of the US National Institutes of Health, Wellcome Trust and other research funding bodies around the world. NPG recognizes the efforts of funding bodies to increase access to the research they fund, and we strongly encourage authors to participate in such efforts.

Authors wishing to use the published version of their article for promotional use or on a web site must request in the normal way.

If you require further assistance please read NPG's online author reuse guidelines.

Note: *British Journal of Cancer* and *Clinical Pharmacology & Therapeutics* maintain copyright polices of their own that are different from the general NPG policies. Please consult these journals to learn more.

* Commissioned material is still subject to copyright transfer conditions

Figure B.2 NPG Permissions. Permission statement from the Nature Publishing Group website, accessed on 29 February 2012: http://www.nature.com/reprints/permission-requests.html

Appendix C: U Sco 2010 SMARTS+SAAO Data Table

This table presents 589 of my observations of the 2010 U Sco eruption from the SMARTS 1.3m Telescope, 223 observations made by G. Handler using the SAAO 0.5m Telescope, and B. Harris's discovery observation. These observations were used to create Figure 4.2.

Table C.1. U Sco 2010 Eruption Multi-Wavelength Light Curve Data

HJD	Filter	Magnitude	1σ Uncertainty	Source
2455224.94	V	7.890	0.010	Harris
2455225.57	B	9.229	0.018	SAAO
2455225.57	I	7.583	0.017	SAAO
2455225.57	V	8.879	0.015	SAAO
2455225.59	B	9.250	0.018	SAAO
2455225.59	I	7.603	0.018	SAAO
2455225.59	R	8.223	0.017	SAAO
2455225.59	U	8.384	0.022	SAAO
2455225.59	V	8.903	0.015	SAAO
2455225.61	B	9.320	0.018	SAAO
2455225.61	I	7.632	0.017	SAAO
2455225.61	R	8.261	0.017	SAAO
2455225.61	U	8.426	0.022	SAAO
2455225.61	V	8.955	0.015	SAAO
2455225.83	B	9.467	0.036	SMARTS
2455225.83	I	7.823	0.008	SMARTS
2455225.83	R	8.391	0.009	SMARTS
2455225.83	V	9.120	0.015	SMARTS
2455225.87	B	9.409	0.022	SMARTS
2455225.87	I	7.864	0.008	SMARTS
2455225.87	R	8.424	0.008	SMARTS
2455225.87	V	9.295	0.011	SMARTS
2455226.58	B	9.979	0.019	SAAO
2455226.58	I	8.641	0.018	SAAO
2455226.58	R	8.990	0.017	SAAO
2455226.58	U	9.295	0.023	SAAO
2455226.58	V	9.813	0.015	SAAO
2455226.60	B	9.994	0.018	SAAO
2455226.60	I	8.672	0.018	SAAO
2455226.60	R	9.004	0.017	SAAO
2455226.60	U	9.326	0.022	SAAO
2455226.60	V	9.847	0.015	SAAO
2455226.61	B	10.025	0.018	SAAO
2455226.61	I	8.700	0.018	SAAO
2455226.61	R	9.025	0.017	SAAO
2455226.61	U	9.343	0.022	SAAO
2455226.61	V	9.856	0.015	SAAO
2455226.88	B	9.906	0.047	SMARTS
2455226.88	I	8.903	0.018	SMARTS
2455226.88	R	9.012	0.022	SMARTS
2455226.89	V	9.929	0.026	SMARTS
2455228.58	B	10.670	0.020	SAAO
2455228.58	I	10.125	0.019	SAAO
2455228.58	R	10.039	0.018	SAAO
2455228.58	U	10.091	0.025	SAAO
2455228.58	V	10.717	0.016	SAAO
2455228.59	B	10.712	0.019	SAAO
2455228.59	I	10.127	0.019	SAAO
2455228.59	R	10.048	0.018	SAAO
2455228.59	U	10.128	0.024	SAAO
2455228.59	V	10.737	0.016	SAAO
2455228.61	B	10.718	0.019	SAAO
2455228.61	I	10.162	0.018	SAAO
2455228.61	R	10.081	0.017	SAAO
2455228.61	U	10.156	0.023	SAAO
2455228.61	V	10.755	0.015	SAAO
2455229.57	B	11.070	0.020	SAAO
2455229.57	I	10.639	0.020	SAAO
2455229.57	R	10.583	0.019	SAAO
2455229.57	U	10.567	0.026	SAAO
2455229.57	V	11.196	0.016	SAAO
2455229.59	B	11.104	0.020	SAAO
2455229.59	I	10.671	0.019	SAAO
2455229.59	R	10.608	0.018	SAAO
2455229.59	U	10.615	0.025	SAAO
2455229.59	V	11.227	0.016	SAAO
2455229.60	B	11.156	0.019	SAAO
2455229.60	I	10.714	0.019	SAAO
2455229.60	R	10.654	0.018	SAAO
2455229.60	U	10.619	0.025	SAAO
2455229.60	V	11.278	0.016	SAAO
2455229.88	J	10.116	0.008	SMARTS
2455229.88	B	11.046	0.027	SMARTS
2455229.88	K	9.361	0.074	SMARTS
2455229.88	I	10.662	0.011	SMARTS
2455229.88	K	9.383	0.076	SMARTS
2455229.88	R	10.638	0.017	SMARTS
2455229.88	H	9.830	0.016	SMARTS
2455229.88	V	11.329	0.018	SMARTS
2455230.57	B	11.350	0.021	SAAO

Table C.1—Continued

HJD	Filter	Magnitude	1σ Uncertainty	Source
2455230.57	I	10.997	0.020	SAAO
2455230.57	R	11.009	0.019	SAAO
2455230.57	U	10.808	0.026	SAAO
2455230.57	V	11.479	0.016	SAAO
2455230.58	B	11.353	0.020	SAAO
2455230.58	I	10.990	0.020	SAAO
2455230.58	R	10.997	0.019	SAAO
2455230.58	U	10.794	0.025	SAAO
2455230.58	V	11.507	0.016	SAAO
2455230.60	B	11.380	0.020	SAAO
2455230.60	I	11.033	0.020	SAAO
2455230.60	R	11.045	0.019	SAAO
2455230.60	U	10.866	0.025	SAAO
2455230.60	V	11.543	0.016	SAAO
2455230.86	J	10.600	0.011	SMARTS
2455230.86	B	11.585	0.020	SMARTS
2455230.86	K	9.652	0.090	SMARTS
2455230.86	I	11.204	0.011	SMARTS
2455230.86	K	9.670	0.086	SMARTS
2455230.86	R	11.245	0.013	SMARTS
2455230.86	H	10.303	0.028	SMARTS
2455230.86	V	11.894	0.013	SMARTS
2455231.83	J	11.151	0.011	SMARTS
2455231.83	B	11.992	0.036	SMARTS
2455231.83	K	10.239	0.114	SMARTS
2455231.83	I	11.695	0.014	SMARTS
2455231.83	K	10.202	0.119	SMARTS
2455231.83	R	11.747	0.024	SMARTS
2455231.83	H	10.839	0.027	SMARTS
2455231.83	V	12.282	0.014	SMARTS
2455232.83	B	12.258	0.114	SMARTS
2455232.83	I	12.225	0.066	SMARTS
2455232.83	R	12.416	0.046	SMARTS
2455232.84	V	12.867	0.133	SMARTS
2455233.58	B	12.847	0.030	SAAO
2455233.58	I	12.596	0.032	SAAO
2455233.58	R	12.666	0.028	SAAO
2455233.58	U	12.267	0.037	SAAO
2455233.58	V	13.102	0.021	SAAO
2455233.60	B	13.082	0.030	SAAO
2455233.60	I	12.667	0.033	SAAO
2455233.60	R	12.794	0.029	SAAO
2455233.60	U	12.526	0.038	SAAO
2455233.60	V	13.235	0.021	SAAO
2455234.60	B	13.100	0.030	SAAO
2455234.60	I	12.801	0.033	SAAO
2455234.60	R	12.898	0.029	SAAO
2455234.60	U	12.418	0.036	SAAO
2455234.60	V	13.277	0.021	SAAO
2455235.57	B	13.992	0.048	SAAO
2455235.57	I	13.470	0.057	SAAO
2455235.57	R	13.642	0.047	SAAO
2455235.57	U	13.264	0.060	SAAO
2455235.57	V	13.986	0.030	SAAO
2455235.60	B	13.916	0.039	SAAO
2455235.60	I	13.290	0.045	SAAO
2455235.60	R	13.554	0.038	SAAO
2455235.60	U	13.209	0.049	SAAO
2455235.60	V	13.854	0.025	SAAO
2455236.84	J	12.997	0.014	SMARTS
2455236.84	B	14.081	0.016	SMARTS
2455236.84	K	11.871	0.091	SMARTS
2455236.84	I	13.443	0.010	SMARTS
2455236.84	K	11.927	0.091	SMARTS
2455236.84	R	13.658	0.013	SMARTS
2455236.84	H	12.610	0.026	SMARTS
2455236.84	V	13.946	0.011	SMARTS
2455237.88	J	13.055	0.009	SMARTS
2455237.88	B	14.022	0.014	SMARTS
2455237.88	K	12.060	0.085	SMARTS
2455237.88	I	13.423	0.009	SMARTS
2455237.88	K	12.106	0.080	SMARTS
2455237.88	R	13.677	0.012	SMARTS
2455237.88	H	12.741	0.013	SMARTS
2455237.88	V	13.904	0.009	SMARTS
2455238.59	B	14.465	0.041	SAAO
2455238.59	I	13.726	0.045	SAAO
2455238.59	R	13.951	0.038	SAAO
2455238.59	U	13.826	0.053	SAAO
2455238.59	V	14.302	0.025	SAAO

Table C.1—Continued

HJD	Filter	Magnitude	1σ Uncertainty	Source
2455239.54	B	14.406	0.035	SAAO
2455239.54	I	13.527	0.036	SAAO
2455239.54	R	13.853	0.032	SAAO
2455239.54	U	13.712	0.047	SAAO
2455239.54	V	14.143	0.022	SAAO
2455239.57	B	14.337	0.038	SAAO
2455239.57	I	13.582	0.046	SAAO
2455239.57	R	13.808	0.038	SAAO
2455239.57	U	13.626	0.047	SAAO
2455239.57	V	14.126	0.025	SAAO
2455239.60	B	14.332	0.038	SAAO
2455239.60	I	13.701	0.048	SAAO
2455239.60	R	13.882	0.038	SAAO
2455239.60	U	13.645	0.046	SAAO
2455239.60	V	14.175	0.025	SAAO
2455239.80	J	13.351	0.011	SMARTS
2455239.80	B	14.499	0.010	SMARTS
2455239.80	K	12.290	0.101	SMARTS
2455239.80	I	13.764	0.006	SMARTS
2455239.81	K	12.302	0.101	SMARTS
2455239.81	R	14.034	0.006	SMARTS
2455239.81	H	12.964	0.029	SMARTS
2455239.81	V	14.311	0.008	SMARTS
2455240.56	B	14.591	0.053	SAAO
2455240.56	I	14.147	0.077	SAAO
2455240.56	R	14.185	0.055	SAAO
2455240.56	U	13.924	0.068	SAAO
2455240.56	V	14.374	0.033	SAAO
2455240.59	B	14.566	0.045	SAAO
2455240.59	I	13.798	0.052	SAAO
2455240.59	R	14.066	0.045	SAAO
2455240.59	U	13.819	0.056	SAAO
2455240.59	V	14.412	0.029	SAAO
2455240.61	B	14.499	0.041	SAAO
2455240.61	I	13.722	0.047	SAAO
2455240.61	R	14.088	0.043	SAAO
2455240.61	U	13.829	0.051	SAAO
2455240.61	V	14.301	0.027	SAAO
2455240.81	J	13.295	0.014	SMARTS
2455240.81	B	14.404	0.013	SMARTS
2455240.81	I	13.679	0.013	SMARTS
2455240.81	R	13.937	0.018	SMARTS
2455240.81	V	14.154	0.034	SMARTS
2455241.55	B	14.446	0.043	SAAO
2455241.55	I	13.662	0.050	SAAO
2455241.55	R	13.861	0.043	SAAO
2455241.55	U	13.770	0.057	SAAO
2455241.55	V	14.140	0.027	SAAO
2455241.57	B	14.378	0.040	SAAO
2455241.57	I	13.996	0.051	SAAO
2455241.57	R	13.873	0.041	SAAO
2455241.57	U	13.685	0.052	SAAO
2455241.57	V	14.114	0.026	SAAO
2455241.83	J	13.416	0.010	SMARTS
2455241.83	B	14.475	0.009	SMARTS
2455241.83	K	12.503	0.092	SMARTS
2455241.83	I	13.801	0.006	SMARTS
2455241.83	K	12.549	0.089	SMARTS
2455241.83	R	14.045	0.006	SMARTS
2455241.83	H	13.045	0.017	SMARTS
2455241.83	V	14.281	0.008	SMARTS
2455242.55	B	14.667	0.047	SAAO
2455242.55	I	13.636	0.043	SAAO
2455242.55	R	14.131	0.043	SAAO
2455242.55	U	13.906	0.064	SAAO
2455242.55	V	14.373	0.027	SAAO
2455242.57	B	14.587	0.044	SAAO
2455242.57	I	13.704	0.043	SAAO
2455242.57	R	14.117	0.042	SAAO
2455242.57	U	13.802	0.058	SAAO
2455242.57	V	14.362	0.027	SAAO
2455242.59	B	14.501	0.038	SAAO
2455242.59	I	13.763	0.039	SAAO
2455242.59	R	14.030	0.036	SAAO
2455242.59	U	13.722	0.050	SAAO
2455242.59	V	14.312	0.024	SAAO
2455242.82	J	13.320	0.010	SMARTS
2455242.82	B	14.359	0.009	SMARTS
2455242.82	K	12.458	0.083	SMARTS
2455242.82	I	13.663	0.006	SMARTS

Table C.1—Continued

HJD	Filter	Magnitude	1σ Uncertainty	Source
2455242.82	K	12.458	0.083	SMARTS
2455242.82	R	13.930	0.006	SMARTS
2455242.82	H	12.984	0.023	SMARTS
2455242.82	V	14.157	0.008	SMARTS
2455243.82	J	13.490	0.010	SMARTS
2455243.82	B	14.527	0.010	SMARTS
2455243.82	K	12.643	0.125	SMARTS
2455243.82	I	13.837	0.006	SMARTS
2455243.82	K	12.693	0.127	SMARTS
2455243.82	R	14.110	0.006	SMARTS
2455243.82	H	13.132	0.016	SMARTS
2455243.82	V	14.347	0.009	SMARTS
2455244.55	B	14.523	0.042	SAAO
2455244.55	I	13.863	0.048	SAAO
2455244.55	R	14.105	0.041	SAAO
2455244.55	U	13.835	0.056	SAAO
2455244.55	V	14.310	0.026	SAAO
2455244.58	B	14.662	0.044	SAAO
2455244.58	I	13.778	0.046	SAAO
2455244.58	R	14.130	0.043	SAAO
2455244.58	U	13.884	0.057	SAAO
2455244.58	V	14.448	0.027	SAAO
2455244.60	B	14.623	0.042	SAAO
2455244.60	I	13.941	0.047	SAAO
2455244.60	R	14.194	0.041	SAAO
2455244.60	U	13.934	0.055	SAAO
2455244.60	V	14.426	0.026	SAAO
2455245.54	B	14.648	0.038	SAAO
2455245.54	I	14.150	0.046	SAAO
2455245.54	R	14.207	0.036	SAAO
2455245.54	U	14.025	0.050	SAAO
2455245.54	V	14.441	0.024	SAAO
2455245.80	J	13.512	0.013	SMARTS
2455245.80	B	14.593	0.010	SMARTS
2455245.80	K	12.598	0.116	SMARTS
2455245.80	I	13.860	0.006	SMARTS
2455245.80	K	12.580	0.114	SMARTS
2455245.80	R	14.145	0.006	SMARTS
2455245.80	H	13.051	0.032	SMARTS
2455245.80	V	14.360	0.009	SMARTS
2455246.54	B	14.472	0.035	SAAO
2455246.54	I	13.874	0.040	SAAO
2455246.54	R	14.014	0.034	SAAO
2455246.54	U	13.701	0.046	SAAO
2455246.54	V	14.283	0.023	SAAO
2455246.56	B	14.557	0.035	SAAO
2455246.56	I	13.865	0.038	SAAO
2455246.56	R	14.045	0.033	SAAO
2455246.56	U	13.785	0.045	SAAO
2455246.56	V	14.340	0.022	SAAO
2455246.59	B	14.528	0.035	SAAO
2455246.59	I	13.985	0.039	SAAO
2455246.59	R	14.223	0.035	SAAO
2455246.59	U	13.741	0.044	SAAO
2455246.59	V	14.415	0.023	SAAO
2455246.88	B	14.499	0.004	SMARTS
2455247.54	B	14.712	0.043	SAAO
2455247.54	I	14.196	0.051	SAAO
2455247.54	R	14.281	0.042	SAAO
2455247.54	U	13.964	0.057	SAAO
2455247.54	V	14.558	0.027	SAAO
2455247.56	B	14.661	0.037	SAAO
2455247.56	I	13.893	0.041	SAAO
2455247.56	R	14.186	0.035	SAAO
2455247.56	U	13.883	0.049	SAAO
2455247.56	V	14.397	0.023	SAAO
2455247.59	B	14.571	0.035	SAAO
2455247.59	I	13.909	0.041	SAAO
2455247.59	R	14.121	0.035	SAAO
2455247.59	U	13.957	0.046	SAAO
2455247.59	V	14.433	0.023	SAAO
2455247.61	B	14.456	0.032	SAAO
2455247.61	I	13.748	0.035	SAAO
2455247.61	R	13.998	0.031	SAAO
2455247.61	U	13.680	0.041	SAAO
2455247.61	V	14.251	0.021	SAAO
2455248.82	J	13.699	0.012	SMARTS
2455248.82	B	14.599	0.009	SMARTS
2455248.82	K	12.974	0.131	SMARTS
2455248.82	I	13.950	0.006	SMARTS

Table C.1—Continued

HJD	Filter	Magnitude	1σ Uncertainty	Source
2455248.82	K	12.959	0.130	SMARTS
2455248.82	R	14.229	0.006	SMARTS
2455248.82	H	13.426	0.019	SMARTS
2455248.82	V	14.387	0.008	SMARTS
2455249.57	B	14.841	0.038	SAAO
2455249.57	I	14.246	0.045	SAAO
2455249.57	R	14.343	0.036	SAAO
2455249.57	U	14.001	0.050	SAAO
2455249.57	V	14.523	0.023	SAAO
2455249.59	B	14.826	0.038	SAAO
2455249.59	I	13.987	0.041	SAAO
2455249.59	R	14.314	0.037	SAAO
2455249.59	U	13.954	0.048	SAAO
2455249.59	V	14.576	0.024	SAAO
2455250.84	J	13.901	0.013	SMARTS
2455250.84	B	14.935	0.009	SMARTS
2455250.84	K	12.822	0.100	SMARTS
2455250.84	I	14.214	0.006	SMARTS
2455250.84	K	12.808	0.103	SMARTS
2455250.84	R	14.491	0.006	SMARTS
2455250.84	H	13.597	0.025	SMARTS
2455250.84	V	14.724	0.020	SMARTS
2455251.91	J	13.908	0.012	SMARTS
2455251.91	B	14.856	0.018	SMARTS
2455251.91	K	13.273	0.085	SMARTS
2455251.91	I	14.134	0.009	SMARTS
2455251.91	K	13.306	0.097	SMARTS
2455251.91	R	14.421	0.009	SMARTS
2455253.78	J	13.929	0.028	SMARTS
2455253.78	B	14.916	0.021	SMARTS
2455253.78	K	13.065	0.241	SMARTS
2455253.78	I	14.256	0.008	SMARTS
2455253.78	K	13.214	0.272	SMARTS
2455253.78	R	14.540	0.008	SMARTS
2455253.78	H	13.531	0.092	SMARTS
2455253.78	V	14.702	0.012	SMARTS
2455255.82	J	14.573	0.016	SMARTS
2455255.82	B	15.674	0.016	SMARTS
2455255.82	K	13.970	0.200	SMARTS
2455255.82	I	14.940	0.009	SMARTS
2455255.82	K	13.930	0.195	SMARTS
2455255.82	R	15.247	0.008	SMARTS
2455255.83	H	14.243	0.040	SMARTS
2455255.83	V	15.436	0.011	SMARTS
2455256.83	J	14.360	0.015	SMARTS
2455256.83	B	15.463	0.018	SMARTS
2455256.83	K	13.898	0.192	SMARTS
2455256.83	I	14.705	0.008	SMARTS
2455256.83	K	13.839	0.187	SMARTS
2455256.83	R	15.013	0.008	SMARTS
2455256.83	H	14.058	0.031	SMARTS
2455256.83	V	15.216	0.012	SMARTS
2455258.83	J	14.717	0.021	SMARTS
2455258.83	B	15.783	0.016	SMARTS
2455258.84	K	14.166	0.225	SMARTS
2455258.84	I	15.054	0.011	SMARTS
2455258.84	K	14.350	0.264	SMARTS
2455258.84	R	15.336	0.010	SMARTS
2455258.84	H	14.406	0.048	SMARTS
2455258.84	V	15.535	0.013	SMARTS
2455259.81	J	14.971	0.023	SMARTS
2455259.81	B	15.980	0.017	SMARTS
2455259.81	I	15.291	0.010	SMARTS
2455259.82	R	15.570	0.009	SMARTS
2455259.82	H	14.728	0.064	SMARTS
2455259.82	V	15.720	0.013	SMARTS
2455261.85	J	15.194	0.031	SMARTS
2455261.85	B	16.464	0.016	SMARTS
2455261.85	I	15.628	0.024	SMARTS
2455261.85	R	15.956	0.013	SMARTS
2455261.85	V	16.191	0.017	SMARTS
2455262.76	J	15.198	0.093	SMARTS
2455262.76	B	16.418	0.031	SMARTS
2455262.76	I	15.755	0.055	SMARTS
2455262.76	V	16.150	0.016	SMARTS
2455264.82	J	15.549	0.024	SMARTS
2455264.82	B	16.849	0.011	SMARTS
2455264.82	H	15.247	0.049	SMARTS
2455264.82	I	15.981	0.010	SMARTS
2455264.82	H	15.245	0.051	SMARTS

Table C.1—Continued

HJD	Filter	Magnitude	1σ Uncertainty	Source
2455264.82	R	16.304	0.008	SMARTS
2455264.82	H	15.258	0.049	SMARTS
2455264.82	V	16.502	0.009	SMARTS
2455266.79	J	16.027	0.043	SMARTS
2455266.79	B	17.504	0.013	SMARTS
2455266.79	H	15.905	0.140	SMARTS
2455266.79	I	16.571	0.014	SMARTS
2455266.80	H	15.895	0.139	SMARTS
2455266.80	R	16.930	0.011	SMARTS
2455266.80	H	15.899	0.136	SMARTS
2455266.80	V	17.158	0.011	SMARTS
2455267.83	J	15.812	0.027	SMARTS
2455267.83	B	17.071	0.011	SMARTS
2455267.83	H	15.569	0.067	SMARTS
2455267.83	I	16.225	0.011	SMARTS
2455267.84	H	15.540	0.065	SMARTS
2455267.84	R	16.546	0.009	SMARTS
2455267.84	H	15.545	0.063	SMARTS
2455267.84	V	16.718	0.009	SMARTS
2455268.78	J	15.887	0.034	SMARTS
2455268.78	B	17.167	0.012	SMARTS
2455268.79	H	15.779	0.117	SMARTS
2455268.79	I	16.465	0.013	SMARTS
2455268.79	H	15.777	0.104	SMARTS
2455268.79	R	16.734	0.010	SMARTS
2455268.79	H	15.752	0.105	SMARTS
2455268.79	V	16.883	0.010	SMARTS
2455269.81	B	17.703	0.013	SMARTS
2455269.81	I	16.740	0.015	SMARTS
2455269.82	R	17.056	0.012	SMARTS
2455269.82	V	17.302	0.012	SMARTS
2455271.82	J	16.079	0.041	SMARTS
2455271.82	B	17.499	0.012	SMARTS
2455271.82	H	15.881	0.114	SMARTS
2455271.82	I	16.644	0.015	SMARTS
2455271.82	H	15.857	0.104	SMARTS
2455271.82	R	16.963	0.011	SMARTS
2455271.82	H	15.904	0.110	SMARTS
2455271.82	V	17.168	0.011	SMARTS
2455272.79	J	15.983	0.033	SMARTS
2455272.79	B	17.410	0.012	SMARTS
2455272.79	H	15.798	0.100	SMARTS
2455272.79	I	16.466	0.013	SMARTS
2455272.79	H	15.720	0.092	SMARTS
2455272.79	R	16.802	0.010	SMARTS
2455272.79	H	15.755	0.097	SMARTS
2455272.79	V	17.009	0.010	SMARTS
2455273.84	J	16.098	0.034	SMARTS
2455273.84	B	17.300	0.011	SMARTS
2455273.84	H	15.904	0.088	SMARTS
2455273.84	I	16.533	0.013	SMARTS
2455273.84	H	15.932	0.097	SMARTS
2455273.84	R	16.830	0.010	SMARTS
2455273.84	H	15.894	0.094	SMARTS
2455273.84	V	16.999	0.010	SMARTS
2455274.85	J	15.877	0.032	SMARTS
2455274.85	B	17.018	0.010	SMARTS
2455274.85	H	15.539	0.082	SMARTS
2455274.85	I	16.280	0.012	SMARTS
2455274.85	H	15.565	0.090	SMARTS
2455274.85	R	16.552	0.009	SMARTS
2455274.85	H	15.550	0.089	SMARTS
2455274.85	V	16.711	0.009	SMARTS
2455275.84	J	16.001	0.043	SMARTS
2455275.84	B	17.427	0.012	SMARTS
2455275.84	H	15.837	0.161	SMARTS
2455275.84	I	16.542	0.014	SMARTS
2455275.84	H	15.920	0.171	SMARTS
2455275.84	R	16.922	0.011	SMARTS
2455275.84	H	15.821	0.155	SMARTS
2455275.84	V	17.115	0.011	SMARTS
2455279.85	J	15.965	0.036	SMARTS
2455279.85	B	17.073	0.011	SMARTS
2455279.86	H	15.853	0.116	SMARTS
2455279.86	I	16.326	0.012	SMARTS
2455279.86	H	15.908	0.126	SMARTS
2455279.86	R	16.639	0.010	SMARTS
2455279.86	H	15.871	0.120	SMARTS
2455279.86	V	16.788	0.010	SMARTS
2455280.90	J	15.961	0.046	SMARTS

Table C.1—Continued

HJD	Filter	Magnitude	1σ Uncertainty	Source
2455280.90	B	17.154	0.011	SMARTS
2455280.90	H	15.713	0.093	SMARTS
2455280.90	I	16.382	0.013	SMARTS
2455280.90	H	15.705	0.093	SMARTS
2455280.90	R	16.657	0.010	SMARTS
2455280.90	H	15.675	0.091	SMARTS
2455280.90	V	16.844	0.010	SMARTS
2455282.83	J	16.295	0.046	SMARTS
2455282.83	B	17.842	0.016	SMARTS
2455282.83	H	15.995	0.129	SMARTS
2455282.83	I	16.900	0.017	SMARTS
2455282.83	H	16.112	0.144	SMARTS
2455282.83	R	17.248	0.014	SMARTS
2455282.83	H	15.962	0.128	SMARTS
2455282.83	V	17.442	0.014	SMARTS
2455283.72	J	16.313	0.054	SMARTS
2455283.72	B	17.889	0.030	SMARTS
2455283.72	H	16.213	0.216	SMARTS
2455283.72	I	16.992	0.023	SMARTS
2455283.72	H	16.265	0.231	SMARTS
2455283.72	R	17.321	0.020	SMARTS
2455283.72	H	16.249	0.226	SMARTS
2455283.72	V	17.469	0.022	SMARTS
2455284.78	J	16.320	0.056	SMARTS
2455284.78	B	17.883	0.030	SMARTS
2455284.78	H	16.156	0.220	SMARTS
2455284.78	I	16.973	0.022	SMARTS
2455284.78	H	16.206	0.230	SMARTS
2455284.78	R	17.299	0.019	SMARTS
2455284.78	H	16.124	0.217	SMARTS
2455284.78	V	17.546	0.023	SMARTS
2455285.72	J	15.953	0.078	SMARTS
2455285.72	B	17.791	0.075	SMARTS
2455285.72	H	15.894	0.214	SMARTS
2455285.72	I	16.959	0.058	SMARTS
2455285.73	H	15.913	0.213	SMARTS
2455285.73	R	17.326	0.054	SMARTS
2455285.73	H	15.930	0.211	SMARTS
2455285.73	V	17.506	0.058	SMARTS
2455287.72	J	16.406	0.078	SMARTS
2455287.72	B	18.391	0.060	SMARTS
2455287.72	H	16.343	0.261	SMARTS
2455287.72	I	17.212	0.047	SMARTS
2455287.72	H	16.242	0.231	SMARTS
2455287.72	R	17.604	0.041	SMARTS
2455287.72	H	16.198	0.218	SMARTS
2455287.72	V	17.871	0.046	SMARTS
2455288.75	J	16.491	0.065	SMARTS
2455288.75	B	18.177	0.042	SMARTS
2455288.75	H	16.324	0.136	SMARTS
2455288.75	I	17.143	0.044	SMARTS
2455288.75	H	16.246	0.131	SMARTS
2455288.75	R	17.474	0.036	SMARTS
2455288.75	H	16.335	0.138	SMARTS
2455288.75	V	17.721	0.039	SMARTS
2455289.75	J	16.591	0.127	SMARTS
2455289.75	B	18.372	0.057	SMARTS
2455289.75	I	17.206	0.064	SMARTS
2455289.76	R	17.509	0.051	SMARTS
2455289.76	V	17.714	0.048	SMARTS
2455292.73	J	16.857	0.117	SMARTS
2455292.73	B	18.474	0.043	SMARTS
2455292.74	I	17.422	0.064	SMARTS
2455292.74	R	17.708	0.048	SMARTS
2455292.74	V	18.110	0.066	SMARTS
2455293.74	J	16.649	0.065	SMARTS
2455293.74	B	18.564	0.025	SMARTS
2455293.74	H	16.505	0.206	SMARTS
2455293.74	I	17.344	0.025	SMARTS
2455293.75	H	16.490	0.205	SMARTS
2455293.75	R	17.769	0.020	SMARTS
2455293.75	H	16.566	0.220	SMARTS
2455293.75	V	17.991	0.022	SMARTS
2455294.77	J	16.963	0.065	SMARTS
2455294.77	B	18.563	0.022	SMARTS
2455294.77	H	16.628	0.140	SMARTS
2455294.77	I	17.400	0.023	SMARTS
2455294.77	H	16.505	0.120	SMARTS
2455294.77	R	17.755	0.017	SMARTS
2455294.77	H	16.542	0.123	SMARTS

Table C.1—Continued

HJD	Filter	Magnitude	1σ Uncertainty	Source
2455294.77	V	17.962	0.019	SMARTS
2455295.73	J	16.580	0.053	SMARTS
2455295.73	B	18.509	0.022	SMARTS
2455295.73	H	16.274	0.165	SMARTS
2455295.73	I	17.350	0.023	SMARTS
2455295.73	H	16.391	0.188	SMARTS
2455295.73	R	17.743	0.018	SMARTS
2455295.73	H	16.322	0.169	SMARTS
2455295.73	V	17.978	0.019	SMARTS
2455296.75	J	16.654	0.060	SMARTS
2455296.75	B	18.706	0.023	SMARTS
2455296.75	H	16.412	0.177	SMARTS
2455296.75	I	17.445	0.024	SMARTS
2455296.75	H	16.447	0.170	SMARTS
2455296.75	R	17.861	0.018	SMARTS
2455296.75	H	16.352	0.149	SMARTS
2455296.75	V	18.095	0.020	SMARTS
2455298.75	J	16.566	0.053	SMARTS
2455298.75	B	18.504	0.022	SMARTS
2455298.75	I	17.317	0.023	SMARTS
2455298.76	R	17.695	0.017	SMARTS
2455298.76	V	17.891	0.018	SMARTS
2455299.63	J	16.470	0.089	SMARTS
2455299.63	B	18.584	0.027	SMARTS
2455299.63	I	17.452	0.029	SMARTS
2455299.64	R	17.811	0.021	SMARTS
2455299.64	V	17.997	0.022	SMARTS
2455300.68	J	16.458	0.065	SMARTS
2455300.68	B	18.343	0.022	SMARTS
2455300.69	I	17.231	0.022	SMARTS
2455300.69	R	17.590	0.016	SMARTS
2455300.69	V	17.819	0.018	SMARTS
2455301.64	J	16.435	0.105	SMARTS
2455301.64	B	18.660	0.029	SMARTS
2455301.64	I	17.350	0.027	SMARTS
2455301.64	R	17.782	0.020	SMARTS
2455301.65	V	18.011	0.022	SMARTS
2455304.67	J	16.452	0.132	SMARTS
2455304.67	B	18.244	0.021	SMARTS
2455304.67	I	17.071	0.024	SMARTS
2455304.68	R	17.447	0.017	SMARTS
2455304.68	V	17.702	0.017	SMARTS
2455305.67	J	16.221	0.056	SMARTS
2455305.67	B	17.719	0.014	SMARTS
2455305.67	H	16.135	0.222	SMARTS
2455305.67	I	16.735	0.016	SMARTS
2455305.67	R	17.088	0.013	SMARTS
2455305.67	H	16.250	0.243	SMARTS
2455305.67	V	17.301	0.013	SMARTS
2455306.61	B	18.140	0.023	SMARTS
2455306.61	I	17.052	0.026	SMARTS
2455306.61	R	17.437	0.018	SMARTS
2455306.61	V	17.657	0.020	SMARTS
2455309.59	J	16.248	0.099	SMARTS
2455309.59	B	18.317	0.044	SMARTS
2455309.59	J	16.271	0.097	SMARTS
2455309.59	I	17.151	0.029	SMARTS
2455309.59	J	16.240	0.094	SMARTS
2455309.59	R	17.515	0.025	SMARTS
2455309.59	J	16.196	0.088	SMARTS
2455309.59	V	17.765	0.029	SMARTS
2455310.63	J	16.238	0.065	SMARTS
2455310.63	B	17.953	0.026	SMARTS
2455310.63	J	16.260	0.066	SMARTS
2455310.63	I	16.911	0.021	SMARTS
2455310.63	J	16.254	0.065	SMARTS
2455310.63	R	17.320	0.019	SMARTS
2455310.64	J	16.307	0.071	SMARTS
2455310.64	V	17.534	0.021	SMARTS
2455315.63	B	18.482	0.103	SMARTS
2455315.63	I	17.286	0.084	SMARTS
2455315.64	R	17.799	0.081	SMARTS
2455315.64	V	17.837	0.071	SMARTS
2455317.75	J	16.782	0.165	SMARTS
2455317.75	B	18.597	0.079	SMARTS
2455317.75	J	16.814	0.180	SMARTS
2455317.75	I	17.201	0.069	SMARTS
2455317.75	J	16.797	0.185	SMARTS
2455317.75	R	17.700	0.075	SMARTS
2455317.75	J	16.836	0.185	SMARTS

Table C.1—Continued

HJD	Filter	Magnitude	1σ Uncertainty	Source
2455317.75	V	18.042	0.071	SMARTS
2455319.66	B	18.726	0.051	SMARTS
2455319.66	I	17.335	0.034	SMARTS
2455319.66	R	17.799	0.030	SMARTS
2455319.67	V	18.052	0.034	SMARTS
2455320.67	J	16.573	0.103	SMARTS
2455320.67	B	18.554	0.031	SMARTS
2455320.67	J	16.576	0.099	SMARTS
2455320.67	I	17.227	0.026	SMARTS
2455320.67	J	16.644	0.106	SMARTS
2455320.67	R	17.618	0.021	SMARTS
2455320.67	J	16.519	0.095	SMARTS
2455320.67	V	17.943	0.024	SMARTS
2455321.65	J	16.657	0.157	SMARTS
2455321.65	B	18.603	0.028	SMARTS
2455321.65	J	16.649	0.137	SMARTS
2455321.65	I	17.299	0.028	SMARTS
2455321.66	J	16.433	0.108	SMARTS
2455321.66	R	17.686	0.021	SMARTS
2455321.66	J	16.549	0.117	SMARTS
2455321.66	V	18.024	0.023	SMARTS
2455324.60	B	18.549	0.023	SMARTS
2455324.60	I	17.276	0.026	SMARTS
2455324.60	R	17.617	0.018	SMARTS
2455324.60	V	17.957	0.020	SMARTS
2455325.71	B	18.347	0.018	SMARTS
2455325.71	I	17.093	0.019	SMARTS
2455325.71	R	17.527	0.016	SMARTS
2455325.71	V	17.861	0.017	SMARTS
2455326.70	B	18.317	0.018	SMARTS
2455326.70	I	17.281	0.022	SMARTS
2455326.70	R	17.633	0.016	SMARTS
2455326.70	V	17.866	0.017	SMARTS
2455327.63	B	18.545	0.023	SMARTS
2455327.63	I	17.217	0.021	SMARTS
2455327.64	R	17.594	0.017	SMARTS
2455327.64	V	17.948	0.020	SMARTS
2455335.64	B	18.364	0.018	SMARTS
2455335.64	I	17.053	0.019	SMARTS
2455335.64	R	17.497	0.015	SMARTS
2455335.64	V	17.830	0.016	SMARTS
2455338.63	B	17.552	0.032	SMARTS
2455338.63	I	16.609	0.032	SMARTS
2455338.63	R	16.938	0.032	SMARTS
2455338.64	V	17.089	0.045	SMARTS
2455340.63	B	18.079	0.028	SMARTS
2455340.63	I	16.887	0.023	SMARTS
2455340.64	R	17.300	0.021	SMARTS
2455340.64	V	17.580	0.022	SMARTS
2455341.65	B	18.333	0.036	SMARTS
2455341.65	I	17.083	0.029	SMARTS
2455341.65	R	17.505	0.025	SMARTS
2455341.66	V	17.824	0.031	SMARTS
2455342.69	B	18.371	0.046	SMARTS
2455342.69	I	17.344	0.042	SMARTS
2455342.69	R	17.672	0.033	SMARTS
2455342.70	V	17.896	0.034	SMARTS
2455343.60	B	18.065	0.056	SMARTS
2455343.61	I	17.123	0.063	SMARTS
2455343.61	R	17.375	0.049	SMARTS
2455343.61	V	17.713	0.051	SMARTS
2455346.74	B	18.536	0.048	SMARTS
2455346.74	I	17.226	0.038	SMARTS
2455346.75	R	17.669	0.035	SMARTS
2455346.75	V	18.005	0.040	SMARTS
2455347.68	B	18.749	0.043	SMARTS
2455347.68	I	17.474	0.029	SMARTS
2455347.68	R	17.897	0.026	SMARTS
2455347.68	V	18.159	0.031	SMARTS
2455348.66	B	18.870	0.043	SMARTS
2455348.66	I	17.410	0.028	SMARTS
2455348.66	R	17.855	0.024	SMARTS
2455348.67	V	18.058	0.029	SMARTS
2455349.63	B	18.710	0.066	SMARTS
2455349.63	I	17.434	0.063	SMARTS
2455349.63	R	17.699	0.036	SMARTS
2455349.64	V	18.039	0.041	SMARTS
2455351.69	B	18.347	0.018	SMARTS
2455351.69	I	17.155	0.019	SMARTS
2455351.69	R	17.510	0.015	SMARTS

Table C.1—Continued

HJD	Filter	Magnitude	1σ Uncertainty	Source
2455351.69	V	17.842	0.017	SMARTS
2455352.66	B	18.733	0.023	SMARTS
2455352.66	I	17.368	0.024	SMARTS
2455352.66	R	17.808	0.018	SMARTS
2455352.66	V	18.156	0.020	SMARTS
2455353.63	B	18.737	0.024	SMARTS
2455353.63	I	17.361	0.024	SMARTS
2455353.63	R	17.815	0.018	SMARTS
2455353.63	V	18.185	0.021	SMARTS
2455356.65	B	19.042	0.040	SMARTS
2455356.65	I	17.504	0.028	SMARTS
2455356.66	R	17.934	0.022	SMARTS
2455356.66	V	18.352	0.024	SMARTS
2455359.77	B	18.379	0.020	SMARTS
2455359.77	I	17.175	0.022	SMARTS
2455359.77	R	17.598	0.016	SMARTS
2455359.77	V	17.912	0.018	SMARTS
2455368.59	B	18.455	0.037	SMARTS
2455368.59	I	17.284	0.028	SMARTS
2455368.59	R	17.696	0.034	SMARTS
2455368.59	V	18.025	0.029	SMARTS
2455369.62	B	17.820	0.025	SMARTS
2455369.62	I	16.864	0.021	SMARTS
2455369.62	R	17.174	0.020	SMARTS
2455369.62	V	17.462	0.025	SMARTS
2455372.70	B	18.373	0.063	SMARTS
2455372.70	I	17.152	0.056	SMARTS
2455372.70	R	17.464	0.049	SMARTS
2455372.70	V	17.747	0.049	SMARTS
2455373.64	B	18.686	0.084	SMARTS
2455373.64	I	17.123	0.054	SMARTS
2455373.65	R	17.538	0.053	SMARTS
2455373.65	V	17.869	0.056	SMARTS
2455374.67	B	18.694	0.072	SMARTS
2455374.67	I	17.515	0.064	SMARTS
2455374.67	R	17.923	0.060	SMARTS
2455374.67	V	18.054	0.056	SMARTS
2455375.54	B	18.300	0.036	SMARTS
2455375.55	I	17.138	0.026	SMARTS
2455375.55	R	17.535	0.023	SMARTS
2455375.55	V	17.936	0.031	SMARTS
2455377.63	B	18.950	0.042	SMARTS
2455377.63	I	17.610	0.031	SMARTS
2455377.63	R	18.028	0.026	SMARTS
2455377.63	V	18.410	0.032	SMARTS
2455378.63	B	19.228	0.047	SMARTS
2455378.63	I	17.561	0.028	SMARTS
2455378.63	R	18.108	0.025	SMARTS
2455378.63	V	18.499	0.031	SMARTS
2455379.61	B	19.152	0.032	SMARTS
2455379.62	I	17.742	0.031	SMARTS
2455379.62	R	18.154	0.023	SMARTS
2455379.62	V	18.518	0.026	SMARTS
2455380.54	B	18.972	0.027	SMARTS
2455380.55	I	17.519	0.025	SMARTS
2455380.55	R	17.997	0.020	SMARTS
2455380.55	V	18.400	0.023	SMARTS
2455382.55	B	18.881	0.030	SMARTS
2455382.55	I	17.480	0.031	SMARTS
2455382.55	R	17.947	0.024	SMARTS
2455382.56	V	18.314	0.028	SMARTS
2455385.70	B	19.033	0.030	SMARTS
2455385.71	I	17.692	0.030	SMARTS
2455385.71	R	18.086	0.022	SMARTS
2455385.71	V	18.283	0.023	SMARTS
2455388.53	B	18.961	0.028	SMARTS
2455388.53	I	17.473	0.026	SMARTS
2455388.54	R	17.938	0.020	SMARTS
2455388.54	V	18.362	0.023	SMARTS
2455390.61	B	18.691	0.022	SMARTS
2455390.61	I	17.392	0.023	SMARTS
2455390.62	R	17.788	0.017	SMARTS
2455390.62	V	18.144	0.020	SMARTS
2455393.56	B	18.864	0.035	SMARTS
2455393.56	I	17.448	0.030	SMARTS
2455393.56	R	17.879	0.021	SMARTS
2455393.57	V	18.260	0.025	SMARTS
2455400.64	B	18.743	0.076	SMARTS
2455400.64	I	17.590	0.075	SMARTS
2455400.64	R	17.971	0.064	SMARTS

Table C.1—Continued

HJD	Filter	Magnitude	1σ Uncertainty	Source
2455400.65	V	18.244	0.070	SMARTS
2455404.53	B	18.441	0.038	SMARTS
2455404.53	I	17.229	0.026	SMARTS
2455404.53	R	17.615	0.022	SMARTS
2455404.53	V	17.942	0.029	SMARTS
2455406.57	B	18.635	0.033	SMARTS
2455406.58	I	17.365	0.026	SMARTS
2455406.58	R	17.794	0.022	SMARTS
2455406.58	V	18.142	0.027	SMARTS
2455409.62	B	18.737	0.037	SMARTS
2455409.62	I	17.412	0.029	SMARTS
2455409.63	R	17.846	0.026	SMARTS
2455409.63	V	18.210	0.028	SMARTS

Vita

Ashley Sara Pagnotta was born in Houston, Texas, and grew up in Kingwood, Texas, graduating from Kingwood High School in 2002. She earned bachelor's degrees in physics and mathematics from Texas A&M University in 2007. She enrolled in graduate school at Louisiana State University in 2007, earned her master's degree in May 2010, and expects to receive her doctoral degree in May 2012. A clear night at a mountain-top observatory is one of her favorite things in the world. In her elusive spare time she knits compulsively, preferably with hand-dyed, natural fiber yarn. She looks forward to wearing all of her handknits when she moves to New York City to start a postdoctoral position at the American Museum of Natural History this fall.